國立交通大學
土木工程學系碩士班
碩士論文

受限緊砂回填土對擋土牆主動土壓力之影響

Active Earth Pressure on Retaining Walls

with Constrained Dense Backfill

研 究 生：黃亭淵

指導教授：方永壽 博士

中 華 民 國 一 百 年 九 月

受限緊砂回填土對擋土牆主動土壓力之影響

Active Earth Pressure on Retaining Walls

with Constrained Dense Backfill

研 究 生: 黃亭淵　　　Student：Ting-Yuan Huang

指導教授：方永壽 博士　Advisor：Dr. Yung-Show Fang

國 立 交 通 大 學 土 木 工 程 學 系 碩 士 班

碩士論文

A Thesis

Submitted to the Department of Civil Engineering

College of Engineering

National Chiao Tung University

in Partial Fulfillment of the Requirements

for the Degree of

Master of Engineering

in Civil Engineering

September, 2010

Hsinchu, Taiwan, Republic of China

中華民國一百年九月

受限緊砂回填土對擋土牆主動土壓力之影響

研究生 ：黃亭淵　　指導教授 ： 方永壽 博士

國立交通大學土木工程學系碩士班

摘要

　　本論文以試驗方法探討作用於垂直剛性擋土牆的側向土壓力，此擋土牆逐漸遠離受限之緊砂回填土。模型擋土牆設備試驗以渥太華砂為回填土材料，回填土高 0.5 公尺，岩石介面與水平線夾角 β 為 0°，60°，70°，80°和 90°。本研究使用震動夯實法製做緊砂回填土，以一座鋼製傾斜界面板模擬束制背填土的岩石介面。試驗結果顯示，震動夯實造成的額外水平應力隨擋土牆主動位移而消散。隨著逐漸減小的水平距離 b，和逐漸增大的介面板傾斜角度 β，介面板逐漸侵入主動土楔，造成位於接近擋土牆底部的側向土壓力減少。於不同的 b 與 β 值，試驗獲得的主動土壓合力比 Coulomb 解大 25.1%至比 Coulomb 解小 24.2%。主動土壓合力作用點位置隨 β 角的增加而上升。於不同的 b 與 β 值，試驗得到的主動土壓合力作用點$(h/H)_a$ 值分布為 0.475 至 0.333。 無因次化的主動土壓力矩介於 0.0801 至 0.0599 之間，大於 Coulomb 主動土壓力矩 33.5%至 0%。鄰近傾斜岩石介面的存在略為降低擋土牆抗傾倒之安全係數，依據 Coulomb 主動土壓力理論預估求出之抗傾倒安全係數將不安全。

關鍵字：主動土壓力、受限背填土、土壓力、模型試驗、擋土牆、緊砂

Active Earth Pressure on Retaining Walls
with Constrained Dense Backfill

Student : Ting-Yuan Huang   Advisor : Dr. Yung-Show Fang

Department of Civil Engineering

National Chiao Tung University

Abstract

This paper presents the experimental data of lateral earth pressure acting on a vertical rigid wall, which moved away from a limited backfill of dry sand. A model retaining-wall facility was used and dense Ottawa sand was used as backfill material. The thickness of backfill was 500 mm and rock face inclination angles of 0, 60, 70, 80 and 90 degrees were investigated. The dense backfill was prepared by vibratory compaction method. To simulate an inclined rock face, a steel interface plate was used. Test results showed that the extra lateral earth pressure due to vibratory compaction dissipated with the active wall movement. As the interface angle β increased or spacing b decreased, the inclined rock face intruded the active soil wedge, the earth pressure decreased near the base of the wall. The experimental active soil thrust for different b and β varied from 25.1% greater to 24.2% less than Coulomb's solution. The point of application of the active soil thrust ascended with increasing β angle. For tests with different b and β, the experimental $(h/H)_a$ varied from 0.475 to 0.333. The experimental normalized driving moment varied from 0.0801 to 0.0599, which was about 33.5% to 0% greater than Coulomb's theoretical solution. The existence of a nearby inclined rock face would slightly decrease the factor of safety against overturning. The estimation of the factor of safety against overturning with Coulomb's theory would be unsafe.

Keywords: Active pressure; Constrained backfill; Earth pressure; Model test;
Retaining wall; Dense Sand

Acknowledgements

Table of Contents

List of Tables

List of Figures

xi

xiv

List of Symbols

b	=	Distance between Interface Plate and Model Wall
C_u	=	Uniformity Coefficient
D_r	=	Relative Density
D_{10}	=	Diameter of Ottawa Sand whose Percent finer is 10%
D_{60}	=	Diameter of Ottawa Sand whose Percent finer is 60%
e_{max}	=	Maximum Void Ratio of Soil
e_{min}	=	Minimum Void Ratio of Soil
F	=	Force
G_s	=	Specific Gravity of Soil
h	=	Location of Total Thrust
$(h/H)_a$	=	Point of Application of Active Soil Thrust
H	=	Effective Wall Height
i	=	Slop of Ground Surface behind Wall
K_o	=	Coefficient of Earth Pressure At-Rest
K_a	=	Coefficient of Active Earth Pressure
K_h	=	Coefficient of Horizontal Earth Pressure
$K_{a,h}$	=	Coefficient of Horizontal Active Earth Pressure
P_a	=	Total Active Force
β	=	Angle of Inclination Rock Face
S	=	Wall Displacement
T	=	Translation
z	=	Depth from Surface
σ_h	=	Horizontal Earth Pressure
σ_N	=	Normal Stress

γ = Unit Weight of Soil

ϕ = Angle of Internal Friction of Soil

δ_i = Angle of Interface Friction

δ_{sw} = Angle of Side-Wall Friction

δ_w = Angle of Wall Friction
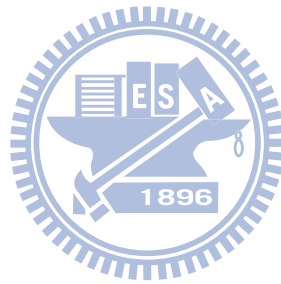
Chapter 1

Introduction

Traditionally, civil engineers build retaining structures to resist the active force from the backfill. In most cases, civil engineers calculate the active earth pressure behind a retaining wall using either Coulomb's or Rankine's theory. They postulate that earth pressure distribution is linear, and the location of resultant force is located at 1/3 of the wall hight above the wall base. If there is a rock face near the retaining wall,see Fig. 1.1. the influence of the adjacent rock face on the active earth pressure deserved to be investigated.This thesis studies the effects of a constrained dense cohesionless backfill on the active earth pressure against a retaining wall as shown in Fig. 1.1. In the figure, an inclined rock face is near the retaining wall. The backfill is constrained and the active soil failure wedge behind the wall can not develop fully. Under such a condition, the active earth pressure may be different from Coulomb's and Rankine's solutions.
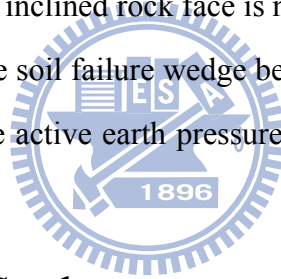
1.1 Objectives of Study

Valuable studies associated with earth pressure on retaining walls with constrained backfill had been conducted. Based on the arching theory, Spangler and Handy (1984) developed a theoretical equation for calculating the lateral earth pressure acting on the wall of a silo. The granular particles in the silo were constrained by the vertical silo walls. Based on the limit equilibrium method and the computer program ReSSA 2.0, Leshchinsky et al. (2004) numerically investigated the lateral earth pressure on a Mechanically-Stabilized-Earth wall with constrained fill. Fan and Fang (2010) used the non-linear finite element program PLAXIS (PLAXIS BV, 2002) to investigate the earth pressure against a rigid wall close to an inclined rock face. Huang (2009) used the model retaining wall facilities at National Chiao Tung University to investigate the active earth pressure on retaining walls

with loose sand backfill near an inclined rock face. Chen (2010) extended the study of Huang (2009) by setting extra position for the inclined rock face (b=150,250,350 and 500 mm). However, the test results reported by Huang (2009) and Chen (2010) were limited for a model wall with a loose backfill (relative density = 36%).

From a practical point of view, it would be necessary to know what is influence of an inclined rock face on active earth pressure for a retaining wall with compacted dense backfill. In this study, the sandy backfill was compacted with a vibratory compactor to a relative density of about 79%. The experimental results are compared with theoretical and numerical solutions.

1.2 Research Outline

To study the effects of an adjacent inclined rock face on the active earth pressure, the National Chiao Tung University (NCTU) model retaining wall facility was modified to investigate the effects of a constrained backfill on the active earth pressure. In Fig. 1.1, the major parameters considered were the horizontal spacing b between the wall and the base of the rock face, and the rock face inclination angle β. Fig. 1.2 shows the model wall with the backfill for b = 2000 mm. Fig. 1.3 to Fig. 1.9 shows all constrained condition for backfill for b = 50, 100, 150, 250, 350, and 500 mm with β = 60°, 70°, 80°, and 90°. For all tests, the height of the backfill H was 0.5 m, and air-dry Ottawa sand was used as the backfill material. To obtain a dense backfill, the soil was compacted by a square and a strip vibratory compactor to achieve the desired relative density of 79%. The variation of lateral earth pressure σ_h was measured with the soil pressure transducers (SPT) on the surface of the model wall. Based on experimental results, the distribution of active earth pressure was obtained. Based on the test results, the magnitude of active soil thrust and the location of the active thrust were calculated and compared with the Coulomb and Rankine solutions.

1.3 Organization of Thesis

This paper is divided into the following parts:

Chapter 1: Introduction of the subject

Chapter 2: Review of past investigations regarding the active earth pressures theories, numerical studies and laboratory test results

Chapter 3: Description of experimental apparatus

Chapter 4: Description of the Interface plate and supporting system

Chapter 5: Characteristics of the backfill and interfaces

Chapter 6: Test results regarding horizontal earth pressure and active soil thrust

Chapter 7: Conclusions and design recommendations
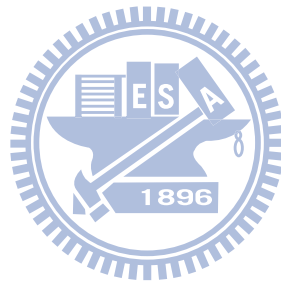
Chapter 2

Literature Review

Geotechnical engineers frequently use the Coulomb and Rankine's earth pressure theories to calculate the active earth pressure behind retaining structures. These theories are discussed in the following sections. Mackey and Kirk (1967), Fang and Ishibashi (1986), Huang (2009) and Chen (2010) made experimental investigations regarding active earth pressure. Frydman and Keissar (1987) used the centrifuge technique to test a small model wall. Numerical investigation was studied by Leshchinsky, et al. (2004) and Fan and Fang (2009). Their major findings are introduced in this chapter.

2.1 Active Earth Pressure Theories

2.1.1 Coulomb Earth Pressure Theory

Coulomb (1776) proposed a method of analysis that determines the resultant horizontal force on a retaining system for any slope of wall, wall friction, and slope of backfill. The Coulomb theory is based on the assumption that soil shear resistance develops along the wall and the failure plane. Detailed assumptions are made as the followings:

1. The backfill is isotropic and homogeneous.

2. The rupture surface is plane, as plane BC in Fig. 2.1(a). The backfill surface AC is a plane surface as well.

3. The frictional resistance is distributed uniformly along the rupture surface BC.

4. Failure wedge is a rigid body.

5. There is a friction force between soil and wall when the failure wedge
   moves toward the wall.

6. Failure is a plane strain condition.

In order to develop an active state, the wall is designed to move away from the soil mass. If the wedge ABC in Fig. 2.1(a) moves down relative to the wall, the wall friction angle δ will develop at the interface between the soil and wall. Let the weight of wedge ABC be W and the force on BC be F. With the given value θ and the summation of vertical forces and horizontal forces, the resultant soil thrust P can be calculated as shown in Fig. 2.1(b).

Similarly, the active forces of other trial wedges, such as ABC_2, ABC_3 in Fig 2.2 can be determined. The maximum value of P_a thus determined is the Coulomb's active force.

$$P_a = \frac{1}{2}\gamma H^2 K_a \qquad (2.1)$$

where

P_a = total active force per unit length of wall

K_a = coefficient of active earth pressure

γ = unit weight of soil

H = height of wall

And

$$K_a = \frac{\sin^2(\phi+\beta)}{\sin^2\beta\sin(\beta-\delta)\left\{1+\sqrt{\dfrac{\sin(\phi+\delta)\sin(\phi-i)}{\sin(\beta-\delta)\sin(\beta+i)}}\right\}^2} \qquad (2.2)$$

where

ϕ = internal friction angle of soil

δ = wall friction angle

β = slope of back of the wall to horizontal

i = slope of ground surface behind wall

2.1.2 Rankine Earth Pressure Theory

Rankine (1857) considered the soil in a state of plastic equilibrium and used essentially the same assumptions as Coulomb. The Rankine theory further assumes that there is no wall friction and failure surfaces are straight planes, and that the resultant force acts parallel to the backfill slope. Detailed assumptions are made as the followings:

1. The backfill is isotropic and homogeneous.

2. The retaining wall is a rigid body. The wall surface is vertical and the friction force between the wall and the soil is neglected.

Rankine assumed no friction between wall surface and backfill, and the backfill is cohesionless. The earth pressure on plane AB of Fig. 2.3(a) is the same as that on plane AB inside a semi-infinite soil mass in Fig. 2.3(b). For active condition, the active earth pressure σ_a at a given depth z can be expressed as:

$$\sigma_a = \gamma z K_a \tag{2.3}$$

The total active force P_a per unit length of the wall is equal to

$$P_a = \frac{1}{2}\gamma H^2 K_a \tag{2.4}$$

The direction of resultant force P_a is parallel to the ground surface as Fig. 2.3(b), where

$$K_a = \cos i \frac{\cos i - \sqrt{(\cos^2 i - \cos^2 \phi)}}{\cos i + \sqrt{(\cos^2 i - \cos^2 \phi)}} \tag{2.5}$$

2.1.3 Terzaghi General Wedge Theory

The assumption of plane failure surface made by Coulomb and Rankine, however, does not apply in practice. Terzaghi (1941) suggested that part of the failure surface in the backfill under an active condition was a log spiral curve, like the curve bd in Fig. 2.4. But the failure surface dc is still assumed a plane.

Fig. 2.5 illustrates the procedure to elevate the active resistance by trial wedge method (Terzaghi and Peck, 1967). The line d_1c_1 makes an angle of $45° + \phi/2$ with the surface of the backfill. The arc bd_1 of trial wedge abd_1c_1 is a logarithmic spiral formulated as the following equation

$$r_1 = r_0 e^{\theta \tan \phi} \tag{2.6}$$

O_1 is the center of the log spiral curve in Fig. 2.5, where $O_1b = r_1$, $O_1d_1 = r_0$, and $\angle bO_1d_1 = \theta$. For the equilibrium and the stability of the soil mass abd_1f_1 in Fig. 2.6, the following forces per unit width of the wall are considered:

1. Soil weight per unit width in abd_1f_1: $W_1 = \gamma \times$ (area of abd_1f_1)

2. The vertical face d_1f_1 is in the zone of Rankine's active state; hence, the force

P_{d1} acting on the face is

$$P_{d1} = \frac{1}{2} \gamma (H_{d1})^2 \tan^2 (45° - \frac{\phi}{2}) \tag{2.7}$$

where

$H_{d1} = d_1f_1$

P_{d1} acts horizontally at a distance of $H_{d1}/3$ measured vertically

upward from d_1.

γ is the unit weight of soil

3. The resultant force of the shear and normal forces dF, acting along the surface of sliding bd_1. At any point of the curve, according to the property of the logarithmic spiral, a radial line makes an angle ϕ with the normal. Since the resultant dF makes an angle ϕ with the normal to the spiral at its point of application, its line of application will coincide with a radial line and will pass through the point O_1.

4. The active force per unit width of the wall P_1 acts at a distance of $H/3$ measured vertically from the bottom of the wall. The direction of the force P_1 is inclined at an angle δ with the normal drawn to the back face of the wall.

5. Moment equilibrium of W_1, P_{d1}, dF and P_1 about the point O_1:

$$W_1[l_2] + P_{d1}[l_3] + dF\ (0) = P_1[l_1] \tag{2.8}$$

or

$$P_1 = \frac{1}{l_1}[W_1 l_2 + P_{d1} l_3] \tag{2.9}$$

where l_2, l_3, and l_1 is the moment arm for force W_1, P_{d1}, and P_1, respectively.

The trial active forces per unit width in various trial wedges are shown in Fig. 2.7. Let P_1, P_2, P_3, …, and P_n be the force that respectively correspond to the trial wedges 1, 2, 3, …, and n. The forces are plotted to the same scale as shown in the upper part of the figure. A smooth curve is plotted through the points 1, 2, 3, …, n. The maximum P_3 of the smooth curve defines the active force P_a per unit width of the wall.

2.1.4 Spangler and Handy's Theory

Spangler and Handy (1984) have applied Janssen's (1895) theory to design

problem of fascia retaining walls. Fig. 2.8 defines the soils with a width B bounded by two unyielding frictional boundaries (the rock face and wall face). The vertical force equilibrium of the thin horizontal soil element in Fig. 2.9 requires

$$(V + dV) + 2K\mu \frac{V}{B} dh = V + \gamma B dh \tag{2.10}$$

This is a linear differential equation, the solution for which is

$$V = \gamma B^2 \frac{1 - e^{-2K\mu(h/B)}}{2K\mu} \tag{2.11}$$

where

$\mu = \tan \delta$, the coefficient of friction between the soil and the wall

$\gamma =$ unit weight of the soil

$B =$ backfill width

$h =$ backfill depth (i.e. z)

$K =$ the coefficient of lateral earth pressure

$V =$ the vertical force

From the solution of eq.(2.11), an equation for lateral earth pressure σ_h can be calculated

$$\sigma_h = \frac{\gamma B}{2\mu} \left[1 - e^{-2K\mu \left(h/B \right)} \right] \tag{2.12}$$

Some solutions for different values of B are shown in Fig. 2.10. The soil pressure, instead of continuing to increase with increasing values of h, levels off at a maximum value $\sigma_{h,max}$ defined as follows.

9

$$\sigma_{h,\max} = \frac{\gamma B}{2\mu} = \frac{\gamma B}{2\tan\delta} \qquad (2.13)$$

2.2 Laboratory Model Retaining Wall Tests

2.2.1 Model Study by Mackey and Kirk

Mackey and Kirk (1967) experimented on lateral earth pressure by using a steel model wall. This soil tank was made of steel with internal dimensions of 36 in. long × 16 in. wide × 15 in. high (914 mm × 406 mm × 381 mm) as shown in Fig. 2.11. In this investigation, when the wall moves away from the soil, the earth pressure decreases (see Fig. 2.12) and then increases slightly until it reaches a constant value. Mackey and Kirk reported that if the backfill is loose, the active earth pressure obtained experimentally are within 14 percent off those obtained theoretically from almost any of the methods list in Table 2.1.

Mackey and Kirk utilized a powerful beam of light to observe the failure surface in the backfill. It could trace the position of the shadow, formed by changes of the sand surface in different level. It was found that for each backfill, the failure surface in the backfill due to the translational wall movement was approximated a curve in the backfill (Fig. 2.13), rather than a plane assumed by Coulomb.

2.2.2 Model Study by Fang and Ishibashi

Fang and Ishibashi (1986) conducted laboratory model experiments to investigate the distribution of the active stresses due to three different wall movement modes: (1) rotation about top (RT mode), (2) rotation about base (RB mode), and (3) translation (T mode). The experiments were conducted at the University of Washington.

Fig. 2.14 shows the horizontal earth pressure distributions at different translational wall movements. The measured active stress is slightly higher than Coulomb's solution at the upper one-third of wall height H is 3.33 ft (1.01 m), approximately in agreement with Coulomb's prediction in the middle one-third, and lower than Coulomb' at the lower one-third of wall surface. However, the magnitude of the active total thrust P_a at S = 20×10^{-3} in. (0.5 mm) is nearly the same as that calculated from Coulomb's theory.

Fig. 2.15 shows lateral earth pressures measured at various depths decreased rapidly with the translational active wall displacement. Most measurements reach the minimum value at approximately 10×10^{-3} in (0.25 mm, or 0.00025H) wall displacement and stay steady thereafter.

Fig. 2.16 shows the K_a as a function of soil density and internal friction angle. In this figure, the K_a value decreases with increasing ϕ angle. The Coulomb's solution might underestimate the coefficient K_a for rotational wall movements.

2.2.3 Model Study by Huang

Huang (2009) used the model retaining wall facilities at National Chiao Tung University, the movable model retaining wall and its driving system are illustrated in Fig. 2.17. The model wall is a 1,000-mm-wide, 550-mm-high, and 120-mm-thick solid plate, and is made of steel. The soil bin is fabricated of steel members with inside dimensions of 2,000 mm x 1,000 mm x 1,000 mm. The effective wall-height H (or height of backfill above wall base) is only 500 mm.

To investigate the active earth pressure on retaining walls near an inclined rock face. The parameters considered for that study were the rock face inclination angles β = 0°, 50°, 60°, 70°, 80° and 90°, the horizontal spacing b = 0, 50 mm and 100 mm. In Fig. 2.17, the interface plate was inserted into the base support block at the horizontal distance of b = 100 mm from the base of the model wall, and with the

inclination angles β =50°.

Distributions of horizontal earth pressure σ_h measured at different stages of horizontal wall displacements S/H was illustrated in Fig. 2.18, Fig. 2.19 and Fig. 2.20. It has been found that for the wall with a nearby inclined rock face, the active earth pressure measured at the upper part of the wall was in good agreement with Coulomb's prediction. However, the active pressure measured at the lower part of the wall was lower than Coulomb's prediction. If the inclined rock face was adjacent to the wall, only a thin layer of backfill was sandwiched between the rock face and the wall. It was impossible for the active soil wedge to develop behind the wall, therefore the active pressure was less than Coulomb's prediction.

For b = 0, Fig. 2.21 (a) presents the variation of horizontal earth pressure coefficient K_h as a function of wall movement for various β angles. The magnitude of active earth pressure coefficient decreased with increasing interface inclination angle β. Fig. 2.21 (b) showed the variations of the point of application of the soil force as a function of wall movement for various β angles. It was apparent that the points of application of the active soil forces ascended with increasing β angle.

2.2.4 Model Study by Chen

Chen (2010) extended the study of Huang (2009) by setting extra position for the inclined rock face (b=150,250,350 and 500 mm). In Fig 2.22, the interface plate was inserted into the base support block at the horizontal distance of b = 150 mm from the base of the model wall, and with the inclination angles β.

Fig. 2.23 shows the distributions of horizontal earth pressure σ_h measured at different stages of horizontal wall displacements S/H for various b and β. For b = 500 mm, the measured σ_h was close to Coulomb's solution, the measured stress was not affected by the existence of the vertical plate. With the approahing of the interface plate, σ_h decreased with the increasing of angles β and the decreasing of

space b.

Variation of earth pressure coefficient K_h with wall movement illustrated in Fig. 2.24. with the approaching of the interface plate, the soil mass behind the wall decreased. The active earth pressure coefficient $K_{a,h}$ decreased with increasing interface inclination angle β or decreasing spacing b.

Fig.2.25 show the variation of total thrust location with wall movement, the point of application of active soil thrust was located at about H/3 above the wall base.

2.3 Numerical Studies

2.3.1 Numerical Study by Leshchinsky et al.

Leshchinsky et al. (2004) used the limit equilibrium method with computer program ReSSA 2.0 (ADAMA, 2003) to numerically investigate the lateral earth pressure acting on a Mechanically-Stabilized-Earth wall. A baseline 5m-high wall was specified, the geometrical modeling was shown in Fig. 2.26(a). A single layer of reinforcement at 1/3 of the height of the wall was simulated in the analysis. In Fig. 2.26 the foundation was considered as competent bedrock to eliminate external effects on its stability. Various types of reinforced cohesionless fill were used in the analysis, all having a unit weight of $\gamma = 20$ kN/m^3 and the internal angle of friction ϕ of the fill varying from 20° to 45°. Fig. 2.26(b) shows the base width of the fill was B, and the slope of the rear section of the fill was m.

Fig. 2.27 shows the results predicted by ReSSA versus values reported by Frydman and Keissar (1987). The bedrock constraining the sand in all tests was vertical (i.e., $m = \infty$). Frydman and Keissar (1987) reported an internal angle of friction of 36° and interface friction between the aluminum and sand $\delta = 20°\sim25°$. Note that rather than using K_a', the ratio K_a'/K_a is used, $K_a = \tan^2(45^\circ - \phi/2)$ is

Rankine's active lateral earth pressure coefficient. Fig. 2.27 implies that as the retained soil space narrows (i.e., H/B increases) both ReSSA and the experimental data show the K_a'/K_a ratio decreases.

Fig. 2.28 presents the variation of active earth pressure coefficient K_a' as a function of the rock face slope m. K_a' was determined with the numerical analysis, and K_a was calculated with the Rankine theory $K_a = \tan^2(45° - \phi/2)$. The normalization of K_a' with K_a produces charts that are independent of ϕ. For B = 0, the coefficient K_a' rapidly decreased with increasing slope m. The amount of fill between the wall and bedrock was very small. For B = 0.1H and 0.2H, K_a' also decreases with increasing slope m, however the space between the wall and the bedrock slope was becoming wider.

2.3.2 Numerical Study by Fan and Fang

Fan and Fang (2010) used the non-linear finite element program PLAXIS (PLAXIS BV, 2002) to investigate the earth pressure against a rigid wall close to an inclined rock face (Fig. 2.29). The wall used for analysis is 5 m high, the back of the wall is vertical, and the surface of the backfill is horizontal. Typical geometry of the backfill zone used in the study is shown in Fig. 2.29. To investigate the influence of the adjacent rock face on the behavior of earth pressure, the inclination angle β of the rock face and the spacing b between the wall and the foot of the rock face were the parameters for numerical analysis. The wall was prevented from any movement during the placing of the fill. After the filling process, active wall movement was allowed until the earth pressure behind the wall reached the active condition. The finite element mesh, for a retaining wall with restrained backfill space (β = 70° and b = 0.5 m) is shown in Fig. 2.30. The finite element mesh consists of 1,512 elements, 3,580 nodes, and 4,536 stress points.
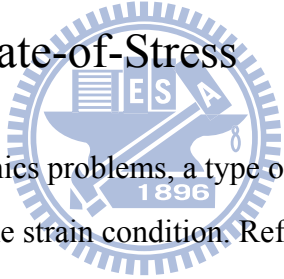
Base on the numerical analysis, distributions of horizontal earth pressures with the depth (z/H) at various wall displacements for b = 0.5 m and β = 80° are shown in Fig.

2.31. In the figure, the distribution of active earth pressure with depth is non-linear. Due to the nearby rock face, the calculated active pressure is considerably less than that computed using the Coulomb's theory.

Fig. 2.32 shows the variation of the active earth pressure coefficient ($K_{a(Computed)} / K_{a(Coulomb)}$) as a function of the inclination angle β of the rock face and the wall-rock spacing b, for walls under translation movement. For $\beta > 60°$, the analytical active K values are less than those calculated with Coulomb's solution. The analytical K value decreased with increasing β angle.

Fig. 2.33 shows the variation of the location of active soil thrust with the β angle and wall-rock spacing b. For $\beta > 60°$, the active soil thrust rises with increasing β angles, and the active h/H value increased with decreasing fill width b.

2.4 Plane Strain State-of-Stress

In many soil mechanics problems, a type of state-of-stress that is often encountered is the plane strain condition. Referring to Fig. 2.34, for the retaining wall, the normal strain in the y direction at any point P in the soil mass is equal to zero ($\varepsilon_y = 0$). To reduce the side wall deflection due to lateral earth pressure, the NCTU model retaining wall used U-shaped steel beams and steel columns to confine the side walls deformation. The soil bin is nearly rigid that lateral deformation of side wall becomes negligible.

The normal stresses σ_y at all sections in the xz plane (intermediate principal plane) are the same, and the shear stresses on these xz planes are zero ($\tau_{yx} = \tau_{yz} = 0$). To minimun the side wall friction on xz plane, the NCTU model retaining wall uesd lubrication layers (Fang et al. 2004) to reduce the interface friction between the sidewall and the backfill.

Under a plane-strain state of stress, the normal and shear stresses on the yz plane are equal to σ_x and τ_{xz}. Similarly, the normal and shear stress on the xy

15

plane are σ_z and τ_{zx} ($\tau_{zx} = \tau_{xz}$). The relationship between the normal stresses can be expressed as

$$\varepsilon_y = \frac{\sigma_y}{E} - v(\frac{\sigma_x}{E}) - v(\frac{\sigma_z}{E}) \qquad (2.14)$$

where v is Poisson's ratio.

for a plane strain condition, $\varepsilon_y = 0$

$$0 = \sigma_y - v\sigma_x - v\sigma_z$$

$$\sigma_y = v(\sigma_x + \sigma_z) \qquad (2.15)$$
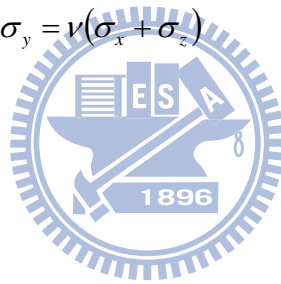
Chapter 3

Experimental Apparatus

To study the earth pressure behind retaining structures, the National Chiao Tung University (NCTU) has built a movable model wall which can simulate different kinds of wall movements. All of the investigations described in the thesis were conducted in this model wall, which will be discussed in this chapter. The entire facility consists of four components namely, model retaining wall, soil bin, driving system, and data acquisition system. The arrangement of the NCTU model retaining wall system is shown in Fig. 3.1.

3.1 Model Retaining Wall

The movable model retaining wall and its driving systems are shown in Fig. 3.1. The model wall is a 1000-mm-wide, 550-mm-high, and 120-mm-thick solid plate, and is made of steel. Note that in Fig. 3.1 the effective wall height H is only 500 mm. The retaining wall is vertically supported by two unidirectional rollers , and is laterally supported by four driving rods. Two sets of wall-driving mechanisms, one for the upper rods and the other for the lower rods, provide various kinds of movements for the wall. A picture of the NCTU model wall facility is shown in Fig. 3.2.

Each wall driving system is powered by variable-speed motor. The motors turn the worm driving rods which cause the driving rods to move the wall back and forth. Fig. 3.3 shows two displacement transducers (Kyowa DT-20D) are installed at the back of retaining wall and their sensors are attached to the movable wall. Such an arrangement of displacement transducers would be effective in describing the wall translation.

To investigate the distribution of earth pressure, nine earth pressure transducers

were attached to the model wall. The arrangement of the earth pressure cells should be able to closely monitor the variation of the earth pressure of the wall with depth. Base on this reason, the earth pressure transducers SPT1 through SPT9 have been arranged at two vertical columns as shown in Fig. 3.4.

A total of nine earth pressure transducers have been arranged within a narrow central zone to avoid the friction that might exist near the side walls of the soil bin as shown in Fig. 3.5. The Kyowa model PGM-02KG (19.62 kN/m^2 capacity) transducer shown in Fig. 3.6 was used for these experiments. To reduce the soil-arching effect, earth pressure transducers with a stiff sensing face are installed flush with the face of the wall. They provide closely spaced data points for determining the earth pressure distribution with depth.

3.2 Soil Bin

The soil bin is fabricated of steel members with inside dimensions of 2,000 mm × 1,000 mm × 1,000 mm (see Fig. 3.1). Both sidewalls of the soil bin are made of 30-mm-thick transparent acrylic plates through which the behavior of backfill can be observed. Outside the acrylic plates, steel beams and columns are used to confine the side walls to ensure a plane strain condition.

The end wall that sits opposite to the model retaining wall is made of 100 mm thick steel plates. All corners, edges and screw-holes in the soil bin have been carefully sealed to prevent soil leakage. The bottom of the soil bin is covered with a layer of SAFETY-WALK to provide adequate friction between the soil and the base of the soil bin.

In order to constitute a plane strain condition, the soil bin is built very rigid so that the lateral deformations of the side walls will be negligible. The friction between the backfill and the side walls is to be minimized to nearly frictionless, so that shear stress induced on the side walls will be negligible. To eliminate the

friction between backfill and sidewall, a lubrication layer with 3 layers of plastic sheets was furnished for all model wall experiments. The "thick" plastic sheet was 0.152 mm thick, and it is commonly used for construction, landscaping, and concrete curing. The "thin" plastic sheet was 0.009 mm thick. It is widely used for protection during painting, and therefore it is sometimes called painter's plastic. Both plastic sheets are readily available and neither is very expensive. The lubrication layer consists of one thick and two thin plastic sheets were hung vertically on each sidewall of the soil bin before the backfill was deposited. The thick sheet was placed next to the soil particles. It is expected that the thick sheet would help to smooth out the rough interface as a result of plastic-sheet penetration under normal stress. Two thin sheets were placed next to the steel sidewall to provide possible sliding planes. For more information regarding the reduction of boundary friction with the plastic-sheet method, the reader is referred to Fang et al. (2004).
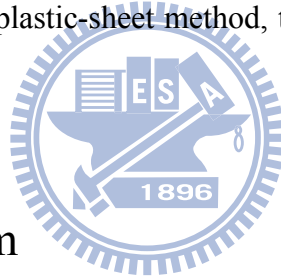
3.3 Driving System

Fig. 3.1 shows the variable speed motors M1 and M2 (Electro, M4621AB) are employed to compel the upper and lower driving rods, respectively. The shaft rotation compels the worm gear linear actuators, while the actuator would pull the model wall. To investigate the variation of earth pressure and the failure wedge caused by the translational wall movement, the motor speeds at M1 and M2 were kept the same speed of 0.005 mm/s for all experiments in this study.

3.4 Data Acquisition System

A data acquisition system was used to collect and store the considerable amount of data generated during the tests. The data acquisition system composed of four

parts: (1) dynamic strain amplifiers (Kyowa: DPM601A and DPM711B); (2) NI adaptor card (NIBNC-2090); (3) AD/DA card; and (4) personal computers shown in Fig. 3.7. An analog-to-digital converter digitized the analog signals from the sensors. The digital data were stored and processed by a personal computer. For more details regarding the NCTU retaining-wall facility, the reader is referred to Wu (1992) and Fang et al. (1994).

3.5 Vibratory Compactor

To simulate compaction of backfill in the field, the vibratory compactor shown in Fig. 3.8 and Fig.3.9 was made by attaching an eccentric motor (Mikasa Sangyo, KJ75-2P) to a 225 mm ×225 mm of square area steel plate. The height of the handle is 1,000 mm. The mass of the vibratory compactor is 12.1 kg. The technical information regarding the eccentric motor is listed in Table 3.1. It should be mentioned that the distribution of contact pressure between the foundation and soil varies with the stiffness of the footing.The square vibratory compactor was used to density large area of loose backfill as shown in Fig. 1.2.

For the model wall with a narrow backfill see Fig. 1.5, the square vibratory compactor is not.   To compact a narrow backfill, a strip vibratory compactor with a 500 mm × 90 mm rectangular footing shown in Fig. 3.10 was used. Fig. 3.11 shows the compactor was made by attaching an eccentric motor (Mikasa Sangyo, KJ75-2P Fig. 3.12 (a)) on a 245 mm × 235 mm flat steel plate at the top of the steel tube. The strip compactor was equipped with a 1,850 mm-long steel tube so that the strip compacting plate (Fig. 3.12(b)) could be inserted in to the narrow-trench, the soil at the bottom of the trench could be properly compacted. The total mass of the strip soil compactor is 25.0 kg. Technical information associated with the eccentric motor are listed in Table 3.1. The steel tube transmitted the compaction energy from the eccentric motor down to the base plate, and the soil blow the plate can be

compacted(see Fig. 3.13).
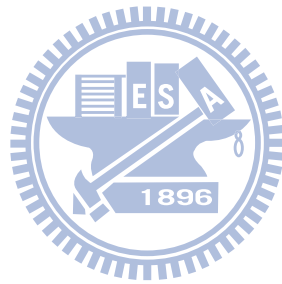
Chapter 4

Interface Plate and Supporting System

A steel interface plate is designed and constructed to fit in the soil bin to simulate the constrained backfill shown in Fig. 1.1. In Fig. 4.1, the plate and its supporting system were developed by Zheng (2008) and Chen (2010) to fit in the NCTU model retaining-wall facility. The interface plate consists of two parts: (1) steel plate; and (2) reinforcing steel beams. The supporting system consists of the following three parts: (1) top supporting beam; (2) base supporting block; and (3) base boards. Details of the interface plate and its supporting system are introduced in the following sections.

4.1 Interface Plate
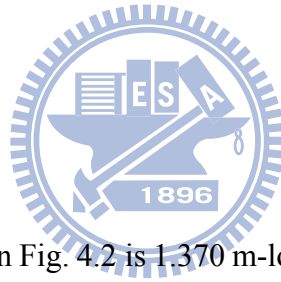
4.1.1 Steel Plate

The steel plate shows in Fig. 4.2 is 1.370 m-long, 0.998 m-wide, and 5 mm-thick. The unit weight of the steel plate is 76.52 kN/m^3 and its total mass is 83 kg (814 N). A layer of anti-slip material (SAFETY-WALK, 3M) was attached on the steel plate to simulate the friction that acts between the backfill and rock face as illustrated in Fig. 4.2 and Fig. 4.3(a). For the wall height H = 0.5 m and the inclination angle β = 50^o(see Fig. 4.4), the length of the interface plate should be at least 1.370 m. On the other hand, the inside width of the soil bin is 1.0 m. In order to put the interface plate into the soil bin, the width of the steel plate has to less than 1.0 m. As a result, the steel plate was designed to be 1.370 m-long and 0.998 m-wide.

4.1.2 Reinforcement with Steel Beams

To simulate the rock face shown in Fig. 1.1, the steel interface plate should be nearly rigid. To increase the rigidity of the 5 mm-thick steel plate, Fig. 4.2 (b) and Fig.

4.4 (b) show 5 longitudinal and 5 transverse steel L-beams were welded to the back of steel plate. Section of the steel L-beam (30 mm × 30 mm × 3 mm) was chosen as the reinforced material for the thin steel plate. At the top of the interface plate, a 65 mm × 65 mm × 8 mm steel L-beam was welded to reinforce the connection between the plate and the hoist ring shown in Fig. 4.3 (b).

4.2 Supporting System

To keep the steel interface plate in the soil bin stable during testing, a new supporting system for the interface plate was designed and constructed by Chen (2010). A top-view of the soil bin and base supporting frame is illustrated in Fig. 4.5. The supporting system composed of the following three parts: (1) top supporting beam; (2) base supporting block and (3) base boards. These parts are discussed in following sections.
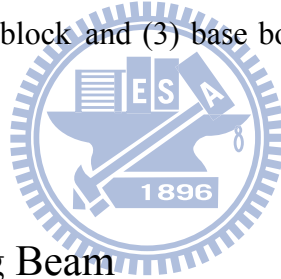
4.2.1 Top Supporting Beam

In Fig. 4.1, the top supporting steel beam was placed at the back of the interface plate and fixed at the bolt slot on the side wall of the soil bin(Fig. 4.5). Details of top supporting beam are illustrated in Fig. 4.6. The section of supporting L-shape steel beam is 65 mm × 65 mm × 8 mm and its length is 1,700 mm. Fig. 4.5 shows bolt slots were drilled on each side of the steel beam on the side wall of the soil bin. Locations of bolt slots were calculated for the interface plate located at difference horizontal spacing b and inclined angle β. Fig. 4.7 showed the top supporting beam was fixed at the slots with bolts.

4.2.2 Base Supporting Block

The base supporting block used to support the steel interface plate is shown in

Fig. 4.8. The base supporting block is 1.0 m-long, 0.6 m-wide, and 0.113 m-thick. Fig.4.8 shows seven trapezoidal grooves were carved to the face of the base supporting block (Fig. 4.9). The different horizontal spacing b adopted for testing included: (1) b = 0; (2) b = 50 mm; (3) b = 100 mm; (4) b = 150 mm; (5) b = 250 mm; (6) b = 350 mm; and (7) b = 500 mm.

4.2.3 Base Boards

Fig. 4.4 shows 6 pieces of base boards are stacked between the base supporting block and the end wall, to keep the base block stable. The base boards show in Fig. 4.10(a) is 1,400 mm-long, 1,000 mm-wide and 113 mm-thick. To provide adequate friction between the backfill and the base board, the surface of the top base board was cover with a layer of anti-slip material SAFETY-WALK(see Fig. 4.10(b)).

Chapter 5

Backfill and Interface Characteristics

This chapter introduces the properties of the backfill soil, and the interface characteristics between the backfill and the wall, backfill and sidewall, and backfill and interface olate. Laboratory experiments have been conducted to investigate the following subjects: (1) backfill properties; (2) model wall friction; (3) side wall friction; (4) interface plate friction; and (5) distribution of soil density in the backfill.

5.1 Backfill Properties

Air-dry Ottawa sand (ASTM C-778) was used throughout this investigation. Physical properties of the soil include G_s= 2.65, e_{max}= 0.76, e_{min}= 0.50, D_{60}= 0.40 mm, and D_{10}= 0.22 mm. Grain-size distribution of the backfill is shown in Fig. 5.1. Major factors considered in choosing Ottawa sand as the backfill material are summarized as follows.

1. Its round shape, which avoids effect of angularity of soil grains.

2. Its uniform distribution of grain size (coefficient of uniformity C_u=1.82), which avoids the effects due to soil gradation.

3. High rigidity of solid grains, which reduces possible disintegration of soil particles under loading.

4. Its high permeability, which allows fast drainage of pore water and therefore reduces water pressure against the wall.

To establish the relationship between the unit weight γ of backfill and its internal friction angle ϕ, direct shear tests have been conducted. The shear box used has a square (60 mm×60 mm) cross-section, and its arrangement is shown in Fig. 5.2.

Chang (2000) established the relationship between the internal friction angle ϕ

and unit weight γ of the Ottawa sand as shown in Fig. 5.3. It is obvious from the figure that soil strength increases with increasing soil density. For the compacted backfill, an empirical relationship between soil unit weight γ and ϕ angle can be formulated as follows:

$$\phi = 7.25\gamma - 79.51 \tag{5.1}$$

where

ϕ = angle of internal friction of soil (degree)

γ = unit weight of backfill (kN/m^3)

Eq. (5.1) is applicable for $\gamma = 15.8 \sim 17.05$ kN/m^3 only.

Assuming the unit weight of compacted soil is $\gamma = 16.8$ kN/m^3 the internal friction angle calculated with Equation (5.1) is 42.30.

5.2 Model Wall Friction

To evaluate the wall friction angle δ_w between the backfill and model wall, special direct shear tests have been conducted. A 88 mm × 88 mm × 25 mm smooth steel plate, made of the same material as the model wall, was used to replace the lower shear box. Ottawa sand was placed into the upper shear box and vertical load was applied on the soil specimen. The arrangement of this test is shown in Fig. 5.4.

To estimate the wall friction angles δ_w developed between the steel plate and sand, soil specimens with different unit weight were tested. Compaction method was used to achieve different soil density, and the test results are shown in Fig. 5.5. For compacted backfill, Ho (1999) suggested the following relationship:

$$\delta_w = 3.08\gamma - 37.54 \tag{5.2}$$

where

δ_w = wall friction of angle (degree)

γ = unit weight of backfill (kN/m^3)

Eq. (5.2) is applicable for γ = 16.0~17.0 kN/m^3 only.

The ϕ angle and δ_w angle obtained in section 5.1 and 5.2 are used for calculation of active earth pressure based on Coulomb, and Rankine's theories.

5.3 Side Wall Friction

To constitute a plane strain condition for model wall experiments, the shear stress between the backfill and sidewall should be eliminated. Lubrication layers fabricated with plastic sheets were equipped for all experiments to reduce the interface friction between the sidewall and the backfill. The lubrication layer consists of one thick and two thin plastic sheets as suggested by Fang et al. (2004). Plastic sheets were vertically hung next to the side-wall as shown in Fig. 5.6.
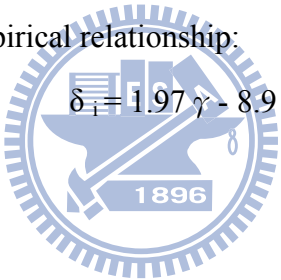
The friction angle between the plastic sheets and the sidewall was determined by the sliding block tests. The schematic diagram and the photograph of the sliding block test suggested by Fang et al. (2004) is illustrated in Fig. 5.7 and Fig. 5.8, respectively. The sidewall friction angle δ_{sw} is determined based on basic physics principles. In Fig. 5.8, the handle was turned to tilt the sliding plate until which the soil box on the plate starts to slide. When the soil starts to slip, the inclination angle that the plate makes with the horizontal is the side wall friction δ_{sw}.

Fig. 5.9 shows the variation of interface friction angle δ_{sw} with normal stress based on the sliding block tests. The friction angle measured was 7.5°. With the plastic – sheet lubrication method, the interface friction angle is almost independent of the applied normal stress. The shear stress between the acrylic side-wall and backfill has been effectively reduced with the plastic-sheet lubrication layer.

5.4 Interface Plate Friction

To evaluate the interface friction between the interface plate and the backfill, special direct shear tests were conducted as shown in Fig. 5.10. In Fig. 5.10(b), a 80 mm × 80 mm × 15 mm steel plate was covered with a layer of anti-slip material "SAFETY-WALK" to simulate the surface of the interface plate. The interface-plate was used to simulate the inclined rock face near the wall shown in Fig. 1.1. Dry Ottawa sand was placed into the upper shear box and vertical stress was applied on the soil specimen as shown in Fig. 5.10(a).

To establish the relationship between the unit weight γ of the backfill and the interface-plate friction angle δ_i, soil specimens with different unit weight were tested. Test results are shown in Fig. 5.11. For compacted backfill, Chen (2005) suggested the following empirical relationship:

$$\delta_i = 1.97\gamma - 8.9 \tag{5.3}$$

where

   δ_i = interface-plate friction angle (degree)

   γ = unit weight of backfill (kN/m^3)

   Eq. (5.3) is applicable for γ = 15.1 ~16.86 kN/m^3 only.

   If   γ = 16.8 kN/m^3, δ_i =24.2

The relationships between soil unit weight γ and friction angle for different interface materials are summarized in Fig. 5.12. The internal friction angle of Ottawa sand ϕ, model wall-soil friction angle δ_w, interface-plate friction angle δ_i, and lubricated sidewall friction angle δ_{sw} as a function of soil unit weight γ are compared in the figure. It is clear in Fig. 5.12 that, with the same unit weight, the order of the four different friction angles involved for the model wall experiment is ϕ＞δ_i ＞δ_w ＞δ_{sw}.

5.5 Control of Soil Density

5.5.1 Air-Pluviated loose Ottawa Sand

To achieve a uniform soil density in the backfill, Ottawa sand was deposited by air-pluviation method into the soil bin. The air-pluviation method had been widely used for a long period of time to reconstitute laboratory sand specimens. Rad and Tumay (1987) reported that pluviation is the method that provides reasonably homogeneous specimens with desired relative density. Lo Presti et al. (1992) reported that the pluviation method could be performed for greater specimens in less time.

Das (2010) suggested that relative densities of 15~50%, and 70~85% are defined as loose and dense condition, respectively. Ho (1999) established the relationship among slot opening, drop height, and density as shown in Fig. 5.13. To achieve a loose backfill (D_r = 32%), Chen (2003) adopted the drop height of 1 m and hopper slot opening of 15 mm. In Fig. 5.14 and Fig. 5.15. show, the soil hopper that let the sand flow through a calibrated slot opening at the lower end.

5.5.2 Compacted Dense Sand

To simulate the field conditions, dense backfill was achieved $D_r \geqq$ 70% for experiments in this study. The loose backfill was placed in 5 lifts, each lift was pluviated into the soil bin, carefully leveled, then compacted with a vibratory compactor. For b = 2000 mm (Fig.1.2), the square vibratory compactor shown in Fig.3.9 was used. As indicated in Fig. 5.16, the soil surface was divided into 4 lanes, and each lane was compacted with the moving speed of 8 mm/sec. Each compacted lift has a thickness of 0.1 m.

For the model wall with a narrow backfill (see Fig. 1.5), the square vibratory

compactor was too big to compacts the thin backfill sandwiched between the model wall and the interface plate. The strip vibratory compactor shown in Fig. 3.11 was developed used. As indicated in Fig. 5.17, the soil surface was divided into 2 lanes, and each lane was also compacted with the moving speed of 8 mm/sec. Each compacted lift has a thickness of 0.1 m.

In special conditions (see Fig. 1.3), even the 90 mm - wide compacting plate could not be inserted into 50 mm – wide the narrowtrench. Under such a circumstance, the 36 mm – thick wood square shown in Fig. 5.18 are used. Fig. 5.18(b), the compactor energy generated by the eccentric dotor was transmitted through the strip compactor plate, and the wood spacer, to density the backfill in the narrow trench.

5.5.3 Distribution of Soil Density

To investigate the distribution of soil density in the soil bin, soil density measurements were made. The soil density control cup made of acrylic is illustrated in Fig. 5.19 and Fig. 5.20, the density cups were used to measure the soil density at different elevations and locations.

In Fig. 5.21, interface plate was placed with the inclination angle $\beta = 90°$ and the horizontal spacing b = 350 mm. A layer of 100 mm-thick Ottawa sand was placed in the soil bin as a soil blanket. The bottom density cup was then put on the surface of soil blanket. Locations of the density cups buried in the fill are illustrated in Fig.5.21. Ottawa sand was placed layer by layer into the soil bin up to 0.5 m thick after compacted.

When the soil has been placed in the soil bin to the top, soil cups were dug out of the backfill carefully. Soil density is determined by dividing the mass of soil in the cup by the inside volume of the cup. The distributions of relative density of loose sand measured at different elevations are shown in Fig. 5.22. In the figure, for loose sand deposited by air-pluviation method, the mean relative density is 34.6%, with a

standard deviation of was 2.9%. After compaction for b = 350 mm and β = 90° with

the square and strip vibratory compactors, the mean relative density is 79.4%, with a

standard deviation of 2.7%.
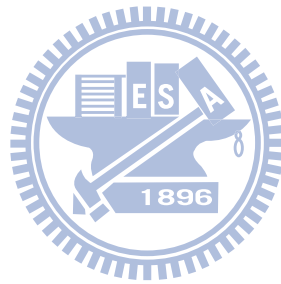
Chapter 6

Test Results

This chapter reports the experimental results of the lateral earth pressure on a retaining wall with constrained dense backfill. Test conditions for the interface plate located at the horizontal spacing b = 0, 50, 100, 150, 250, 350, 500 and 2,000 mm are illustrated in Fig. 1.2 to Fig. 1.9, respectively. The height of backfill H is 0.5 m and the vibratory compaction method was used to prepare the dense backfill for five 0.1 m –thick lifts. Dense Ottawa sand has a relative density D_r = 79.4 % and a unit weight γ = 16.7 kN/m^3. Based on direct shear tests by Ho, (1999) the corresponding internal friction angle ϕ for the dense backfill would be 42.4^o. The γ and ϕ values are used to calculate earth pressures based on the Jaky and Coulomb theories. The testing program for this study is summarized in Table 6.1.

6.1 Horizontal Earth Pressure without Interface Plate

The variation of horizontal earth pressure against the wall as function of active wall movement was investigated for b = 2,000 mm (Fig 6.1). After the dense backfill was placed into the soil bin as shown in Fig. 6.2 and Fig. 6.3, the model wall slowly moved away from the soil mass in a translation mode at the constant speed of 0.0050 mm/s.

Distributions of horizontal earth pressure σ_h measured at different stages of wall displacements S/H (S: horizontal wall displacement, H: backfill height) for Test 0427 and Test 0511 are illustrated in Fig. 6.4 and Fig. 6.5. Due to the extra stress induced by vibratory compaction, at S/H = 0 the measured σ_h was obviously higher than Jaky's solution. As the wall started to move, the earth pressure decrease, and eventually a limiting active pressure was reached. Active earth pressures calculated with Rankine and Coulomb theories are also indicated in the figure. The ultimate

experiment active pressure distribution at S/H = 0.003 approach the estimated with Coulomb and Rankine theories.

The variation of horizontal earth-pressure coefficient K_h as a function of wall displacement is shown in Fig. 6.6. The coefficient K_h is defined as the ratio of the horizontal component of total soil thrust P_h to $\gamma H^2/2$. The horizontal soil thrust P_h was calculated by summing the pressure diagram shown in Fig. 6.4 and Fig. 6.5. In Fig. 6.6 the coefficient K_h decreased with increasing wall movement S/H until a minimum value was reached then remained approximately a constant. The ultimate value of K_h is defined as the horizontal active earth-pressure coefficient $K_{a,h}$. In Fig. 6.6, the active condition was reached at approximately S/H = 0.0023.

In Fig. 6.6, it may not be an easy task to define the point of active wall movement S_a. For a wall that moved away from a dense sandy backfill in a translational mode, Mackey and Kirk (1967) concluded the wall displacement required to reach an active state is $S_a = 0.003$ H. The S_a values recommended by Mackey and Kirk (1967), NAVFAC DM-7.2 (1982) and Bowles (1988) are illustrated in Fig. 6.6. In this study the active wall movement is assumed to be $S_a = 0.003$ H.

Fig. 6.7 showed the point of application of the soil force as a function of wall movement. Note that h is defined as the vertical distance between the point of application of total resultant and wall base. The distance h is calculated by dividing the sum of moment of all measured pressure areas about the wall base by the horizontal soil resultant P_h. Theoretically, the point of application of the total soil thrust should act at about H/3 above the wall base (h/H = 0.333). Test results in Fig. 6.7 shows that the points of application of soil thrust are located at about 0.333 H above the wall base at the active wall movement (S/H)$_a$ = 0.003.

6.2 Horizontal Earth Pressure for b = 0

The model wall with a steel interface plate with b = 0 and β = 60° is shown in

Fig. 6.8 (a) and (b). The distributions of horizontal earth pressure at different stages of wall movement are shown in Fig. 6.9 and Fig. 6.10. The at-rest lateral pressure measured at S/H = 0 was much higher than Jack's prediction. For more information regarding the earth pressure due to vibratory compaction, the reader is referred to Chen and Fang (2008). The active pressure distribution was slightly less than Coulomb's solution at lower H/3 of the wall. Fig. 6.8 (a) shows the interface plate was near the lower part of wall face, thus the measured lateral stress was affected by the existence of the steel interface plate. The extra lateral earth pressure due to vibratory compaction dissipated with the active wall movement and lateral extension of the backfill.

Fig. 6.11 (a) and (b) show the inclined plate was installed in the soil bin with b = 0 and β = 70°. The distributions of earth pressure at different stages of wall movement are shown in Fig. 6.12 and Fig. 6.13. In Fig. 6.11 (a), the interface plate intruded the active soil wedge. As a result, the measured active earth pressure was less than Coulomb's solution at lower H/3 of the wall.

Fig. 6.14 (a) and (b) show the steel interface plate was placed in the soil bin for b = 0 and β = 80°. The distributions of earth pressure at different stages of wall movement are illustrated in Fig. 6.15 and Fig. 6.16. It was clear in Fig. 6.14 (a), the interface plate intruded the active soil wedge. It was possible that the active soil wedge cannot develop fully in the backfill. As a result, the measured active earth pressure at the active wall movement $(S/H)_a = 0.003$ was less than Coulomb's solution.

Fig. 6.17 to Fig. 6.19 presents the variation of horizontal earth pressure coefficient K_h as a function of wall movement for β = 60°, 70° and 80°. At S/H = 0, due to vibratory compaction, the earth pressure coefficient at-rest was much greater than the K_0 coefficient estimated with the Jaky equation. As the wall started to move, the lateral soil thrust decreased with increasing wall movement until a stable value was reached, then remained approximately a constant. The ultimate value of K_h was defined as the horizontal active earth pressure coefficient $K_{a,h}$. For b = 0, the active

condition was observed at approximately $(S/H)_a = 0.003$. At $(S/H)_a = 0.003$, the measured $K_{a,h}$ was close to Coulomb's solution. The extra lateral earth pressure locked-in the backfill dissipated with the active wall movement. In Fig. 6.19, for $\beta = 80°$, the measure $K_{a,h}$ coefficient was lower than Coulomb's prediction.

Fig. 6.20 to Fig. 6.22 demonstrate the variation of the point of application of the soil thrust as a function of active wall movement for $\beta = 60°$, $70°$ and $80°$. At the active wall movement of 0.003 H, for $\beta = 60°$, $70°$ and $80°$, the $(h/H)_a$ value was 0.45, 0.47 and 0.49, respectively. The point of application of the active soil thrust was located at a position higher than 1/3 H above the base of the wall. The point of application of active soil thrust rises with the increasing β angle. In Fig. 6.15 and Fig. 6.16, for $\beta = 80°$ the active earth pressure near the wall base was lower than Coulomb's prediction. Therefore, the active soil thrust moved to a higher location.

6.3 Horizontal Earth Pressure for b = 50 mm

The model wall with a steel interface plate with b = 50 mm and $\beta = 60°$ is shown in Fig. 6.23 (a) and (b). The distributions of horizontal earth pressure at different stages of wall movement are shown in Fig. 6.24 and Fig. 6.25. The at-rest lateral pressure measured at S/H = 0 was much higher than Jack's prediction. The active pressure distribution was close to Coulomb's solution, And Fig. 6.23 shows the interface plate was relatively far from the wall face, thus the measured lateral stress was not be strongly affected by the existence of the steel interface plate.

Fig. 6.26 (a) and (b) show the inclined plate was installed in the soil bin with b = 50 mm and $\beta = 70°$. The distributions of earth pressure at different stages of wall movement are shown in Fig. 6.27 and Fig. 6.28. It was clear in Fig. 6.26, the interface plate did not intrude the active soil wedge. It was possible for the active soil wedge to develop fully in the backfill. As a result, the measured active earth pressure was close to Coulomb's solution.

Fig. 6.29 (a) and (b) show the steel interface plate was placed in the soil bin for

b = 50 mm and β = 80°. The distributions of earth pressure at different stages of wall movement are illustrated in Fig. 6.30 and Fig. 6.31. At the active wall movement $(S/H)_a$ = 0.003, the measured σ_h was close to Coulomb's solution.

Fig. 6.32 (a) and (b) show the steel interface plate was placed in the soil bin for b = 50 mm and β = 90°. It is clear in the figures that only a thin layer of soil was sandwiched between the wall and the vertical interface plate. The distributions of earth pressure at different stages of wall movement are illustrated in Fig. 6.33 and Fig. 6.34. At the wall movement $(S/H)_a$ = 0.003, the active earth pressure near wall base is less than Coulomb's solution. Fig. 6.32 shows, the interface plate invaded so that the active soil wedge cannot develop fully. It is reasonable to expect the measured active σ_h to be less than Coulomb's prediction.

Fig. 6.35 to Fig. 6.38 presents the variation of horizontal earth pressure coefficient K_h as a function of wall movement for β = 60°, 70°, 80° and 90°. At S/H = 0, the earth pressure coefficient at-rest was much greater than the K_0 coefficient estimated with the Jaky equation. As the wall started to move, the lateral soil thrust decreased with increasing wall movement until a stable value was reached, then remained approximately a constant. The ultimate value of K_h was defined as the horizontal active earth pressure coefficient $K_{a,h}$. For b = 50 mm, the active condition was observed at approximately $(S/H)_a$ = 0.003. In Fig. 6.33 and Fig. 6.34, for β = 90°, the measure $K_{a,h}$ coefficient was lower than Coulomb's prediction.

The Fig. 6.39 to Fig. 6.42 demonstrate the variation of the point of application of the soil thrust as a function of active wall movement for β = 60°, 70°, 80° and 90°. At the $(S/H)_a$ = 0.003, for β = 60°, 70°, 80° and 90°, the $(h/H)_a$ values were 0.38, 0.40, 0.42 and 0.46. The point of application of the active soil thrust was located at a position higher than 1/3 H above the base of the wall. The point of application of active soil thrust rises with the increasing β angle.

6.4 Horizontal Earth Pressure for b = 100 mm

The steel interface plate with b = 100 mm and β = 60° is shown in Fig. 6.43 (a) and (b). The distributions of earth pressure at different stages of wall movement are shown in Fig. 6.44 and Fig. 6.45.

Fig. 6.46 (a) and (b) show the inclined plate was standing in the soil bin with b = 100 mm and β = 70°. In Fig. 6.46 (a), the interface plate does not intrude the active soil wedge. The distributions of earth pressure at different stages of wall movement are shown in Fig. 6.47 and Fig. 6.48. The active earth pressure was close to Coulomb's solution.

Fig. 6.49 (a) and (b) show the steel interface plate was placed in the soil bin for b = 100 mm and β = 80°. The distributions of earth pressure at different stages of wall movement are illustrated in Fig. 6.10 and Fig. 6.11. At S/H = 0.003, the measured σ_h was slightly lower than Coulomb's solution. It may be observed in Fig. 6.49 (a), the interface plate constrained the backfill so the active soil wedge can not develop fully. It is reasonable to expect the measured σ_h to be less than Coulomb's prediction.

Fig. 6.52 (a) and (b) show the steel interface plate was placed in the soil bin for b = 100 mm and β = 90°. It is clear in the figures that only a thin layer of soil was sandwhiched between the wall and the interface plate. The distributions of earth pressure at different stages of wall movement are illustrated in Fig. 6.53 and Fig. 6.54. At the wall movement S/H = 0.003, the active earth pressure is slightly less than Coulomb's solution at lower H/3 of the wall. In Fig. 6.52(a), the interface plate constrained the backfill so the active soil wedge cannot develop fully.

Fig. 6.55 to Fig. 6.58 presents the variation of horizontal earth pressure coefficient K_h as a function of wall movement for β = 60°, 70°, 80° and 90°. As the wall started to move, the lateral soil thrust decreased with increasing wall movement until a stable value was reached, then remained approximately a constant. For b =

100 mm, the active condition was observed at approximately S/H = 0.003.

Fig. 6.59 to Fig. 6.62 demonstrate the variation of the point of application of the soil thrust as a function of active wall movement for β = 60°, 70°, 80° and 90°. At the active wall movement of 0.003 H, for β = 60°, 70°, 80° and 90°, the $(h/H)_a$ values were 0.35, 0.37, 0.42 and 0.44. The point of application of the active soil thrust was located at a position higher than H/3 above the base of the wall.

6.5 Horizontal Earth Pressure for b = 150 mm

Fig. 6.63 (a) and (b) show the steel interface plate was placed in the soil bin for b = 150 mm and β = 70°. The distributions of earth pressure at different stages of wall movement are illustrated in Fig. 6.64 and Fig. 6.65. The measured σ_h was higher than Jaky's solution at S/H = 0. At the wall movement S/H = 0.003, the active earth pressure is close to Coulomb's solution.

Fig. 6.66 (a) and (b) show the steel interface plate was placed in the soil bin for b = 150 mm and β = 80°. In Fig. 6.66 (a), the interface plate does not intrude the active soil wedge. The distributions of earth pressure at different stages of wall movement are illustrated in Fig. 6.67 and Fig. 6.68. The measured σ_h was higher than Jaky's solution at S/H = 0. At S/H = 0.003, the measured σ_h was close to Coulomb's solution.

Fig. 6.69 (a) and (b) show the inclined plate was standing in the soil bin with b = 150 mm and β = 90°. The distributions of earth pressure at different stages of wall movement are shown in Fig. 6.70 and Fig. 6.71. The stress measured at S/H = 0 was higher than Jaky's solution, the active earth pressure was close to Coulomb's solution.

Fig. 6.72 to Fig. 6.74 presents the variation of horizontal earth pressure coefficient K_h as a function of wall movement for β = 70°, 80° and 90°. As the wall started to move, the lateral soil thrust decreased with increasing wall movement until a stable value was reached, then remained approximately a constant. For b = 150

mm, the active condition was observed at approximately S/H = 0.003. In Fig. 6.74 (β =90°), the K_h value at S/H = 0.003 was slightly lower than Coulomb's solution. In Fig. 6.69 (a), the interface plate constrained the backfill so the active soil wedge can not develop fully.

The Fig. 6.75 to Fig. 6.77 demonstrate the variation of the point of application of the soil thrust as a function of active wall movement for β = 70°, 80° and 90°. At the active wall movement of 0.003 H, for β = 70°, 80° and 90°, the $(h/H)_a$ values were 0.36, 0.40 and 0.42.

6.6 Horizontal Earth Pressure for b = 250 mm

Fig. 6.78 (a) and (b) illustrate the steel interface plate was placed in the soil bin for b = 250 mm and β = 80°. In Fig. 6.79 and Fig. 6.80, the distributions of earth pressure at different stages of wall movement are presented. The active earth pressure at S/H = 0.003 was close to Coulomb's solution.

Fig. 6.81 (a) and (b) show the steel interface plate was placed in the soil bin for b = 250 mm and β = 90°. The distributions of earth pressure at different stages of wall movement are shown in Fig. 6.82 and Fig. 6.83. The active earth pressure at S/H = 0.003 was close to Coulomb's solution. In Fig. 6.81 (a), the interface plate does not intrude the active soil wedge. The active soil wedge can develop fully, therefore, the measured active earth pressure was close to Coulomb's solution.

Fig. 6.84 to Fig. 6.85 show the variation of lateral soil thrust as a function of wall movement for β = 80° and 90°. As the wall started to move, the lateral soil thrust decreased with increasing wall movement until a stable value was reached, then remained approximately a constant.

Fig. 6.86 to Fig. 6.87 show the point of application of the soil thrust as a function of wall movement. At the active wall movement of 0.003 H, the $(h/H)_a$ values were 0.347 and 0.359 for β = 80°and 90°, respectively.

6.7 Horizontal Earth Pressure for b = 350 mm

Fig. 6.88 (a) and (b) illustrate the steel interface plate was placed in the soil bin for b = 350 mm and β = 90°. In Fig. 6.88 (a), the steel interface plate is away from the active soil wedge. The distributions of earth pressure at different stages of wall movement are shown in Fig. 6.89 and Fig. 6.90. At S/H = 0, the measured σ_h was higher than Jaky's solution. At active wall movement, the σ_h measured at S/H = 0.003 was close to Coulomb's solution.

Fig. 6.91 shows the variation of lateral soil thrust as a function of wall movement. As the wall started to move, the lateral soil thrust decreased with increasing wall movement until a stable value was reached, then remained approximately a constant. For b = 350 mm, the active condition was observed at approximately S/H = 0.003.

The Fig. 6.92 shows the point of application of the soil thrust as a function of wall movement. At the active wall movement of 0.003 H the $(h/H)_a$ values reached about 0.333. It may be concluded that the point of application of the total thrust was located at H/3 above the base of the wall.

6.8 Horizontal Earth Pressure for b = 500 mm

Fig. 6.93 (a) and (b) show the steel interface plate was placed in the soil bin for b = 500 mm and β = 90°. Fig. 6.94 and Fig. 6.95 show the distributions of earth pressure at different stages of wall movement. The lateral stress measured at S/H = 0 was higher than Jaky's solution, and the measured active earth pressure was close to Coulomb's solution. In Fig. 6.93 (a), the interface plate was relatively far from the wall and the active soil wedge. As a result, the measured stress was in good agreement with Jaky's and Coulomb's predictions.

Fig. 6.96 present the variation of lateral soil thrust as a function of active wall movement. As the wall started to move, the lateral soil thrust decreased with

increasing wall movement until a stable value was reached, then remained approximately a constant. For b = 500 mm, Fig. 6.96 shows the active condition was reached at the wall movement about S/H = 0.003.

Fig. 6.97 shows the point of application of the soil thrust as a function of wall. At the active wall movement of 0.003 H, the $(h/H)_a$ value was 0.333. It means that the active thrust was located at H/3 above the base of the wall.

6.9 Active Soil Thrust

The distributions of active earth pressure for interface plates with horizontal spacing b = 0, 50, 100, 150, 250, 350 and 500 mm with the difference interface inclination angle β were shown in Fig. 6.98 to Fig. 6.104. In Fig. 6.98, for b = 0 and β = 80°, the active earth pressure was lower than that for β = 60° and 70°. In Fig 6.8(a) and Fig 6.14(a), the plate inclination angle was β = 60° and β = 80°. In these figures, the amount of soil mass behind the wall decreased with increasing β angle. In Fig 6.8(a), the active soil wedge can fully develop in the backfill. The interface was relatively far from the retaining wall. It would be reasonable to expect the active earth pressure on the wall would to Coulomb's solution.

The variation of horizontal earth pressure coefficient K_h as a function of wall movement S/H for b = 0, 50, 100, 150, 250, 350 and 500 mm are shown in Fig. 6.105 to Fig. 6.111. In these figures, the active condition can be observed at the wall movement of S/H = 0.003. In Fig. 6.106, the active earth pressure coefficient $K_{a,h}$ for β = 60°, 70°, 80° and 90° is 0.195, 0.181, 0.167 and 0.134, respectively. With δ = 14.2°, the Coulomb's solution for $K_{a,h}$ was 0.179. It was clear in Fig. 6.106 that the active earth pressure coefficient $K_{a,h}$ increased with decreasing β angle. In Fig. 6.32 (a), the interface plate invaded so that the active soil wedge cannot develop fully. It is reasonable to expect the measured active σ_h to be less than Coulomb's prediction.

Fig. 6.112 to Fig. 6.118 present the point of application of the soil thrust as a function of wall movement for b = 0, 50, 100, 150, 250, 350 and 500 mm. In Fig.

6.113, from β = 60° to β = 90°, the value of h/H was increasing with the angle β. In Fig. 6.32 (a), the interface plate invaded so that the active soil wedge cannot develop fully. In Fig. 6.33, the active earth pressure near the wall base was lower than Coulomb's prediction. Therefore, the active soil thrust moved to a higher location. Without the interface plate invaded, see Fig. 6.117 and Fig. 6.118, the point of application of active soil thrust was located at about H/3 above the wall base.

6.10 Design Considerations

In the design of a rigid retaining structure, it is often necessary to check its adequacy. It is important to evaluate how the constrained backfill influence the Factor of Safety (F.S.) against sliding and overturning of the retaining wall.

6.10.1 Factor of Safety against Sliding

The factor of safety against sliding ($FS_{sliding}$) was defined as:

$$FS_{sliding} = \frac{\sum F_R}{\sum F_D} \tag{6.1}$$

where $\sum F_R$ = the sum of horizontal resisting forces and $\sum F_D$ = the sum of horizontal driving forces. For the retaining wall shown in Fig. 1.1, the horizontal driving force on the wall was the horizontal component of the active soil force. The horizontal active earth pressure coefficient $K_{a,h}$ as a function of β angle for b = 0, 0.1, 0.2, 0.3, 0.5, 0.7 and 1.0 H were shown in Fig. 6.119. In Fig. 6.119, for the β angle greater than 70°, the magnitude of active force decreased with increasing β angle. Based on Coulomb's theory, the calculated $K_{a,h}$ = 0.1759. The experimental $K_{a,h}$ for different b and β varied from 25.1% greater to 24.2% less than Coulomb's solution.

In Eq. (6.1), if the driving force on the wall was reduced and the resisting force remained the same, the factor of safety against sliding would increase. From Fig. 6.119, the constrained backfill (for β = 90°) might result in a greater FS against

sliding. In other words, the evaluation of FS against sliding with Coulomb's theory would be on the safe side.

6.10.2 Factor of Safety against Overturning

The factor of safety against overturning was expressed by the following equation:

$$FS_{overturning} = \frac{\sum M_R}{\sum M_O} \qquad (6.2)$$

where $\sum M_R$ = the sum of resisting moments and $\sum M_O$ = the sum of overturning moments about toe. The overturning moment in Eq. (6.2) is the product of the horizontal active force $P_{a,h}$ and the moment arm h. To obtain dimensionless quantities for comparison, the horizontal active resultant $P_{a,h}$ was normalized with $\gamma H^2/2$ and the moment arm h was normalized with the wall height H. The normalized moment arms h/H as a function of β angle for b = 0, 0.1, 0.2, 0.3, 0.5, 0.7 and 1.0 H were shown in Fig. 6.120. Experimental result indicated that the point of application of the active soil thrust ascended with increasing β angle. For tests with different b and β, the experimental $(h/H)_a$ varied from 0.475 to 0.333.

Fig. 6.121 showed the normalized overturning moment $K_{a,h}$ x $(h/H)_a$ as a function of the β angle. For the data obtained, the overturning moment was not significantly influenced by the β angle. The experiment normalized driving moment varied from 0.0801 to 0.0599, which was about 33.5% to 0% greater than the theoretical solution.

If the resisting moment remained the same and the overturning moment was increased, the factor of safety against overturning calculated with Eq. (6.2) would decrease. For this study result, the existence of a nearby inclined rock face would slightly decrease the factor of safety against overturning. Coulomb's theory underestimated the actual driving moment acting on the retaining wall with a dense

backfill. The estimation of the factor of safety against overturning with Coulomb's theory would be unsafe.

6.11 Soil Arching in Backfill

The essential feature of soil arching was demonstrated by the test illustrated in Fig. 6.122 by Terzaghi et al. (1996). A layer of dry cohesionless sand with unit weight γ is placed on a platform that contains a trap door ab. As long as the trap door occupies its original position, the pressure on the trap door as well as that on the adjoining platform is equal to γH per unit area.

However, as soon as the trap door is allowed to yield in a downward direction, the pressure on the door decreases to a small fraction of its initial value. Whereas the pressure on the adjoining part of the platform increases. It was assumed that a soil bridge was formed on top of the trap door. The pressure formerly exerted on the boards that were removed was transferred onto the those that remain in place.

In Fig. 6.16, horizontal stresses due to compaction were observed on the wall surface at S/H = 0. When the wall moved to an active state $(S/H)_a$ = 0.003, the horizontal stress remained at the depth Z = 0.1 m and 0.2 m was higher than Coulomb's solution. The σ_h measured near wall base was extremely low. The observation may be explained with the soil arching phenomenon shown in Fig. 6.123. As the wall moved away from the backfill, a new space was generated behind the wall. Soil near the wall base moved to fill the new space. The soils below were extracted and soil bridges formed in the backfill. The overburden pressure σ_v' was partially supported by the soil arch. Part of the σ_v' was transferred to the wall surface and the nearby interface plate. That is the reason why the double-arching stresses were observed in Fig 6.16.

Due to the soil arching effect, the experimental $K_{a,h}$ was greater than Coulomb's solution. With the active wall movement, the backfill under the soil arch

intended to fill the new space, thus the measured lateral stress decreased. Due to the pressure increase at the upper part of the wall and the pressure reduction at the lower part of the wall, the point of application of active soil thrust was located at a position higher than H/3 above the base of the wall. As a result, the normalized overturning moment $K_{a,h}$ x $(h/H)_a$ was greater than Coulomb's estimation.
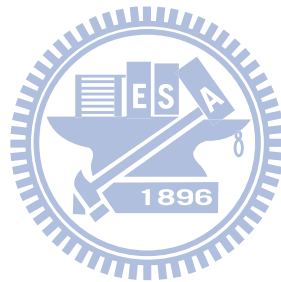
Chapter 7

Conclusions

In this study, the effects of a constrained backfill on active earth pressure were investigated. The dense backfill was prepared with the vibratory compaction method. Based on the experimental data, the conclusions are summarized as follows:

1. Without interface plate (b = 2,000 mm), for the wall with dense backfill, the ultimate pressure was measured at the active wall movement of 0.003 H. The measured active pressure distribution was slightly greater than Coulomb's solution. The point of application h/H of the active soil thrust is located at about 0.333H above the base of the wall.

2. The extra lateral earth pressure due to vibratory compaction dissipated with the active wall movement. The measured σ_h remained approximately a constant at S/H = 0.003.

3. With the approaching of the interface plate, the plate intruded the active soil wedge, so that the active soil wedge cannot develop fully behind the wall. The active earth pressure coefficient $K_{a,h}$ decreased with decreasing wall-plate spacing b and increasing plate inclination angle β.

4. As the interface angle β increased or spacing b decreased (the rock face approached the wall face), the inclined rock face intruded the active soil wedge, the earth pressure decreased near the base of the wall. This change of earth pressure distribution caused the active thrust to rise to a higher location.

5. For β = 90° (interface parallel to vertical wall), the lateral pressure distribution was not linear with depth as assumed by Coulomb and Rankine thoery.

6. The experimental $K_{a,h}$ for different b and β varied from 25.1% greater to 24.2% less than Coulomb's solution.

7. The point of application of the active soil thrust ascended with increasing β angle. For tests with different b and β, the experimental $(h/H)_a$ varied from

0.475 to 0.333.

8. The experimental normalized driving moment varied from 0.0801 to 0.0599, which was about 33.5% to 0% greater than Coulomb's theoretical solution.The existence of a nearby inclined rock face would slightly decrease the factor of safety against overturning. Coulomb's theory underestimated the actual driving moment acting on the retaining wall. The estimation of the factor of safety against overturning with Coulomb's theory would be unsafe.
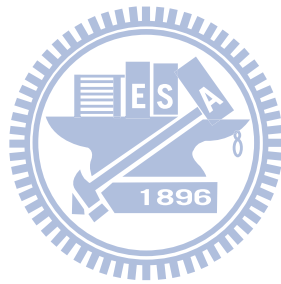
References

1. Ang, A. H., and Tang, W. H., (1975) "Probability Concepts in Engineering Planning and Design Volumn Ⅰ - Basic Principles," John Wiley and Sons, Inc, New York, N.Y., pp. 286-294.

2. Brinch Hansen, J., (1953), "Earth Pressure Calculation," Danish Technical Press, Copenhagen.

3. Bowles, J. E., (1988), Foundation analysis and design, 4th Edition, McGraw-Hill Book Co., Singapore, 474.

4. Bros, B., (1972), "The Influence of Model Retaining Wall Displacements on Active and Passive Earth Pressure in Sand," Proceedings, 5th European Conference on Soil Mechanics, Vol.1, Madrid, Spain, pp. 241-249.

5. Chang, S. Y., (2000), "Effect of Backfill Density on Active Earth Pressure," Master of Engineering Thesis, Dept. of of Civil Engineering, National Chiao Tung University, Hsinchu, Taiwan.

6. Chen, C. Y., (1995), "Active Earth Pressure with Inclined Backfill," Master of Engineering Thesis, National Chiao Tung University, Hsinchu, Taiwan.

7. Chen, H. R., (1997), "Earth Pressure At-Rest with Different Soil Densities and Backfill Inclinations," Master of Engineering Thesis, National Chiao Tung University, Hsinchu, Taiwan.

8. Chen, K. H., (2006), "Earth Pressure of Retaining Walls near Faces" Master of Engineering Thesis, Department of Construction Engineering, National Kaohsiung First University of Science and Technology, Kaohsiung, Taiwan.

9. Chen, N. C., (2005), "Earth Pressure at-Rest near A Vertical Rock Face" Master of Engineering Thesis, National Chiao Tung University, Hsinchu, Taiwan.

10. Chen, T. J., (2003). "Earth Pressures Due to Vibratory Compaction." Ph.D. dissertation, National Chiao Tung University, Hsinchu, Taiwan.

11. Chen, T. J., and Fang, Y. S., (2008). "Earth Pressure Due to Vibratory Compaction." Journal Geotechnical and Geoenvironmental Engineering, 134 (4),

437-444.

12. Chen, W. T., (2010), "Effects of Constrained Backfill on Active Earth Pressure" Master of Engineering Thesis, National Chiao Tung University, Hsinchu, Taiwan.

13. Chien, Y. L., (2007). "Variation of Soil Density and Earth Pressure due to a Strip Compaction," Master of Engineering Thesis, National Chiao Tung University, Hsinchu, Taiwan.

14. Clough, G. W., and Duncan, J. M., (1971), "Finite Element Analysis of Retaining Wall Behavior," Journal of Geotechnical Engineering, ASCE, Vol. 87, No. SM12, pp. 1657-1673.

15. Das, B. M. (2011), "Principles of Foundation Engineering", 7th Ed.(SI Edition), Cengage Learning, Stamford, CT, USA.

16. Das, B. M., (2010), "Principles of Geotechnical Engineering," 7th Ed. (SI Edition), Cengage Learning , Stamford, CT, USA.

17. Fan, C. C., and Fang, Y. S., (2010), "Numerical Solution of Active Earth Pressure on Rigid Retaining Walls near Rock Faces." Computers and Geotechnics, 37, pp.1023-1029.

18. Fang, Y. S., and Ishibashi, I., (1986), "Static Earth Pressures with Various Wall Movements," Journal of Geotechnical Engineering, ASCE, Vol. 112, No. 3, Mar., pp. 317-333.

19. Fang, Y. S., Cheng F. P., Cheng, R. T., and Fan, C. C., (1993), "Earth Pressure under General Wall Movements," Geotechnical Engineering, SEAGS, Vol. 24, No. 2, December., pp. 113-131.

20. Fang, Y. S., Chen, J. M., and Chen, C. Y., (1997), "Earth Pressures with Sloping Backfill" Journal of Geotechnical and Geoenvironmental Engineering, ASCE, 123(3), March, 250-259.

21. Fang, Y. S., Chen, T. J., and Wu, B. F., (1994), "Passive Earth Pressure with Various Wall Movements," Journal of Geotechnical Engineering, ASCE, Vol. 120, No. 8, Aug., pp. 1307-1323.

22. Fang, Y. S., Chen, J. J., Holtz, R. D., and Lee, W. F. (2004), "Reduction of Boundary Friction in Model Tests," Geotechnical Testing Journal, ASTM, 27(1), 1-10.

23. Ho, Y. C., (1999), "Effects of Backfill Compaction on Passive Earth Pressure," Master of Engineering Thesis, National Chaio Tung University, Hsinchu, Taiwan.

24. Huang, S. F., (2009) "Active Earth Pressure on Retaining Walls near Rock Faces" Master of Engineering Thesis, National Chiao Tung University, Hsinchu, Taiwan.

25. Ishibashi, I., and Fang, Y. S., (1987), "Dynamic Earth Pressures with Different Wall Movements Modes," Soils and Foundations, JSSMFE, Vol. 27, No. 4, Dec., pp. 11-22.

26. Janbu, N., (1957), "Earth Pressure and Bearing Capacity Calculation by Gerneral Procedure of Slices," Proceedings, 4th Int. Conf. Soil Mechs. Found. Eng., 2, pp. 207-212.

27. Janssen, H. A., (1895), "Versuche uber Getreidedruck in Silozenllen," Aeitschrift, Verein Deutscher Ingenieure, 39: 1045-1049. (Partial English Translation in Proceedings of Institute of Civil Engineers, London, England, 1896)

28. Lee, C. C., (1998), "Passive Earth Pressure with Various Backfill Densities," Master of Engineering Thesis, National Chiao Tung University, Hsinchu, Taiwan.

29. Leshchinsky, D., Hu, Y.,and Han, J. (2004). "Limited Reinforced Space in Segmental Retaining Walls." Geotextiles and Geomembranes, 22(6),543-553.

30. Lo Presti, D. C. F., Pedroni, S., and Crippa, V. (1992). "Maximum dry density of cohesionless soils by pluviation and by ASTM D 4253-83 : A comparative study." Geotechnical Testing Journal, ASTM, 15(2),180-189.

31. Mackey, R. D., and Kirk, D. P., (1967), "At Rest, Active and Passive Earth Pressures," Proceedings, South East Asian Conference on Soil Mechanics and Foundation Engineering, Bangkok, pp. 187-199.

32. Nakai, (1985), "Finite Element Computions for Active and Passive Earth Pressure Problems of Retaining Wall," Soils and Foundations, JSSMFE, Vol. 25, No. 3, pp. 98-112.

33. Naval Facilities Engineering Command. (1982). Foundations and earth structures design manual 7.2, NAVFAC DM-7.2, Dept. of the Navy, Naval Facilities Engineering Command, Virginia.NAVFAC DM-7.2.

34. PLAXIS BV. (2002): User's manual of PLAXIS, A.A. Balkema Publishers.

35. PLAXIS (2005). Plaxis Finite Element Code for Soil and Rock Analyses, Version 8.2, Delft, Netherlands.

36. Potts, D. M., and Fourie, A. B., (1986), "A Numerical Study of the Effects of Wall Deformation on Earth Pressures," International Journal for Numerical and Analytical Methods in Geomechanics, Vol. 10, pp. 383-405.

37. Potyondy, J. G.,(1961). "Skin Friction between Various Soils and Construction Materials." Geotechnique, 11, 329-353.

38. Rad, N.S., and Tumay, M. T. (1987). "Factors affecting sand specimen preparation by raining." Geotechnical Testing Journal, ASTM, 10(1), 31-37.

39. Rankine, W.J.M. (1857). "On the stability of loose earth," Phil. Trans. Roy. Soc., London, 147, Part 1, pp. 9-27.

40. Rowe, P. W., and Barden, L. (1964). "Importance of Free Ends in Triaxial Testing." Journal of the Soil Mechanics and Foundations Division, ASCE, 90(SM1), 1-77.

41. Sherif, M. A., Fang, Y. S., and Sherif, R. I., (1984), "Ka and Ko behind Rotating and Non-Yielding Walls," Journal of Geotechnical Engineering, ASCE, Vol. 110, No. 1, Jan., pp. 41-56.

42. Sowers, G. F. (1979), "Introductory Soil Mechanics and Foudations" 4th Ed., Macmillian Publishing Co., New York.

43. Spangler, M.G and Handy, R.L. (1984):Soil Engineering, Harper and Row, New York.

44. Tatsuoka, F., and Haibara, O., (1985), "Shear Resistance between Sand and Smooth or Lubricated Surface," Soils and Foundations, JSSMFE, Vol. 25, No. 1, Mar., pp. 89-98.

45. Tatsuoka, F., Molenkamp, F., Torii, T., and Hino, T. (1984). "Behavior of Lubrication Layers of Platens in Element Tests." *Soils and Foundations*, JSSMFE, 24(1), 113-128.

46. Tejchman, J., and Wu, W., (1995) "Experimental and Numerical Study of Sand-Steel Interfaces", International Journal for Numerical and Analytical Methods in Geotechanics, Vol. 19, No. 8, pp.513-536.

47. Terzaghi, K., (1932), "Record Earth Pressure Testing Mechine," Engineering News-Record, Vol. 109, Sept., 29, pp. 365-369.

48. Terzaghi, K., (1941), "General Wedge Theory of Earth Pressure," ASCE Transaction, Vol. 106, pp. 68-80.

49. Terzaghi, K., Peck, R. B. and Mesri, G. (1966), "Soil Mechanics in Engineering practice. 3rd edition, John Wiley & Sons, Inc., NewYork.

50. Terzaghi, K., and Peck, R. B., (1967), Soil Mechanics in Engineering Practice,Wiley, New York.

51. Wang, F. J., (2005), "Effects of Ajacent Rock Face Inclination on Earth Pressure At-Rest," Master of Engineering Thesis, National Chiao Tung University, Hsinchu, Taiwan.

52. Wu, B. F., (1992), "Design and Construction of National Chiao Tung University Model Retaining Wall," Master of Engineering Thesis, National Chiao Tung University, Hsinchu, Taiwan.

53. Zheng, Y. C., (2008) "Active Earth Pressure on Retaining Walls with Intrusion of a Stiff Interface into Backfill," Master of Engineering Thesis, National Chiao Tung University, Hsinchu, Taiwan.

Table 2.1. Comparison of experimental and theoretical values (after Mackey and Kirk, 1967)

Theories	Active Pressure Coefficient					
	Sand 1		Sand 2		Sand 3	
	Loose	Dense	Loose	Dense	Loose	Dense
Coulomb	0.25	0.13	0.22	0.14	0.19	0.13
Rankine	0.26	0.13	0.24	0.14	0.19	0.13
Krey(ϕ circle)	0.26	0.21	0.25	0.21	0.21	0.19
Ohde	0.26	0.21	0.25	0.21	0.21	0.19
Caquot and Kerisel	0.25	0.13	0.23	0.14	0.19	0.13
Janbu	0.27	0.12	0.22	0.13	0.18	0.13
Rowe	0.21	0.16	0.21	0.16	0.21	0.16
Experimental	0.22	0.32	0.19	0.29	0.17	0.27

Table 3.1. Technical Information of the Eccentric Motor

Manufacture	Mikasa
Type	KJ75-2P
Power (Watt)	75
Voltage (Volt)	220
Frequency (Hz)	50/60
Vibration per Minute	3000/3600
Mass (kg)	6.2
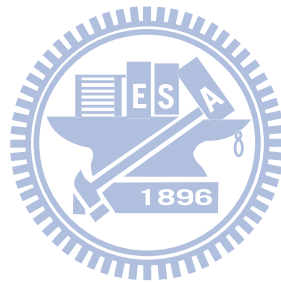
Table 6.1 Test Program

Horizontal Spacing b, (mm)	Interface Inclination Angle, β (degree)	Test No.	
2,000	90	0427-1	0511-1
0	80	0825-2	0825-3
	70	0820-3	0825-1
	60	0820-1	0820-2
50	90	0730-1	0730-2
	80	0801-1	0801-2
	70	0723-1	0723-3
	60	0722-2	0722-3
100	90	0711-1	0714-2
	80	0715-2	0715-4
	70	0716-2	0716-3
	60	0718-2	0718-3
150	90	0627-2	0628-2
	80	0702-1	0702-2
	70	0708-1	0708-2
250	90	0613-1	0615-1
	80	0621-2	0622-2
350	90	0603-1	0606-2
500	90	0518-1	0530-1
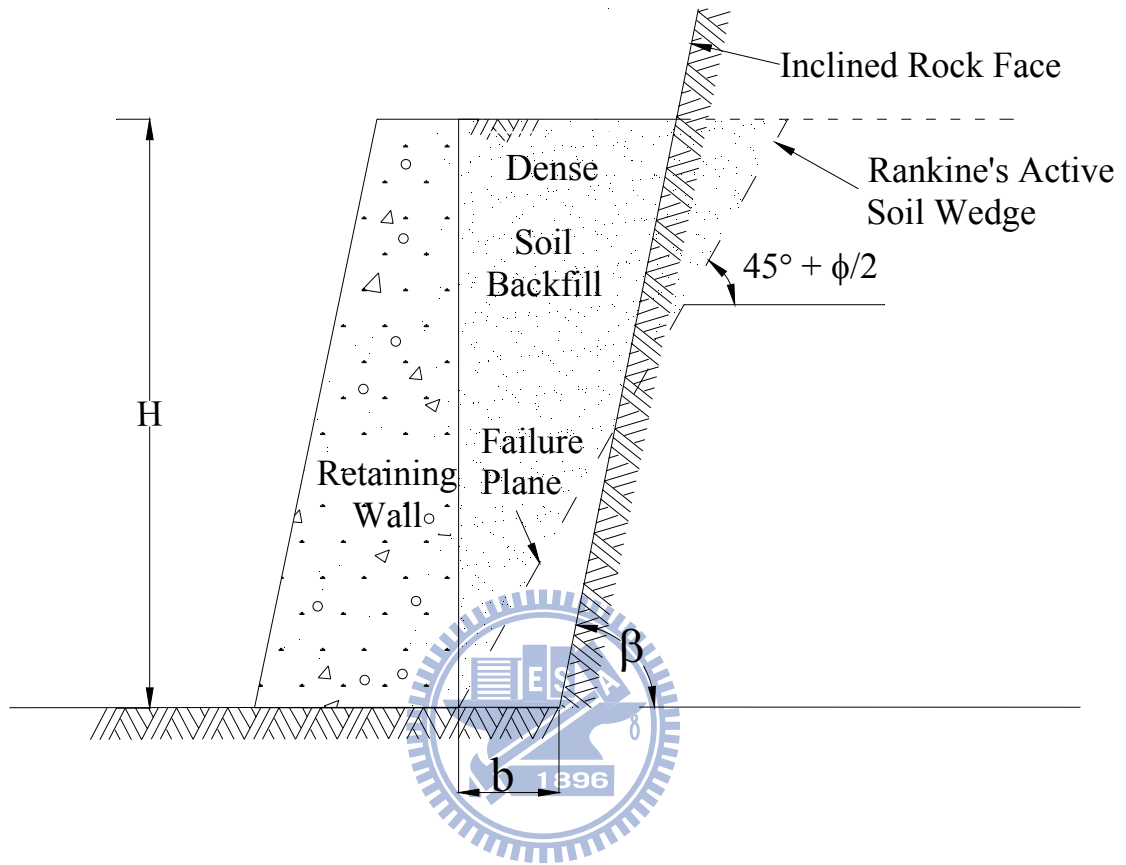
Fig. 1.1. Retaining walls with constrained backfill
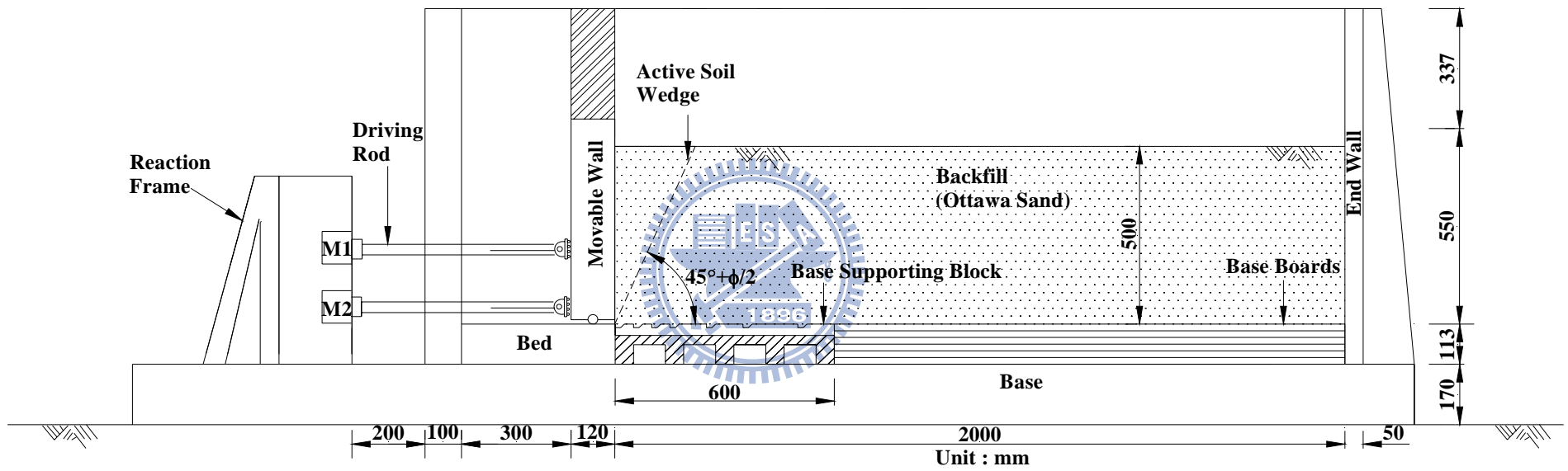
Fig. 1.2. Model test for b = 2000 mm
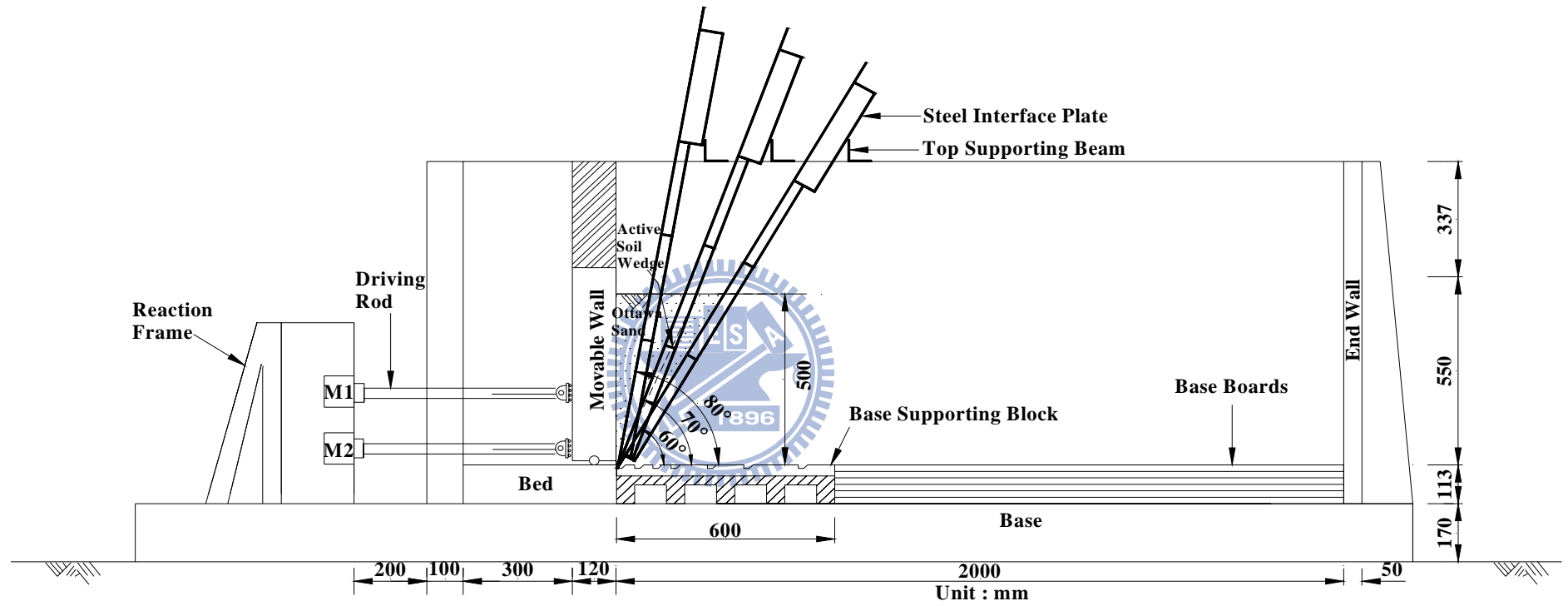
Fig. 1.3. Model test for b = 0
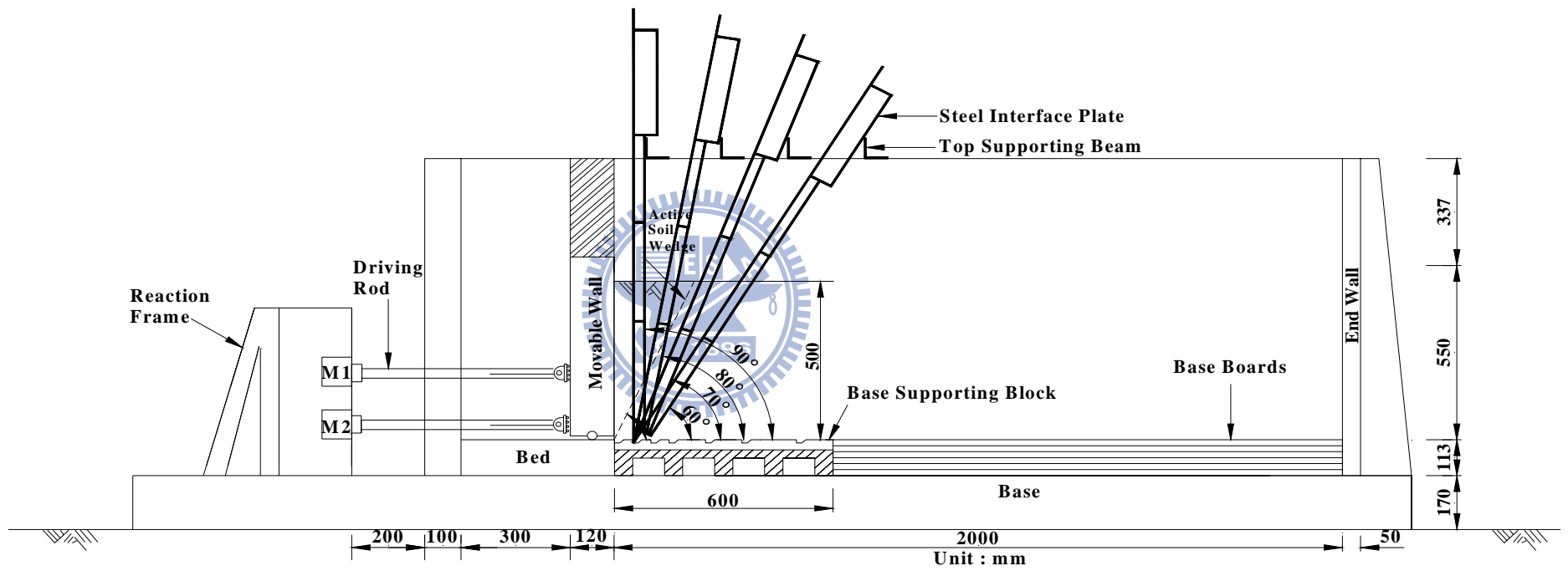
Fig. 1.4. Model test for b = 50 mm
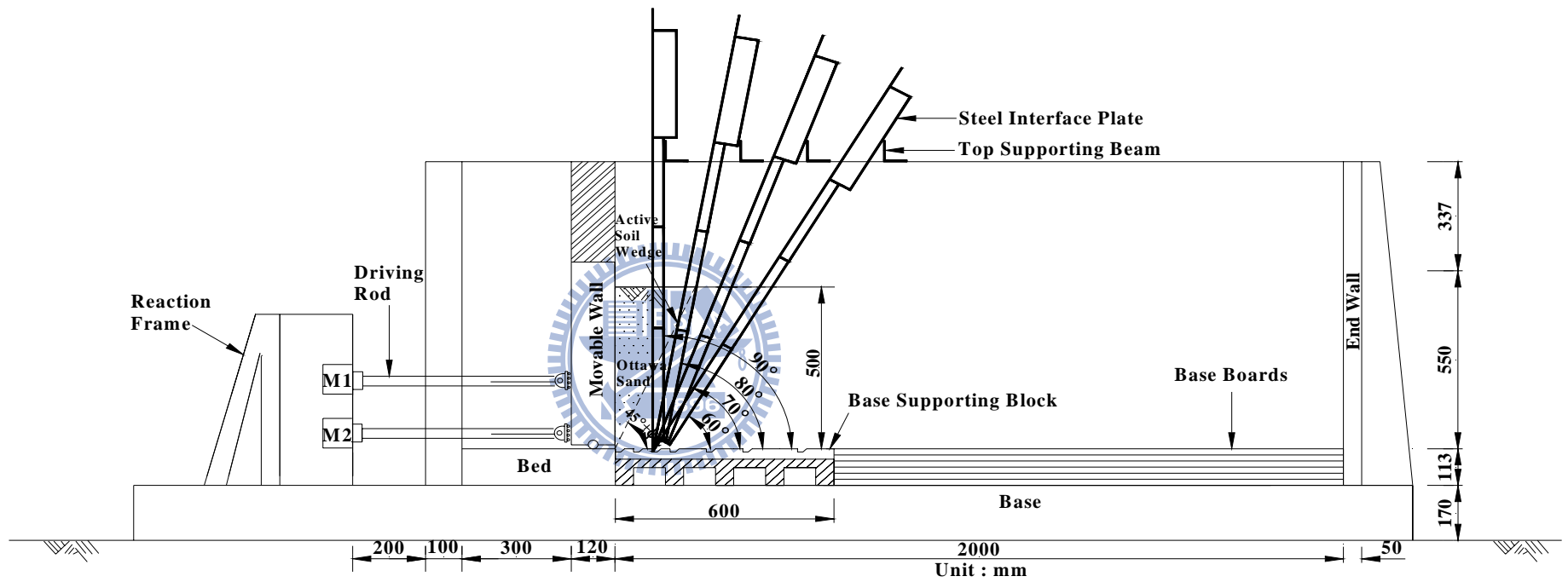
Fig. 1.5. Model test for b = 100 mm
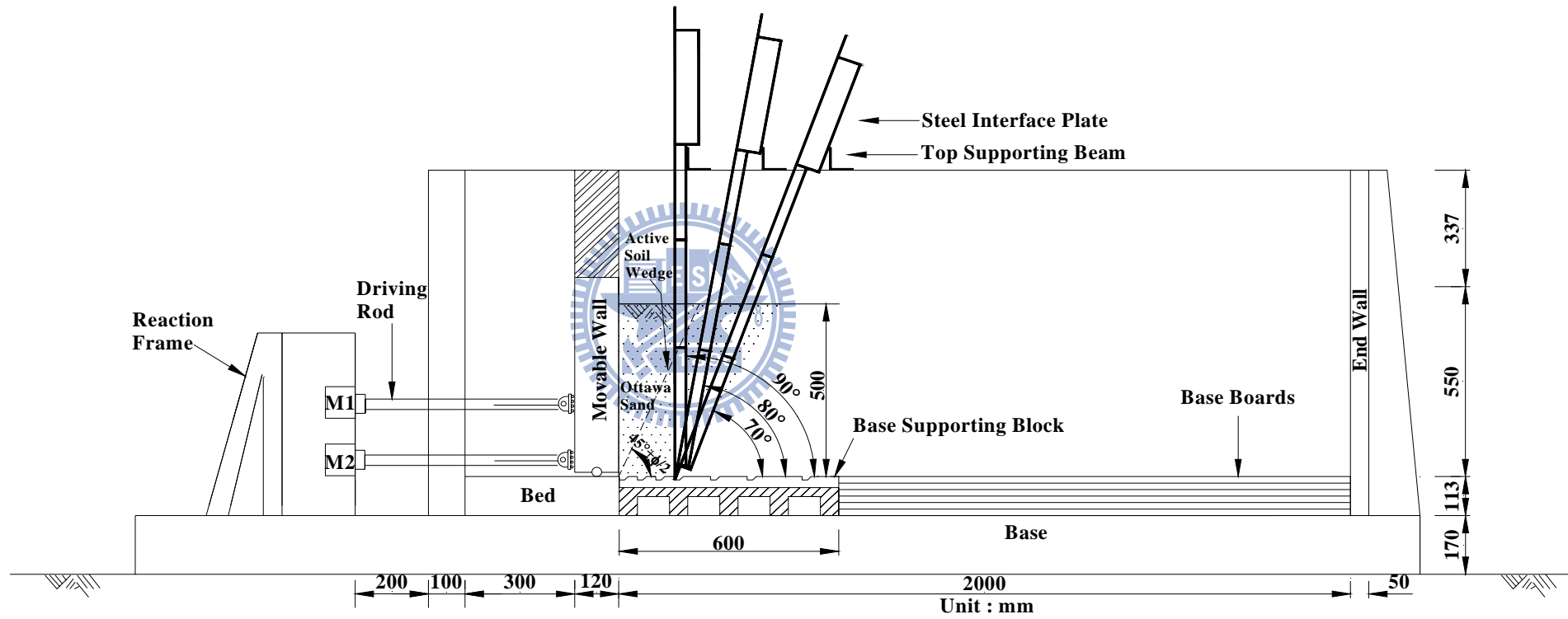
Fig. 1.6. Model test for b = 150 mm

61
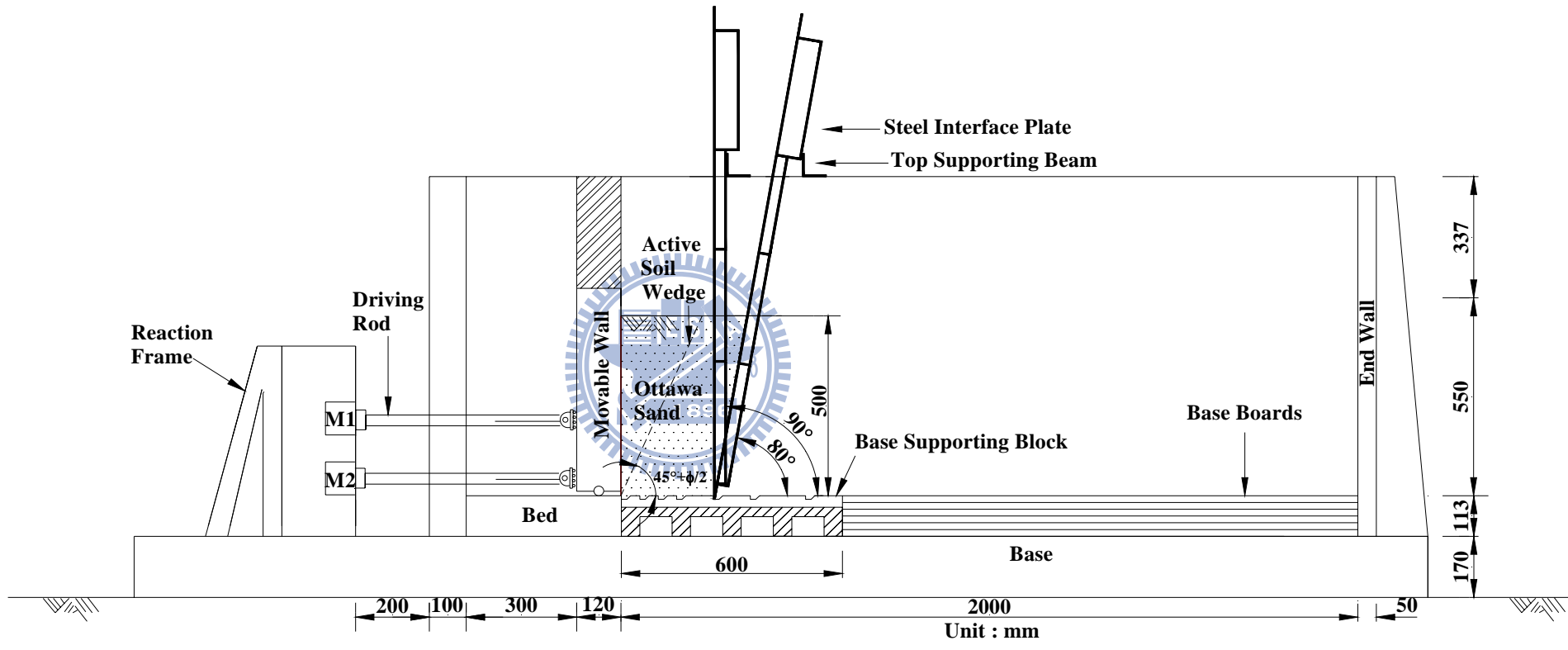
Fig. 1.7. Model test for b = 250 mm

62
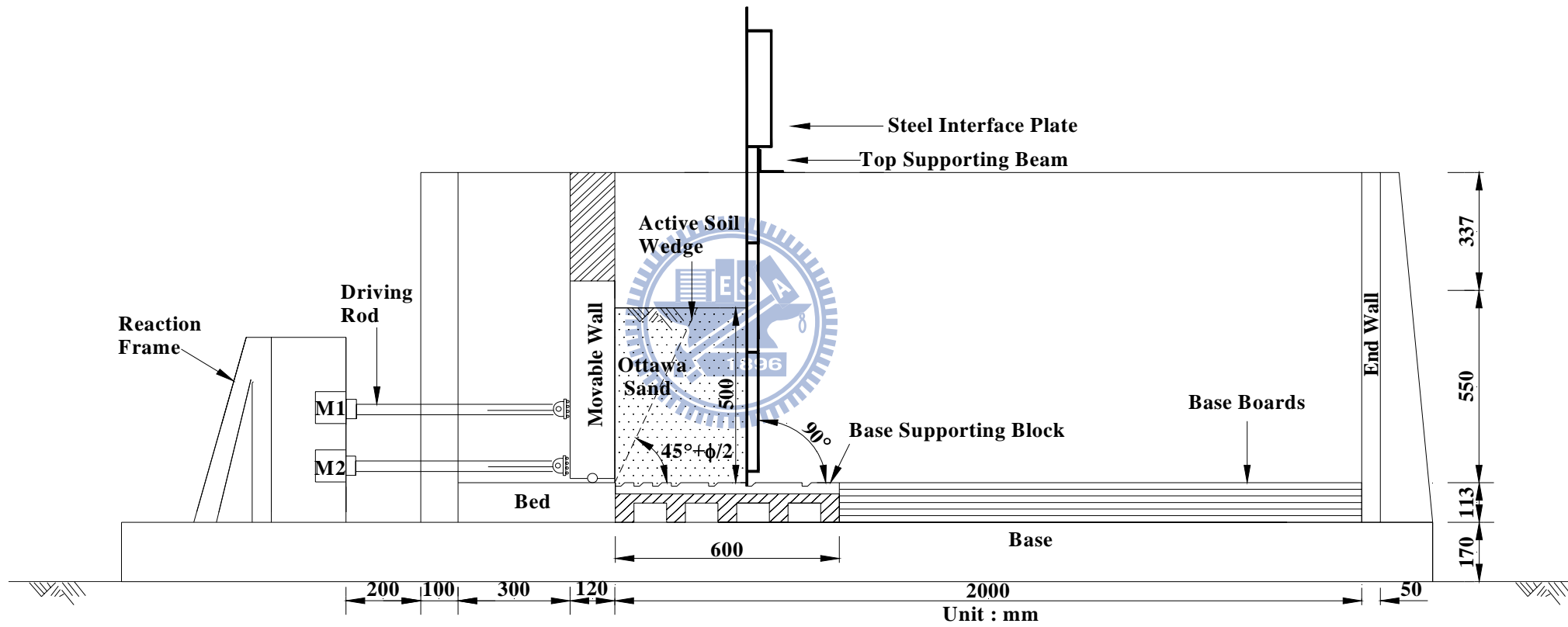
Fig. 1.8. Model test for b = 350 mm

63
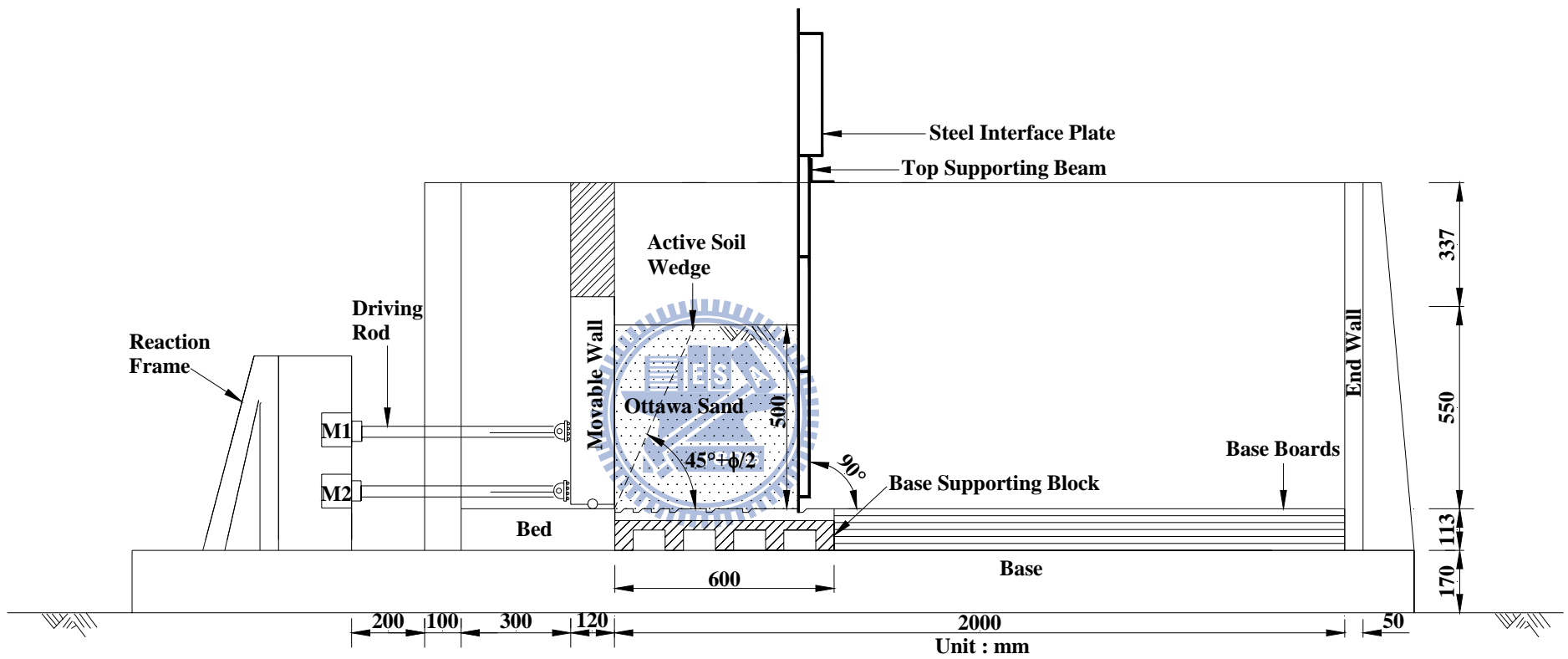
Fig. 1.9. Model test for b = 500 mm
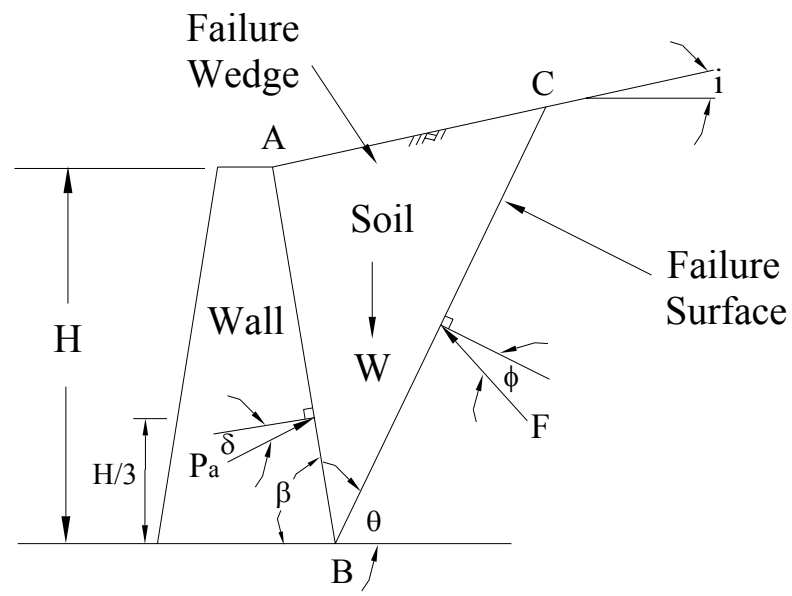
(a)
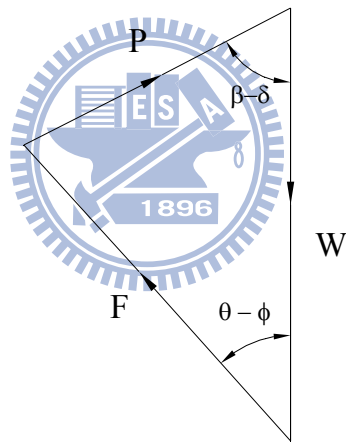
(b)

Fig. 2.1. Coulomb's theory of active earth pressure
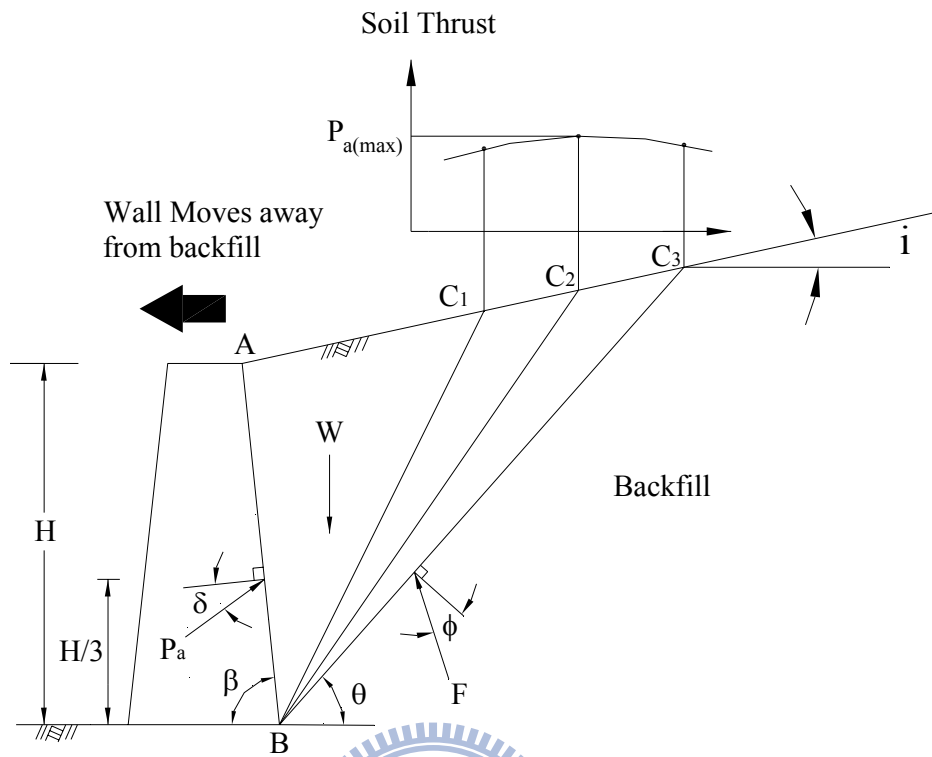
Fig. 2.2. Coulomb's active pressure determination

(a)   (b)
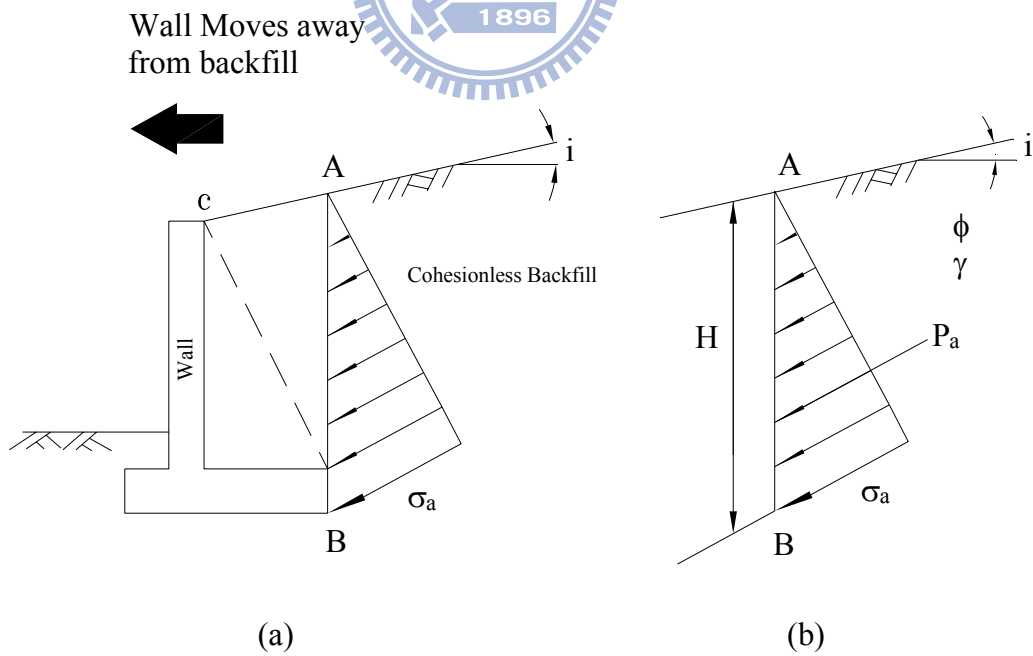
Fig. 2.3. Rankine's theory of active earth pressure
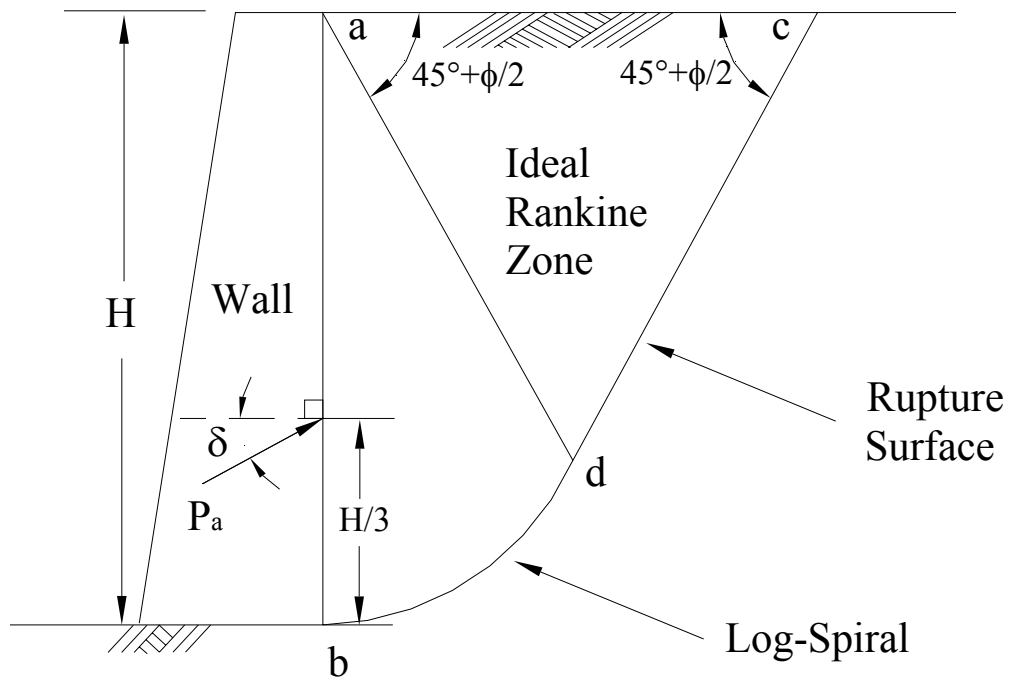
Fig. 2.4. Failure surface in soil by Terzaghi's log-spiral method
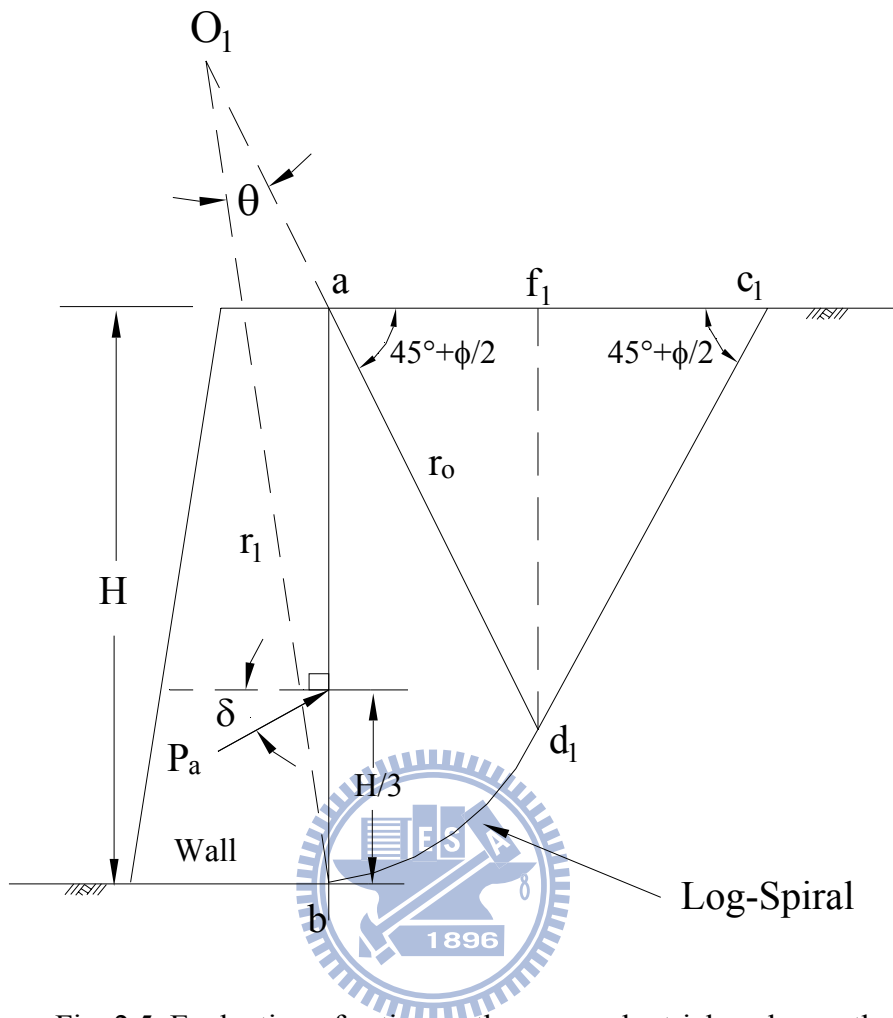
Fig. 2.5. Evaluation of active earth pressure by trial wedge method
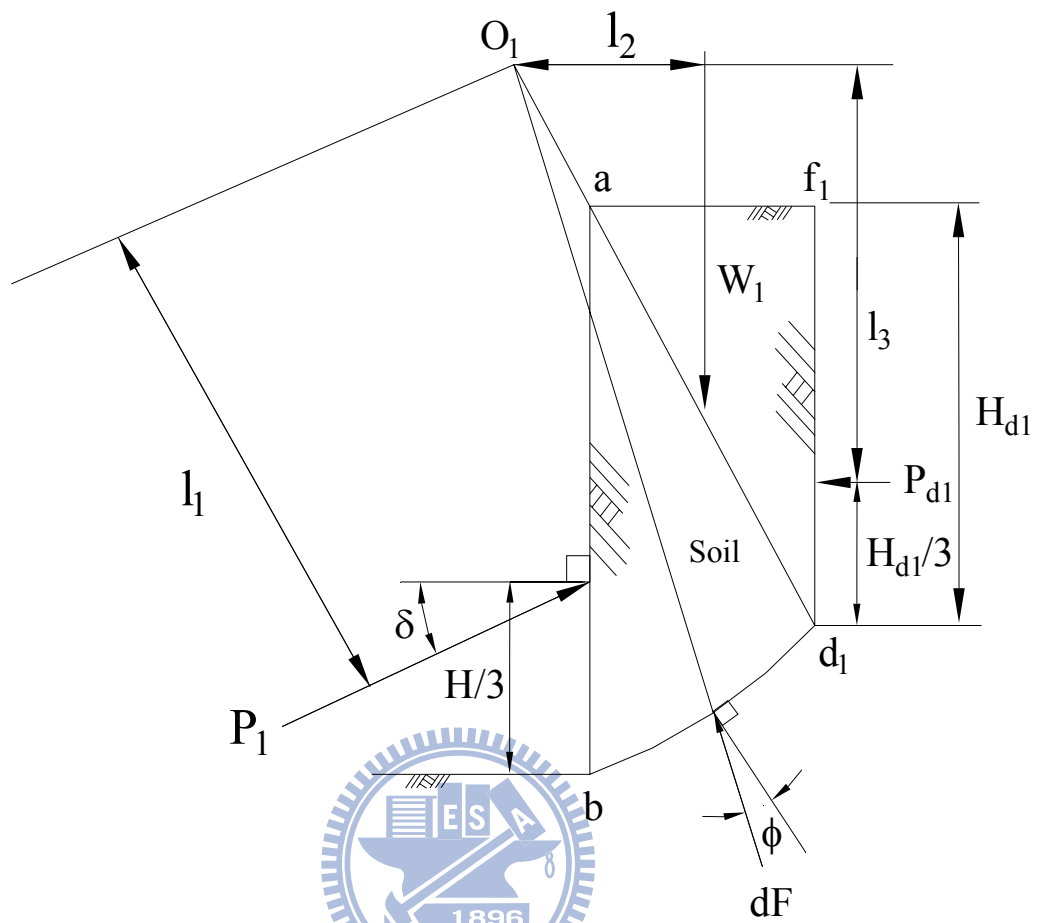
Fig. 2.6 Stability of soil mass abd_1f_1

Fig. 2.7. Active earth pressure determination with Terzaghi's log-sprial failure surfaces
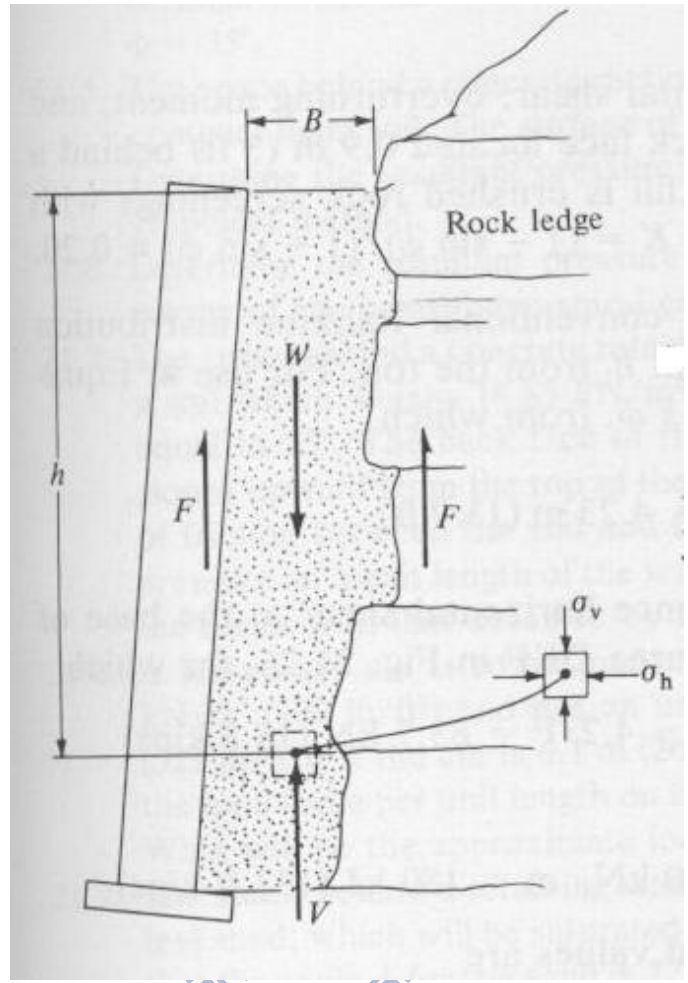
Fig. 2.8. Fascia retaining wall of backfill width B and wall friction F
(after Spangler and Handy, 1984)
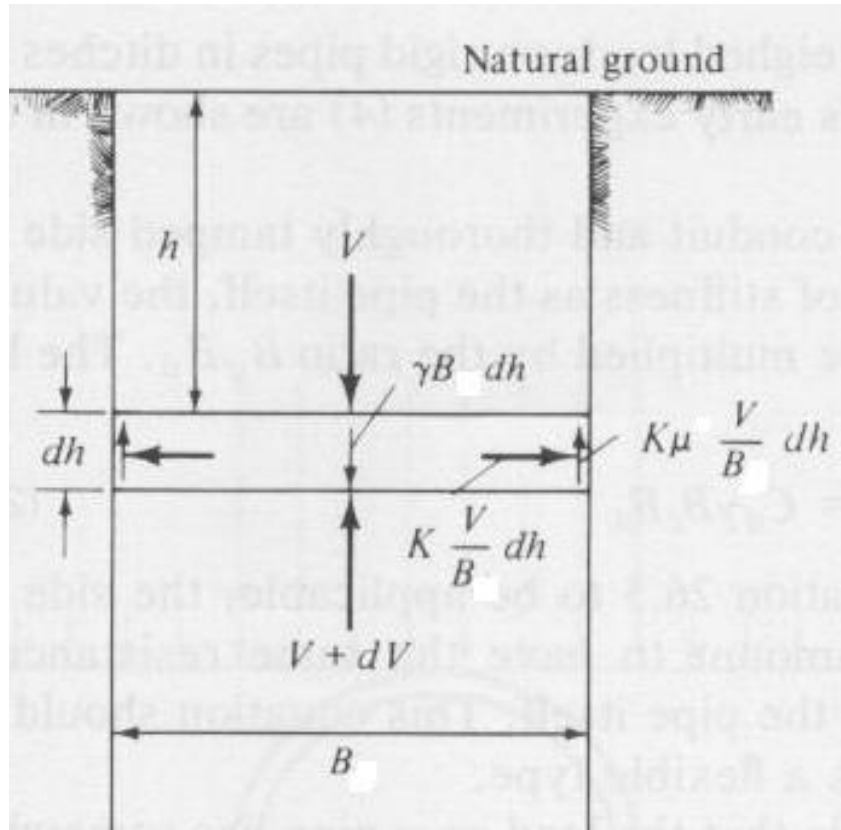
Fig. 2.9. Horizontal element of backfill material
(after Spangler and Handy, 1984)
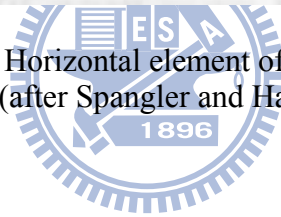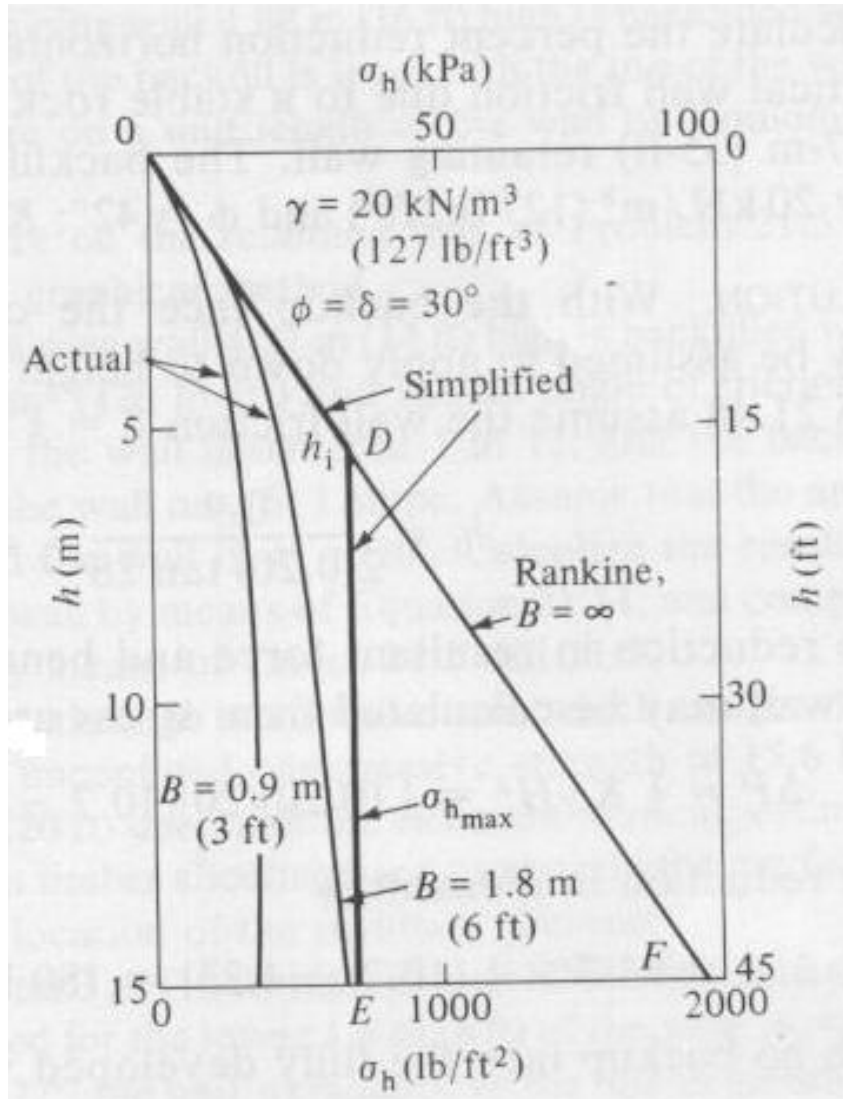
Fig. 2.10. Distribution of soil pressure against fascia walls due to partial
support from wall friction F (after Spangler and Handy, 1984)

C B A — D

Pressure measerment device

16'

B
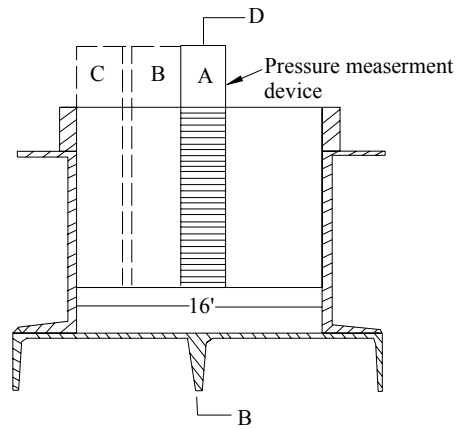
SECTIONAL   ELEVATION A-A

A

Drive shaff wheel

Wall Face

12'

Removable Bars
1'*1'

36'

Fixed Slep

3'

12' *4'   Base Channel

A
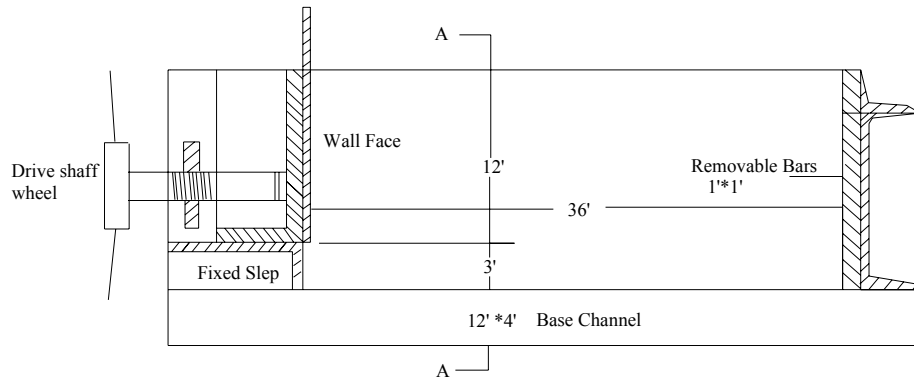
SECTIONAL   ELEVATION B-B

Fig. 2.11. University of Manchester model retaining wall
(after Mackey and Kirk, 1967)
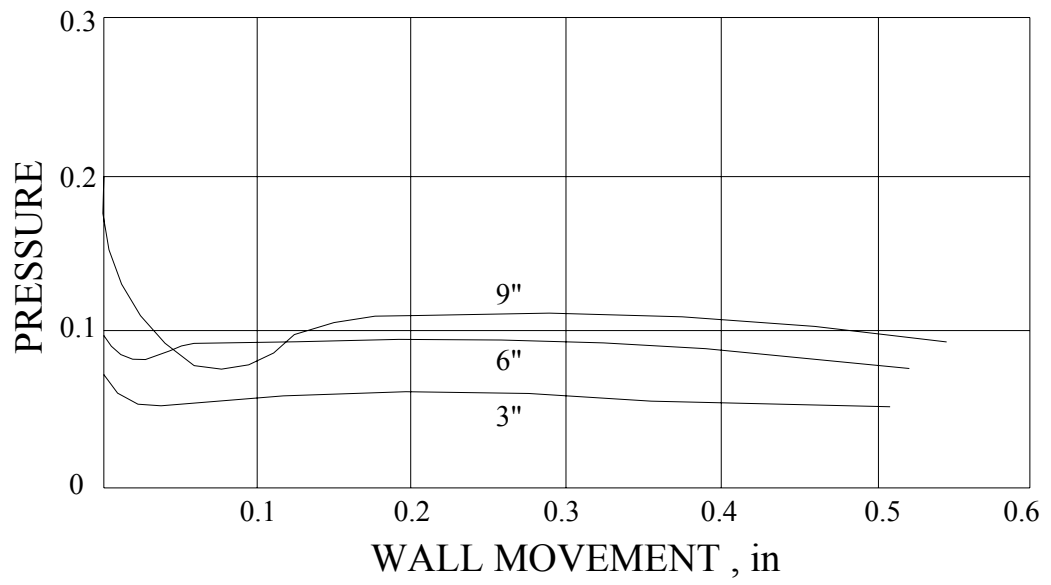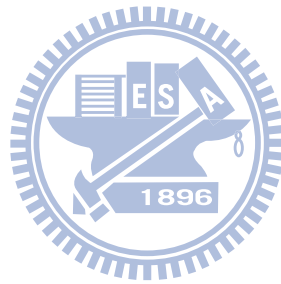
Fig. 2.12. Earth pressure with wall movement (after Mackey and Kirk, 1967)

Fig. 2.13. Failure surfaces (after Mackey and Kirk, 1967)
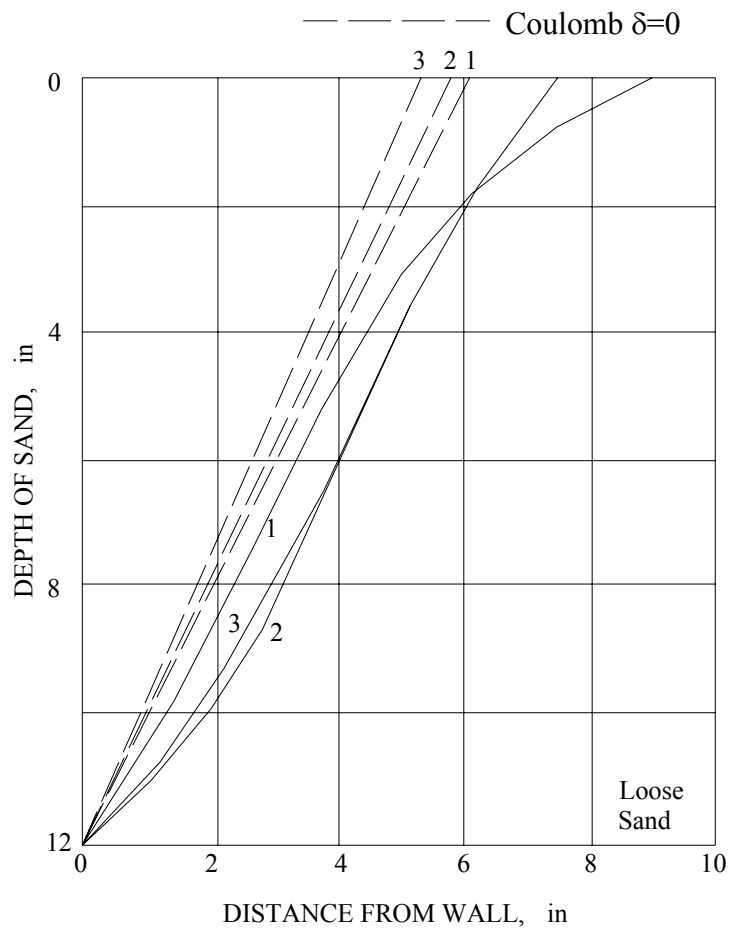
Sand 1: A uniformly graded fine sand
Sand 2: A medium graded sand
Sand 3: A uniformly graded coarse sand
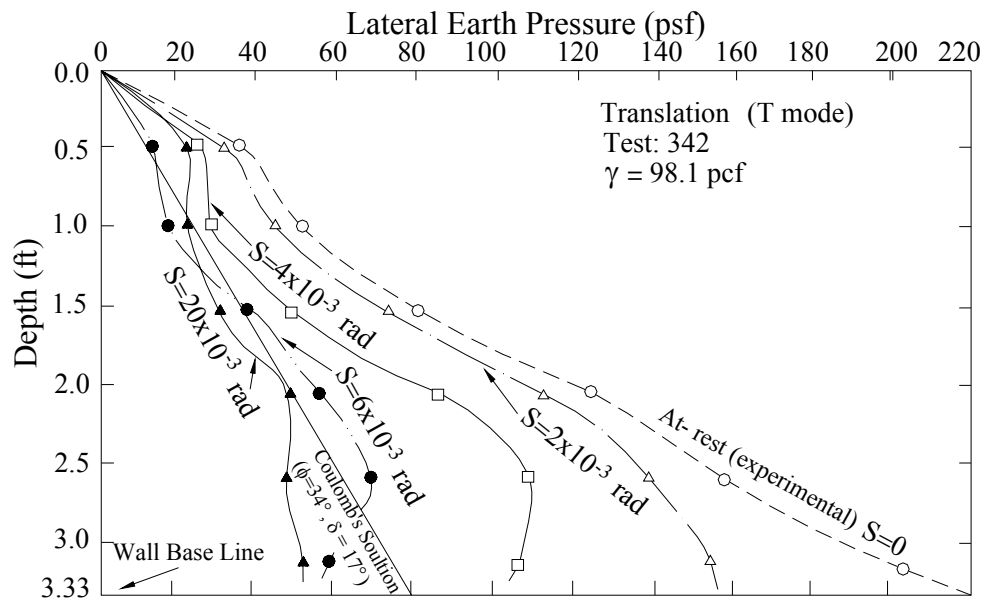
Fig. 2.14. Distributions of horizontal earth pressure at different wall displacement
(after Fang and Ishibashi, 1986)
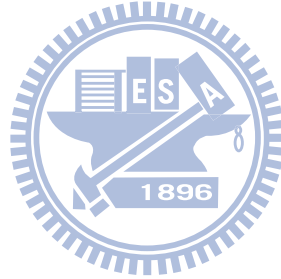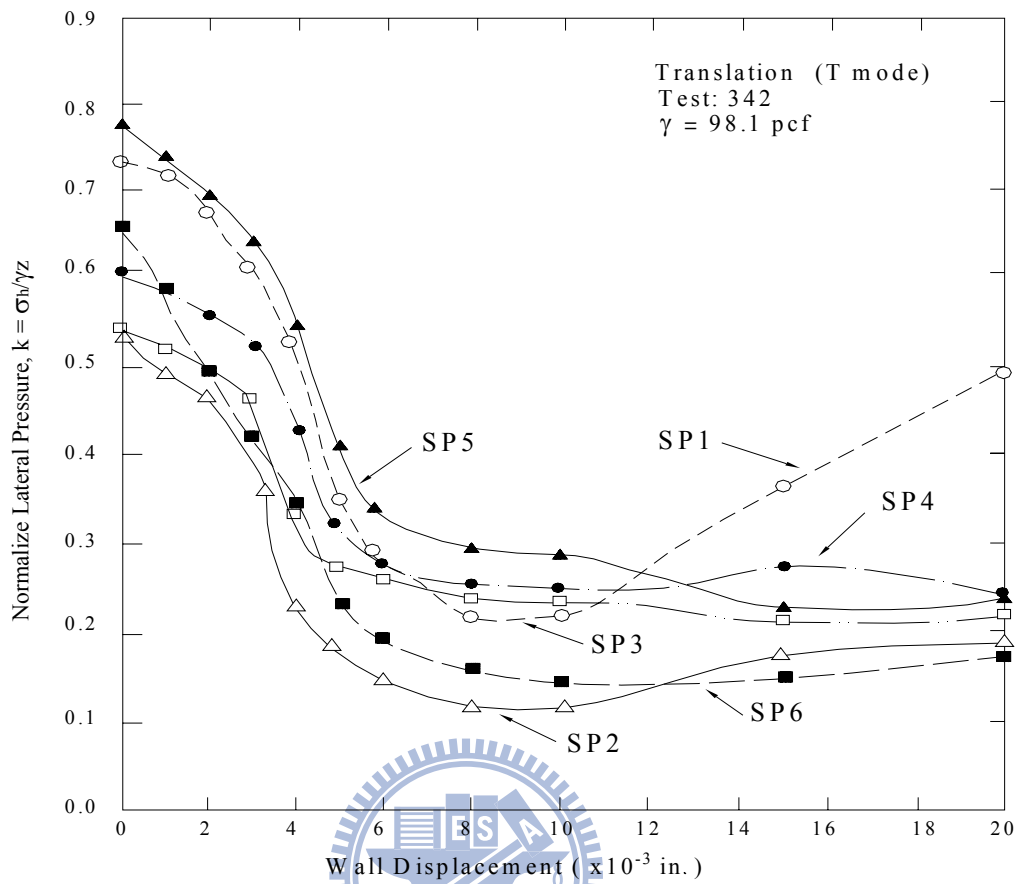
Fig. 2.15. Change of normalized lateral pressure with translation wall displacement
(after Fang and Ishibashi, 1986)
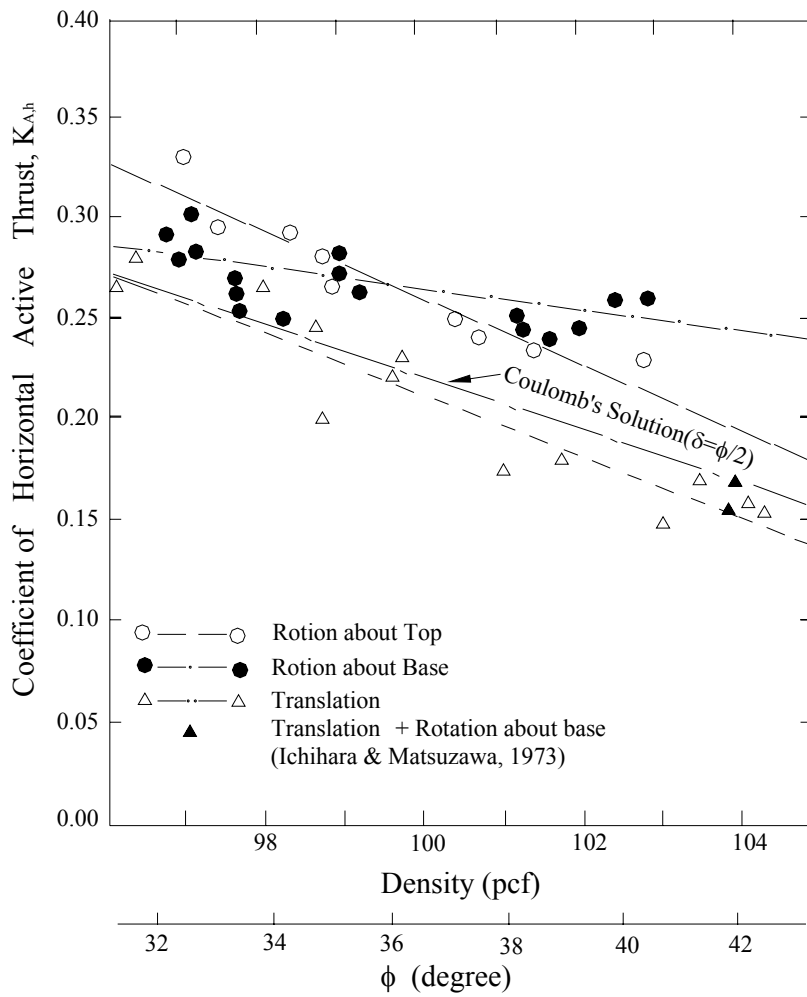
Fig. 2.16. Coefficient of horizontal active thrust as a function of soil density
(after Fang and Ishibashi, 1986)
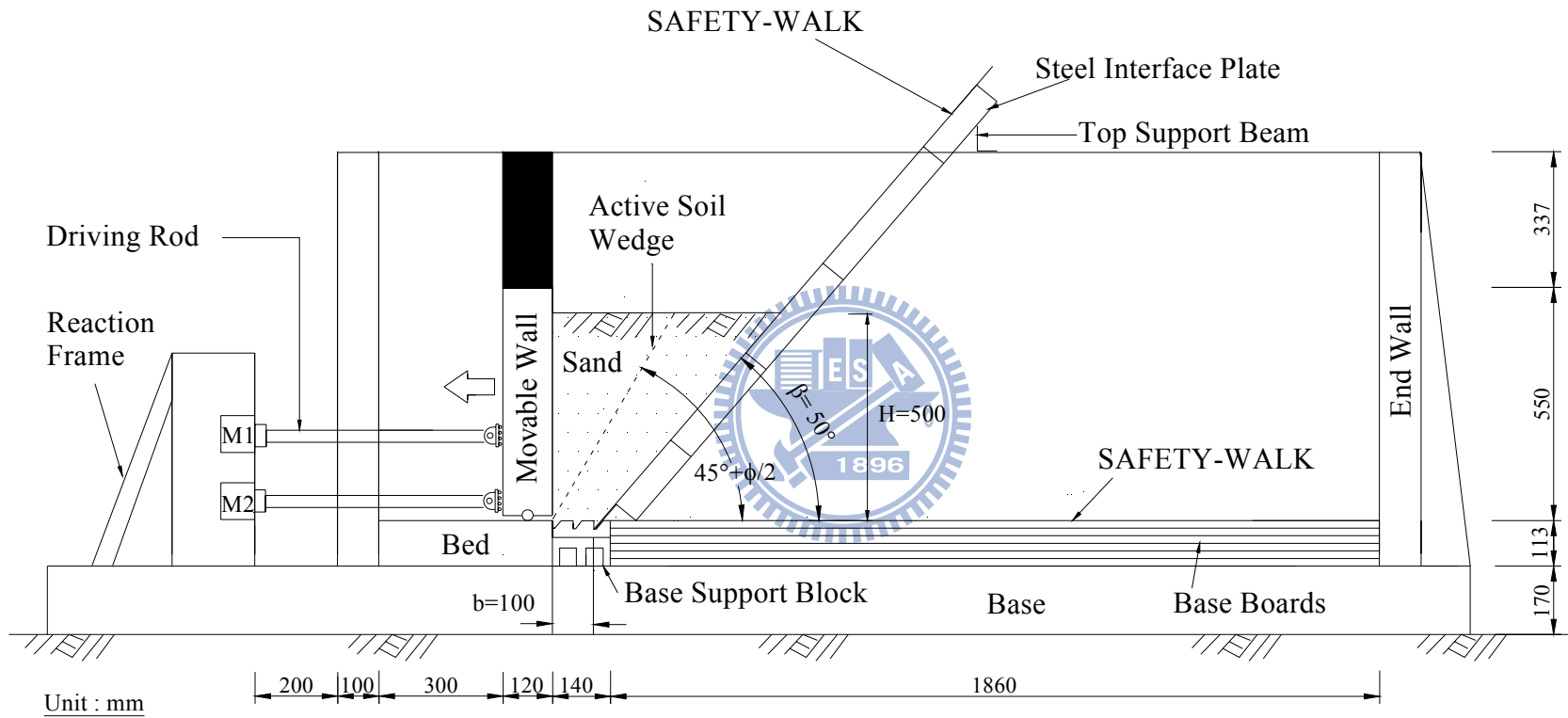
Fig. 2.17. Model wall test with b = 100 mm and β = 50° (after Huang, 2009)
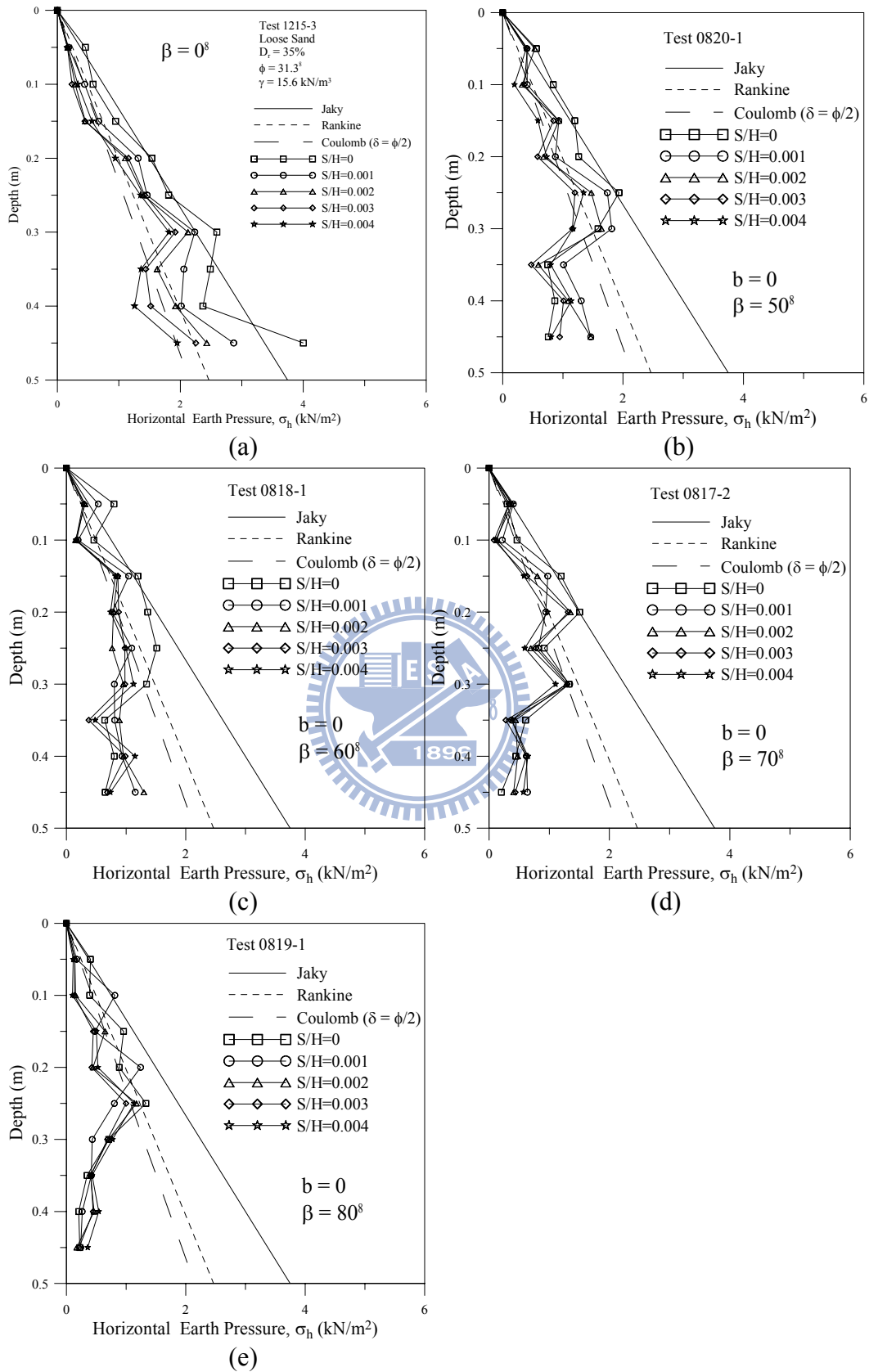
Fig. 2.18. Distribution of horizontal earth pressure for b = 0 and various β angles (after Huang, 2009)
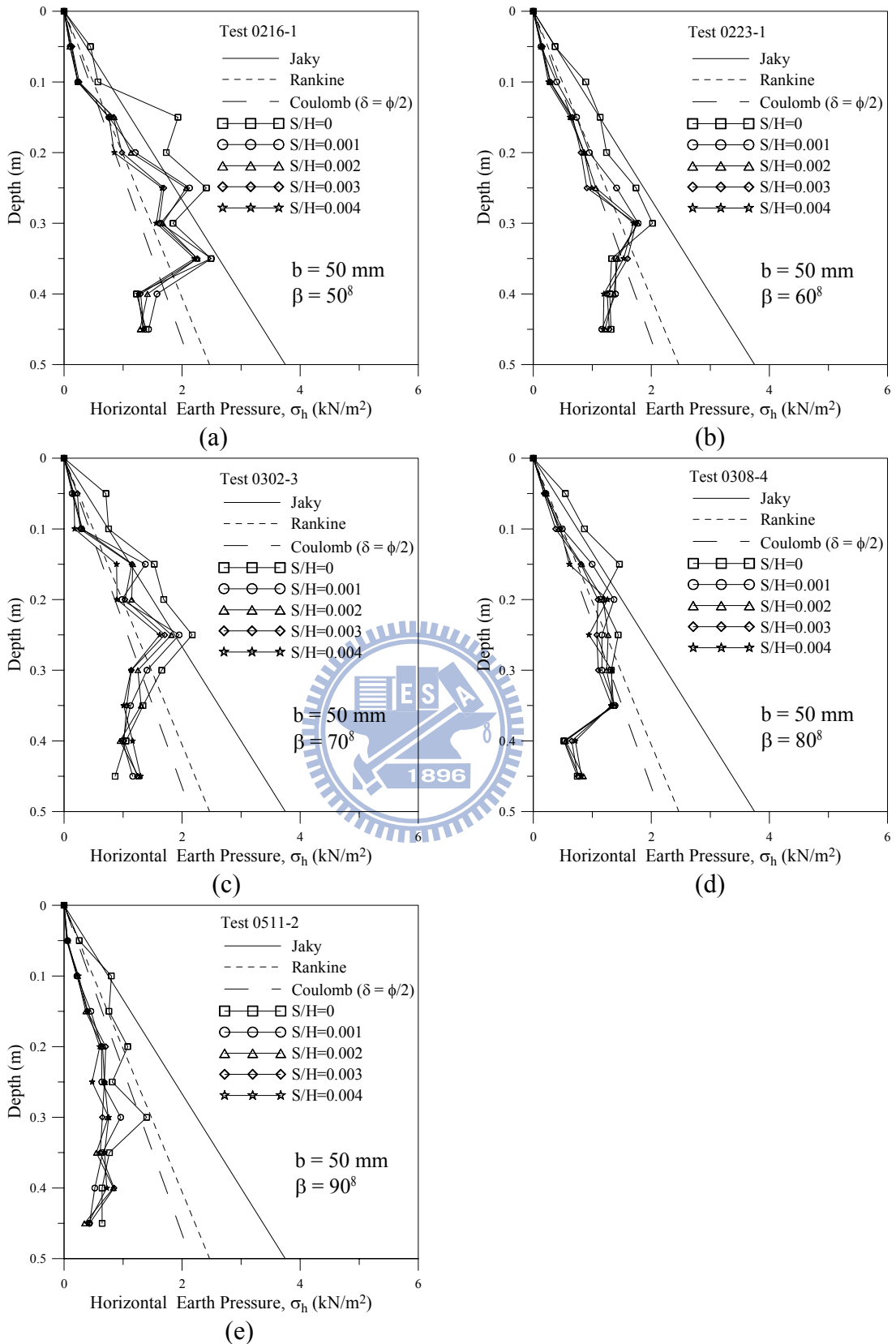
Fig. 2.19. Distribution of horizontal earth pressure for b = 50 mm
and various β angles (after Huang, 2009)
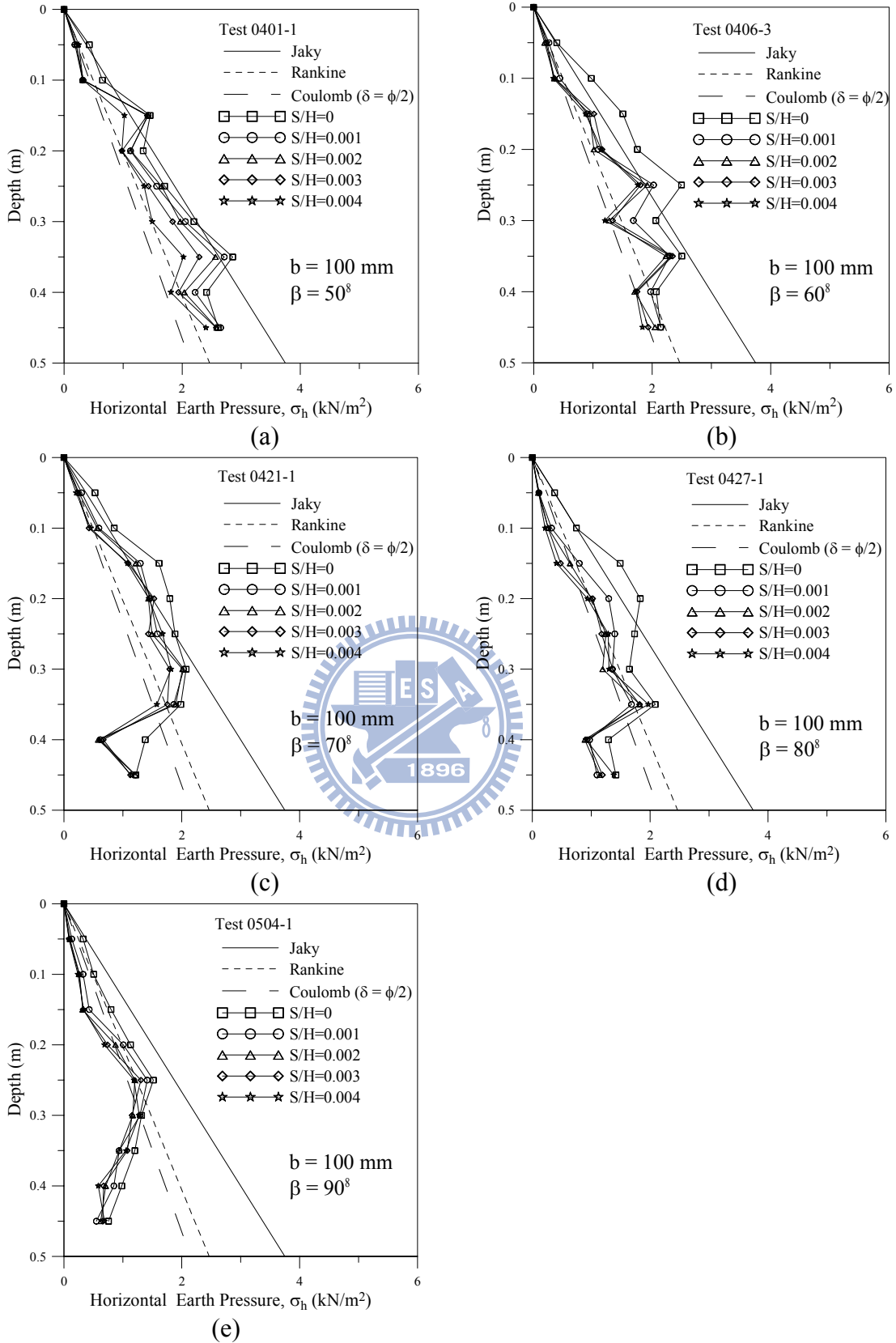
Fig. 2.20. Distribution of horizontal earth pressure for b = 100 mm
and various β angles (after Huang, 2009)
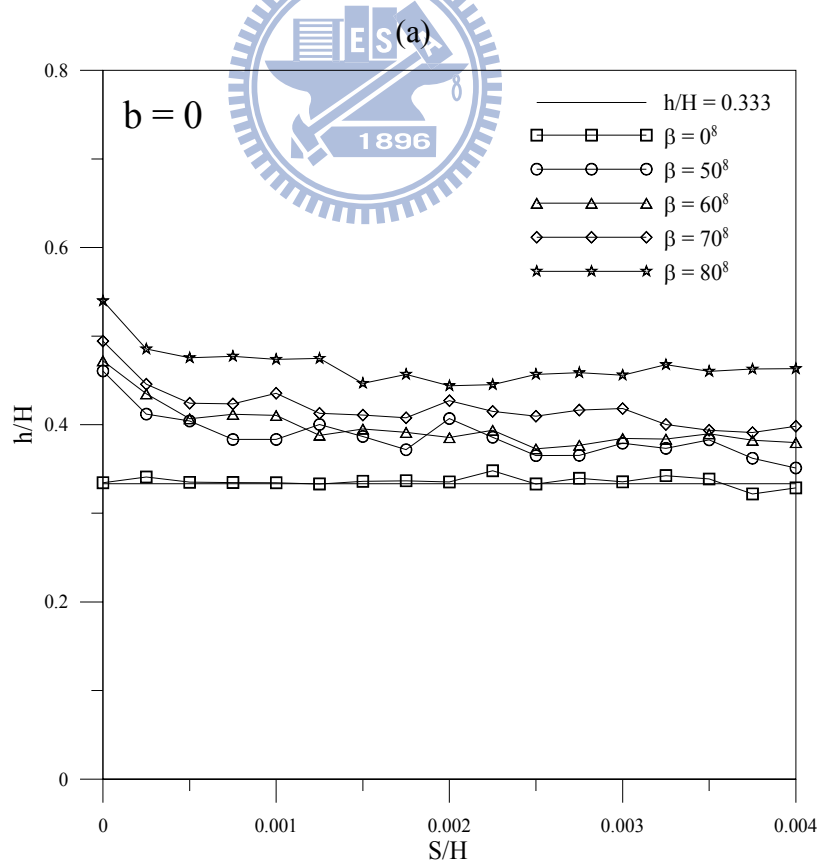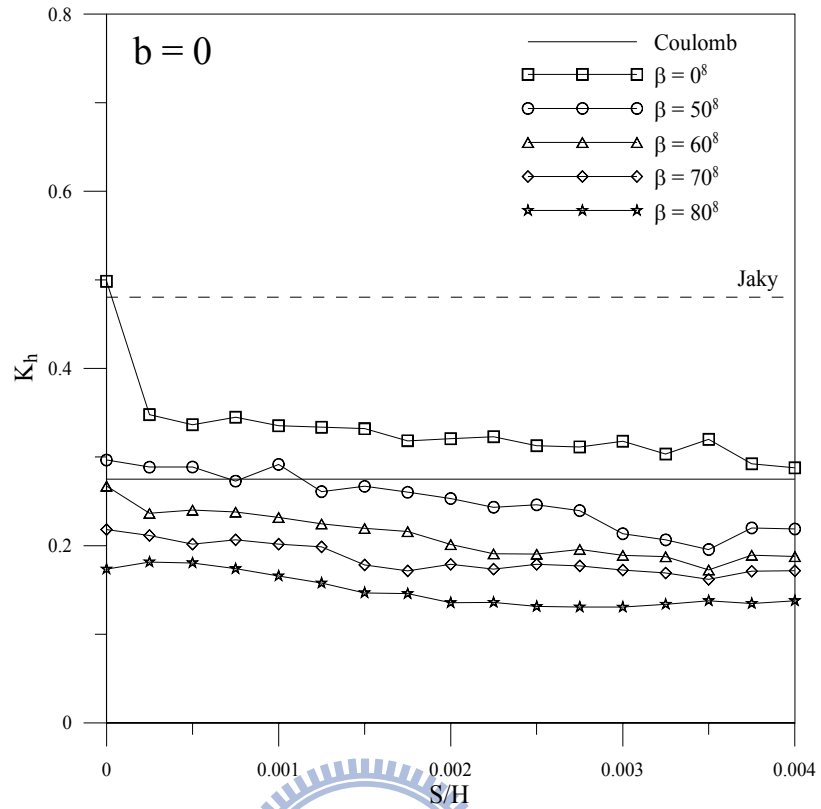
Fig. 2.21. Variation of K_h and h/H with wall movement for b = 0 (after Huang, 2009)

84
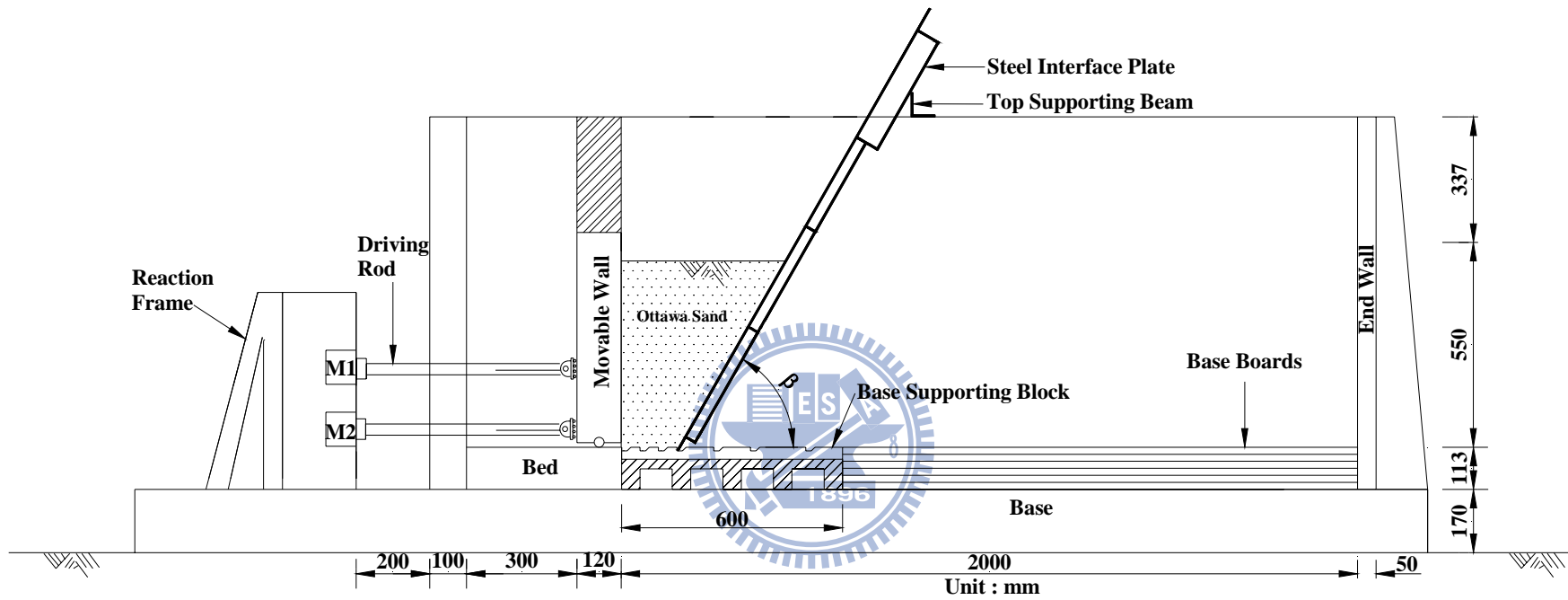
Fig. 2.22. NCTU model retaining wall with interface plate supports
(after Chang, 2010)
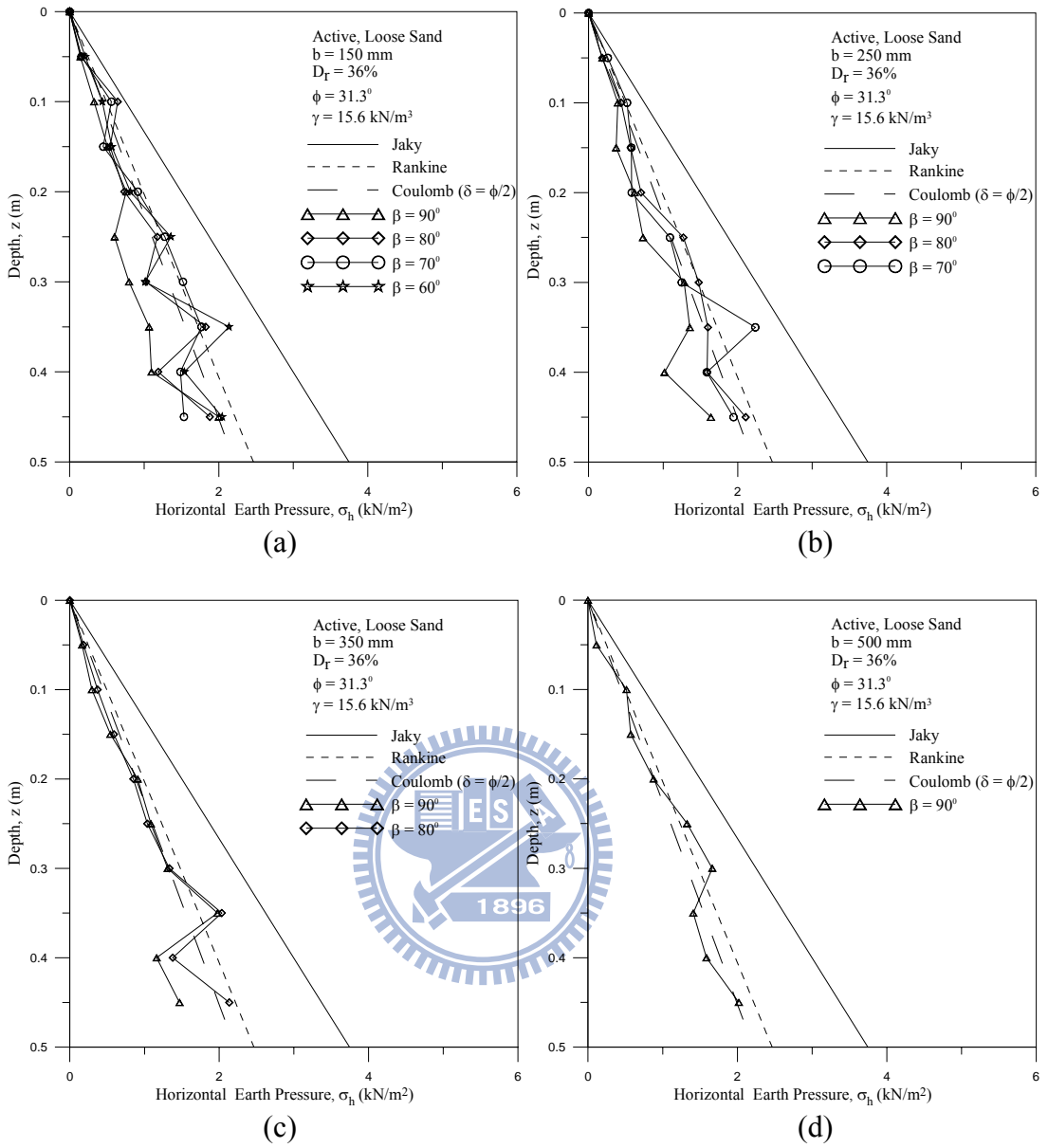
Fig. 2.23. Distribution of active earth pressure at different interface inclination angle β for b = 150, 250, 350 and 500 mm (after Chang, 2010)
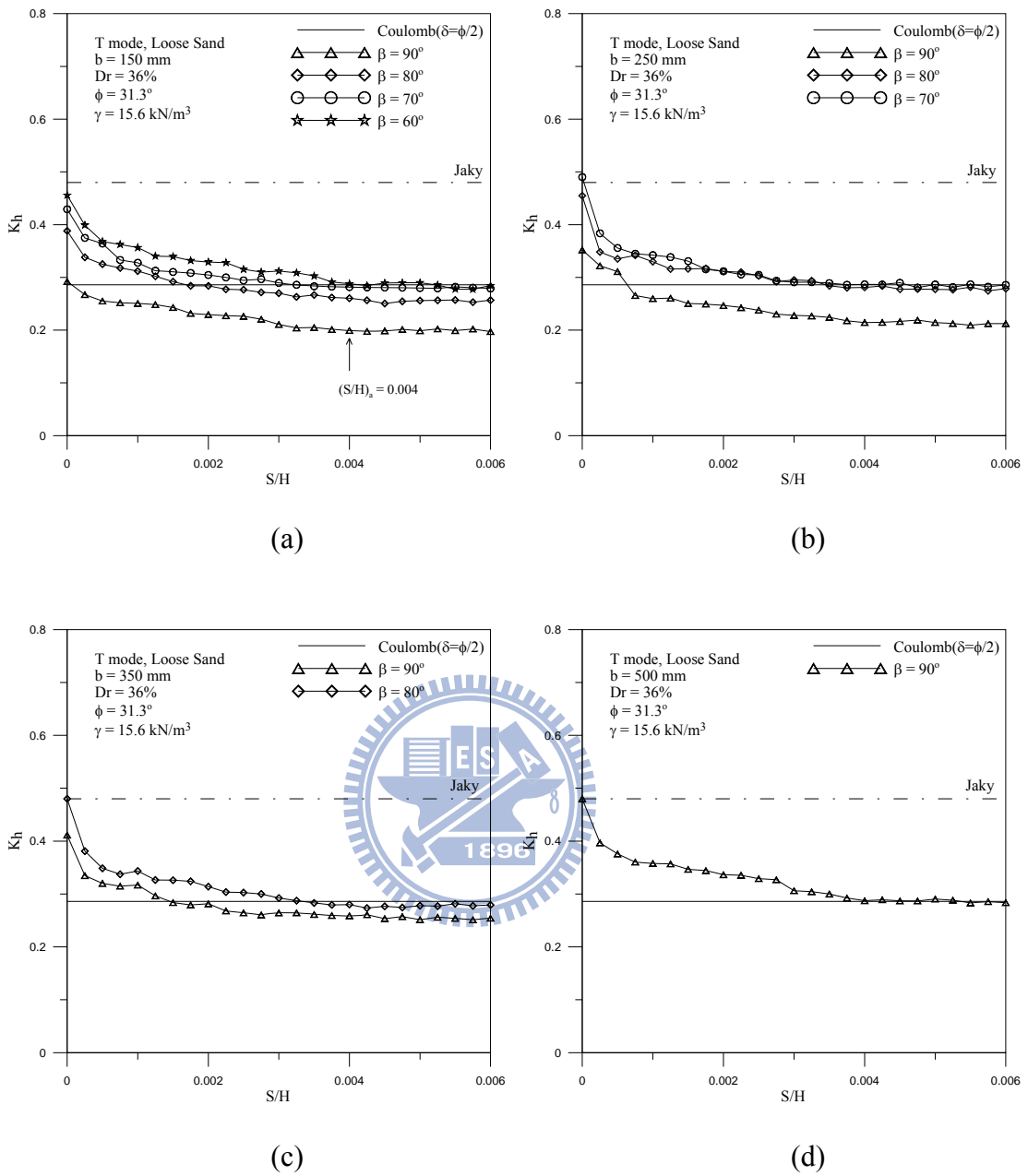
Fig. 2.24. Variation of earth pressure coefficient K_h with wall movement
for b = 150, 250, 350 and 500 mm (after Chang, 2010)
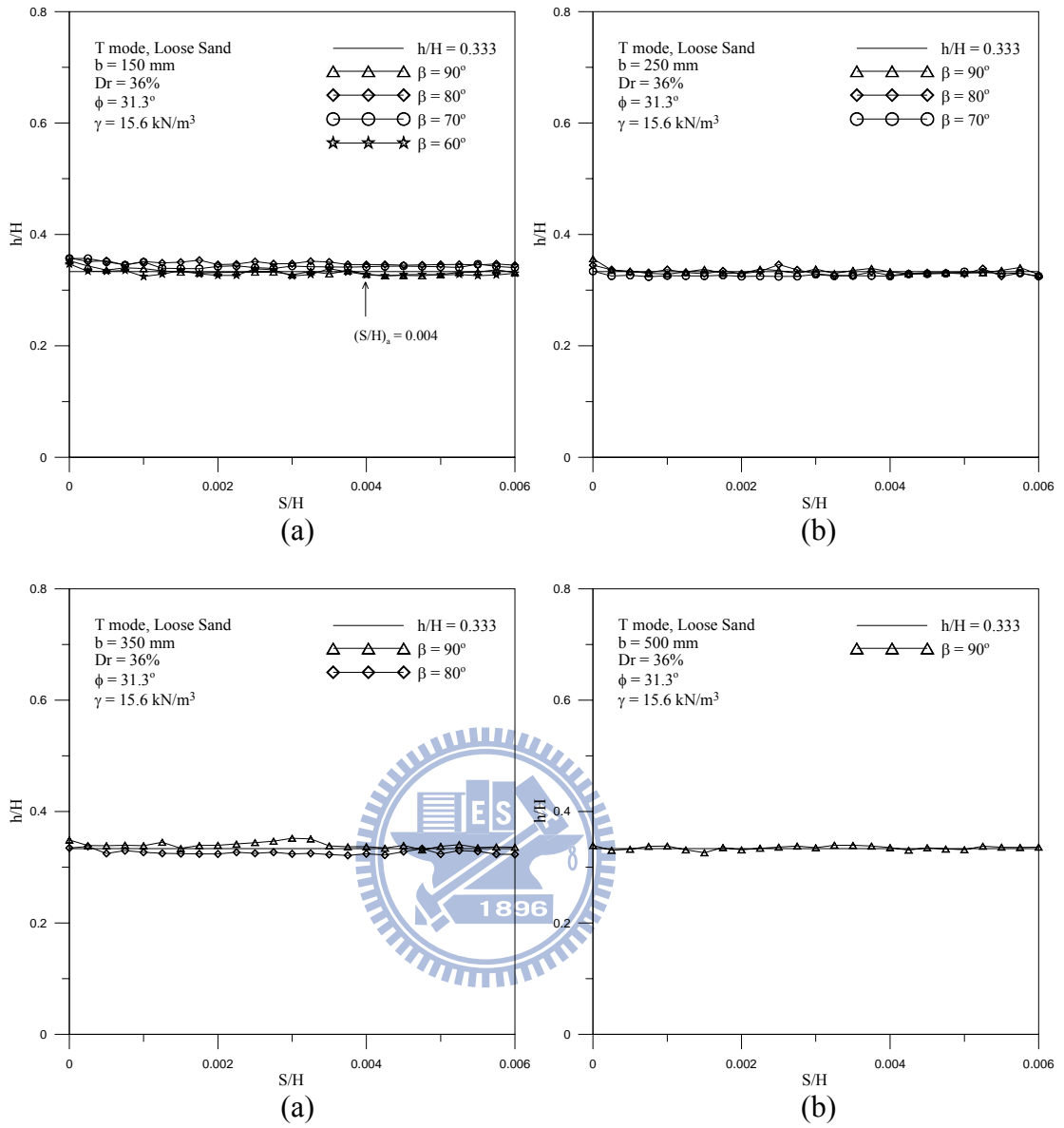
Fig. 2.25. Variation of total thrust location with wall movement for
b = 150, 250, 350 and 500 mm (after Chang, 2010)
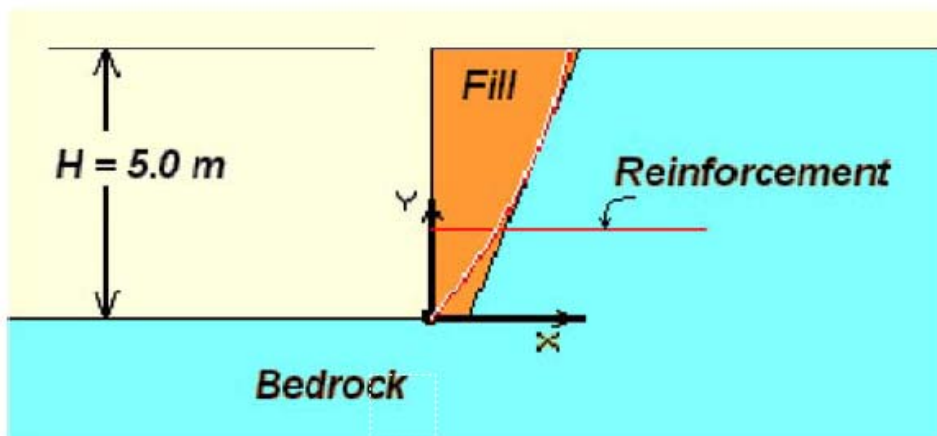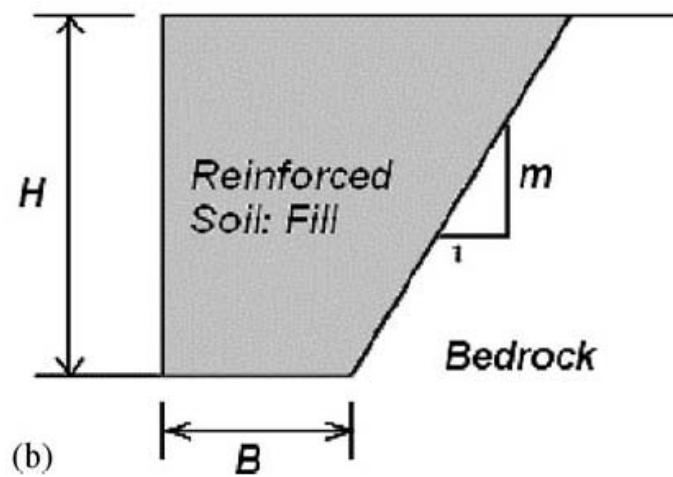
Fig. 2.26. Typical geometry: (a) analyzed (b) notation
(after Leshchinsky et al. 2004)
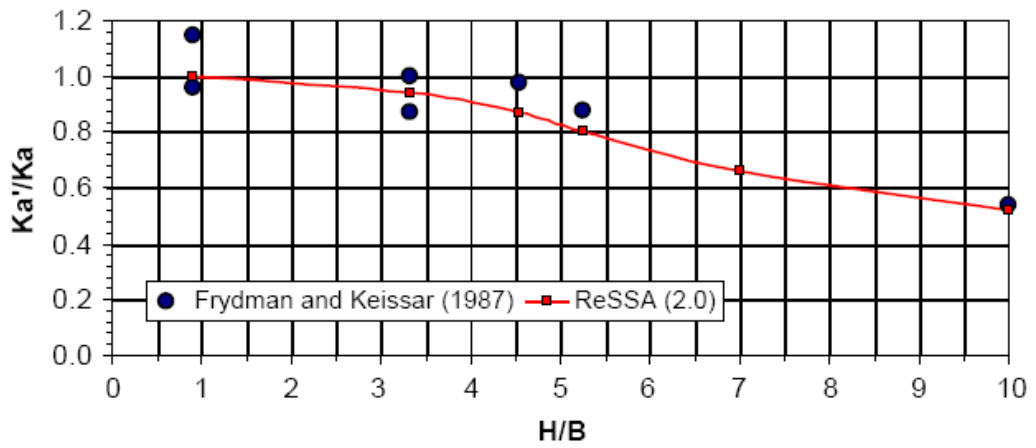
Fig. 2.27. Predictions by ReSSA versus centrifugal test results
for $\phi = 36°$ and m $= \infty$ (after Leshchinsky et al. 2004)

$$Ka = tan^2 (45° - \phi/2)$$
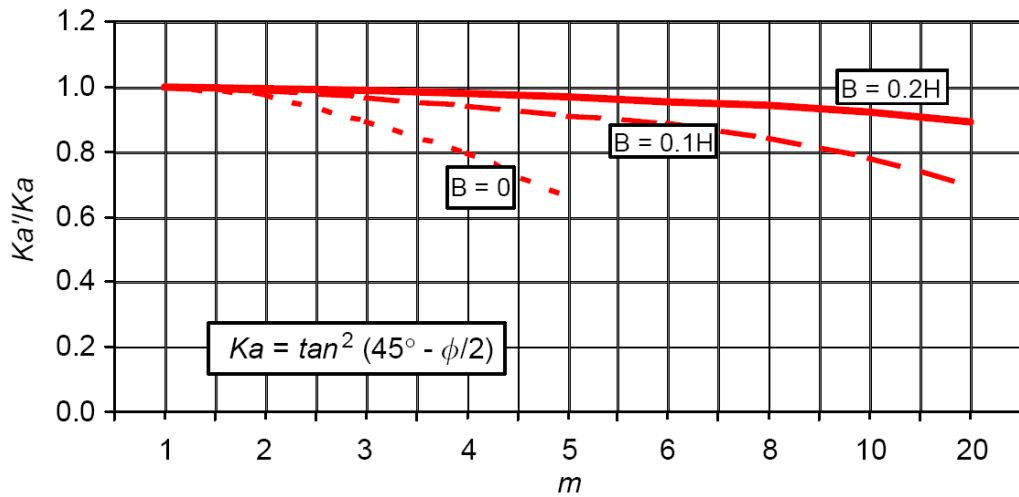
Fig. 2.28. Analysis results (after Leshchinsky et al. 2004)
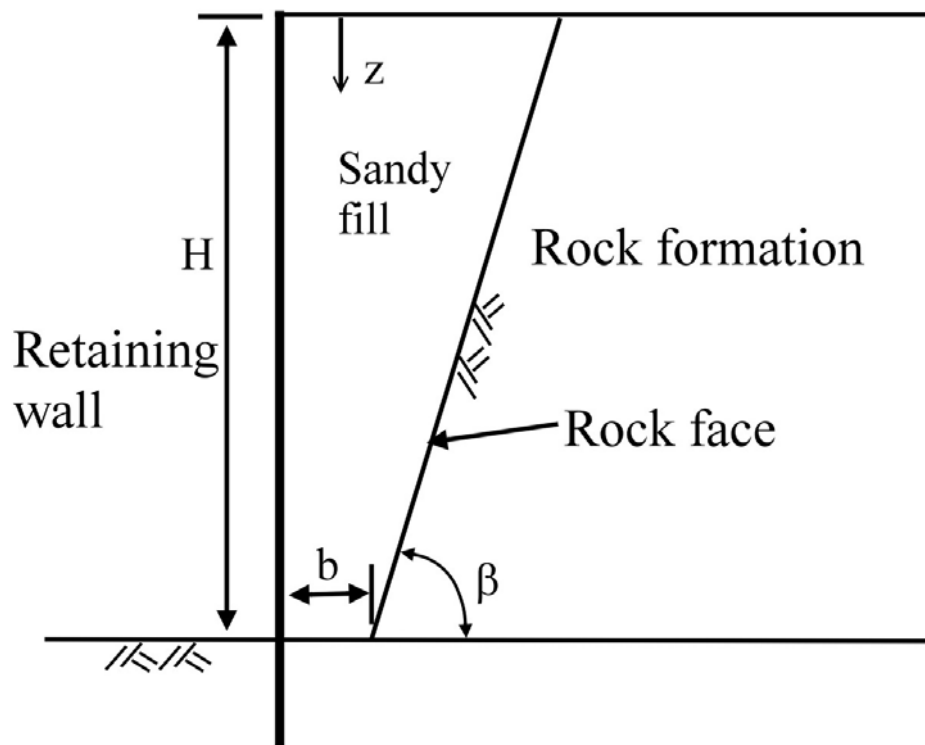
Fig. 2.29. Typical geometry of backfill zone behind a
retaining wall used in this study
(after Fan and Fang, 2010)
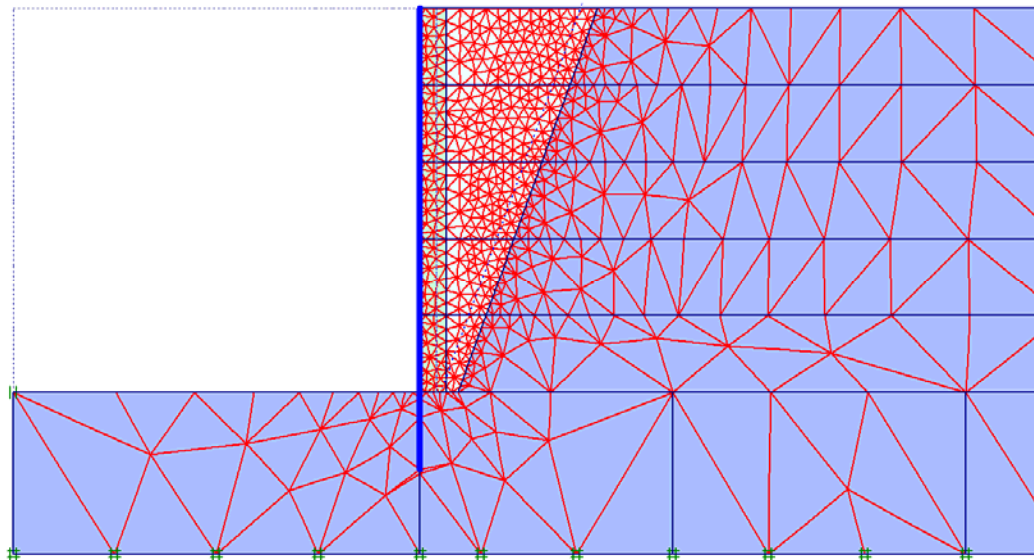
Fig. 2.30. The finite element mesh for a retaining wall with limited backfill
space (β=70° and b=0.5m)
(after Fan and Fang, 2010)

91
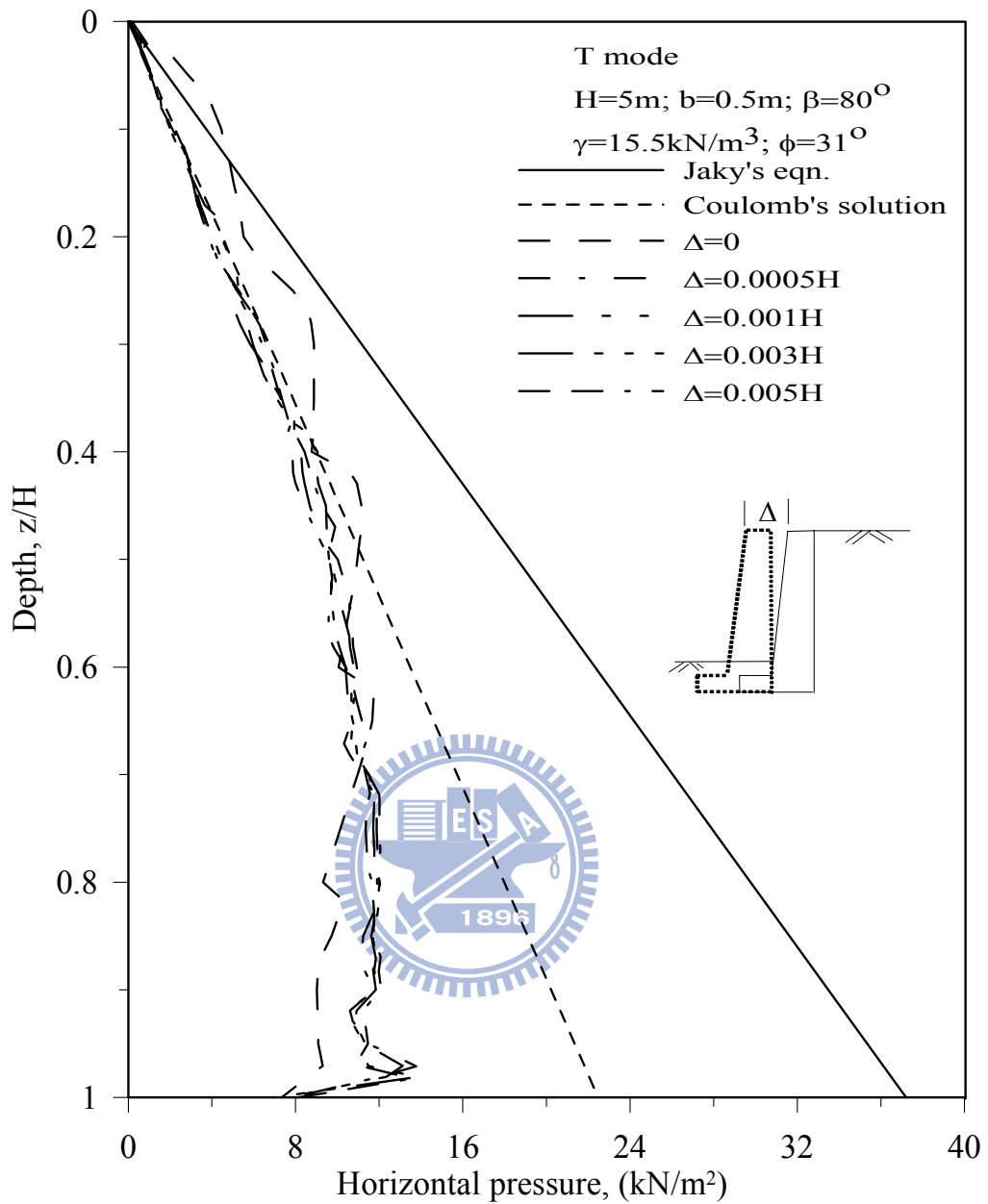
Fig. 2.31. Distribution of earth pressures with the depth at various wall
displacements for walls in translation (T mode)
(after Fan and Fang, 2010)
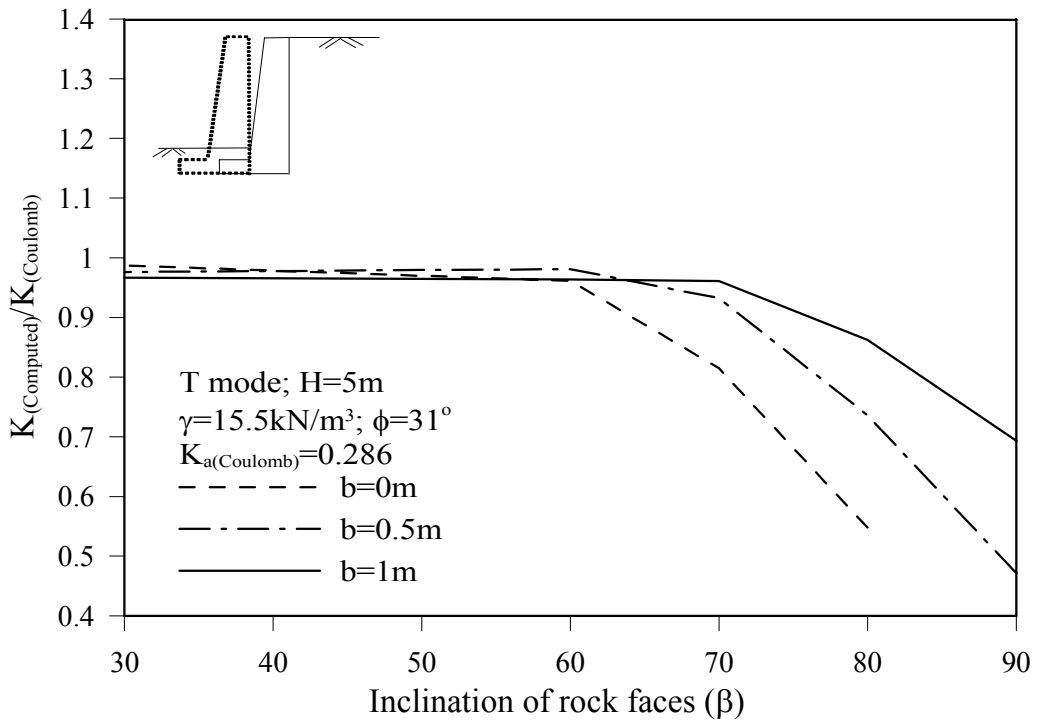
Fig. 2.32. Variation of the coefficient of active earth pressures ($K_{a(Computed)}/K_{a(Coulomb)}$) with the inclination of rock faces at various fill widths (b) for walls undergoing translation (after Fan and Fang, 2010)
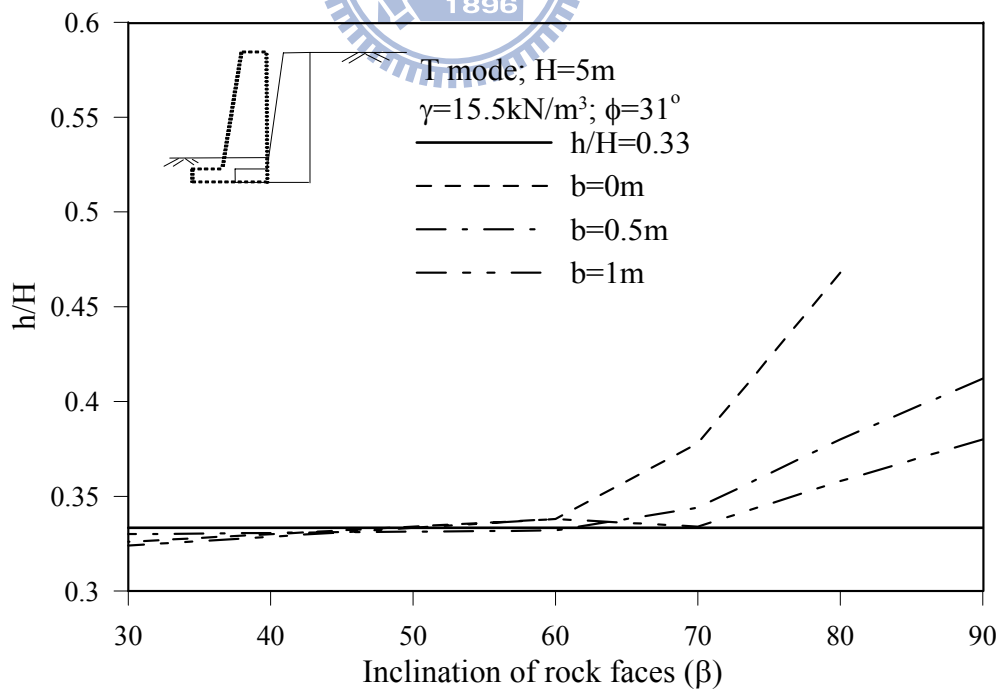
Fig. 2.33. Variation of the location of resultant (h/H) of active earth pressures with the inclination of rock faces at various fill widths (b) for walls undergoing translation (T mode). (after Fan and Fang, 2010)

93
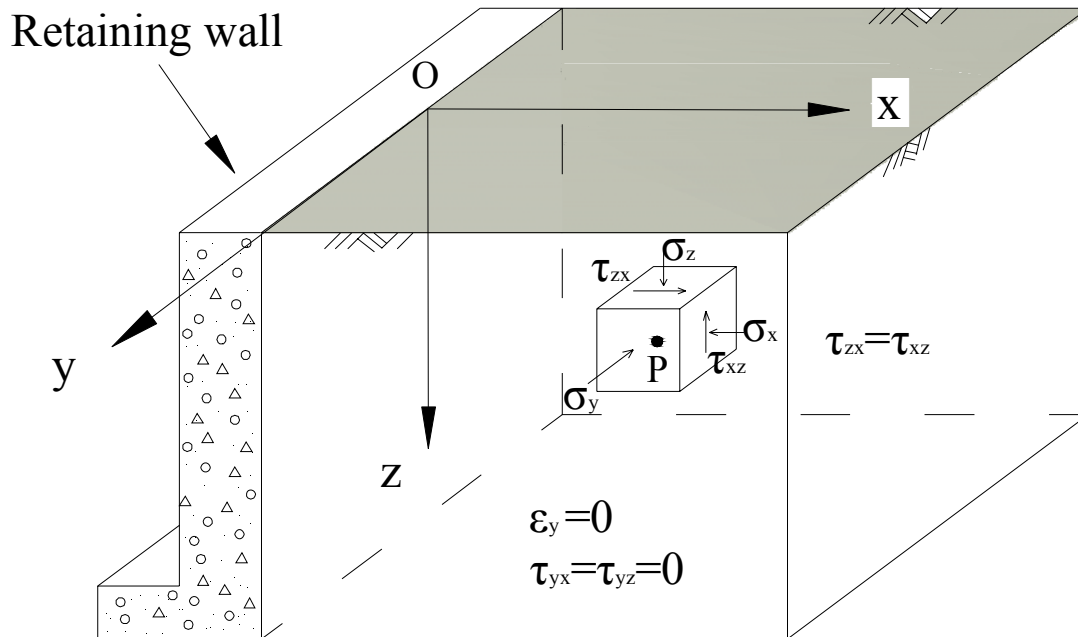
Fig. 2.34. Definition of plane strain state-of-stress
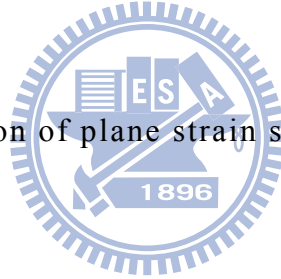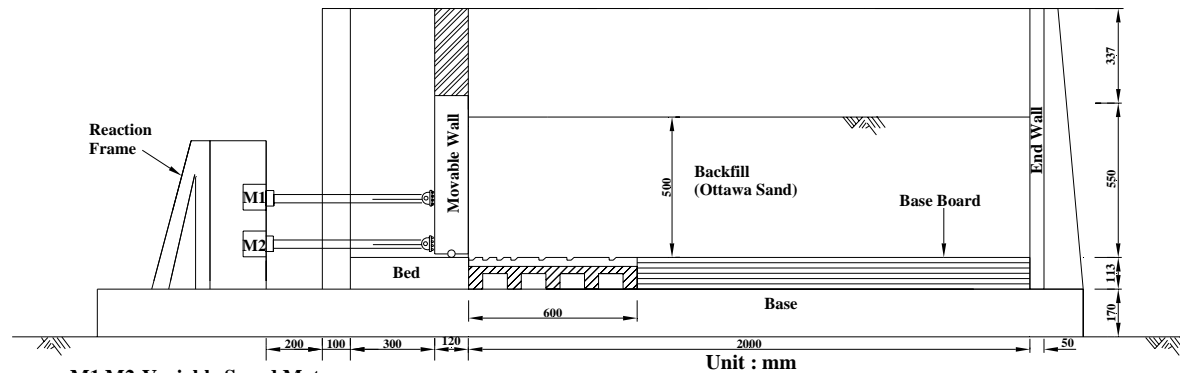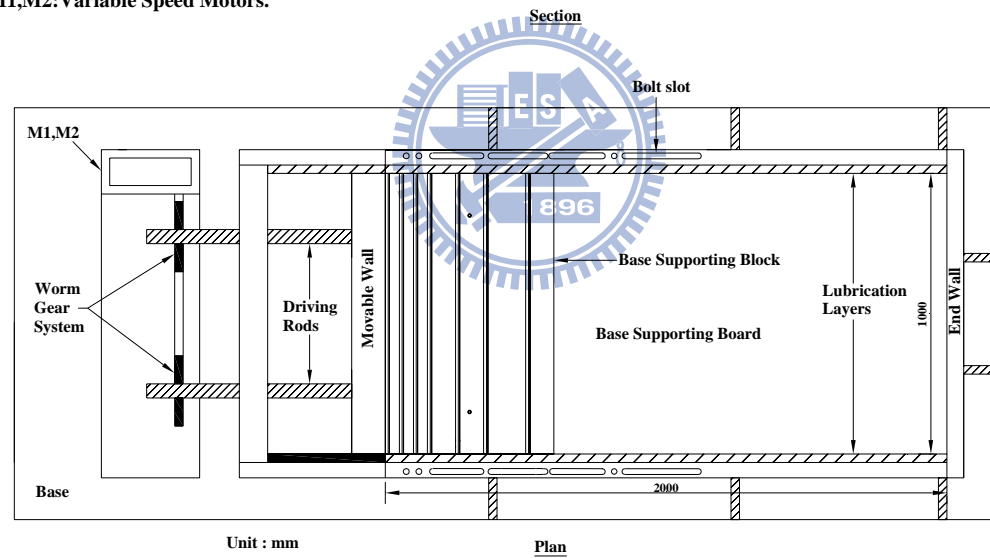
Unit: mm

Fig.3.1. NCTU Model Retaining-Wall Facility
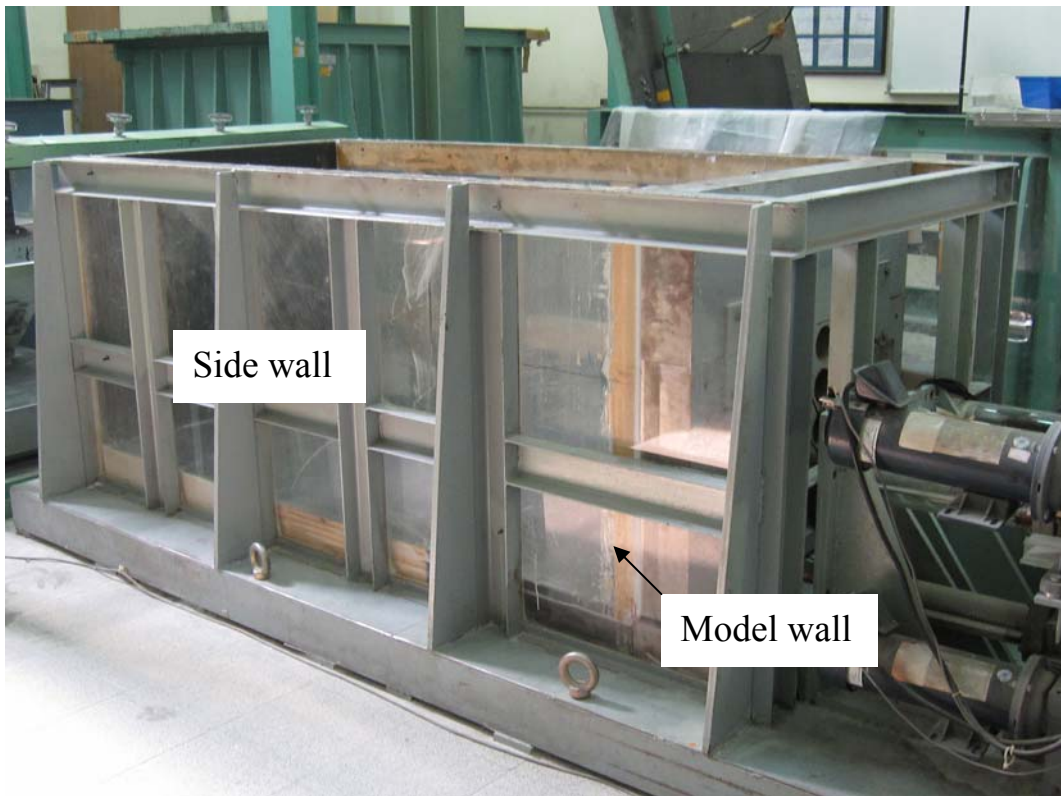
Fig.3.2. NCTU model retaining wall
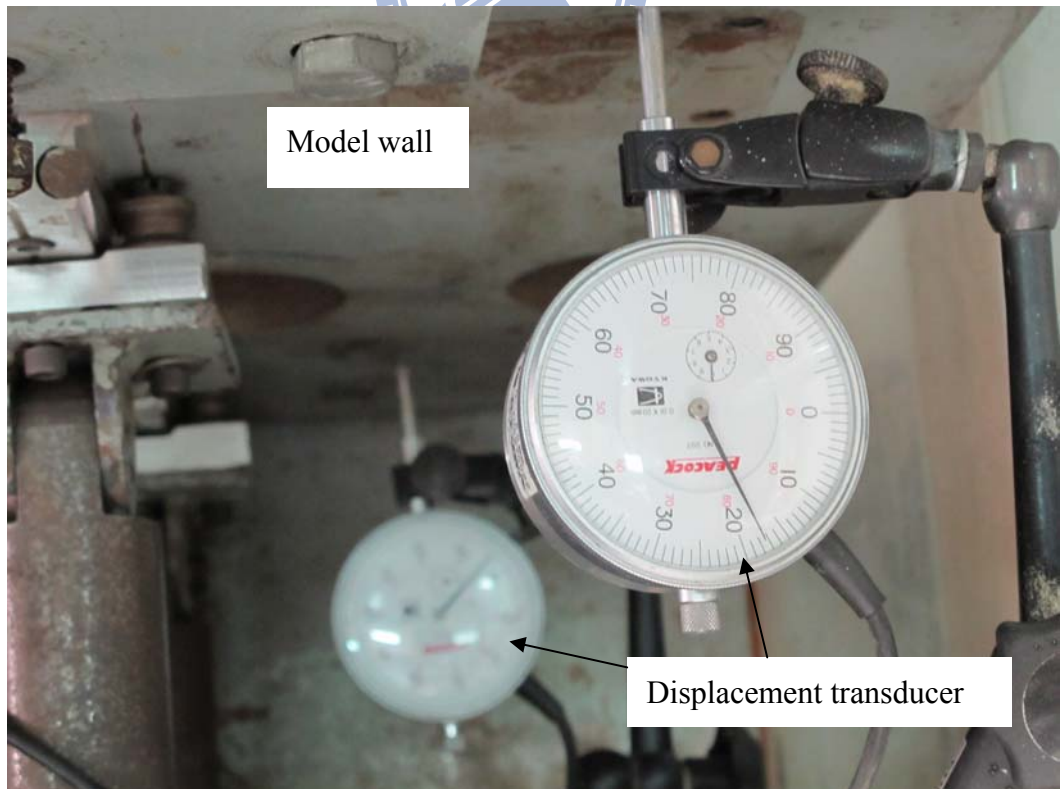
Fig.3.3. Displacement transducer (Kyowa DT-20D)
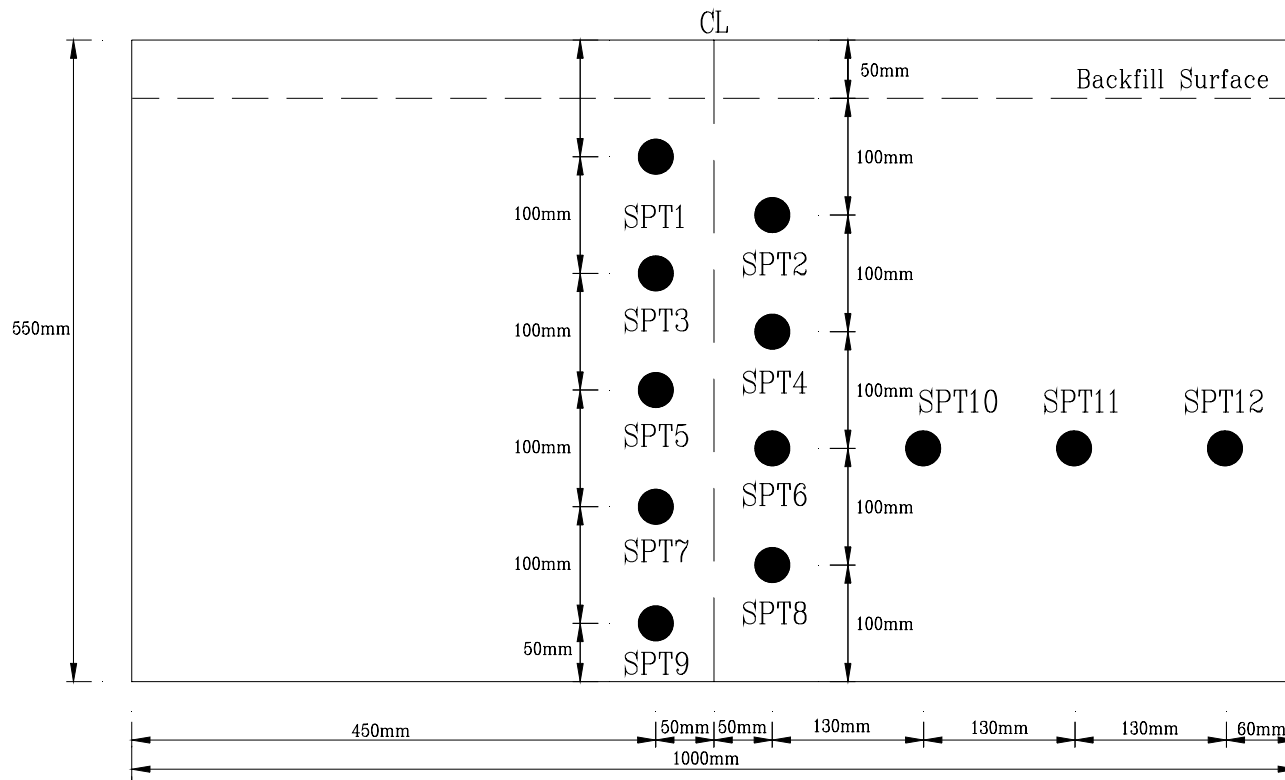
Front-view

Unit : mm

Fig. 3.4. Locations of pressure transducers on NCTU model wall
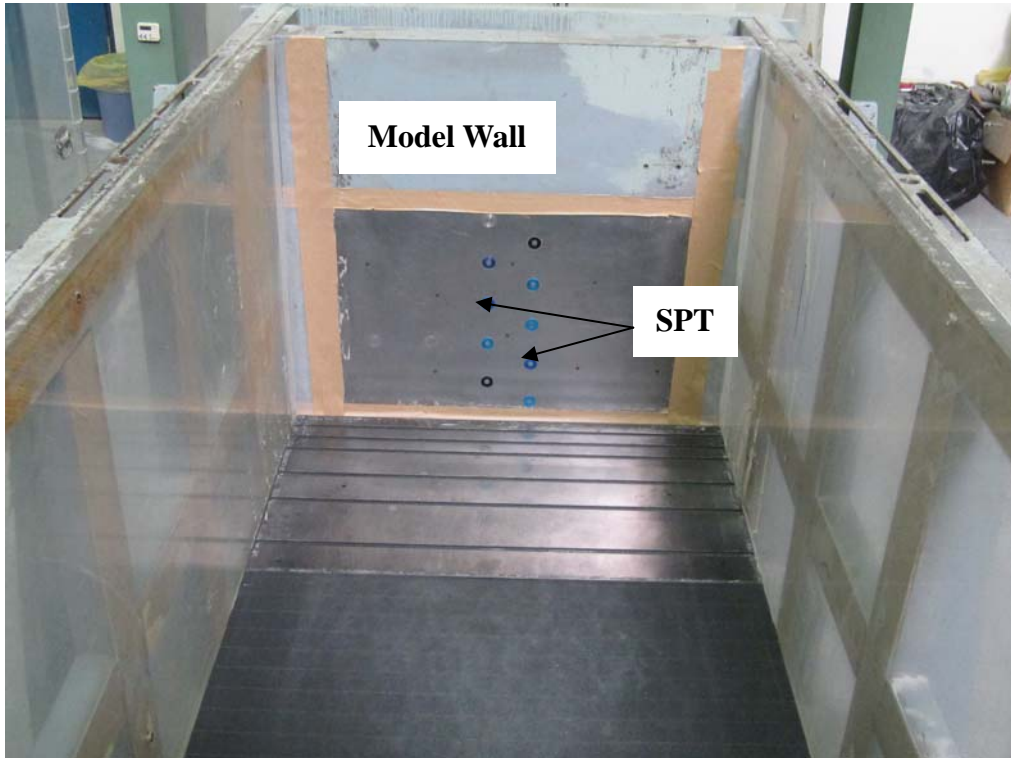
Fig.3.5. Locations of pressure transducers on model wall

Fig. 3.6. Soil pressure transducer (Kyowa PGM-0.2KG)

(a)

(b)

Fig. 3.7. Data acquisition system

Power Cord
(5 m-Long)

Switch

Handle

Eccentric
Motor

20

1000

10

15

40

27

48

225

48

360

Unit : mm
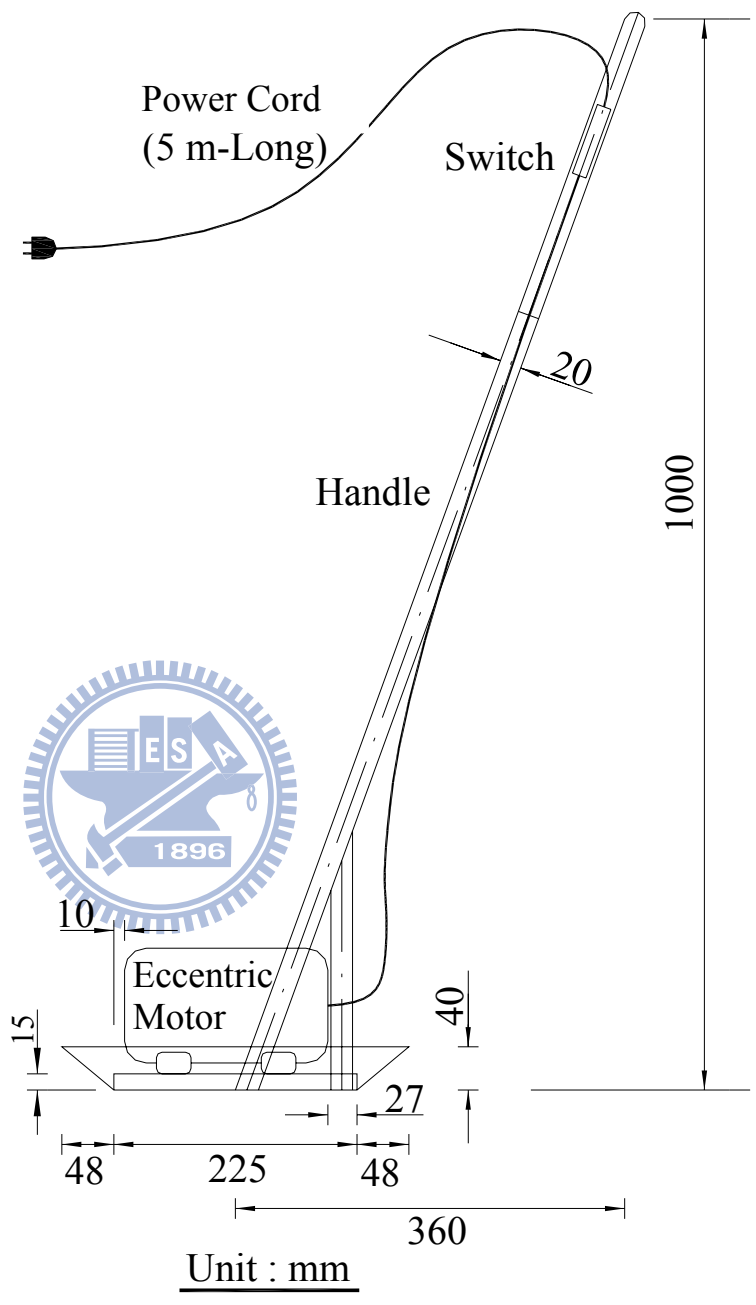
Fig. 3.8. Side-View of Square Vibratory Compactor (after Chen, 2002)

Handle

Eccentric Motor

Square Compaction Plate (225 mm × 225 mm)

Fig. 3.9. Square Vibratory Soil Compactor (after Chen, 2002)
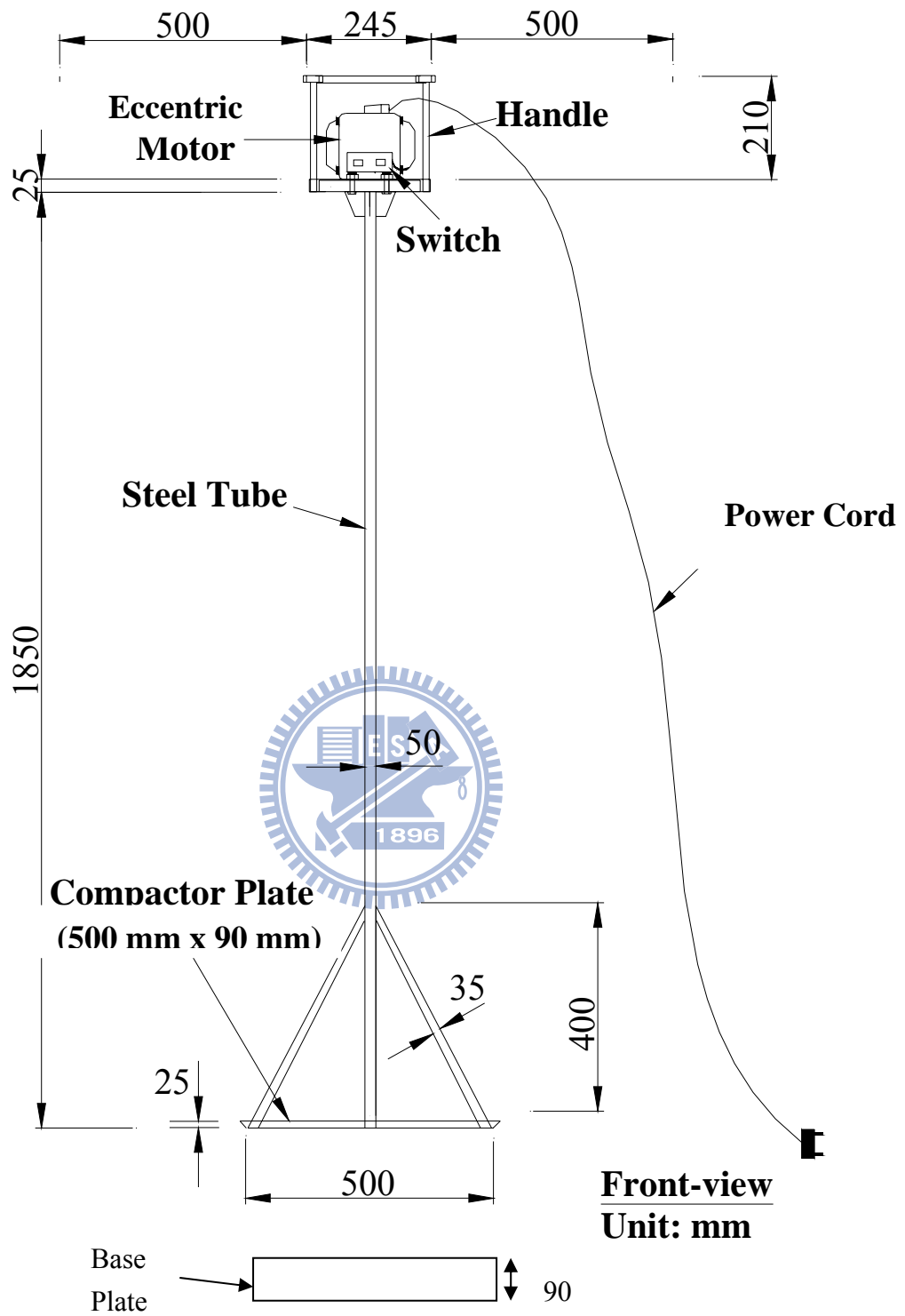
Fig. 3.10. 500 mm × 90 mm vibratory strip compactor

Eccentric Motor

Steel Tube

Compaction Plate
(500 mm $\times$ 90 mm)
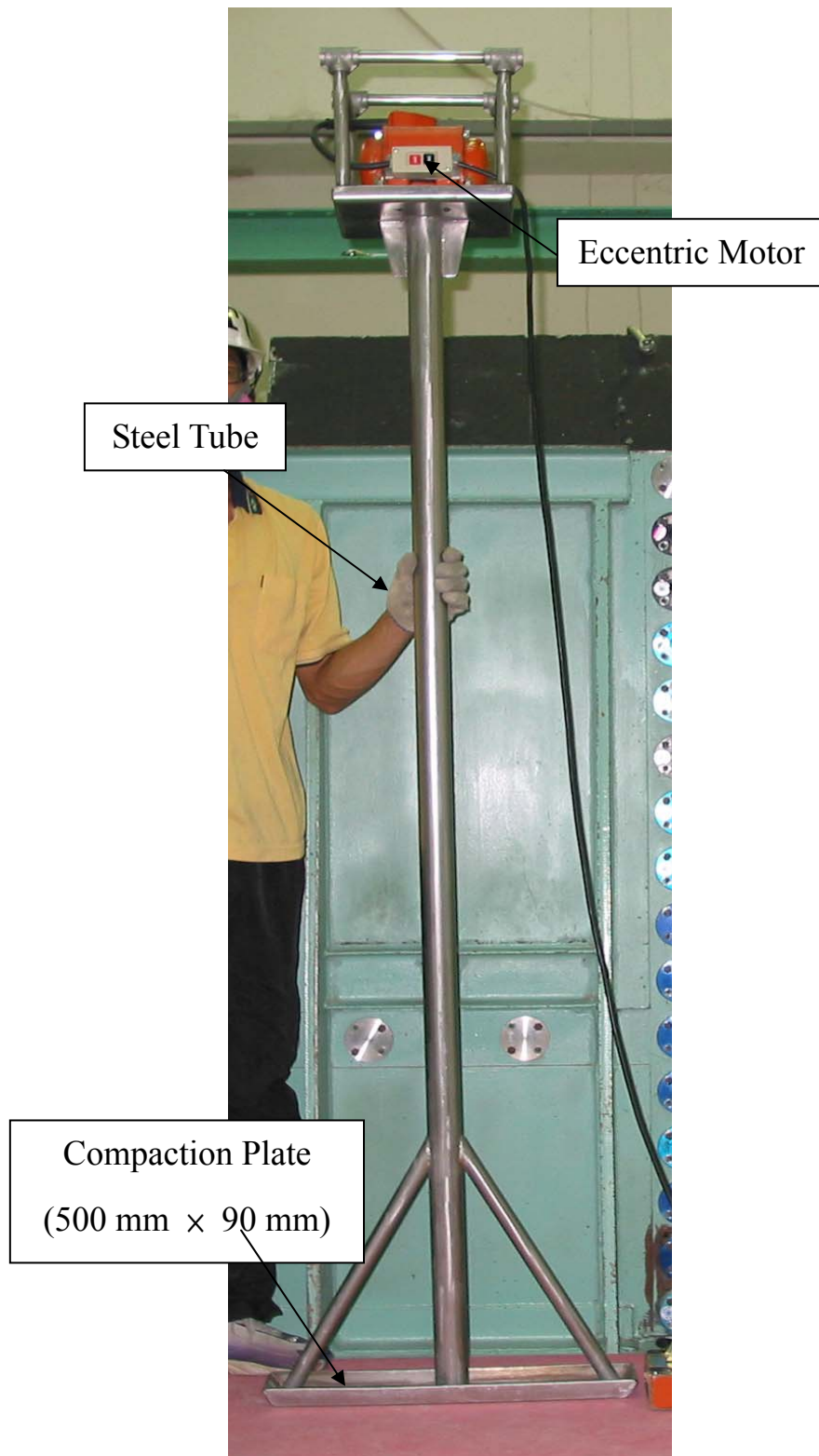
Fig. 3.11. Strip vibratory compactor
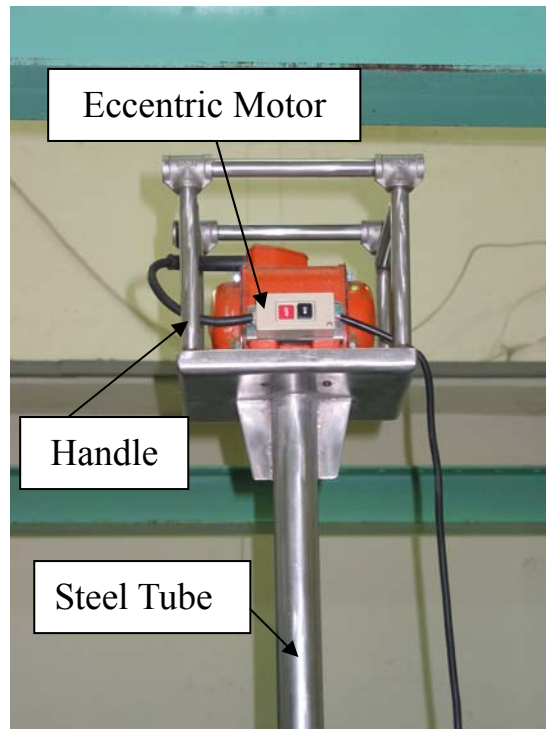
(a) eccentric motor on strip compactor
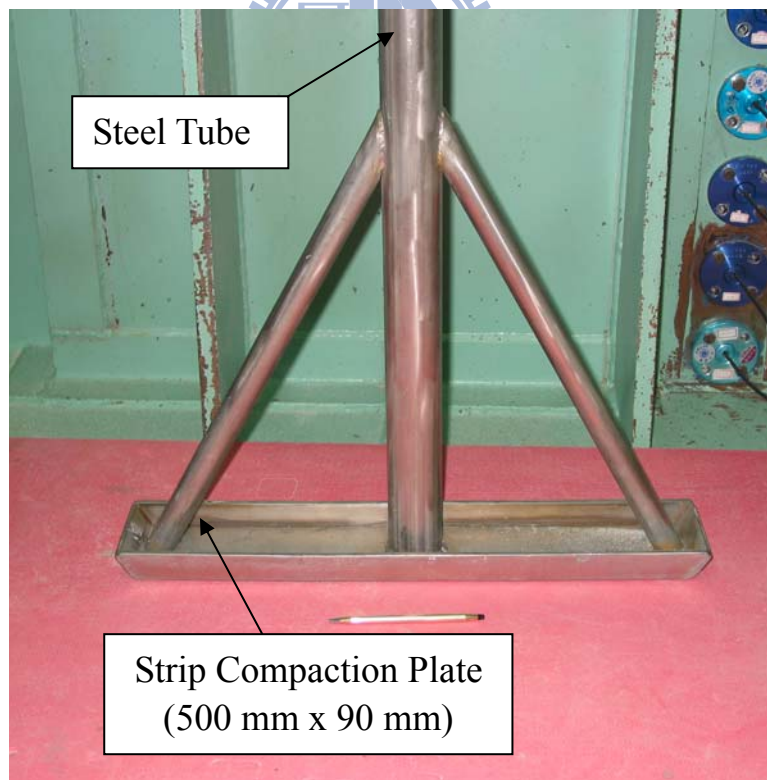
(b) Rectangular compaction plate

Fig. 3.12. Top and bottom of Strip vibratory soil compactor
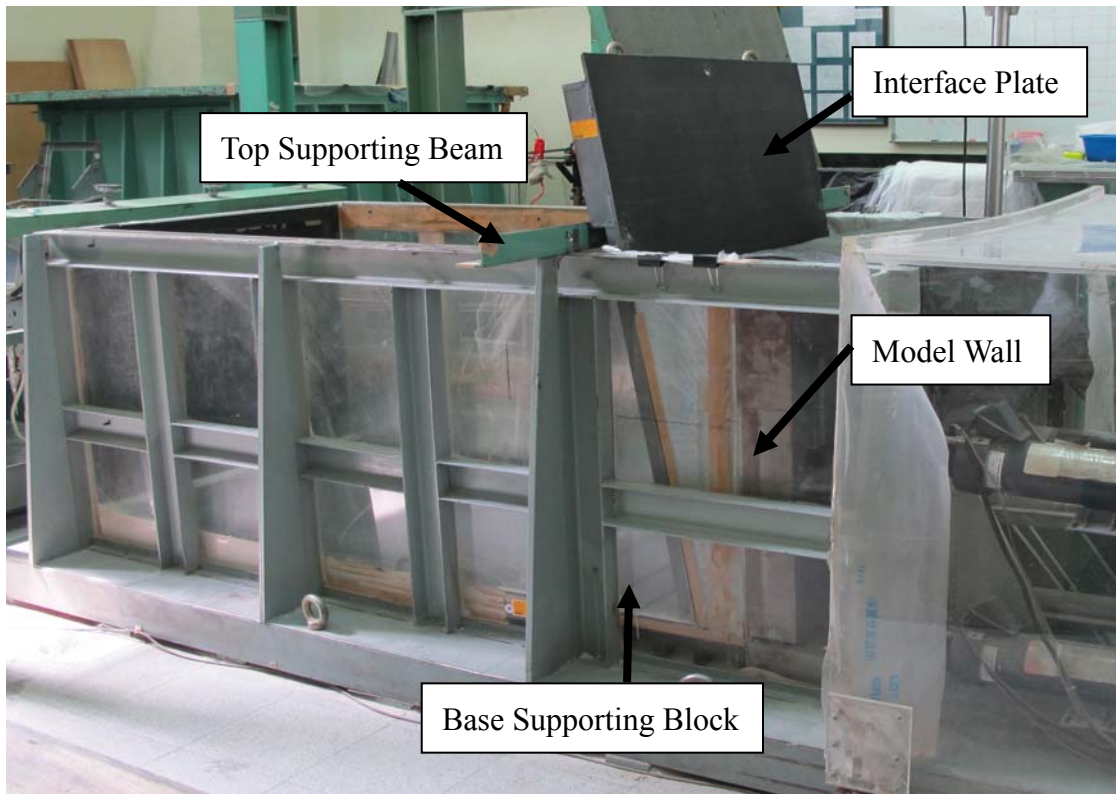
Fig. 4.1. NCTU model retaining wall with inclined interface plate

Fig. 4.2. Steel interface plate (after Zheng, 2008)

106

Steel Plate with SAFETY-WALK

(a) Front-view

Steel L-Beams

Steel Plate
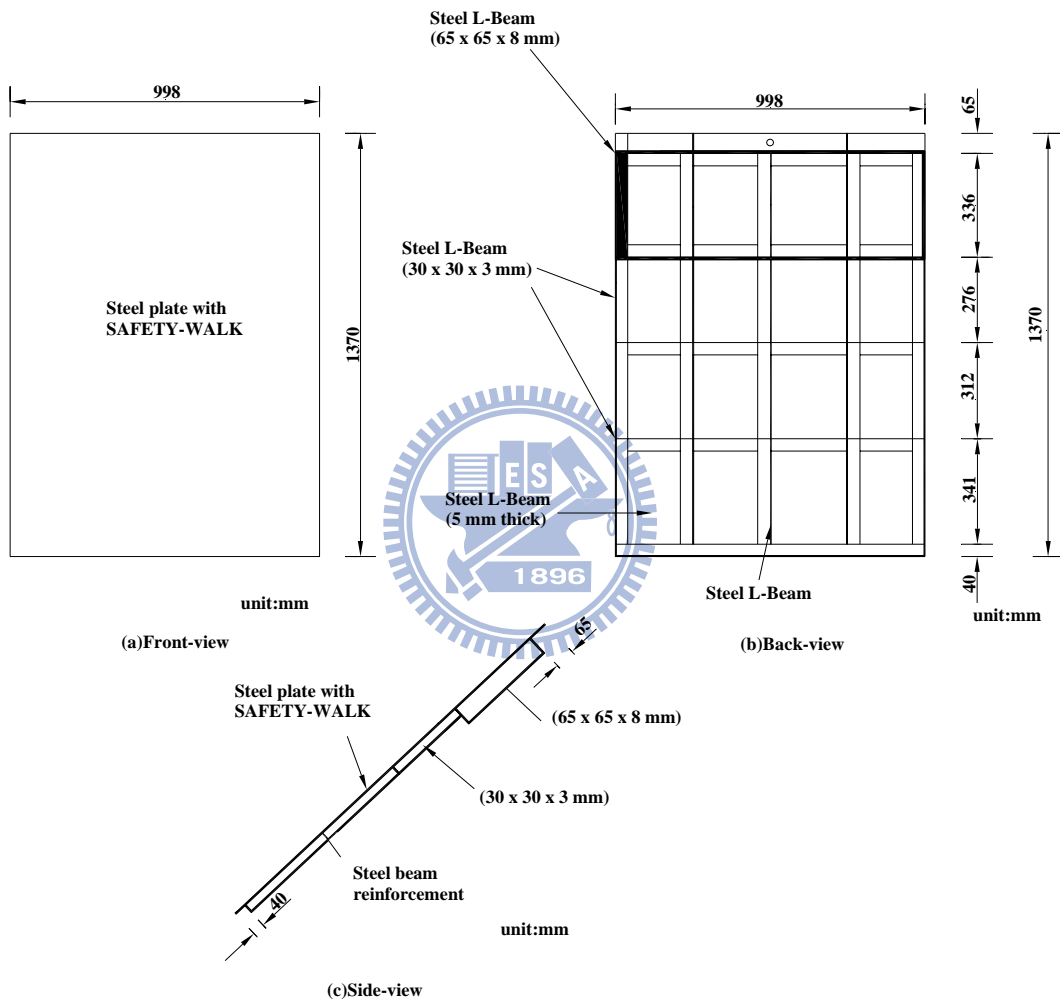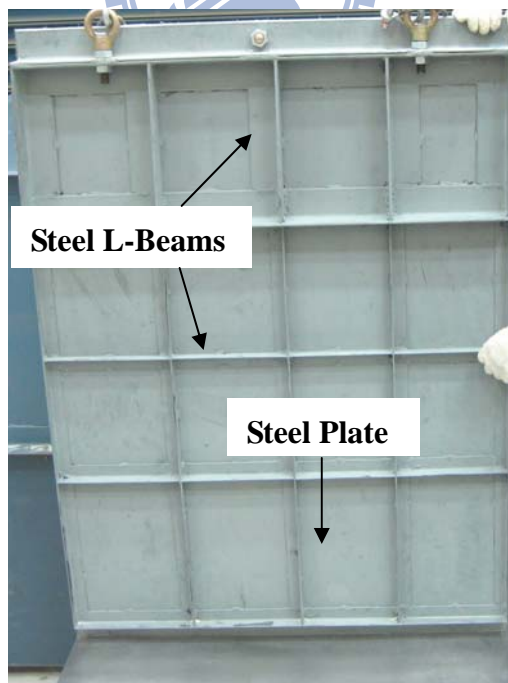
(b) Back-view

Fig. 4.3. Steel interface plate (after Zheng, 2008)
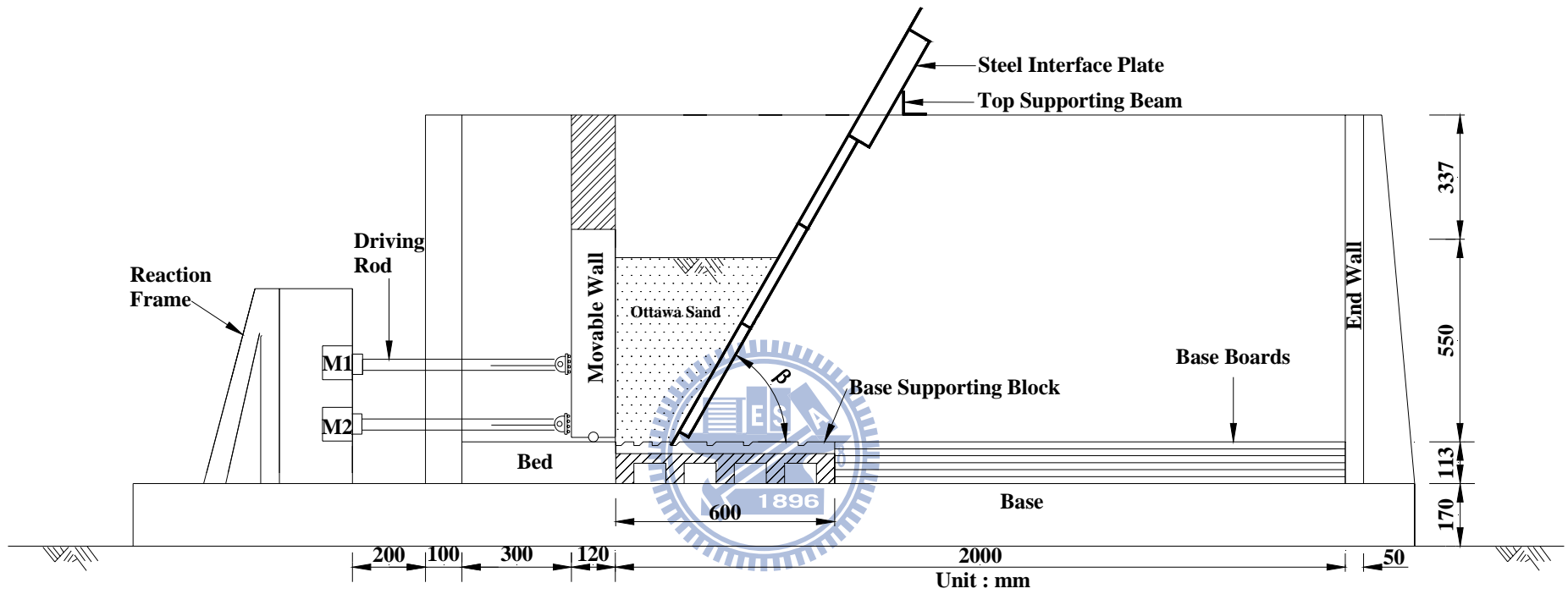
Fig. 4.4. NCTU model retaining wall system with interface plate and supports

End Wall

1000

Base Boards

Bolt slot

2000

Base Supporting Block

Movable Wall

Driving Rods

M1,M2

Worm Gear System

Base

Unit : mm
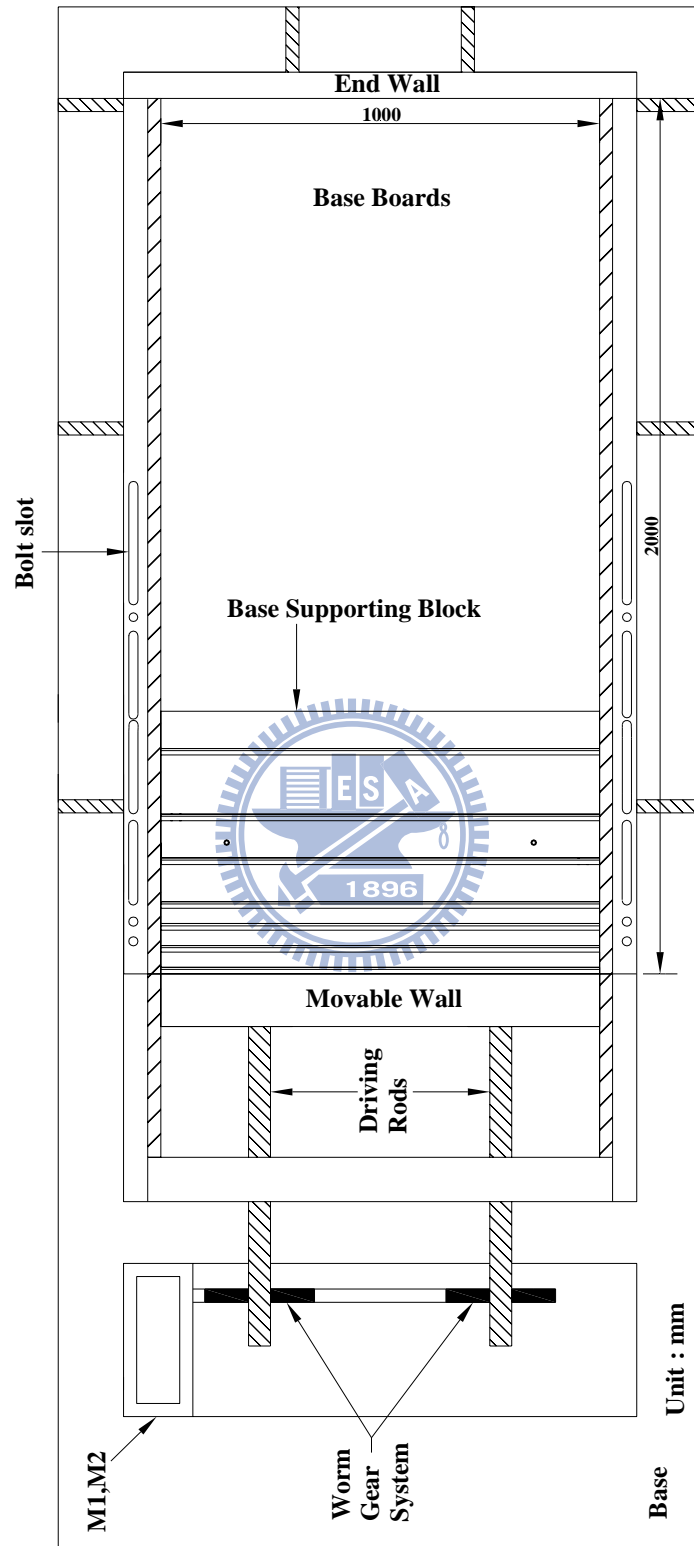
Fig. 4.5 Soil bin with base support block

109

(a)

unit:mm
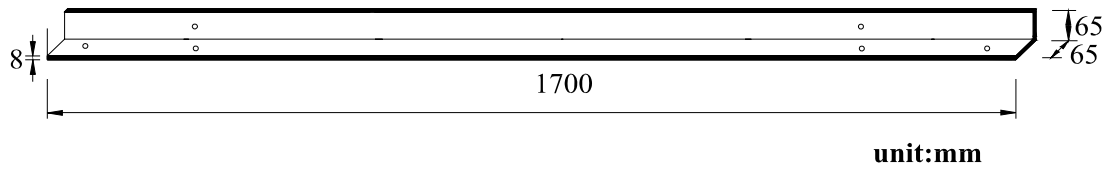
(b)

Fig. 4.6. Top supporting beam (after Zheng, 2008)
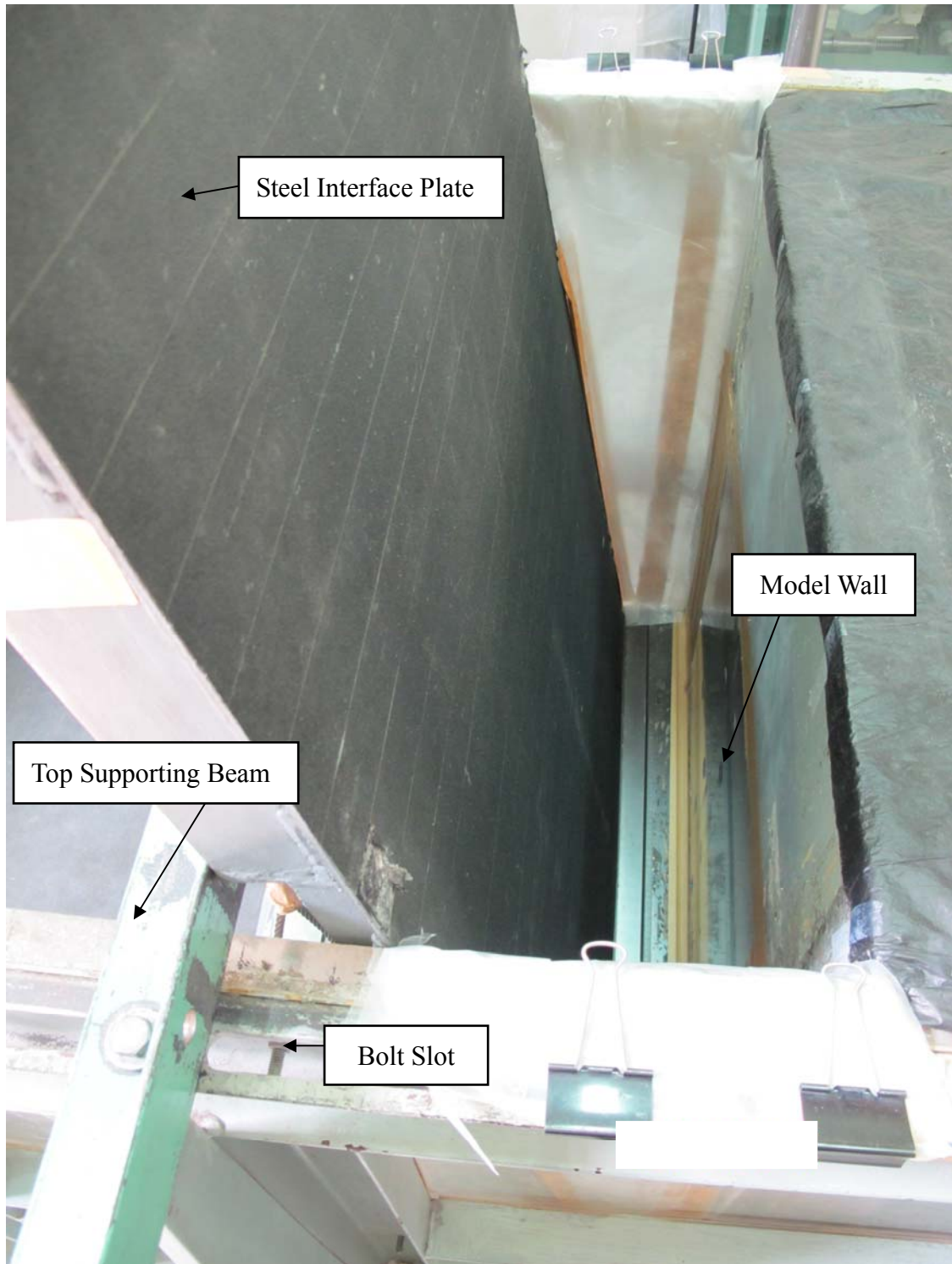
Fig. 4.7. Steel interface plate and top supporting beam
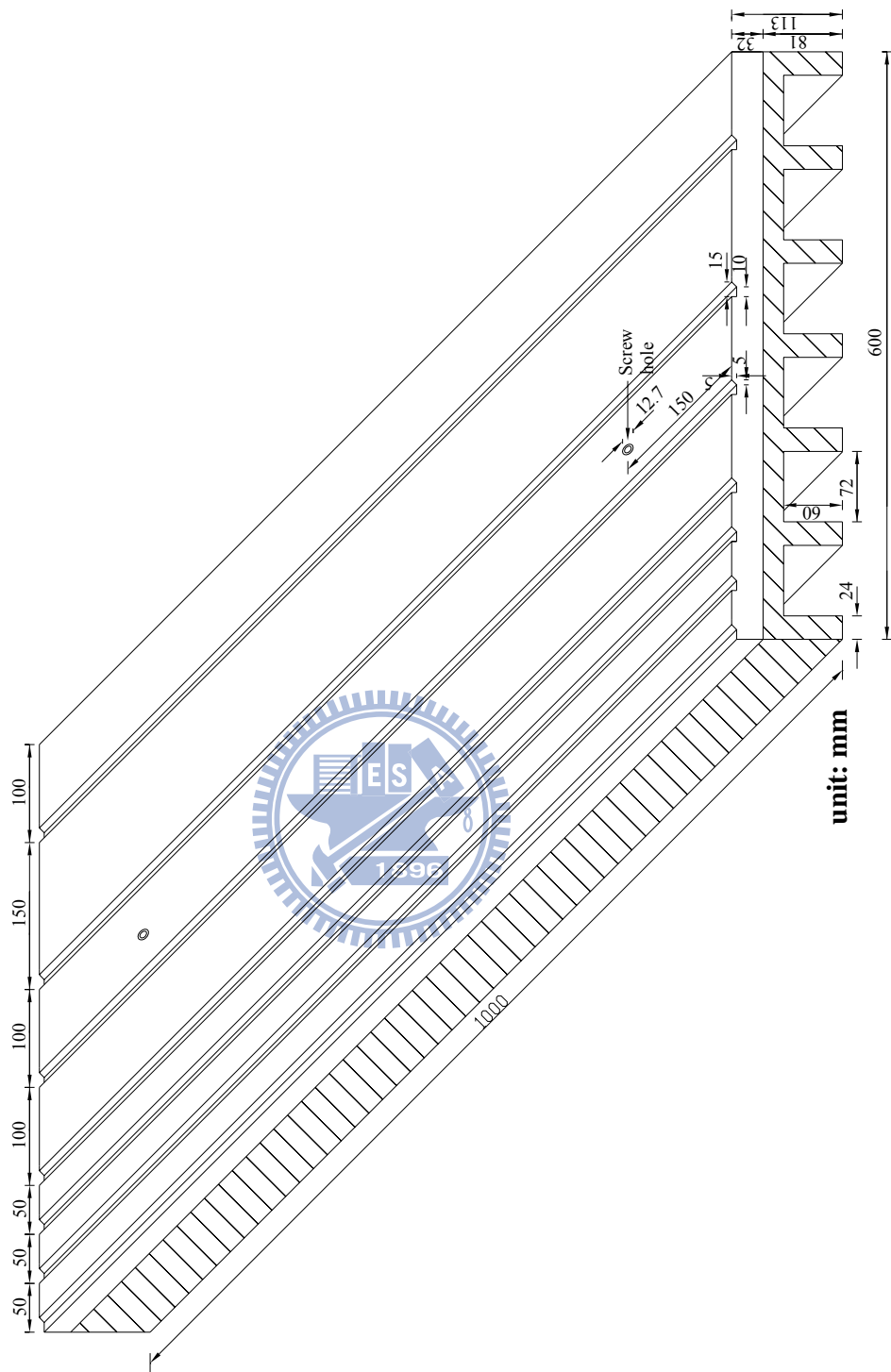
Fig. 4.8. Dimensions of base supporting block (after Chen, 2010)

(b)

Fig. 4.9. Base supporting block (after Chen, 2010)

(a)

SAFETY -WALK

Base Supporting
Boards
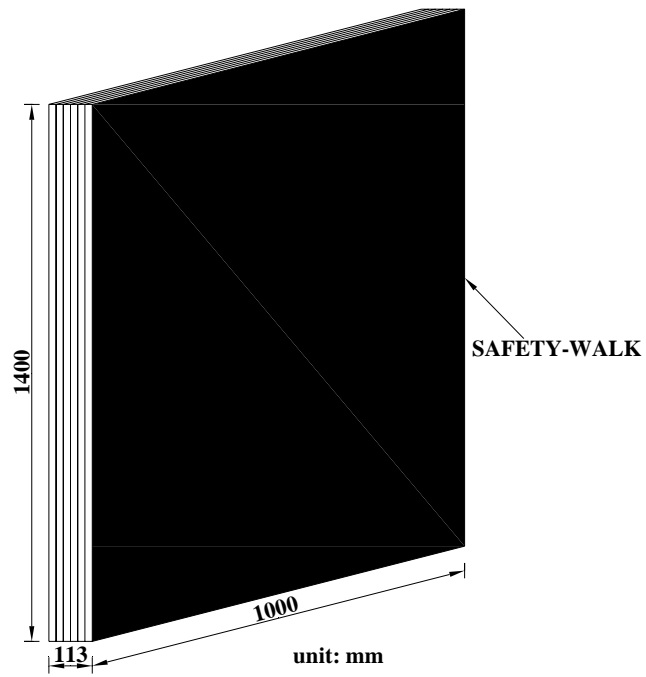
(b)

Fig. 4.10. Base supporting boards

114
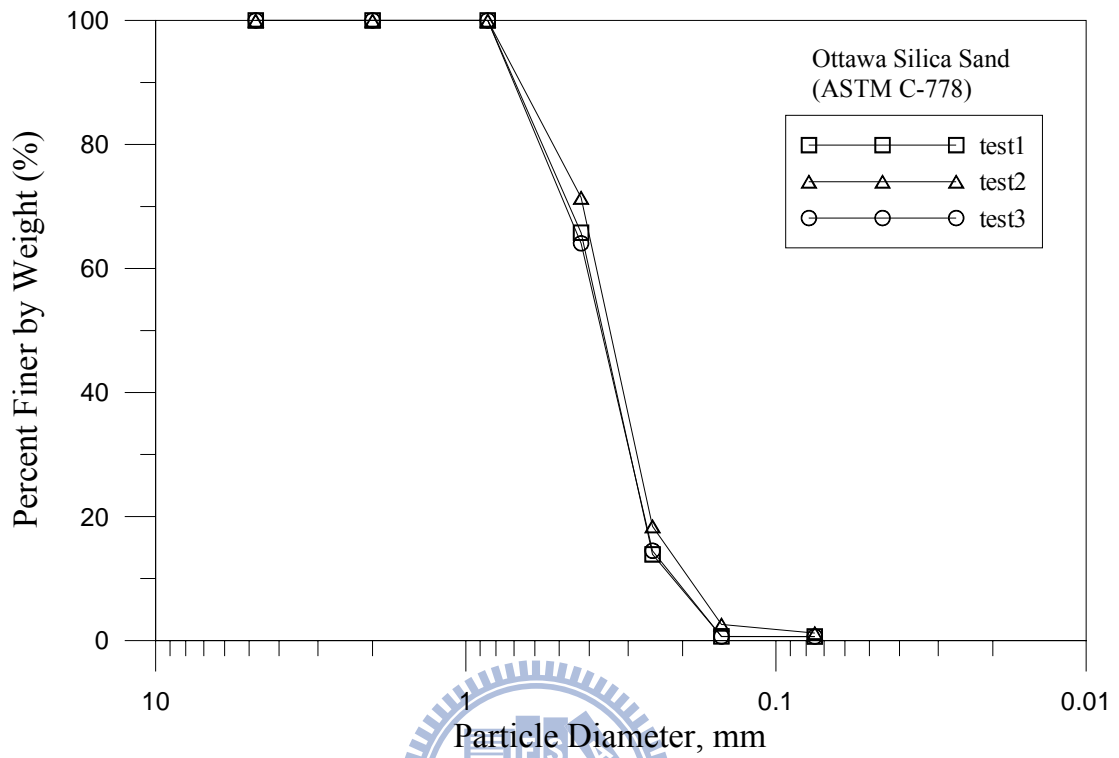
Fig. 5.1. Grain size distribution of Ottawa sand (after Chen,2010)

60 × 60

Loading Block

Dry Ottawa sand

Upper Shear Box

Lower Shear Box

Porous Stone

unit : mm
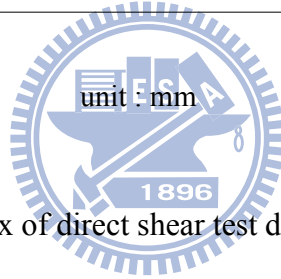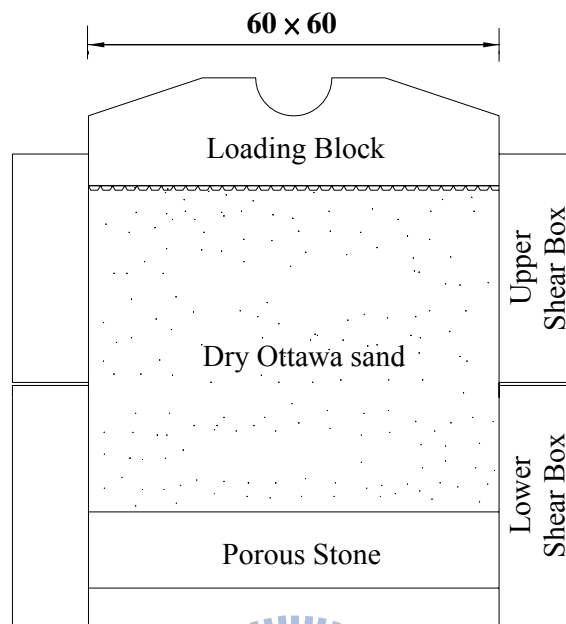
Fig. 5.2. Shear box of direct shear test device (after Wu, 1992)
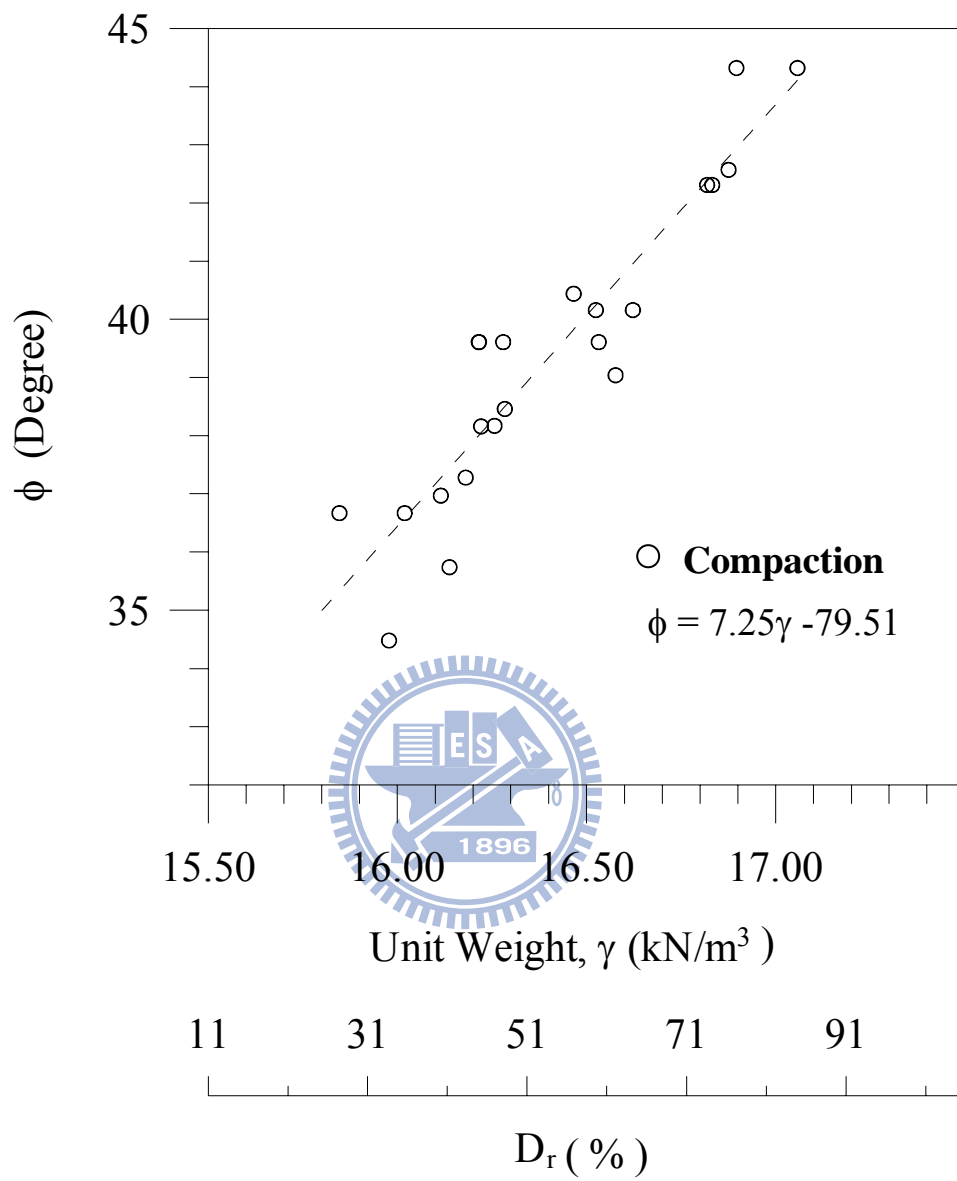
Fig. 5.3. Relationship between unit weight γ and internal friction angle φ (after Chang, 2000)
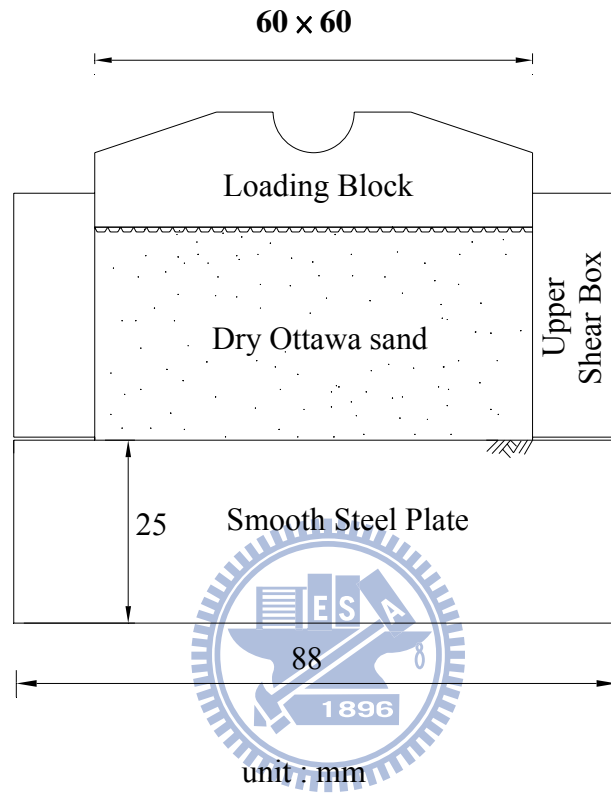
Fig. 5.4. Direct shear test to determinate wall friction (after Chang, 2000)

Fig.5.5. Relationship between unit weight γ and wall friction anglę δ_w (after Ho, 1999)
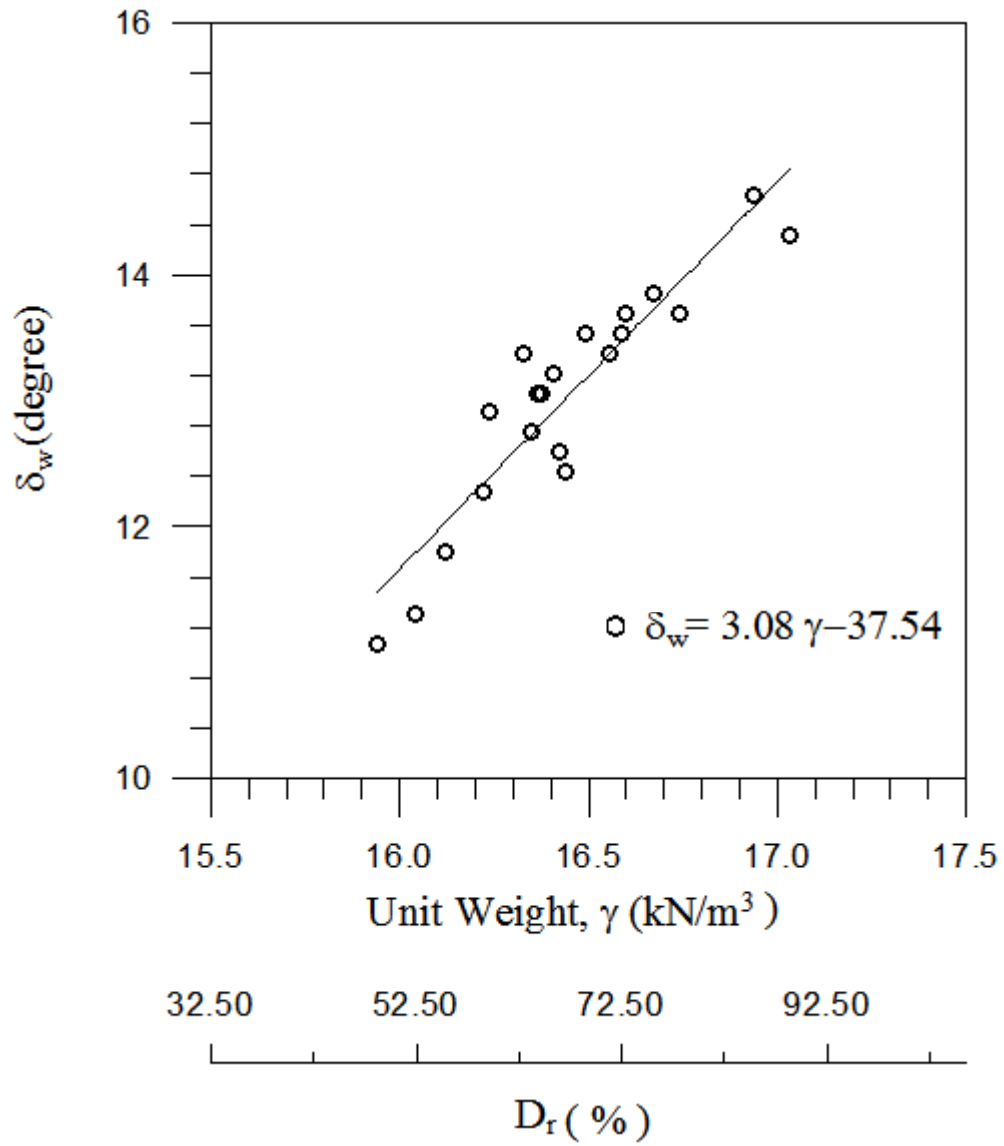
Fig. 5.6. Plastic-sheet lubrication layers on side walls
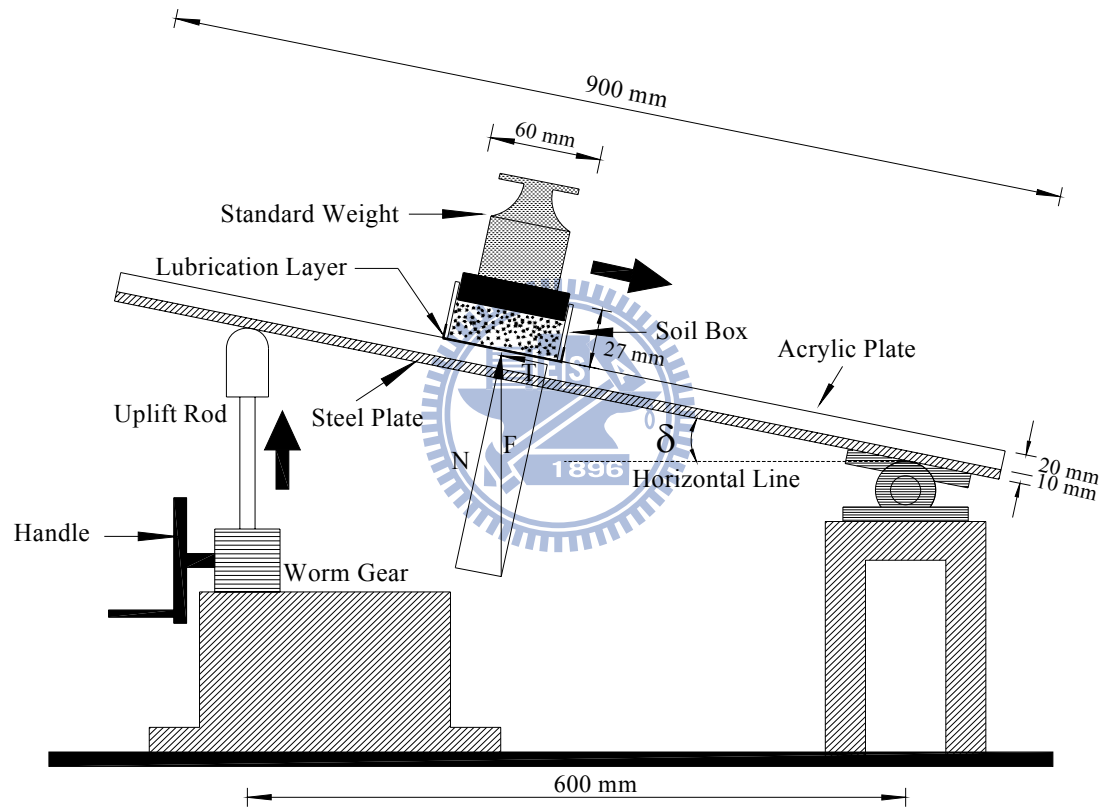
Fig. 5.7. Schematic diagram of sliding block test (after Fang et al., 2004)
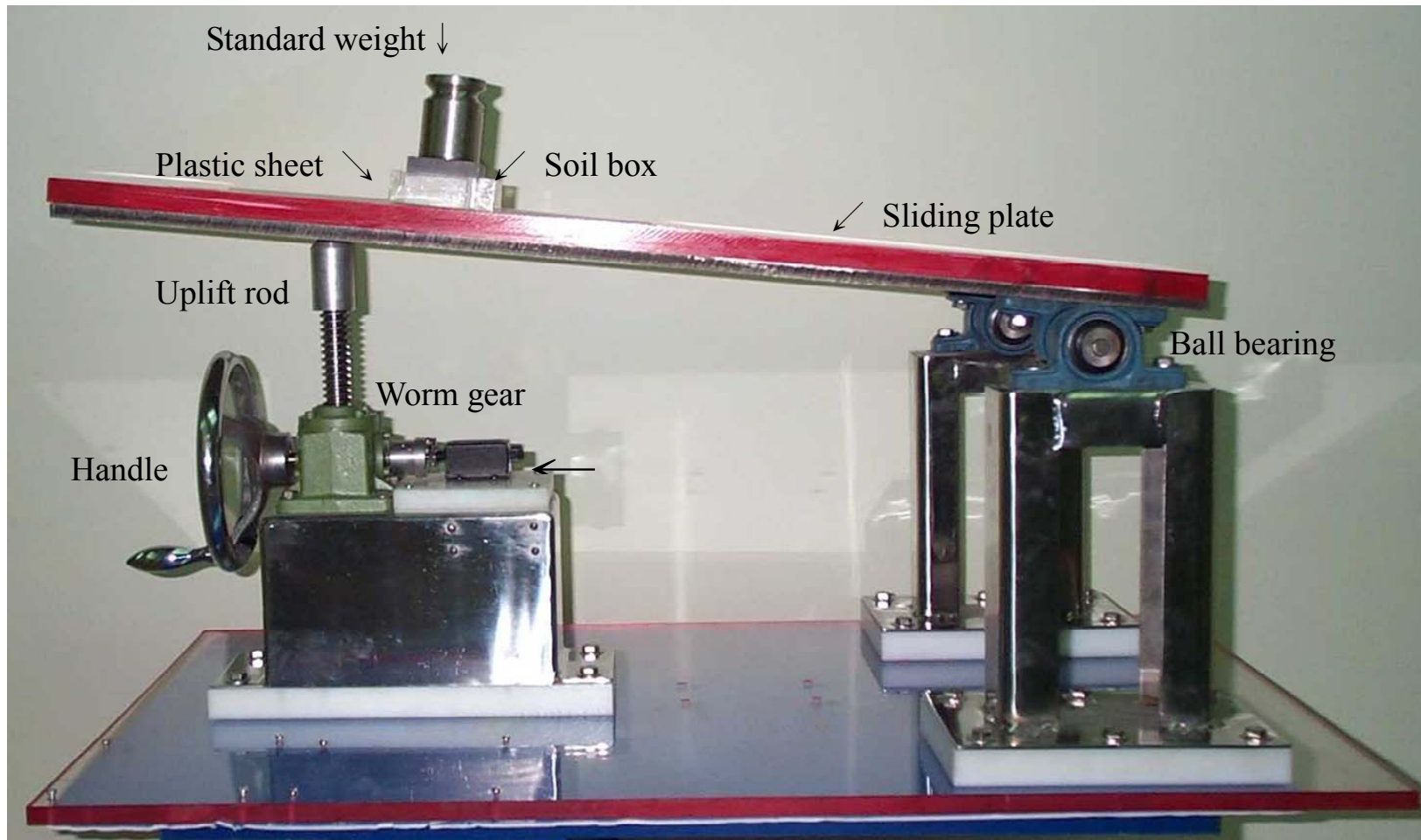
Fig.5.8 Sliding block test apparatus (after Fang et al., 2004)
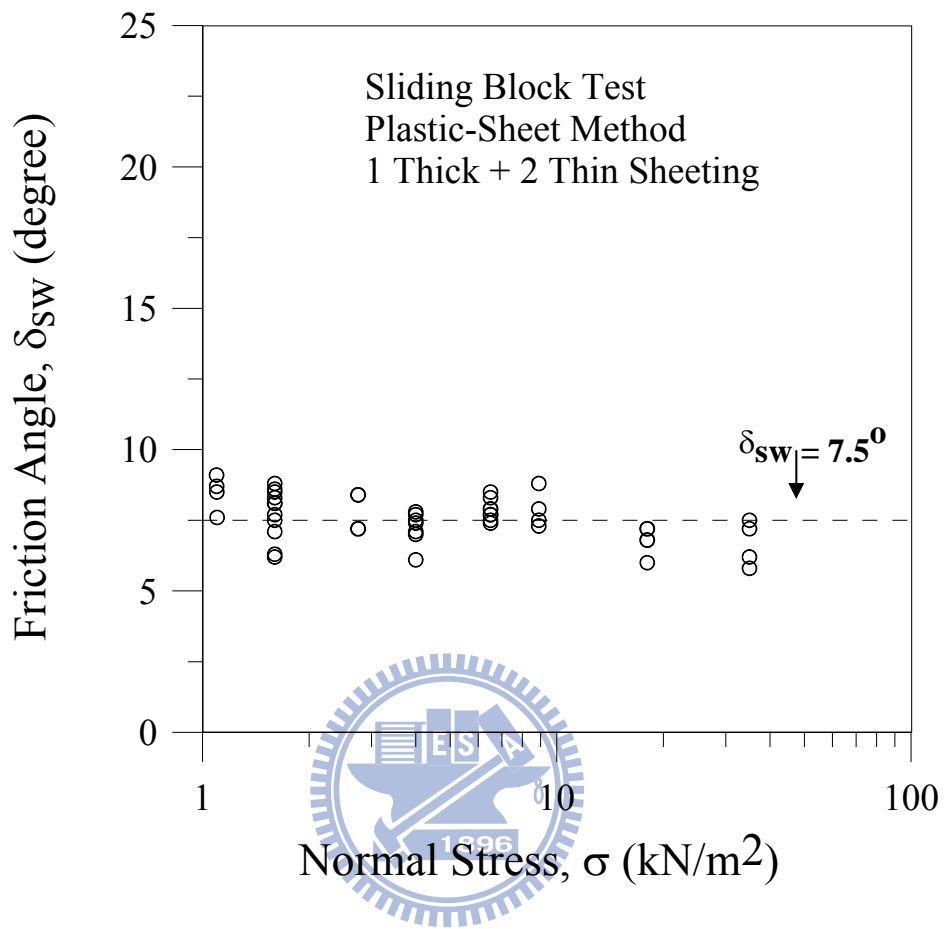
Fig. 5.9 Variation of side-wall friction angle with normal stress

(after Fang et al., 2004)

63 × 63

N

8.5   Upper Shear Box

8.5

Dry Ottawa Sand

SAFETY-WALK

20

20

20

Smooth Steel Plate

5

120

Unit : mm

(a)

80

Anti-Slip Material
SAFETY-WALK

80

120

15

20

5

80

Unit : mm
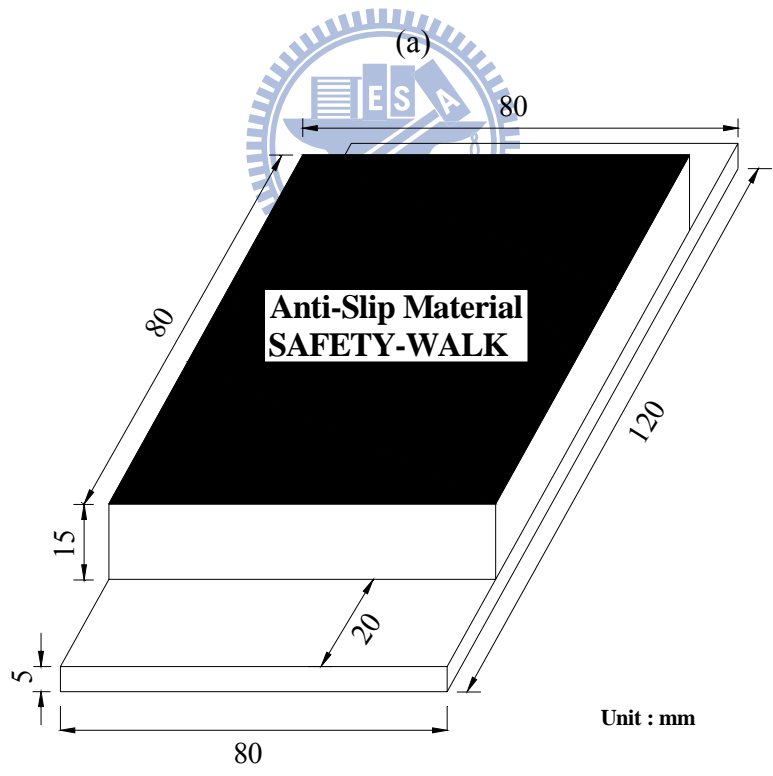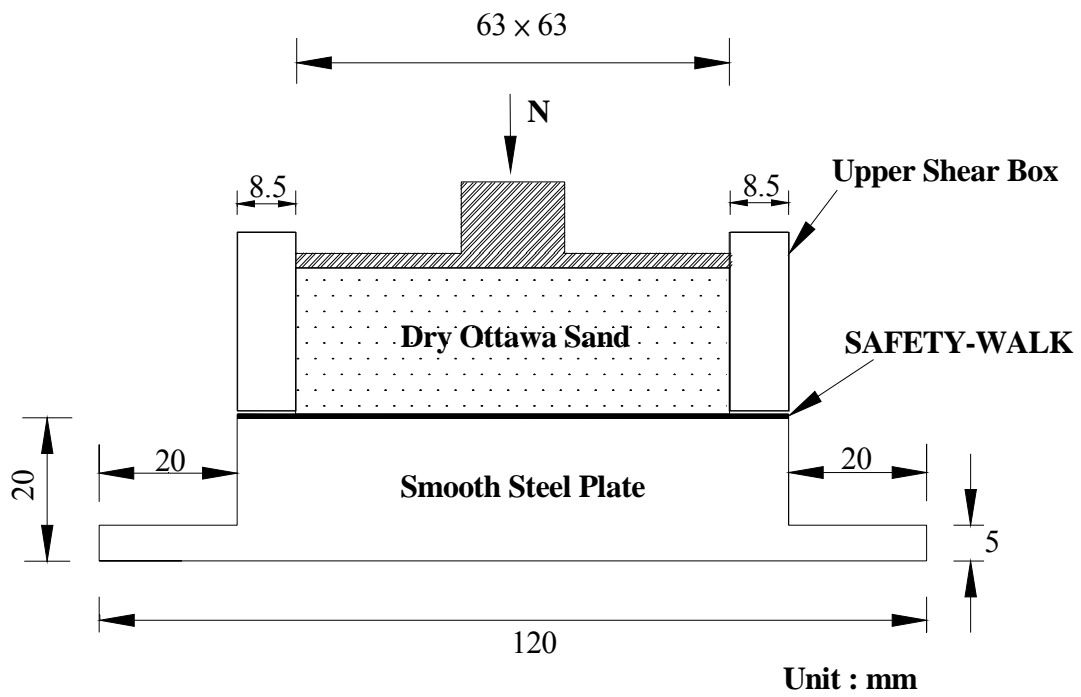
(b)

Fig. 5.10. Direct shear test to determine interface friction angle
(after Wang, 2005)
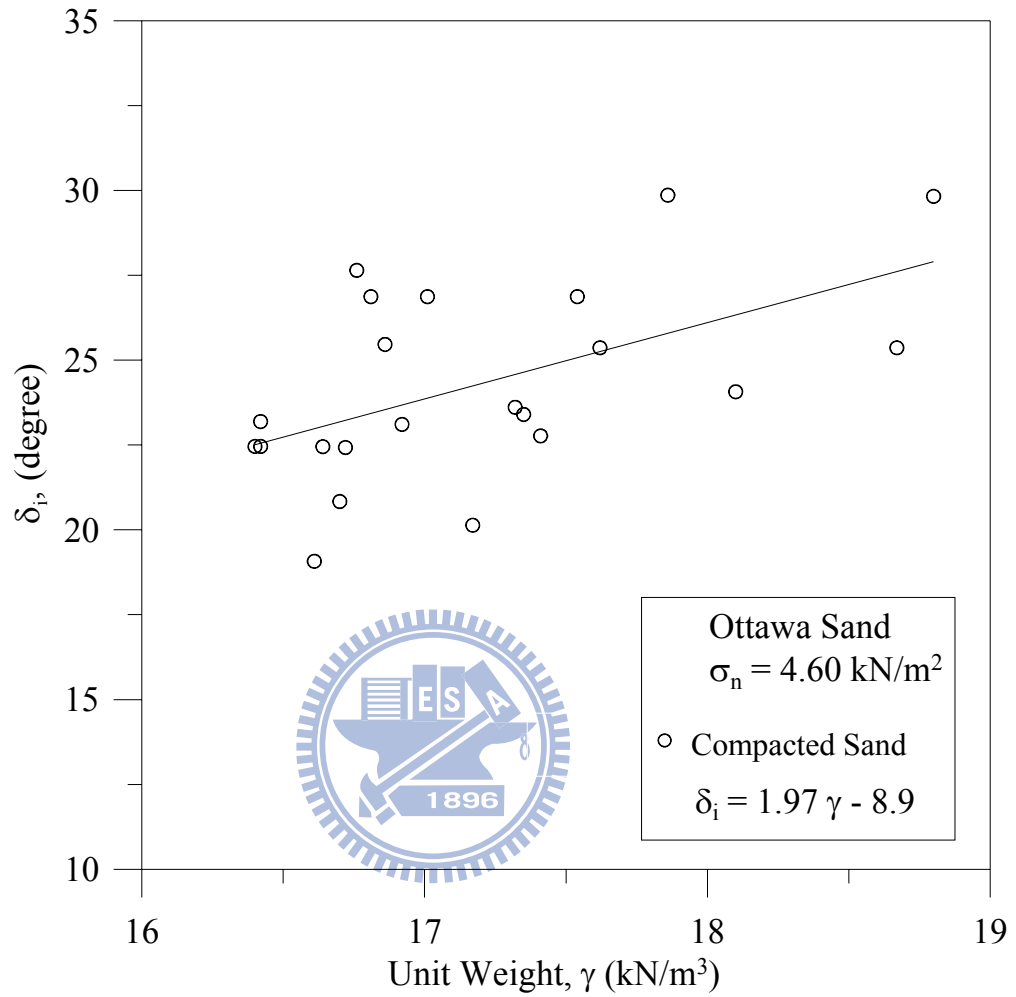
Fig. 5.11. Relationship between unit weight γ and interface plate friction angle δ_i (after Chen, 2005)
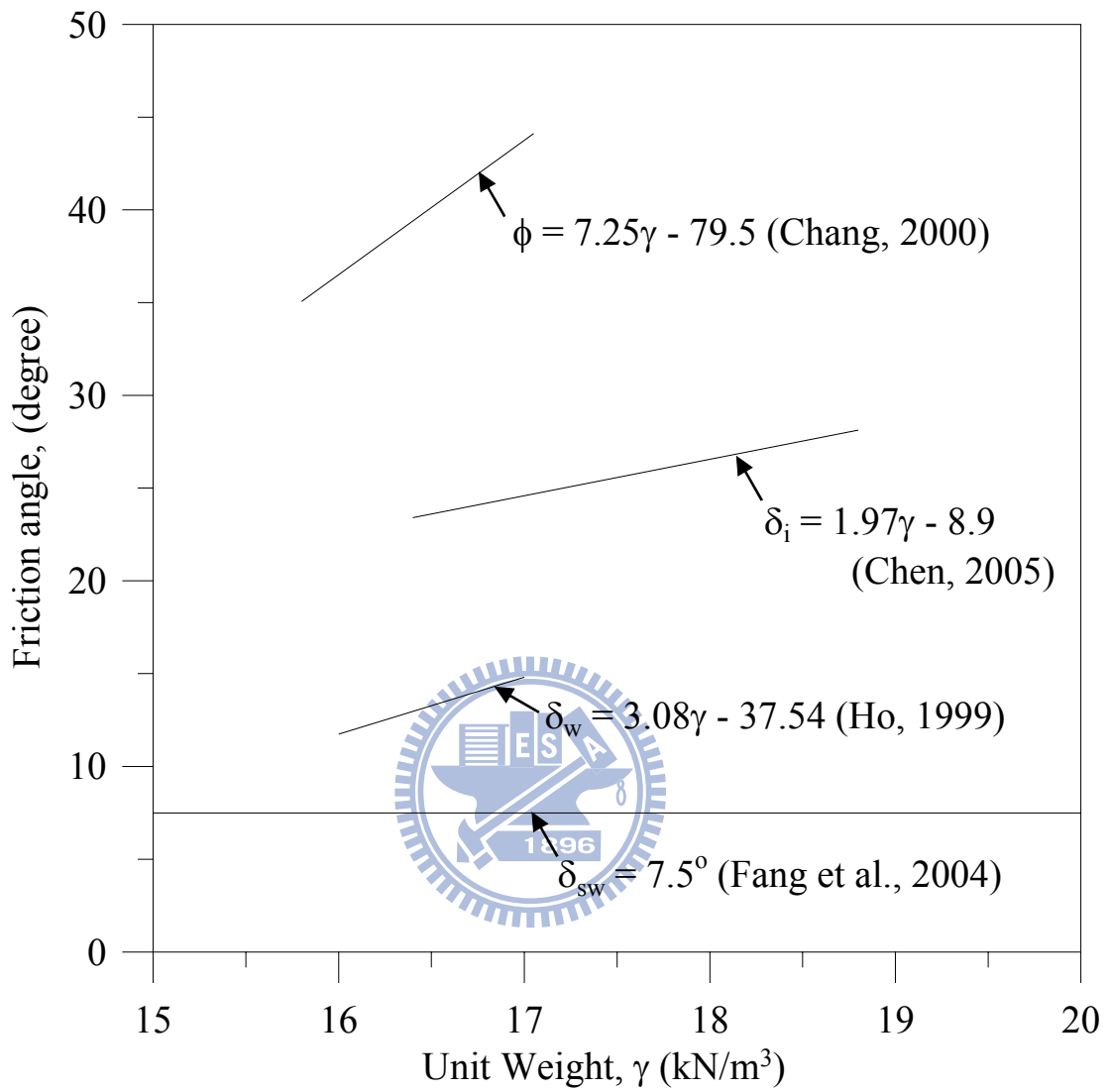
Fig. 5.12. Variation of friction angles ϕ, δ_i, δ_w, δ_{sw} with soil unit weight γ
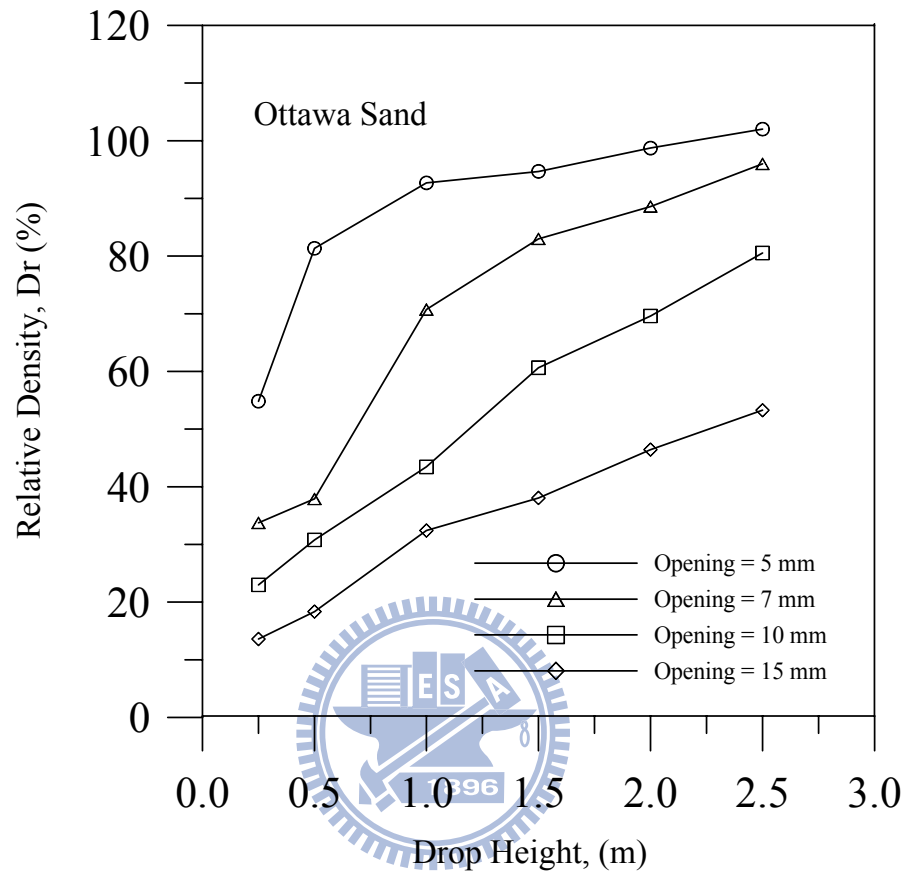
Fig. 5.13. Relationship between relative density of soil and drop height
(after Ho, 1999)
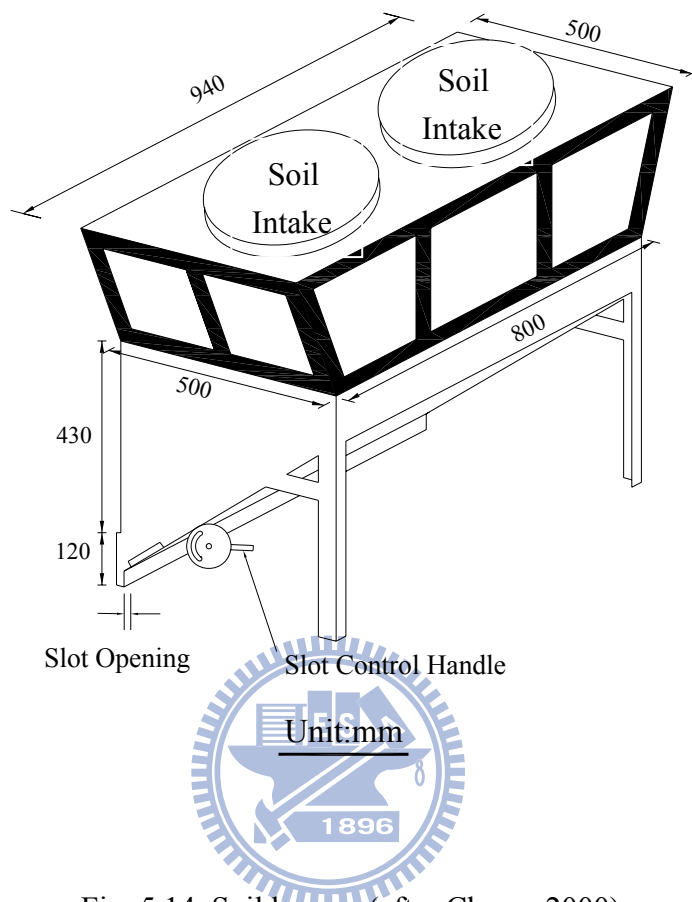
Fig. 5.14. Soil hopper (after Chang, 2000)
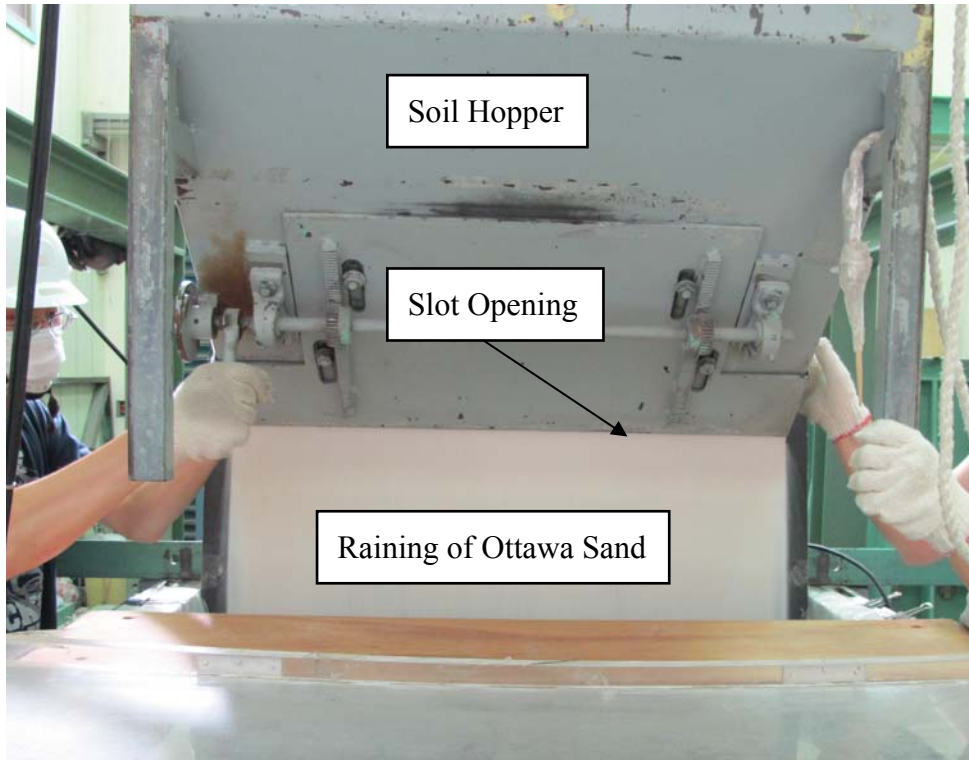
(a) front view

(b) side view

Fig. 5.15. Raining of sand from soil hopper
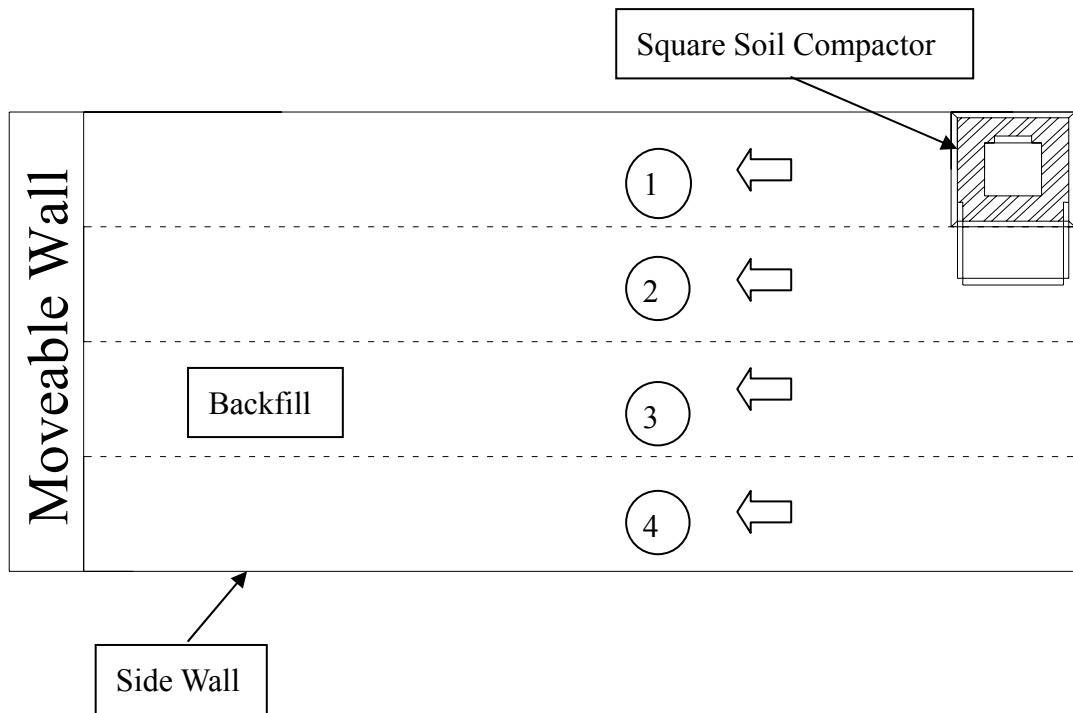
Fig. 5.16. Compaction Procedure with Square Soil Compactor　(Top-View).
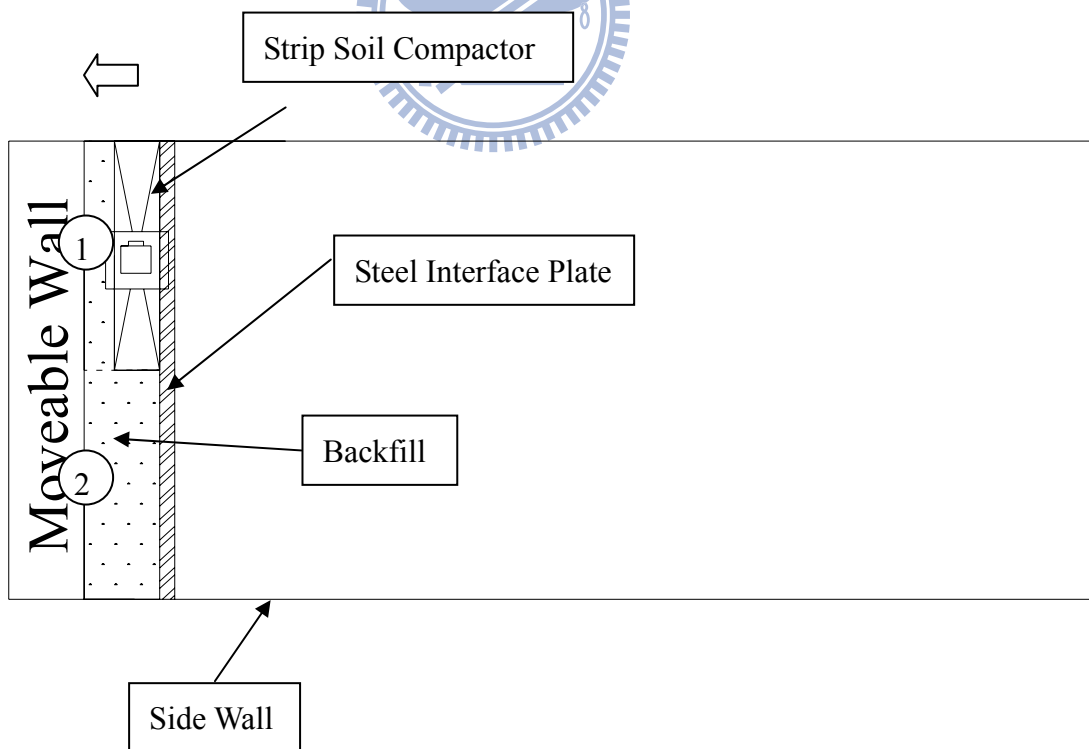
Fig. 5.17. Compaction Procedure with Strip Soil Compactor　(Top-View).

(a)
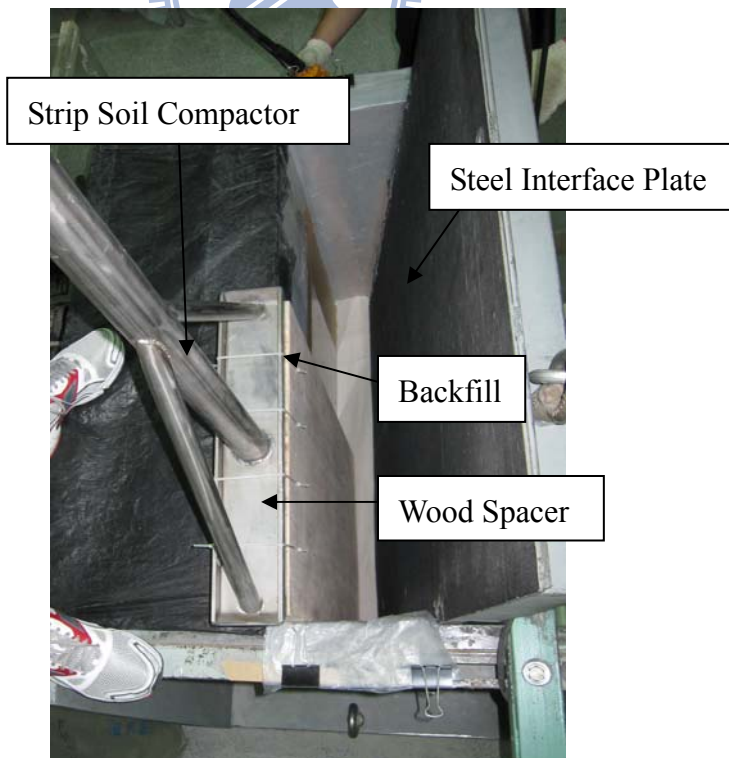
(b)

Fig. 5.18. Strip Soil Compactor with Wood spacer

43

3.5

Acrylic Tube

30

Acrylic Base Plate

70

5

Side-view

70

43

70

50
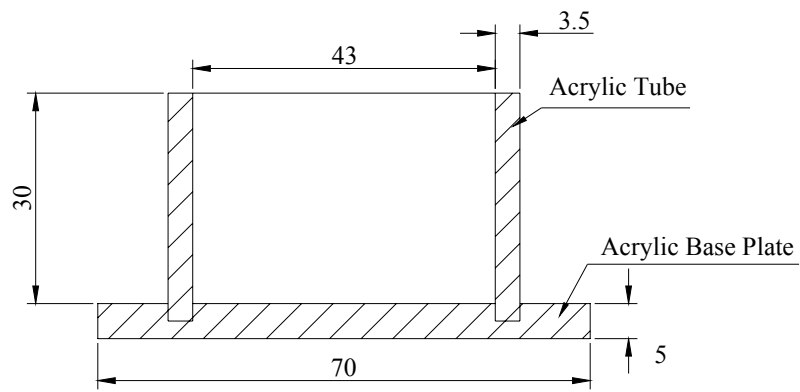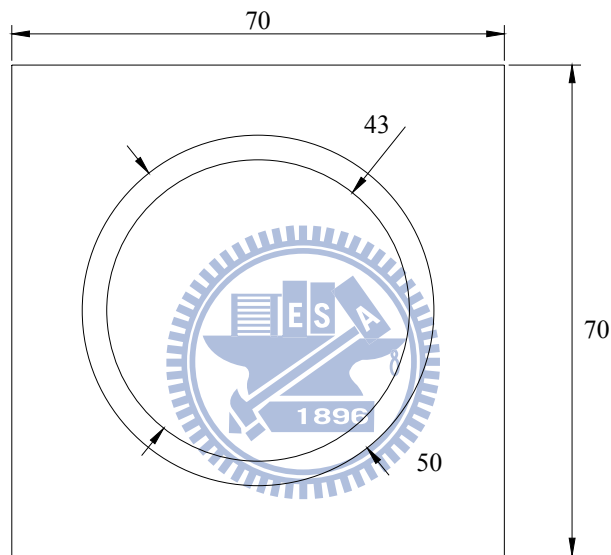
Top-view

unit：mm

Fig. 5.19. Soil-density control cup
(after Ho, 1999)
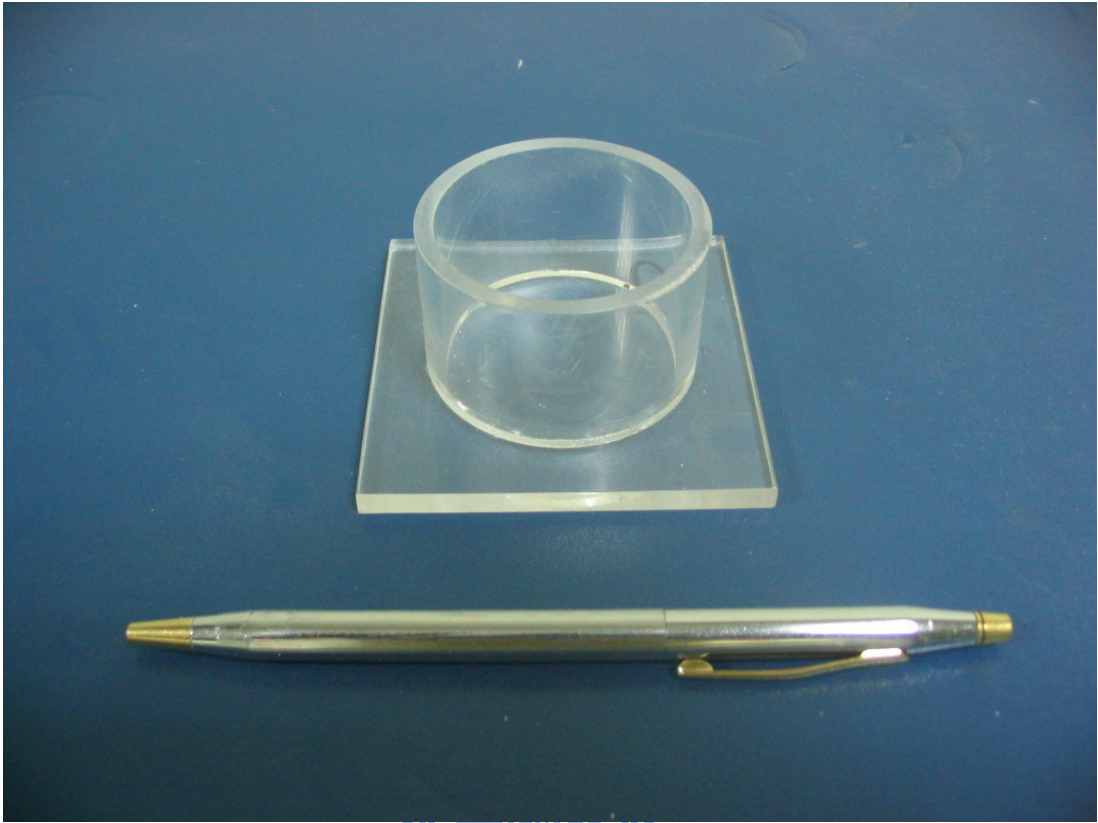
Fig. 5.20. Soil-density cup (after Chien, 2007)
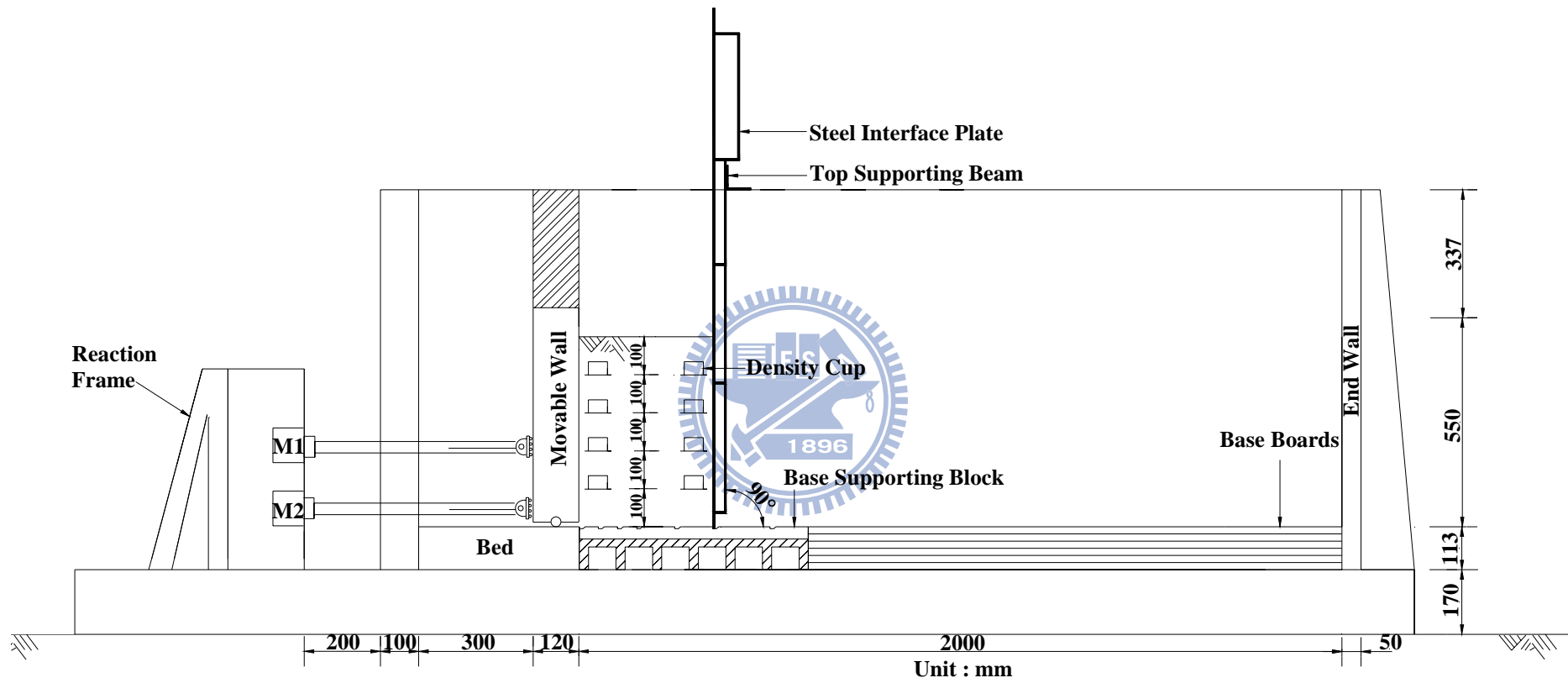
Fig. 5.21 (a). Locations of density cups for b = 350 mm and β = 90°.
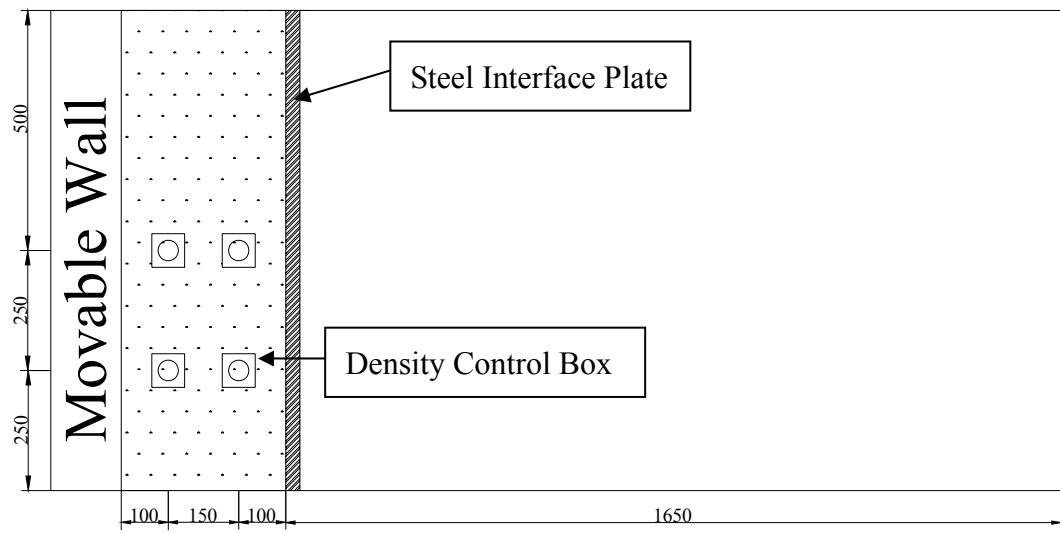
Fig. 5.21 (b). Locations of density cups for b = 350 mm and β = 90°.
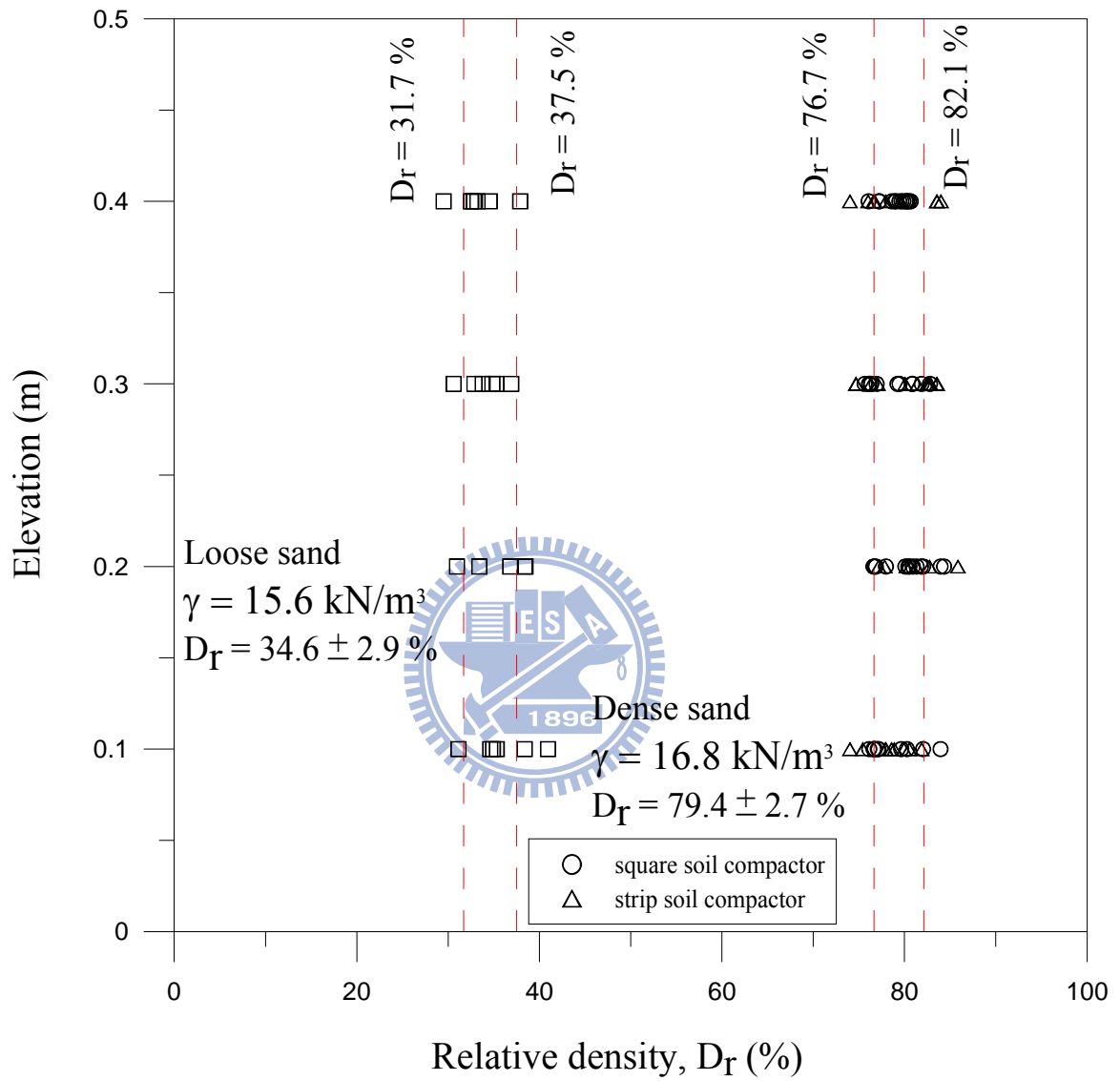
Fig. 5.22 Distribution of relative density for b = 350 mm and β = 90°
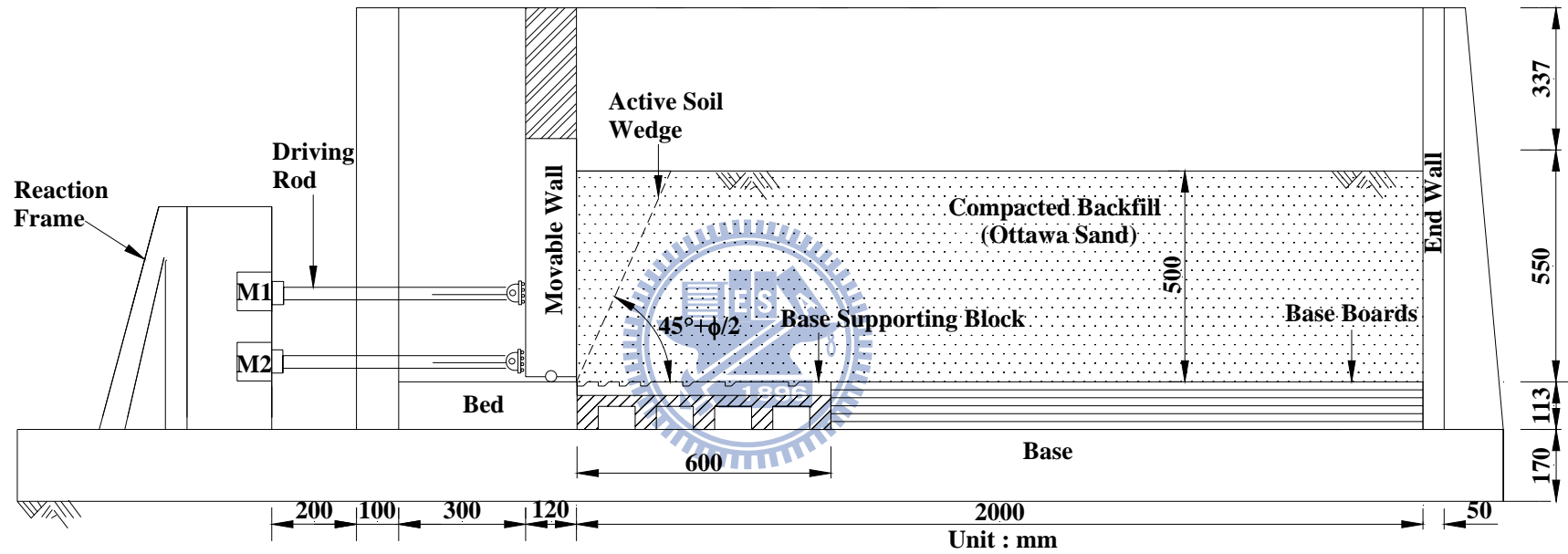
(a)

Fig. 6.1. Model wall test without adjacent interface plate (b = 2,000 mm)

(b)

Fig. 6.1. Model wall test without adjacent interface plate (b = 2,000 mm)
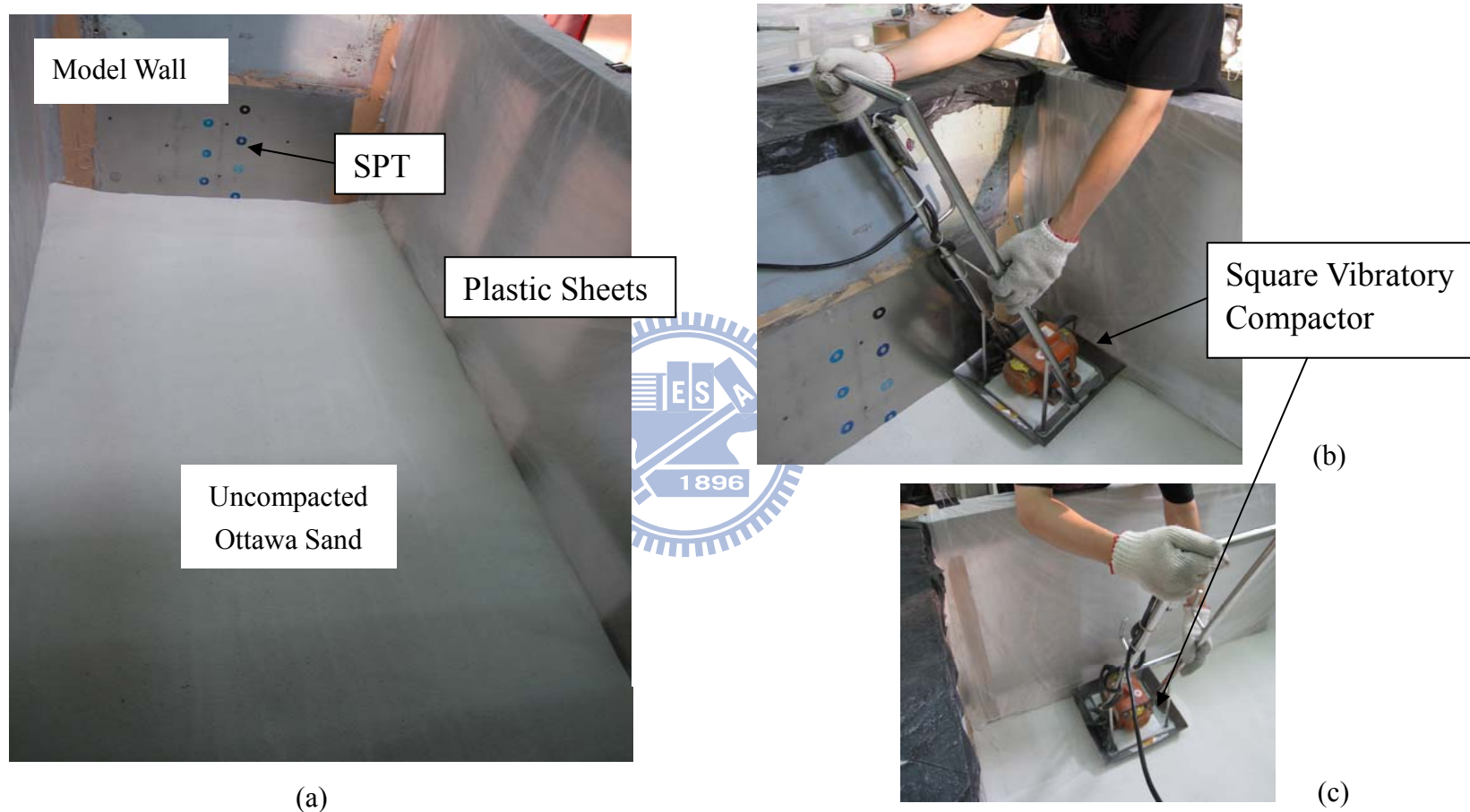
Fig. 6.2. Model wall test without adjacent interface plate for layer 1 (b = 2,000 mm)
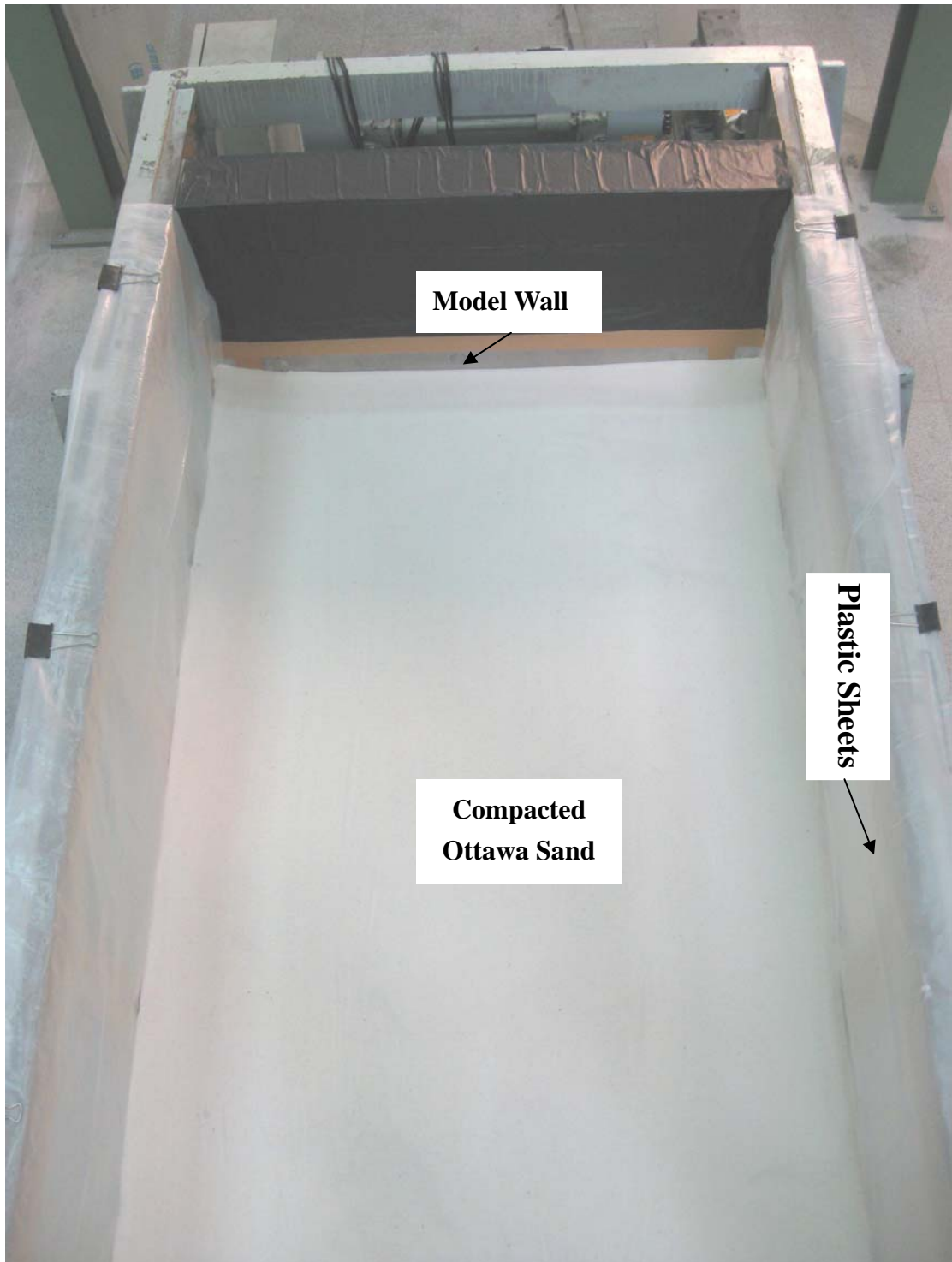
Fig. 6.3. Model wall test without interface plate (b = 2,000 mm)
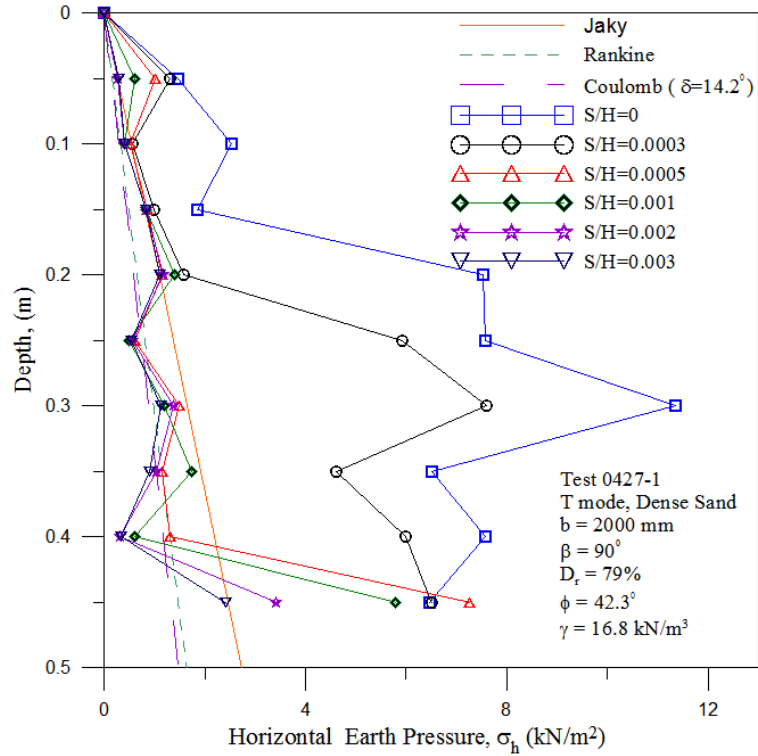
Fig. 6.4. Distribution of horizontal earth pressure for
b = 2,000 mm (Test 0427-1)
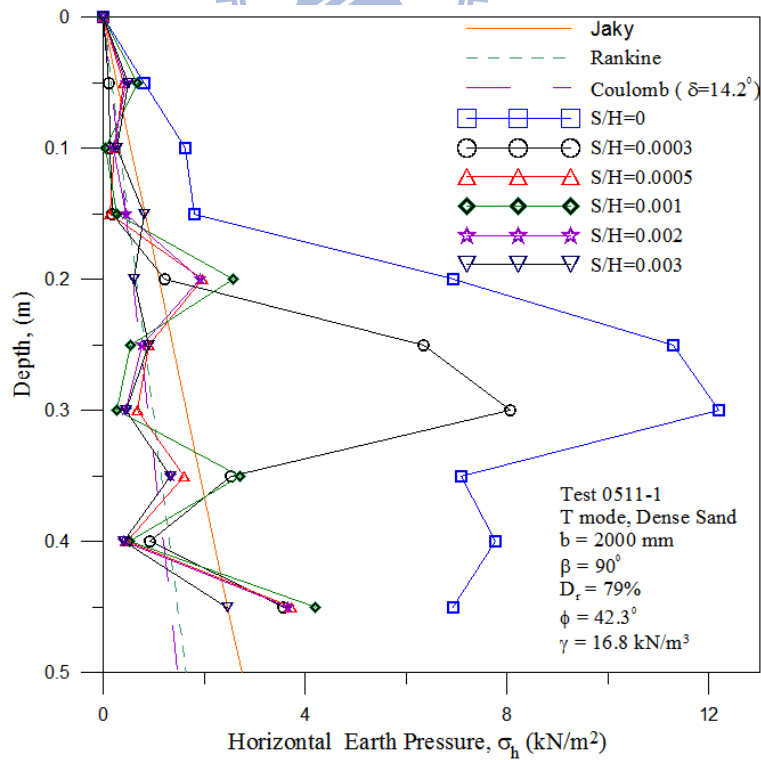
Fig. 6.5. Distribution of horizontal earth pressure for
b = 2,000 mm (Test 0511-1)

141
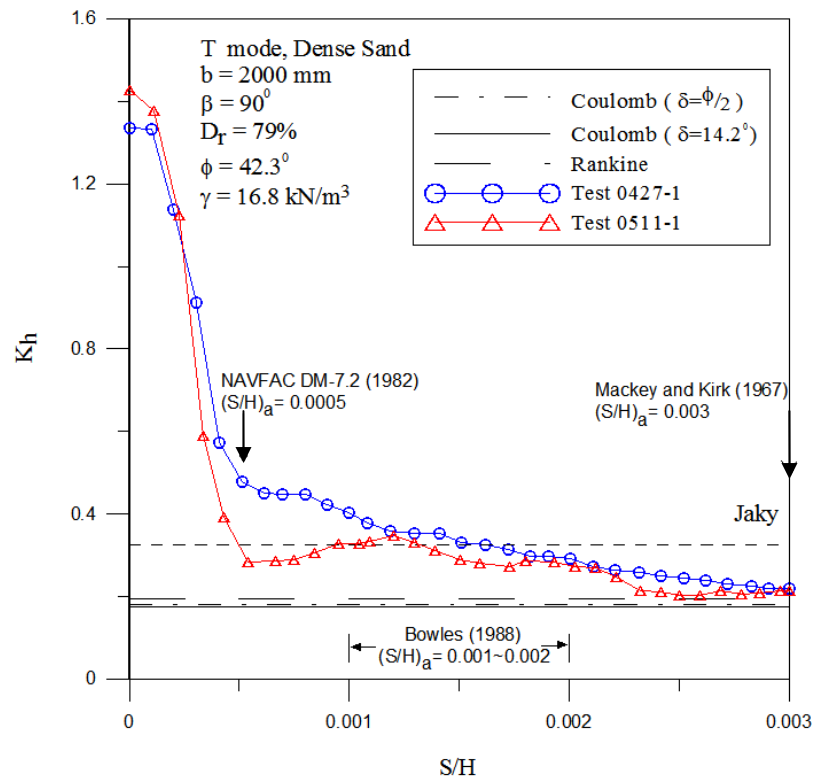
Fig. 6.6. Earth pressure coefficient K_h versus wall movement for
b = 2,000 mm
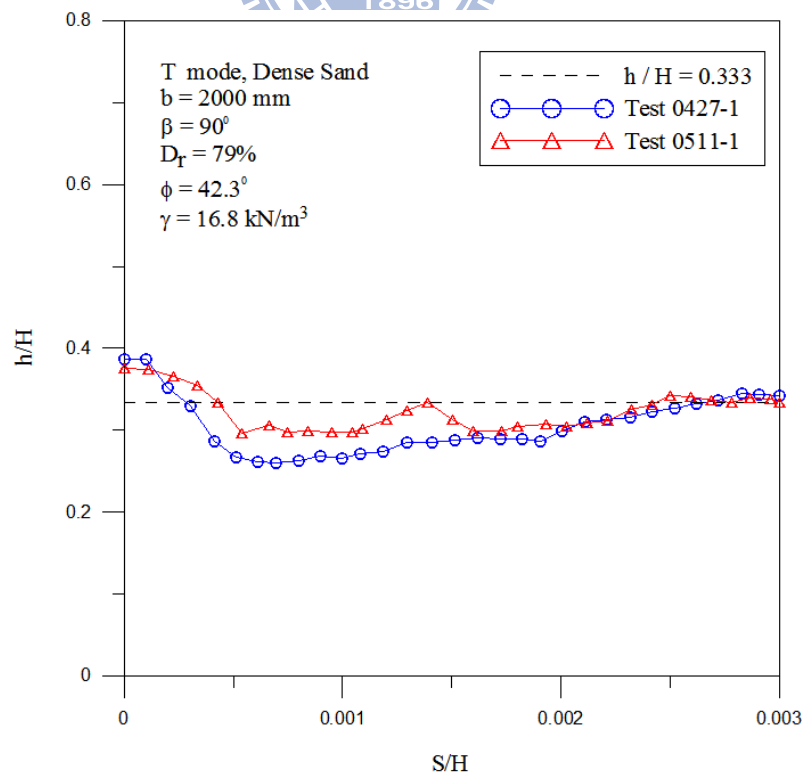
Fig. 6.7. Location of total thrust application for b = 2,000 mm

142
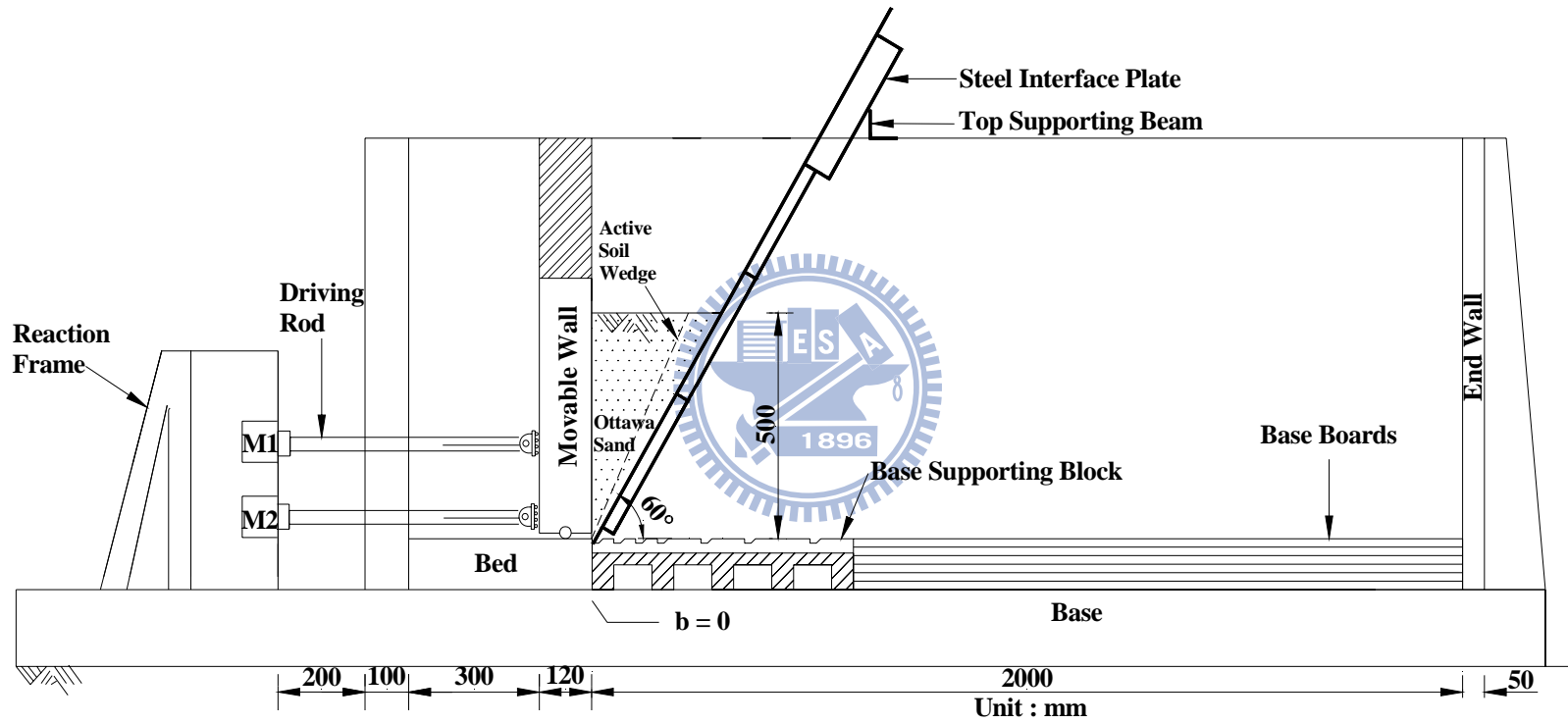
(a)

Fig. 6.8. Model wall test with interface inclination β = 60° and b = 0

(b)

Fig. 6.8. Model wall test with interface inclination β = 60° and b = 0
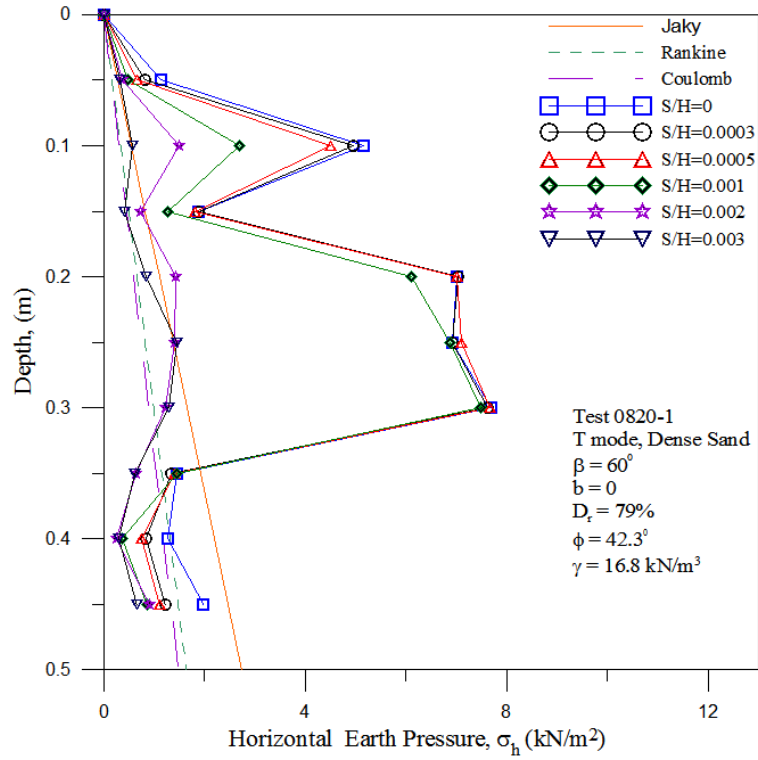
Fig. 6.9. Distribution of horizontal earth pressure for
b = 0 and β = 60° (Test 0820-1)
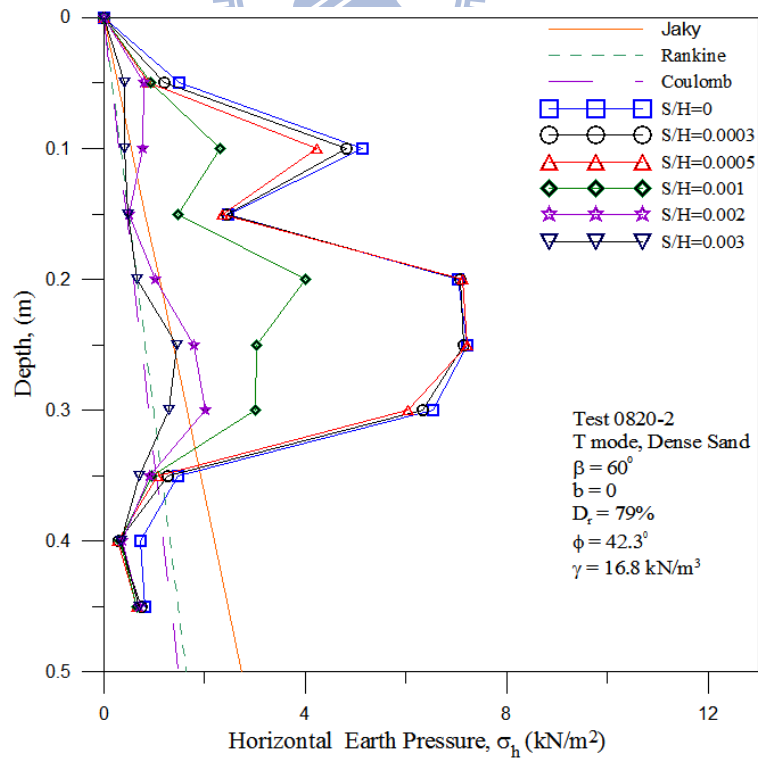
Fig. 6.10. Distribution of horizontal earth pressure for
b = 0 and β = 60°(Test 0820-2)

145
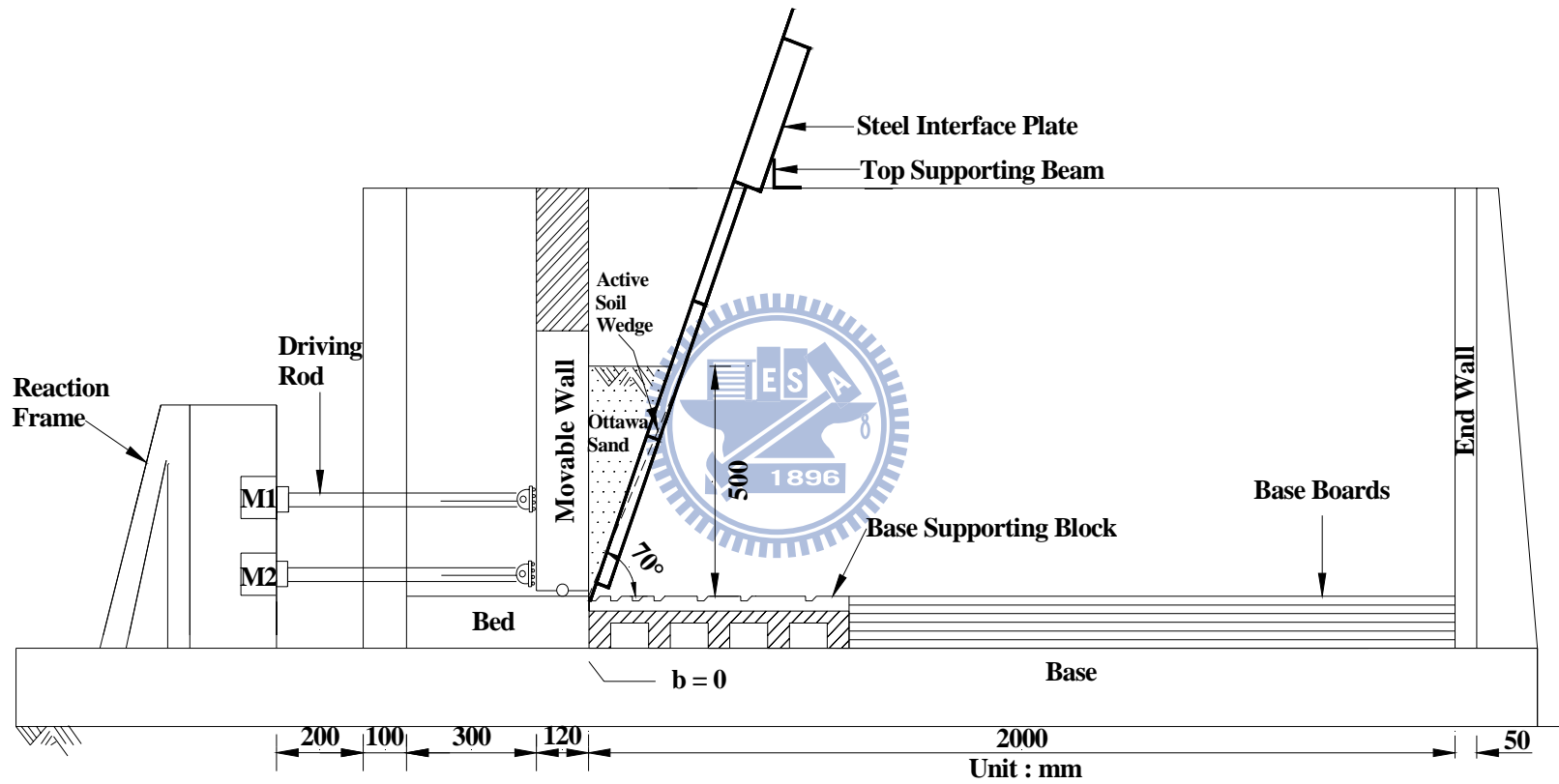
(a)

Fig. 6.11. Model wall test with interface inclination β = 70° and b = 0

146

(b)

Fig. 6.11. Model wall test with interface inclination β = 70° and b = 0
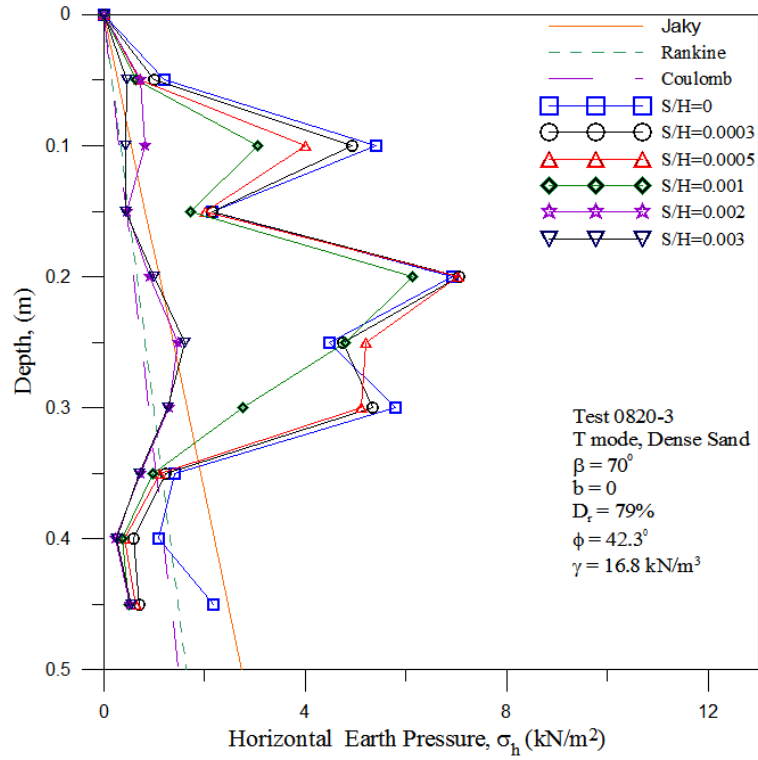
Fig. 6.12. Distribution of horizontal earth pressure for
b = 0 and β = 70° (Test 0820-3)
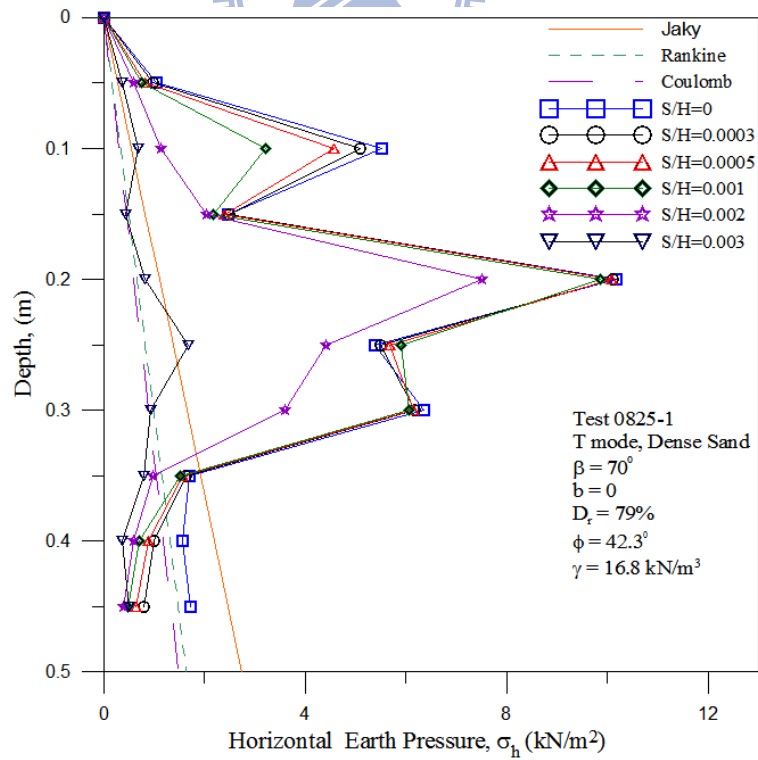
Fig. 6.13. Distribution of horizontal earth pressure for
b = 0 and β = 70°(Test 0825-1)

148
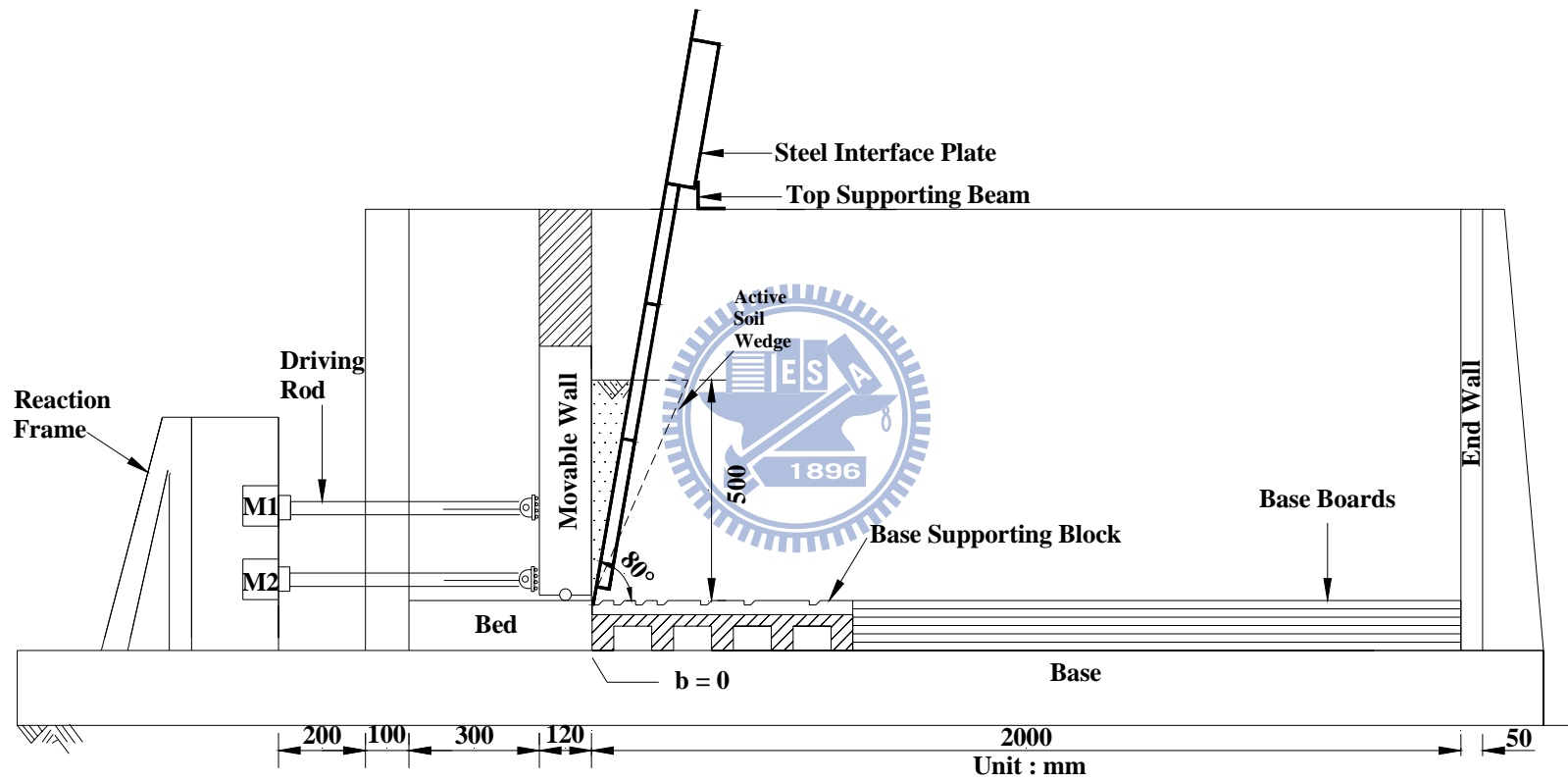
(a)

Fig. 6.14. Model wall test with interface inclination β = 80° and b = 0

(b)

Fig. 6.14. Model wall test with interface inclination β = 80° and b = 0
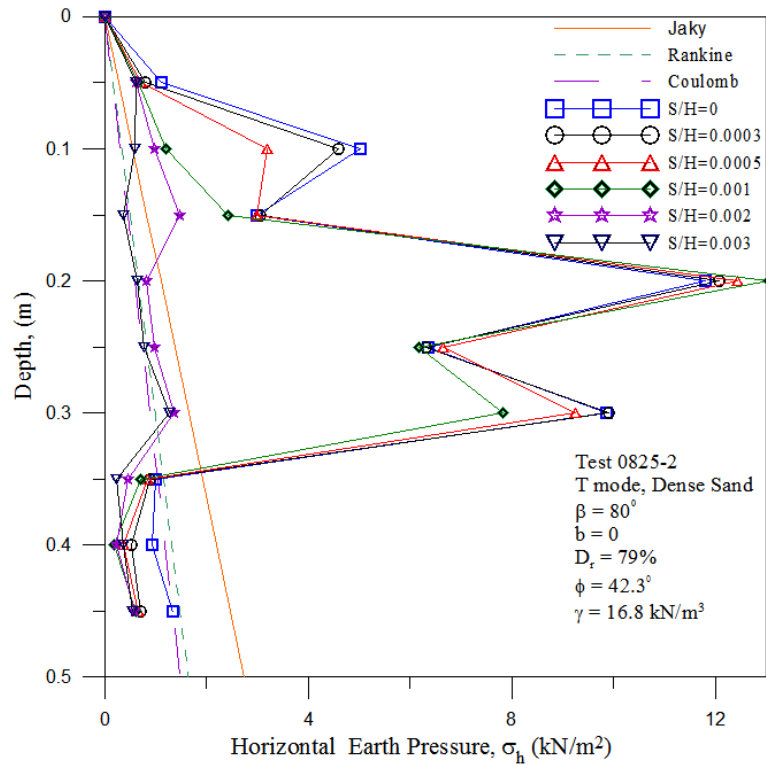
Fig. 6.15. Distribution of horizontal earth pressure for
b = 0 and β = 80° (Test 0825-2)
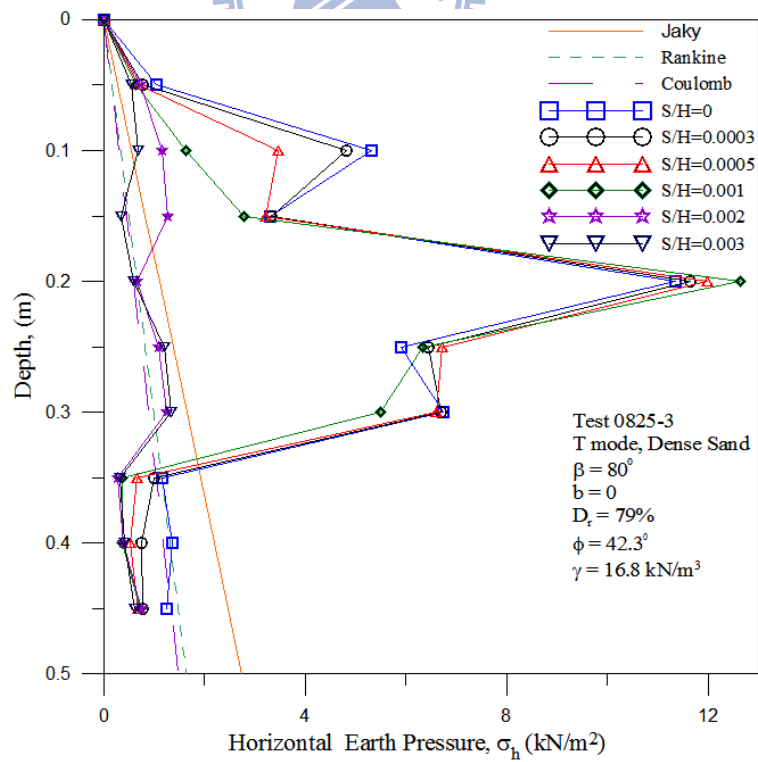
Fig. 6.16. Distribution of horizontal earth pressure for
b = 0 and β = 80°(Test 0825-3)
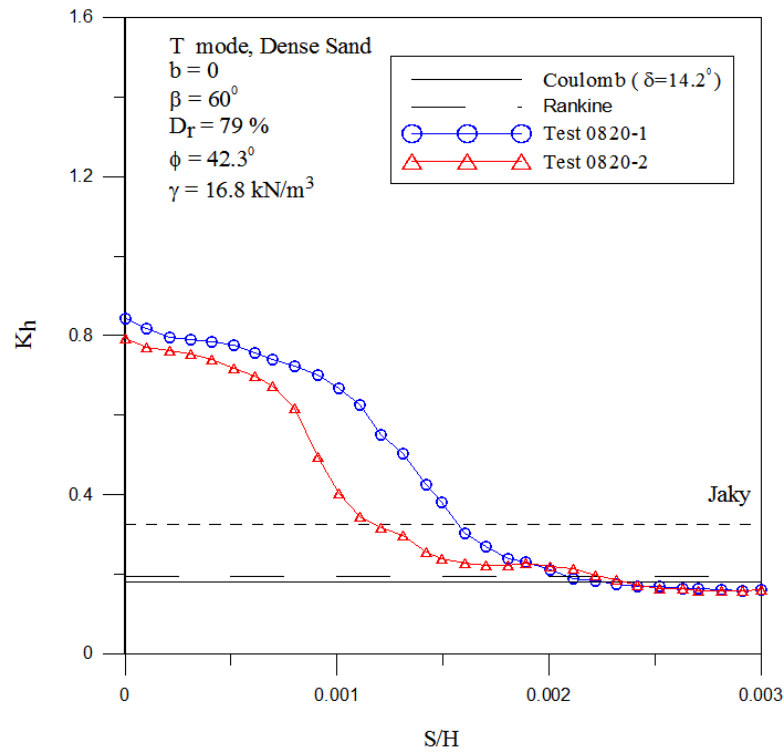
Fig. 6.17. Earth pressure coefficient K_h versus wall movement for
$b = 0$ and $\beta = 60°$
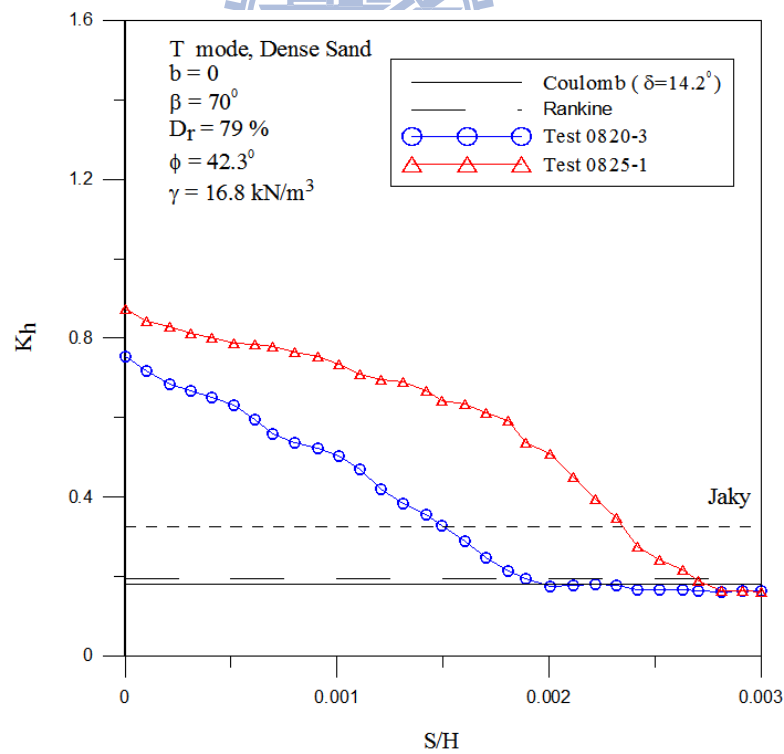
Fig. 6.18. Earth pressure coefficient K_h versus wall movement for
$b = 0$ and $\beta = 70°$

152
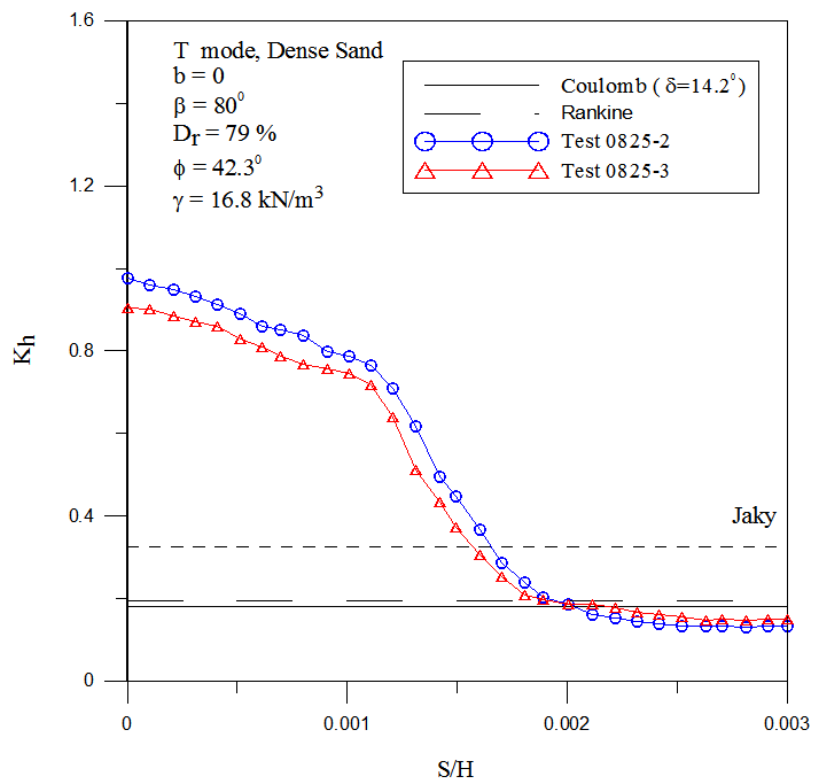
Fig. 6.19. Earth pressure coefficient K_h versus wall movement for
b = 0 and β = 80°
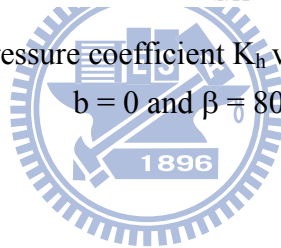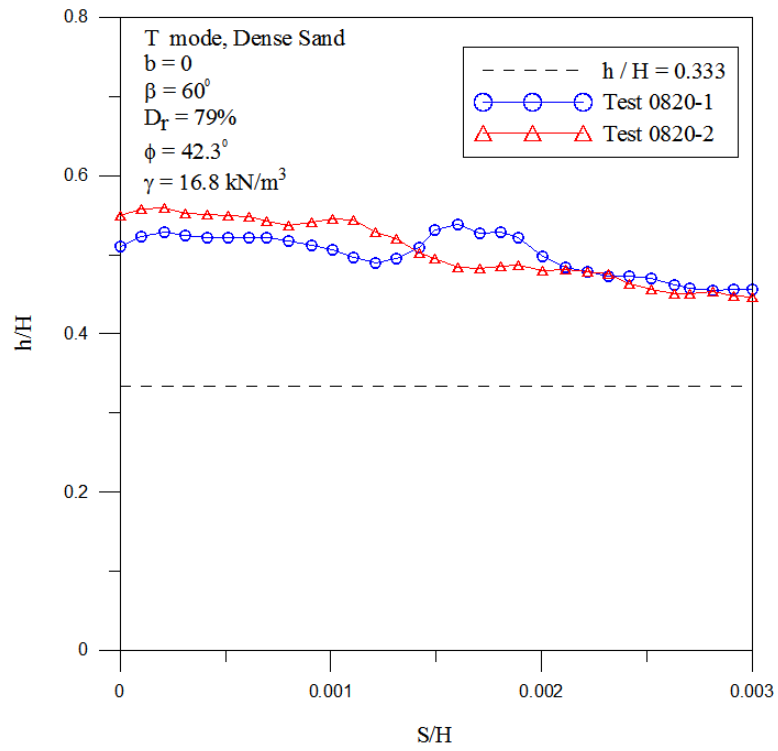
Fig. 6.20. Location of total thrust application for b = 0 and β = 60°
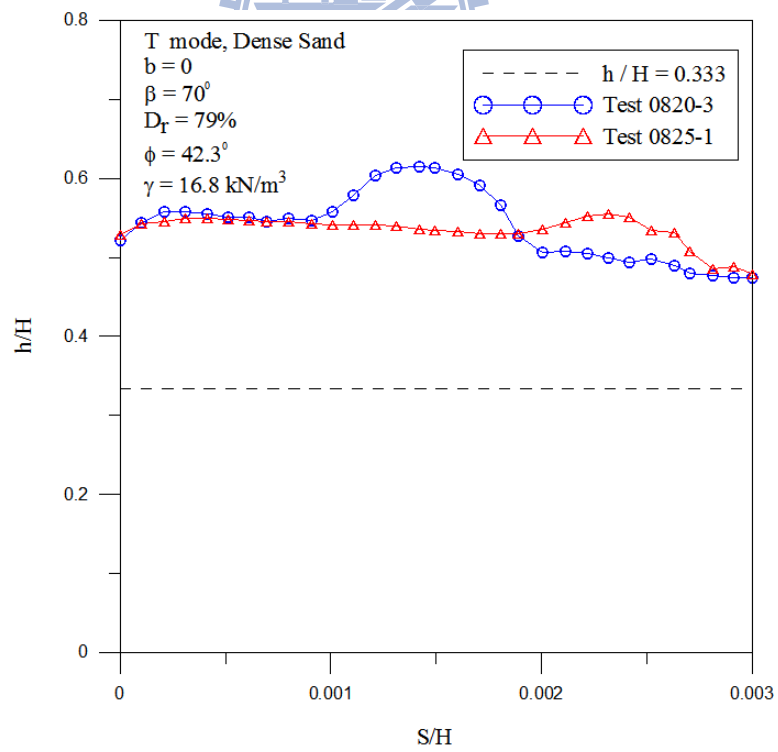
Fig. 6.21. Location of total thrust application for b = 0 and β = 70°

154
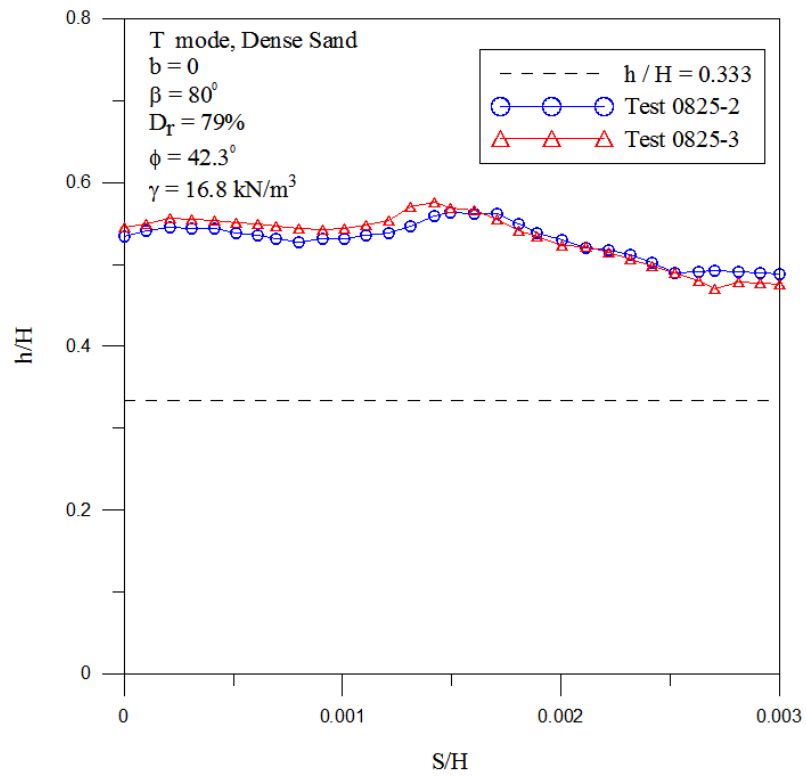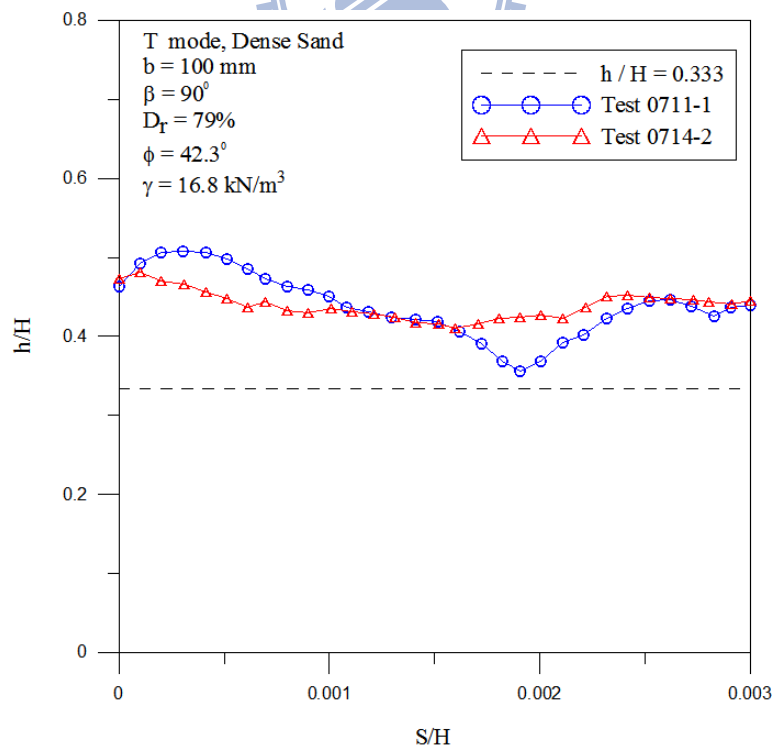
Fig. 6.22. Location of total thrust application for b = 0 and β = 80°
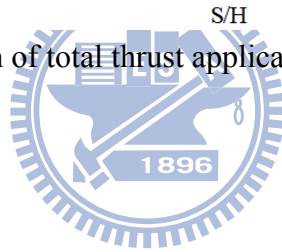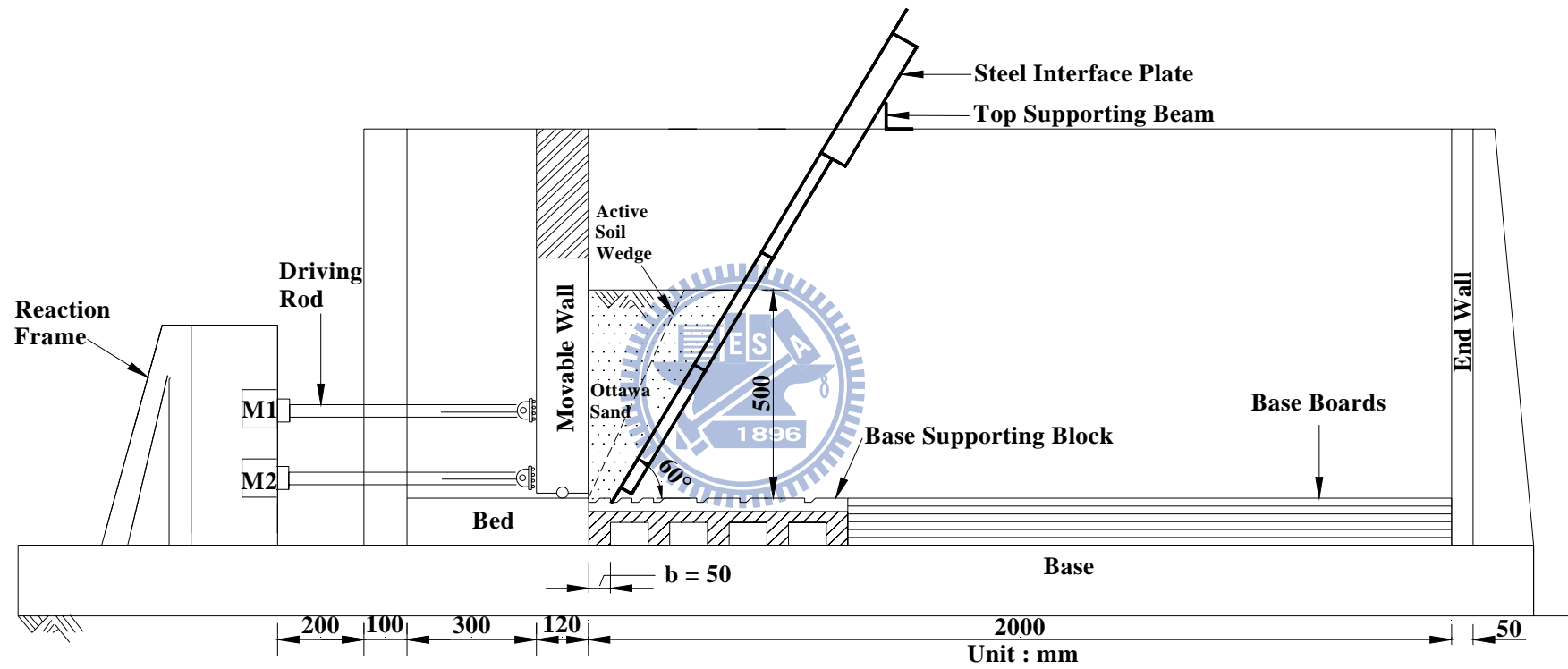
(a)

Fig. 6.23. Model wall test with interface inclination β = 60° and b = 50 mm

156

(b)

Fig. 6.23. Model wall test with interface inclination β = 60° and b = 50 mm
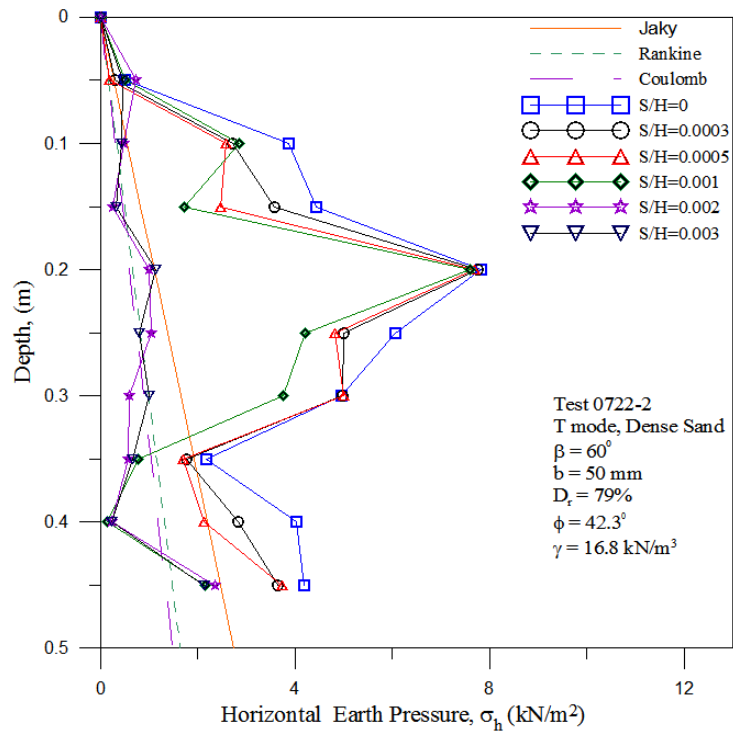
Fig. 6.24. Distribution of horizontal earth pressure for
b = 50 mm and β = 60° (Test 0722-2)
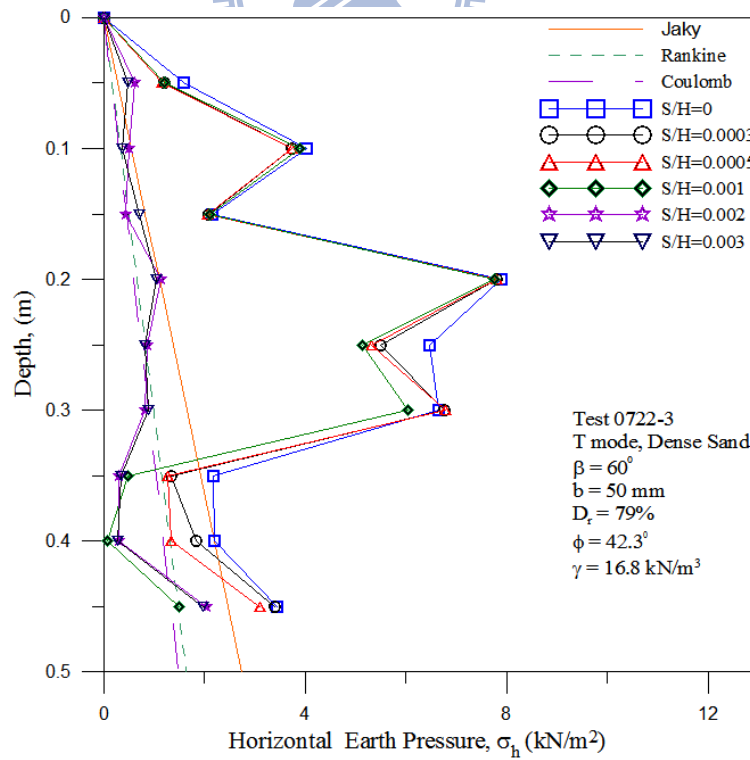
Fig. 6.25. Distribution of horizontal earth pressure for
b = 50 mm and β = 60°(Test 0722-3)
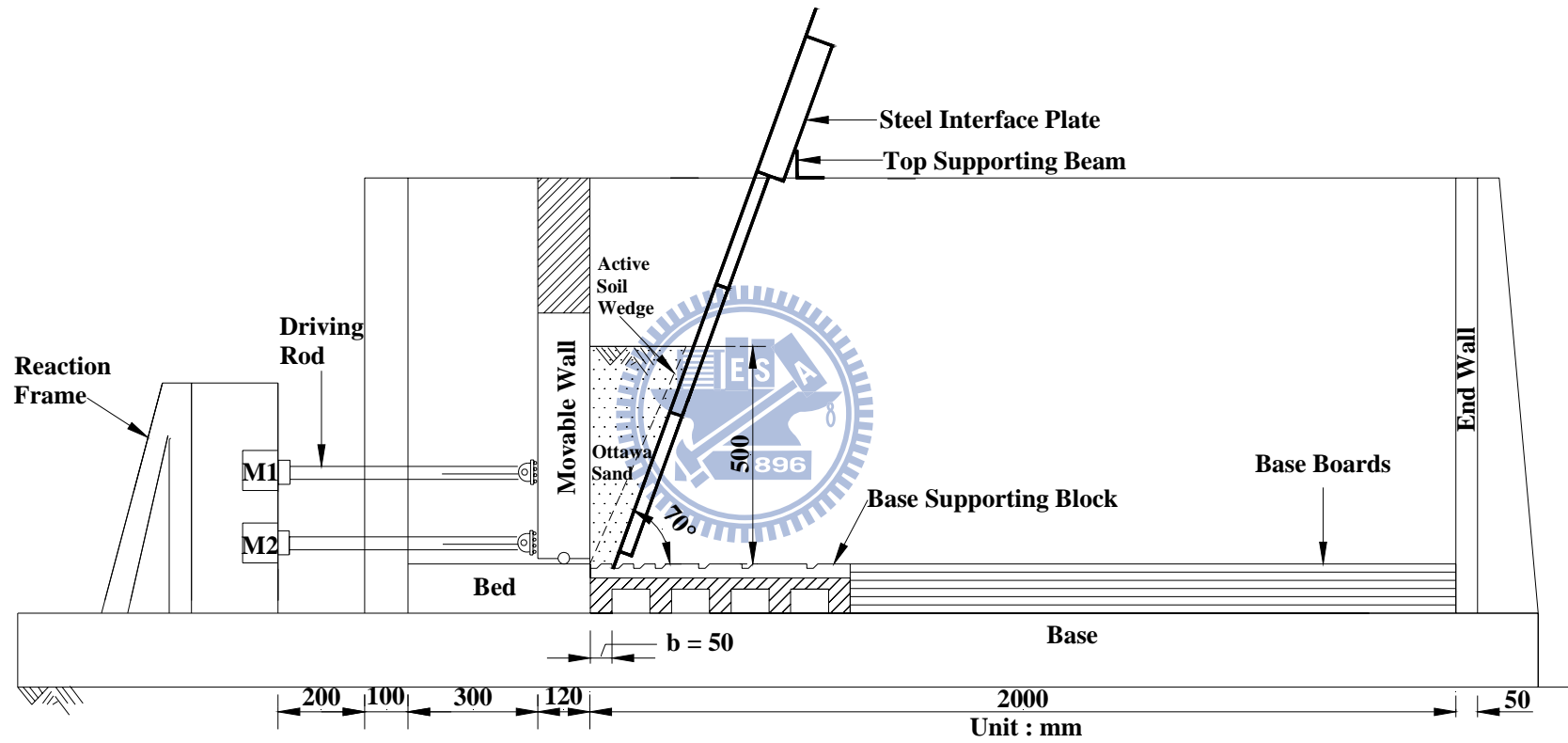
(a)

Fig. 6.26. Model wall test with interface inclination β = 70° and b = 50 mm

159

(b)

Fig. 6.26. Model wall test with interface inclination β = 70° and b = 50 mm
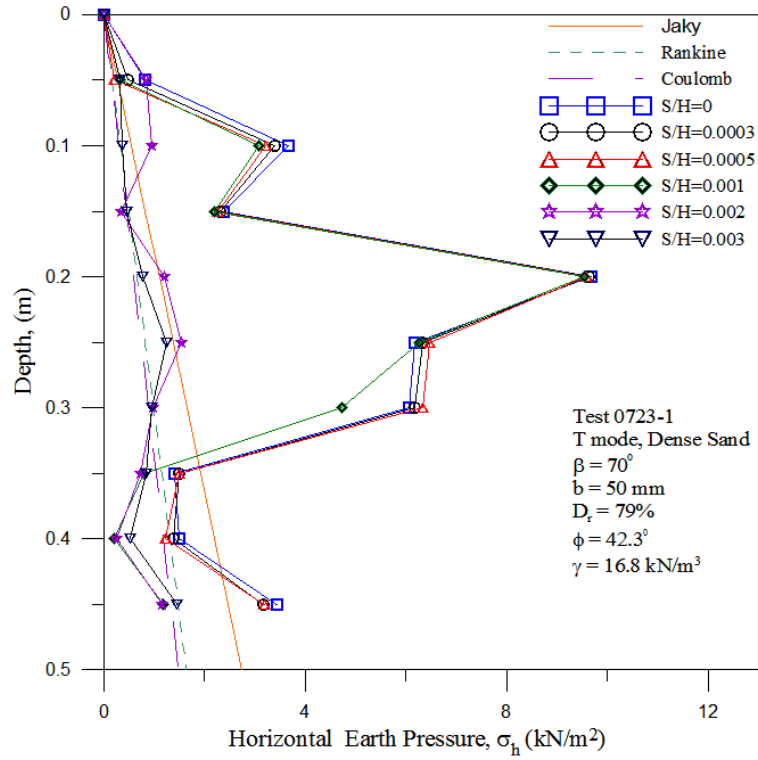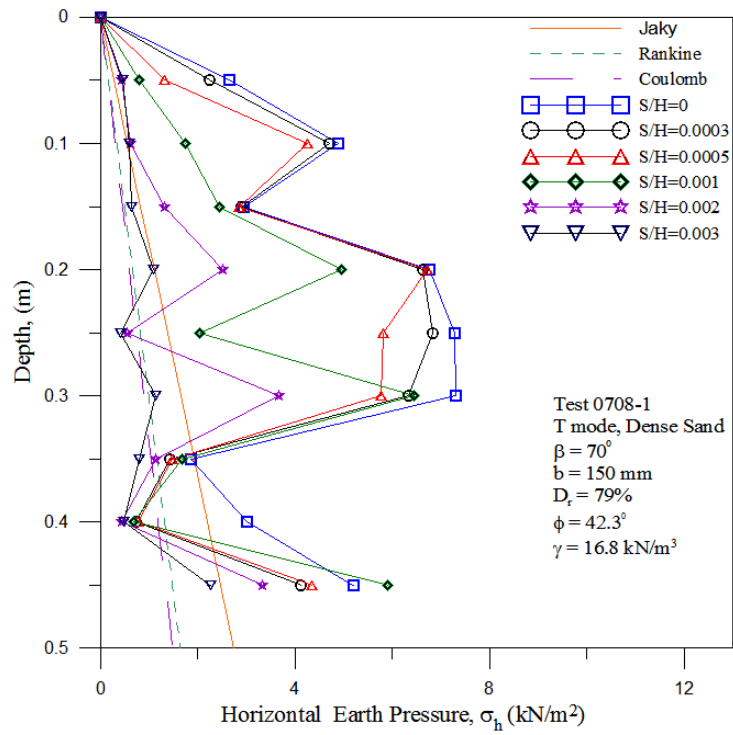
Fig. 6.27. Distribution of horizontal earth pressure for
b = 50 mm and β = 70° (Test 0723-1)
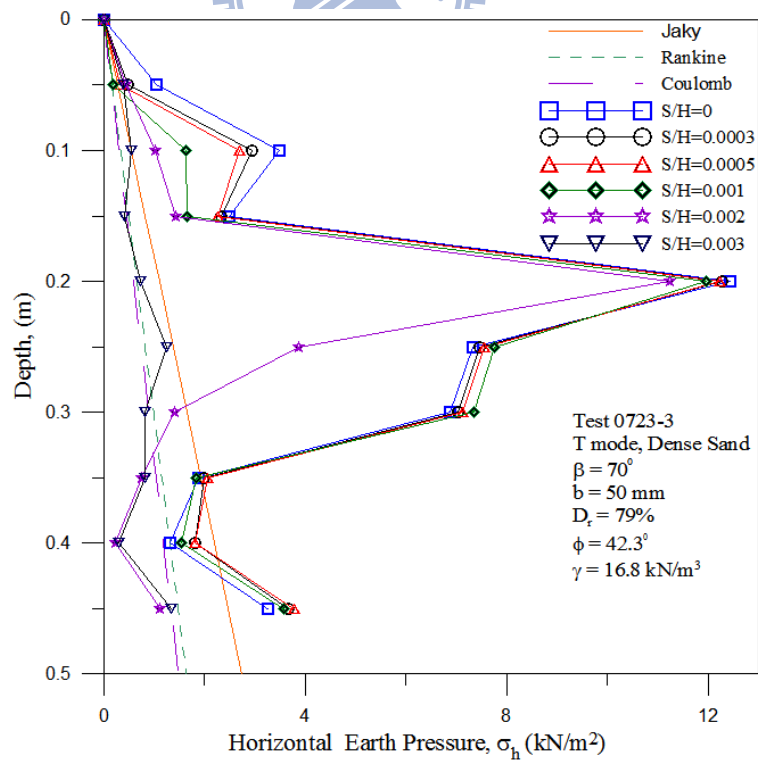
Fig. 6.28. Distribution of horizontal earth pressure for
b = 50 mm and β = 70°(Test 0723-3)

161
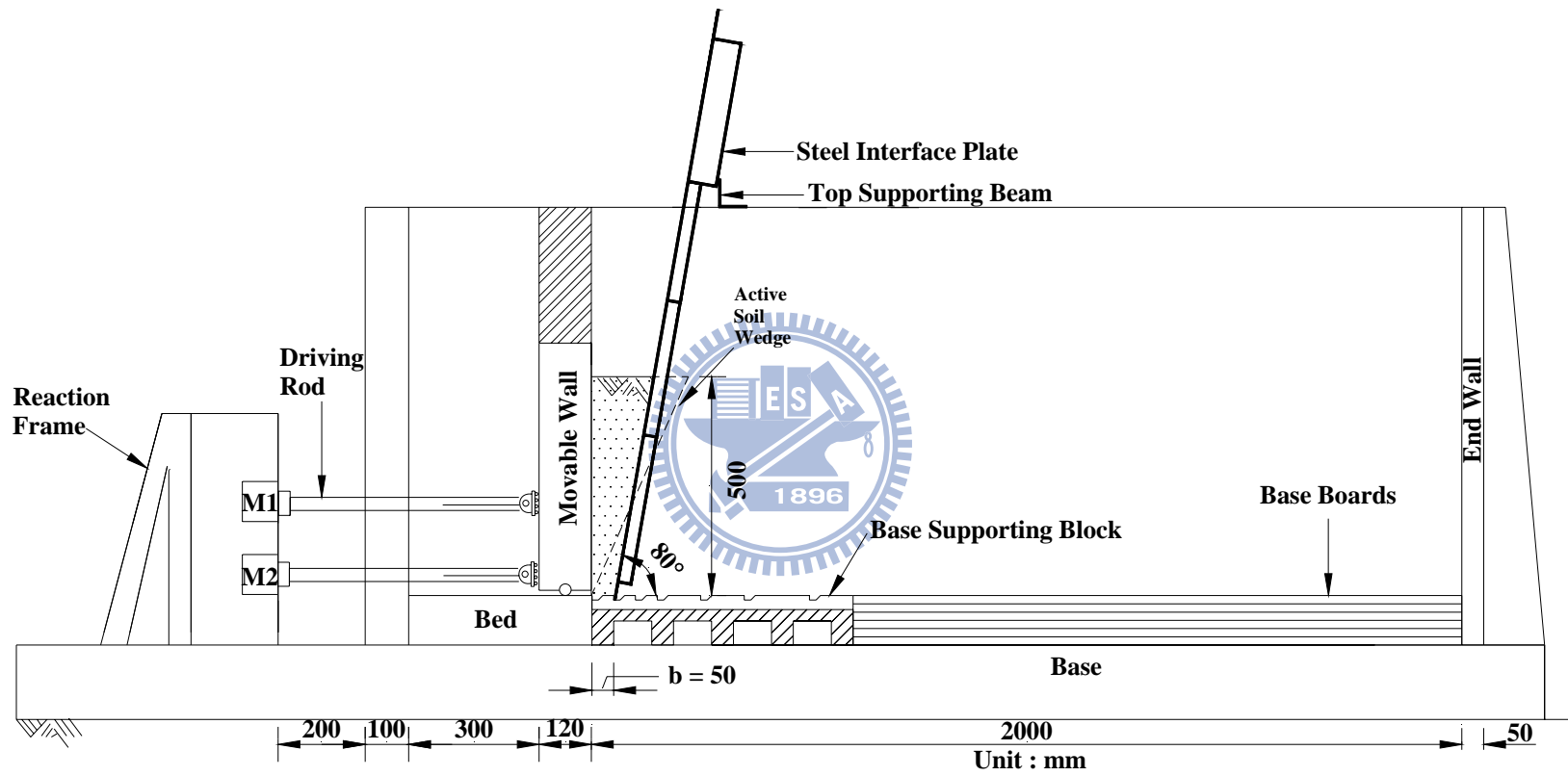
(a)

Fig. 6.29. Model wall test with interface inclination β = 80° and b = 50 mm

162

(b)
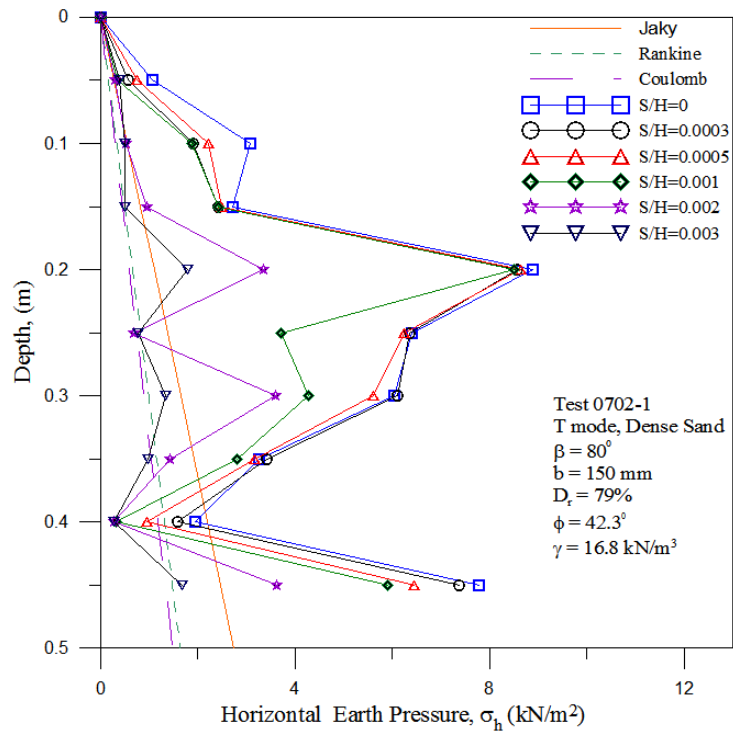
Fig. 6.29. Model wall test with interface inclination β = 80° and b = 50 mm
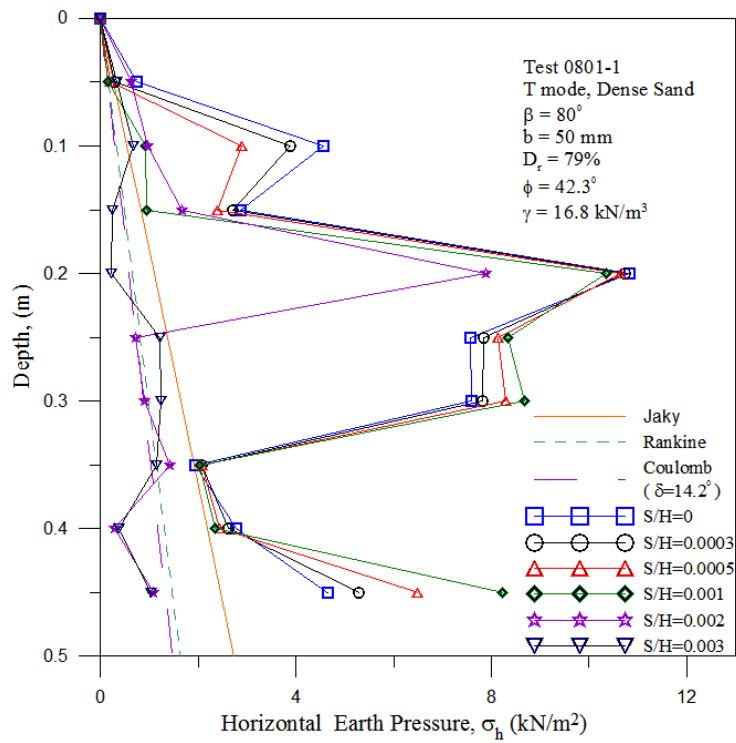
Fig. 6.30. Distribution of horizontal earth pressure for
b = 50 mm and β = 80° (Test 0801-1)
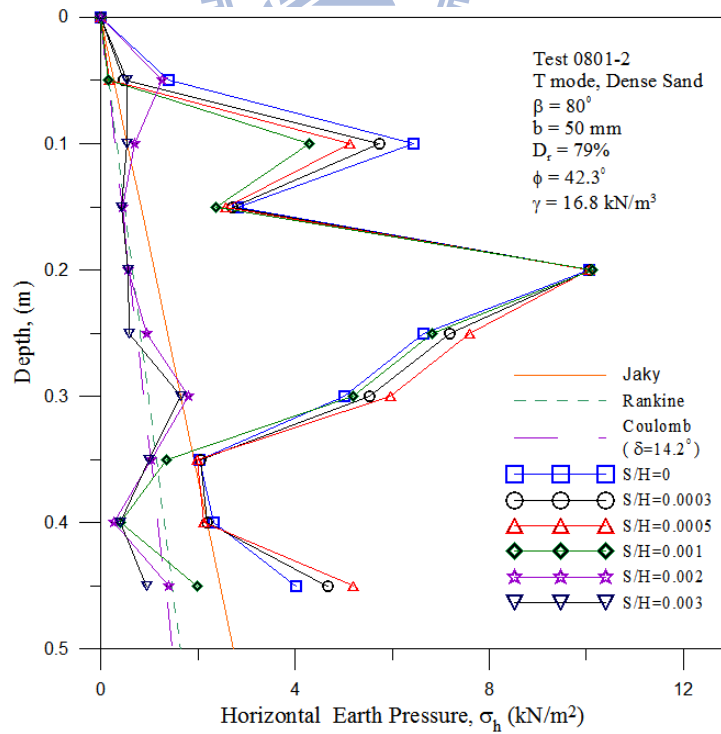
Fig. 6.31. Distribution of horizontal earth pressure for
b = 50 mm and β = 80°(Test 0801-2)

164

Steel Interface Plate

Top Supporting Beam

Active Soil Wedge

Driving Rod

Reaction Frame

Movable Wall

End Wall

M1

M2

500

Base Boards

Base Supporting Block

Bed

90°

b = 50

Base

200   100   300   120   2000   50

Unit : mm
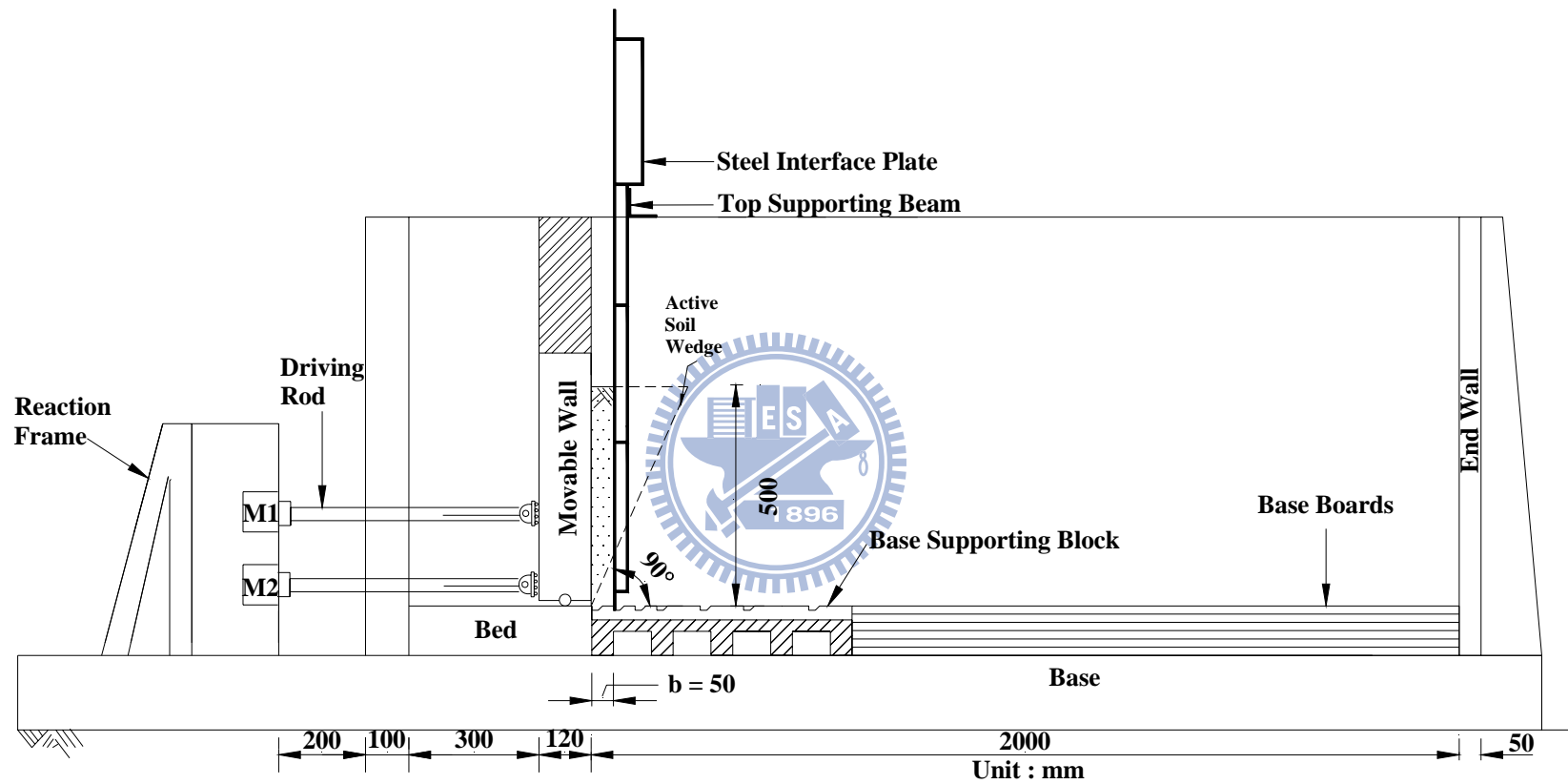
(a)

Fig. 6.32. Model wall test with interface inclination β = 90° and b = 50 mm

165

(b)

Fig. 6.32. Model wall test with interface inclination β = 90° and b = 50 mm
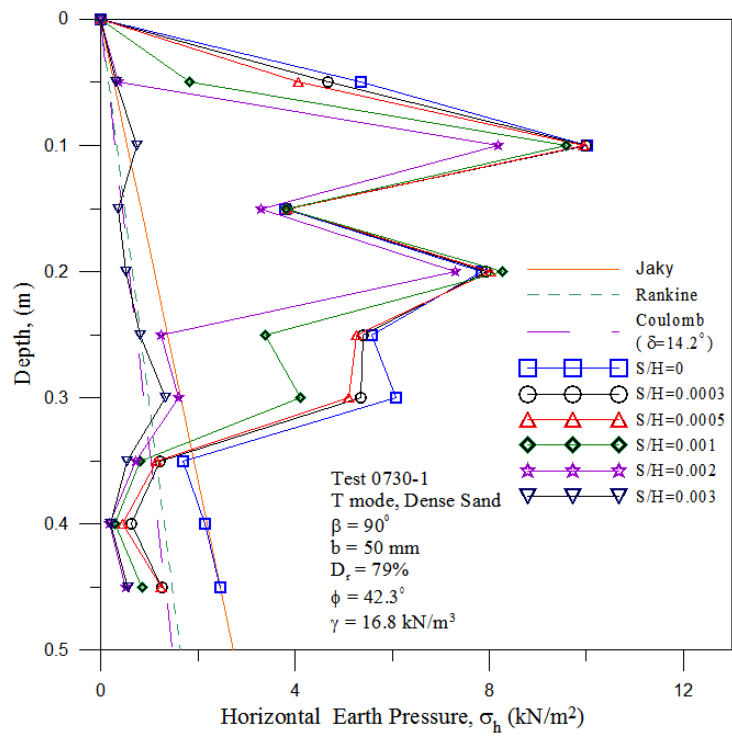
Fig. 6.33. Distribution of horizontal earth pressure for
b = 50 mm and β = 90° (Test 0730-1)
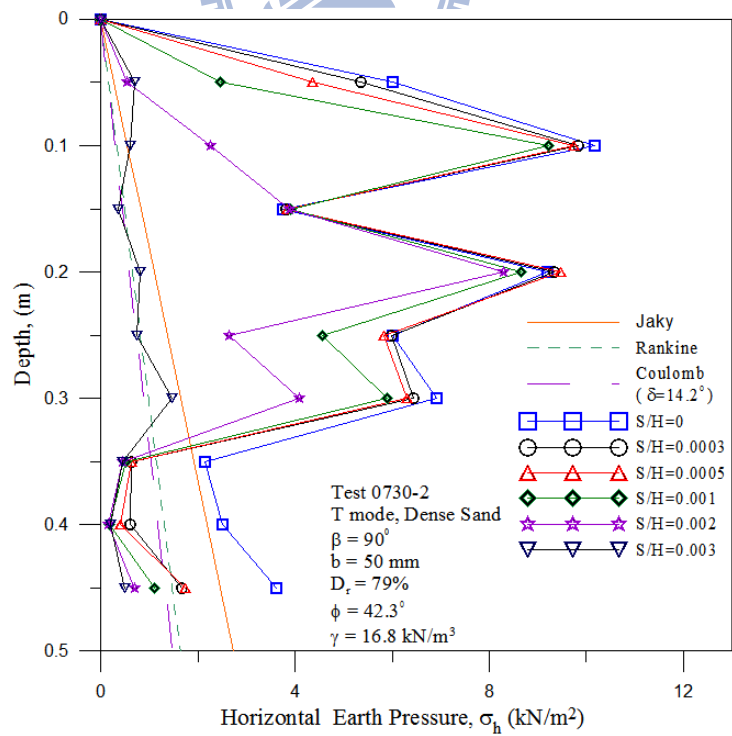
Fig. 6.34. Distribution of horizontal earth pressure for
b = 50 mm and β = 90°(Test 0730-2)
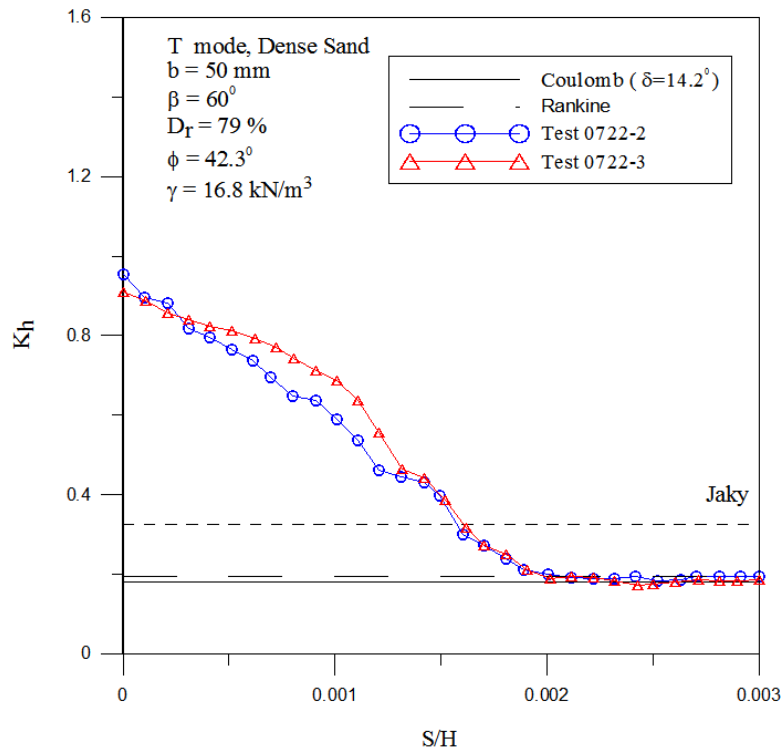
Fig. 6.35. Earth pressure coefficient K_h versus wall movement for
b = 50 mm and   β = 60°
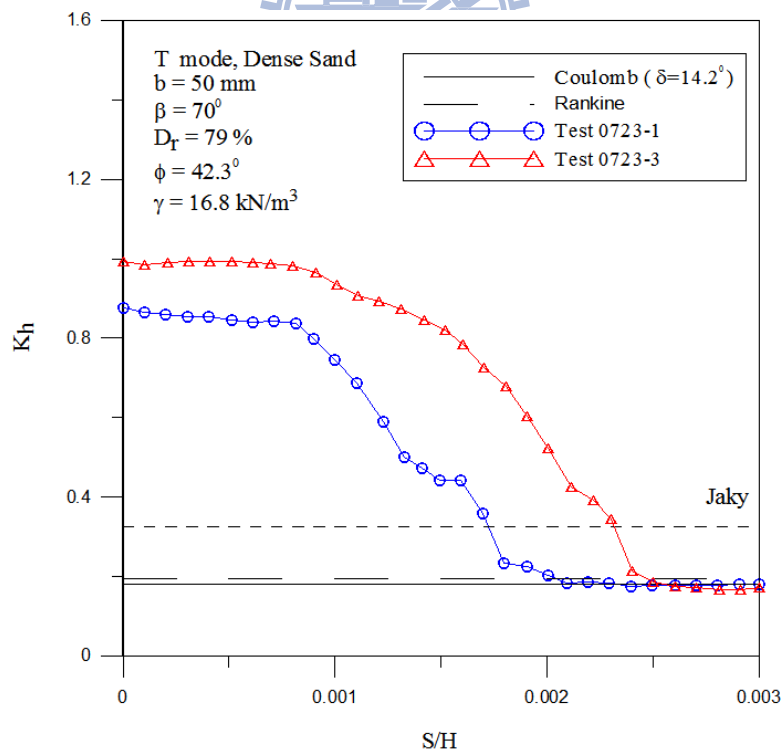
Fig. 6.36. Earth pressure coefficient K_h versus wall movement for
b = 50 mm and   β = 70°

168
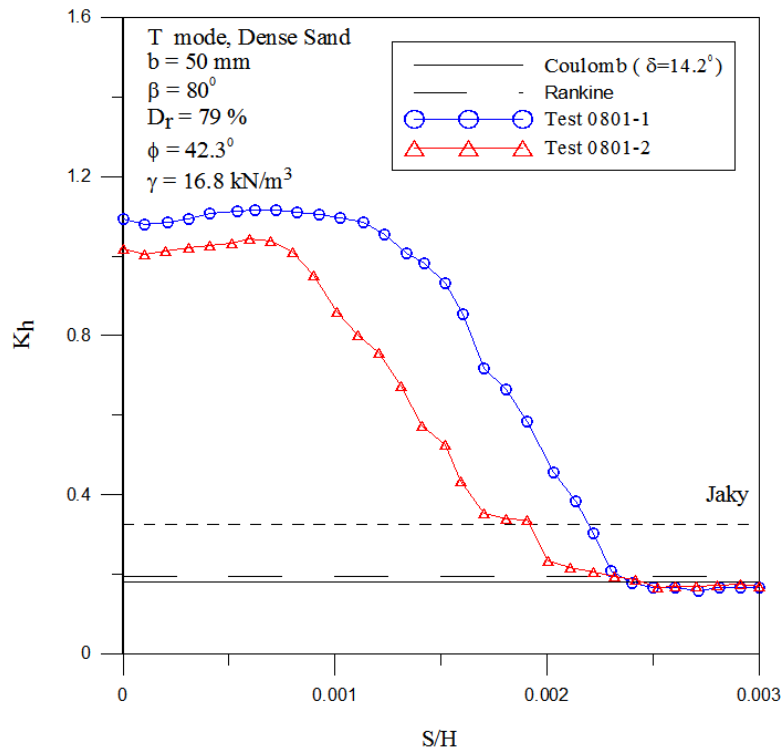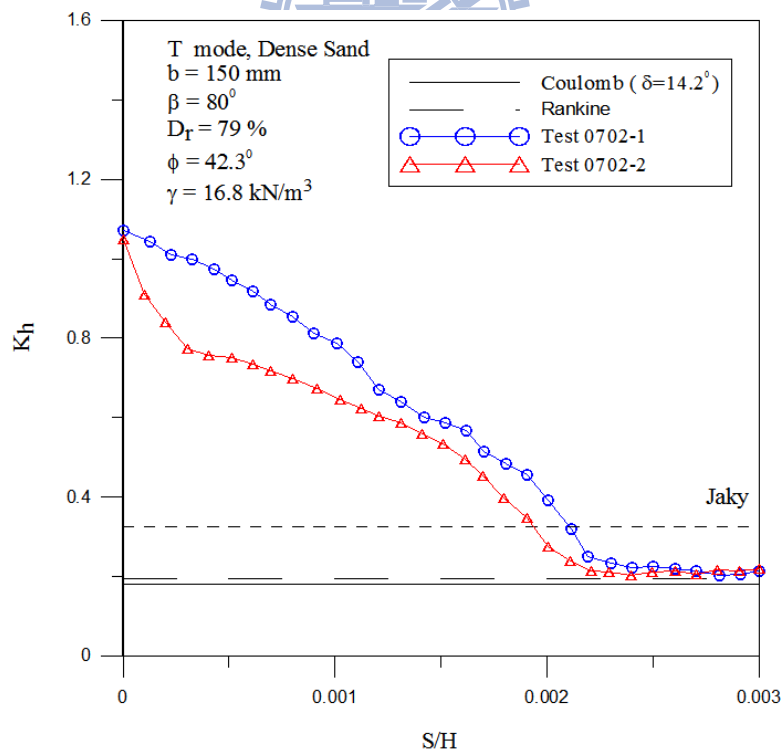
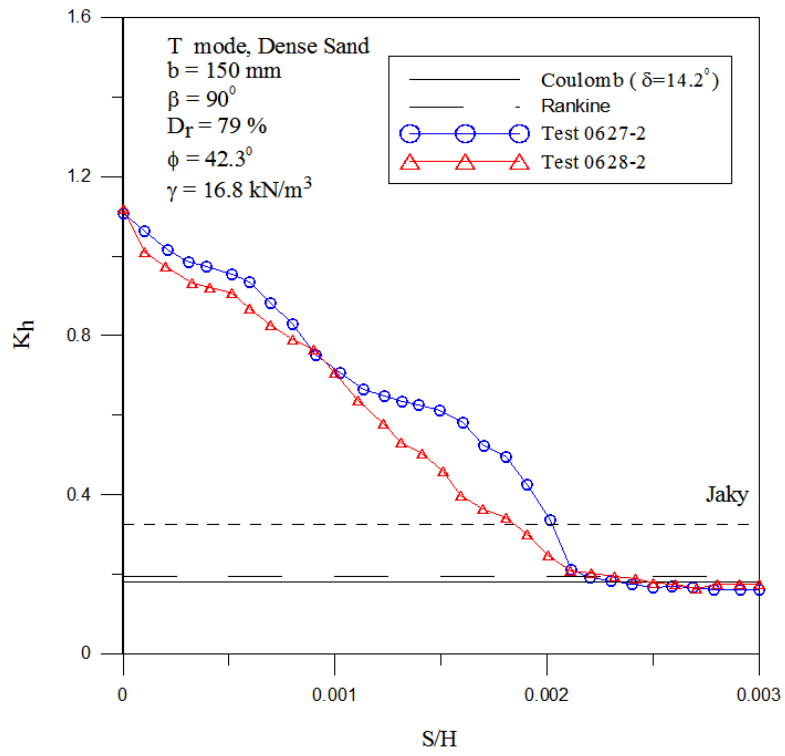Fig. 6.37. Earth pressure coefficient K_h versus wall movement for b = 50 mm and β = 80°
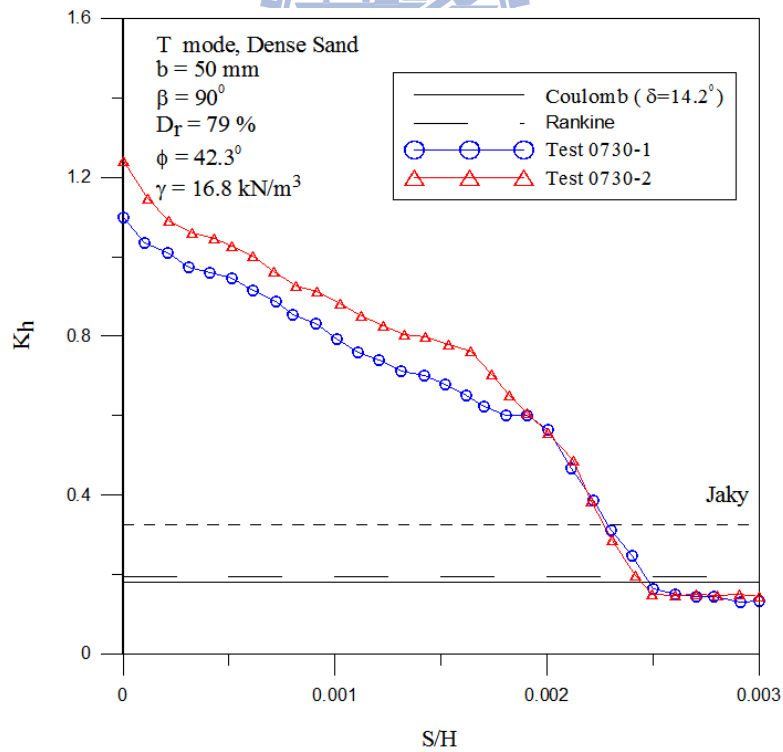


Fig. 6.38. Earth pressure coefficient K_h versus wall movement for b = 50 mm and β = 90°

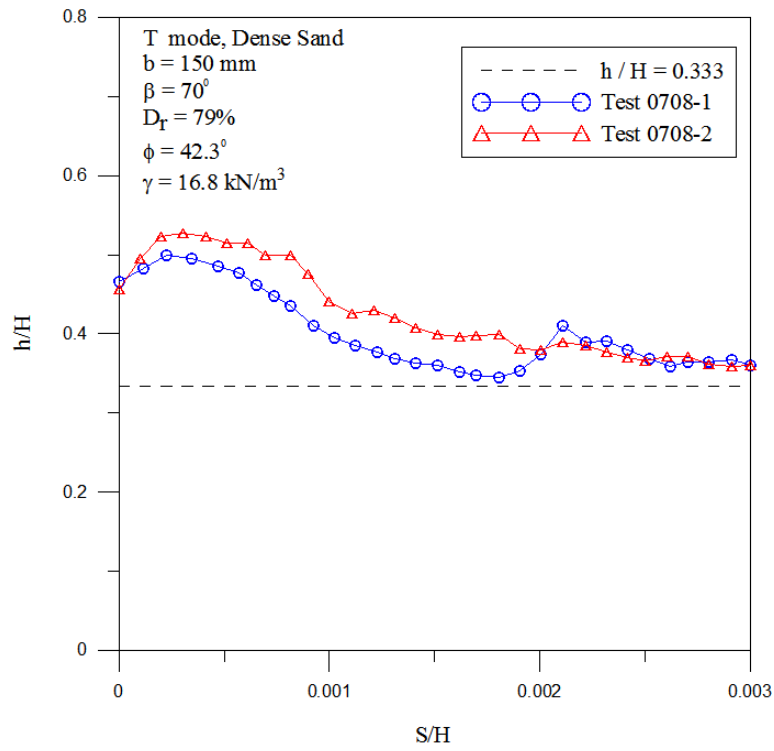169
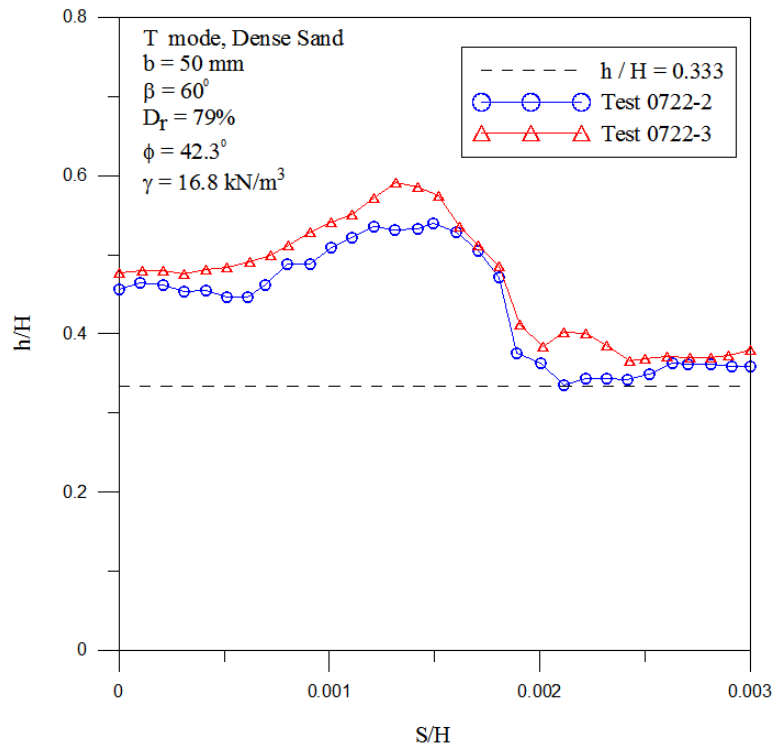
Fig. 6.39. Location of total thrust application for b = 50 mm and β = 60°
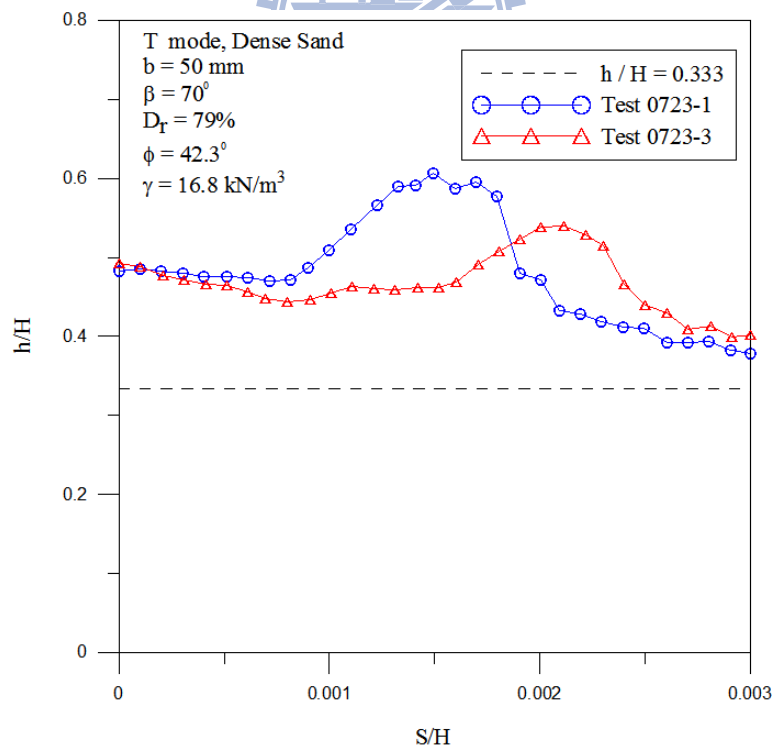
Fig. 6.40. Location of total thrust application for b = 50 mm and β = 70°
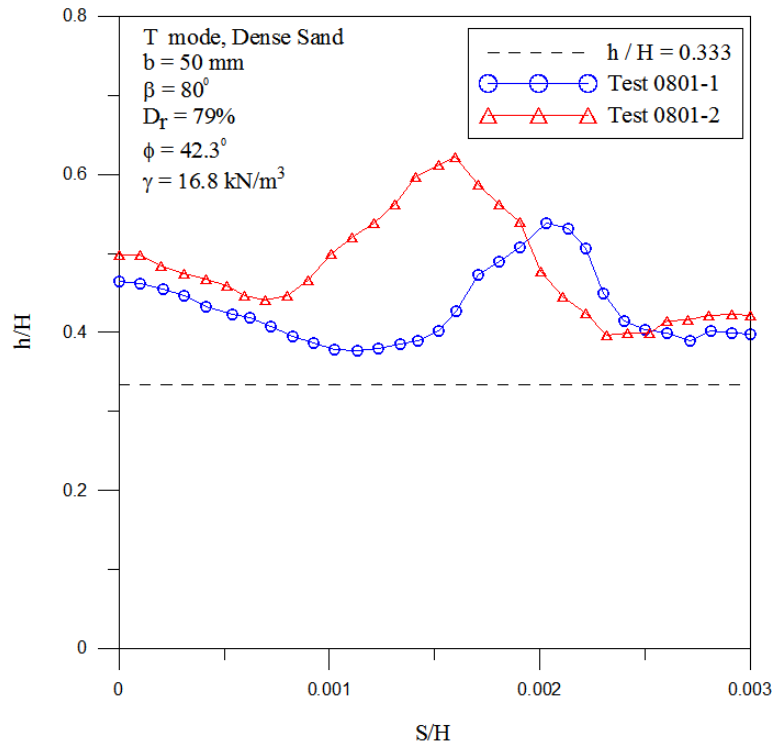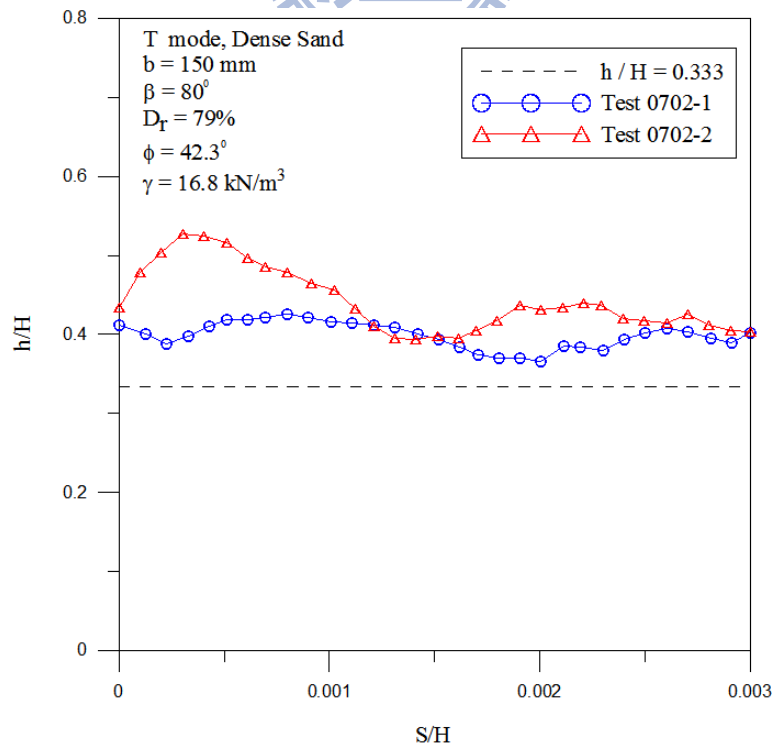
Fig. 6.41. Location of total thrust application for b = 50 mm and β = 80°
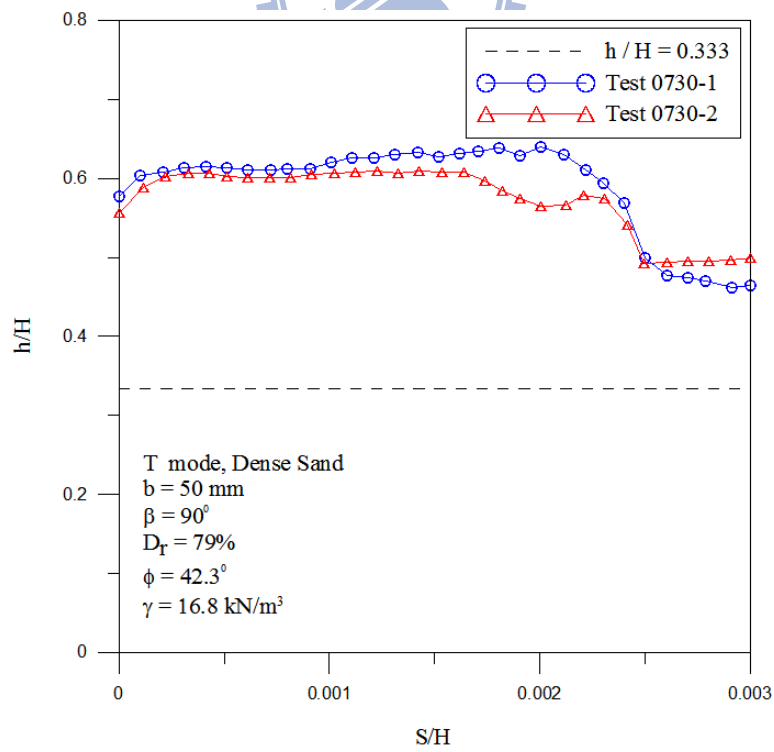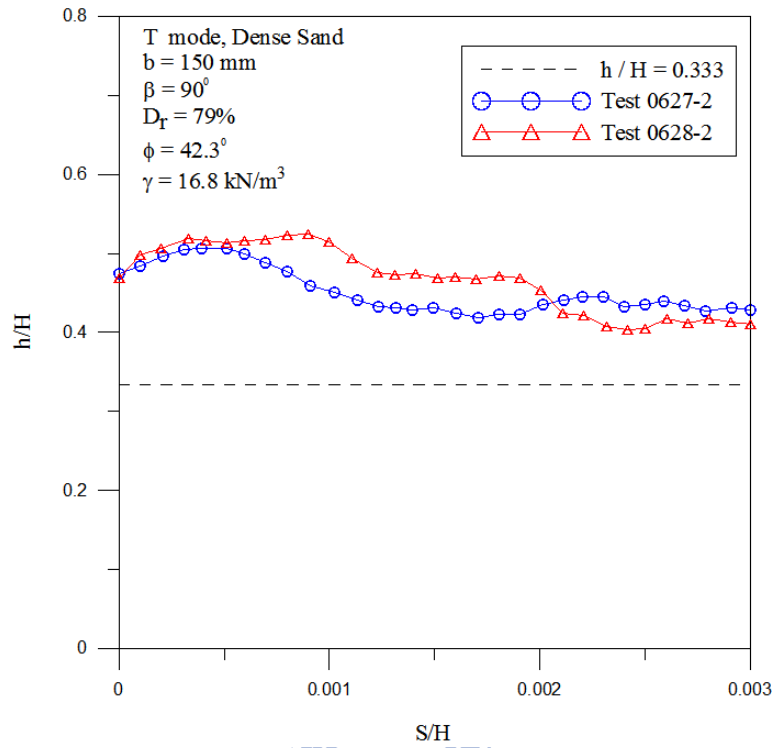

Fig. 6.42. Location of total thrust application for b = 50 mm and β = 90°

171
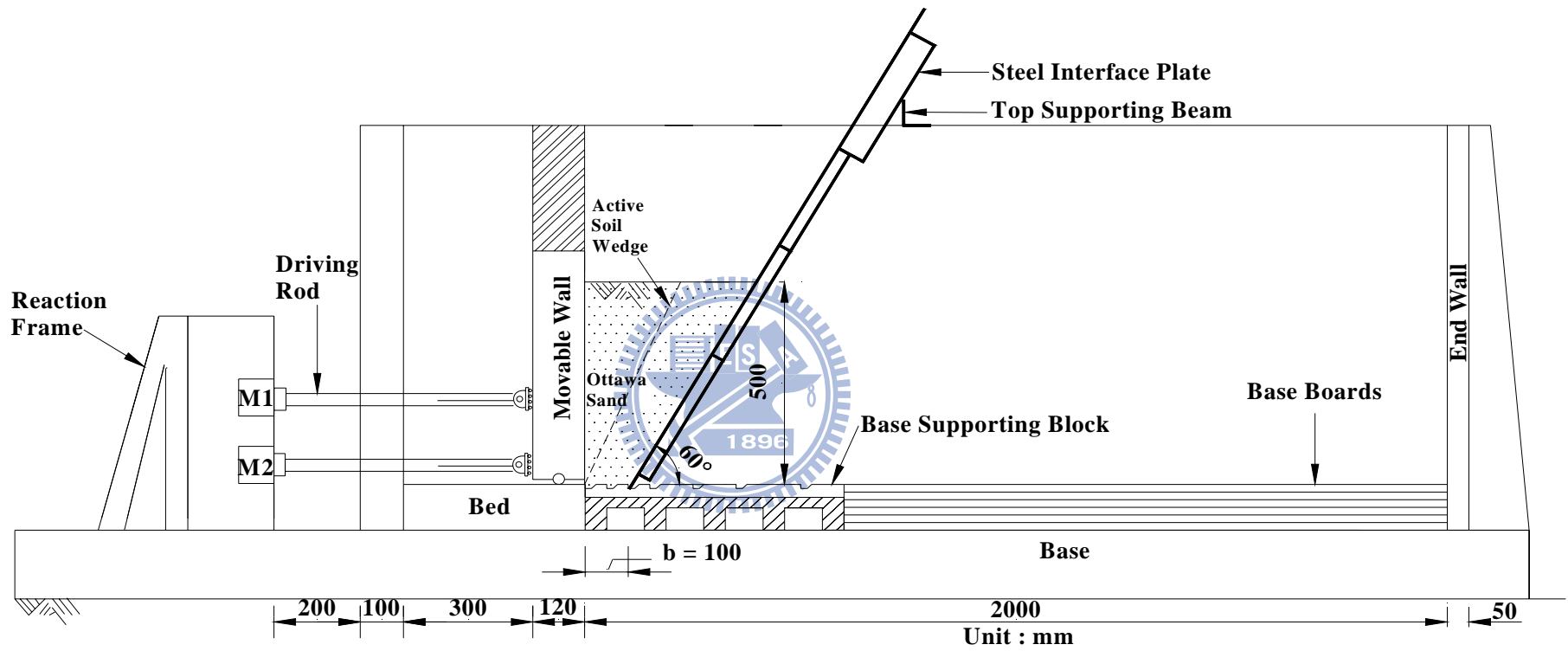
(a)

Fig. 6.43. Model wall test with interface inclination β = 60° and b = 100 mm

172

(b)

Fig. 6.43. Model wall test with interface inclination β = 60° and b = 100 mm
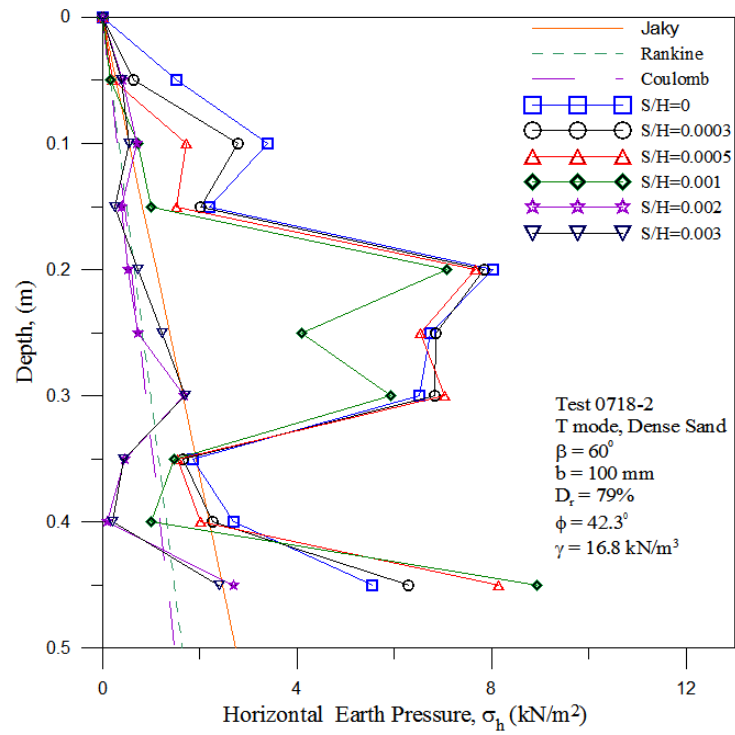
Fig. 6.44. Distribution of horizontal earth pressure for
b = 100 mm and β = 60° (Test 0718-2)
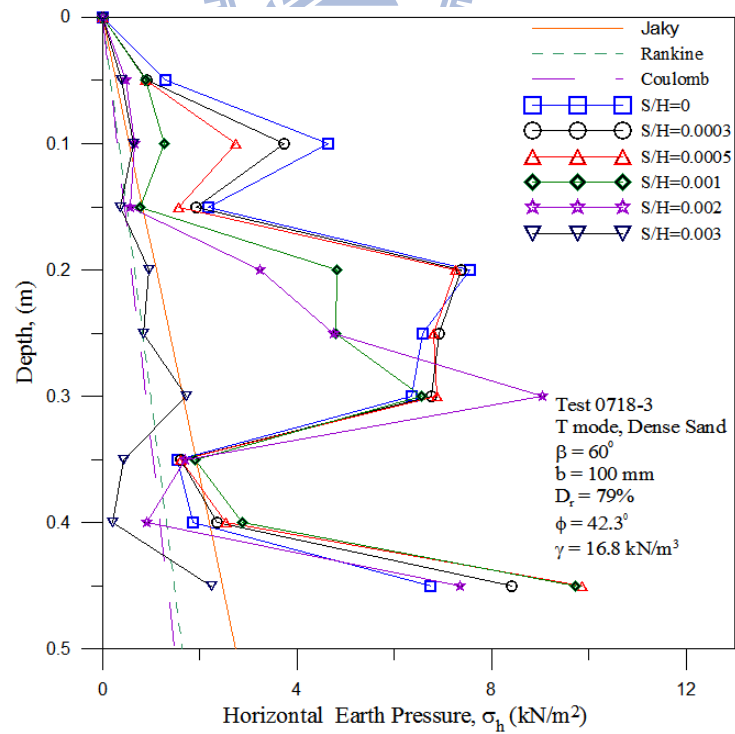
Fig. 6.45. Distribution of horizontal earth pressure for
b = 100 mm and β = 60°(Test 0718-3)
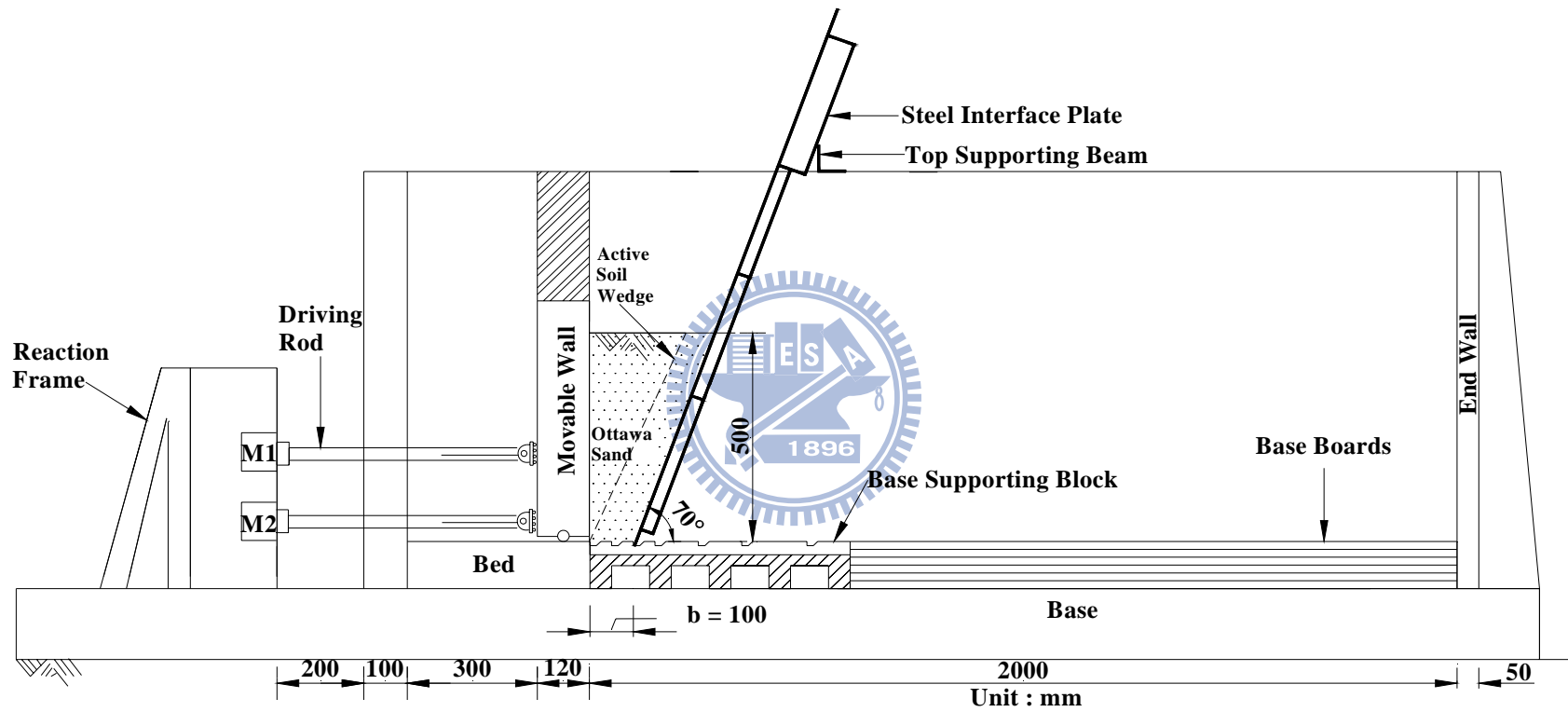
(a)

Fig. 6.46. Model wall test with interface inclination β = 70° and b = 100 mm

175

(b)

Fig. 6.46. Model wall test with interface inclination β = 70° and b = 100 mm
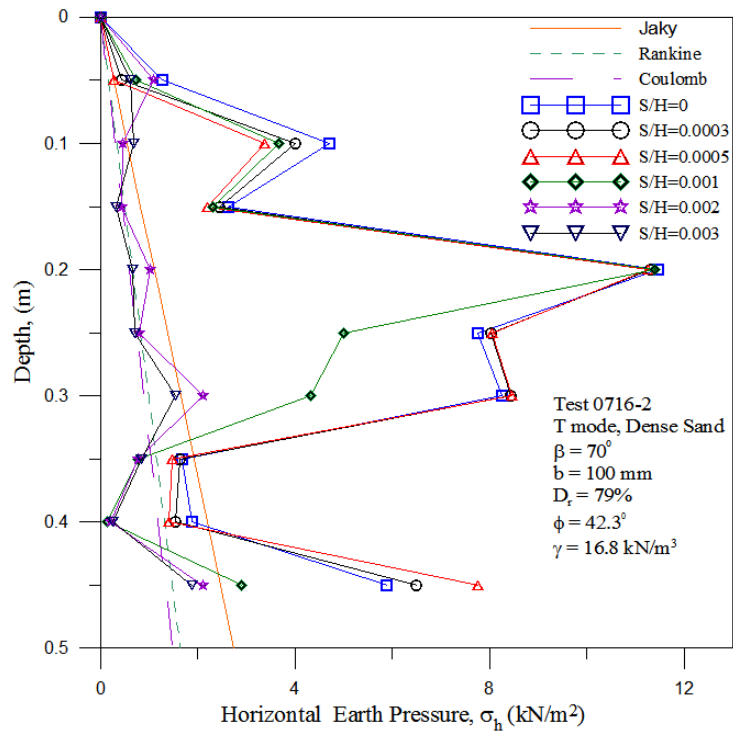
Fig. 6.47. Distribution of horizontal earth pressure for
b = 100 mm and β = 70° (Test 0716-2)
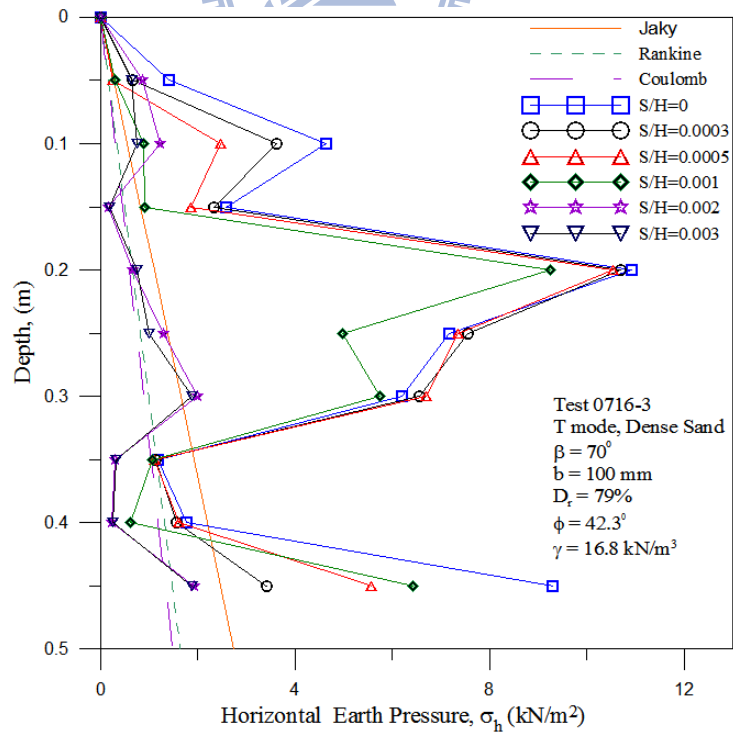
Fig. 6.48. Distribution of horizontal earth pressure for
b = 100 mm and β = 70°(Test 0716-3)
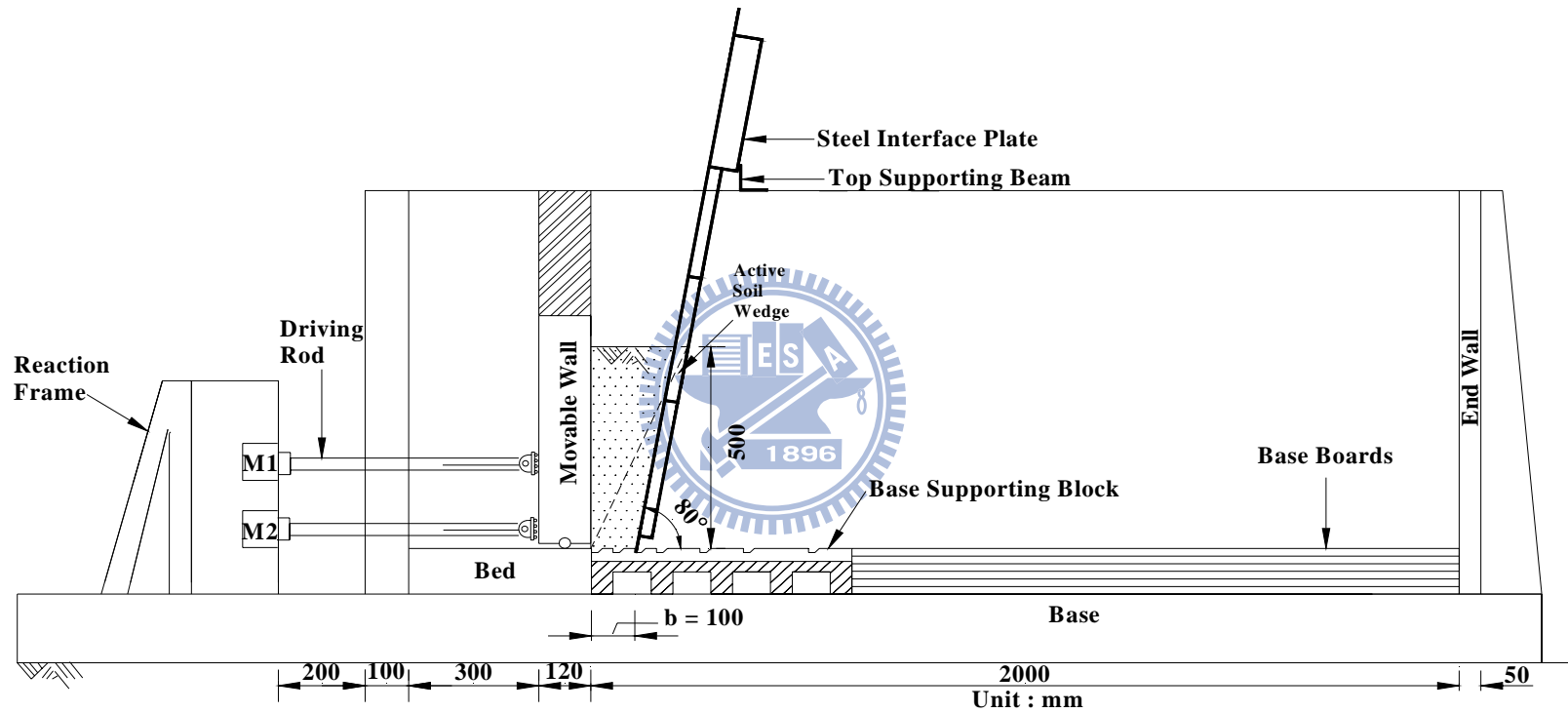
(a)

Fig. 6.49. Model wall test with interface inclination β = 80° and b = 100 mm

(b)

Fig. 6.49. Model wall test with interface inclination β = 80° and b = 100 mm
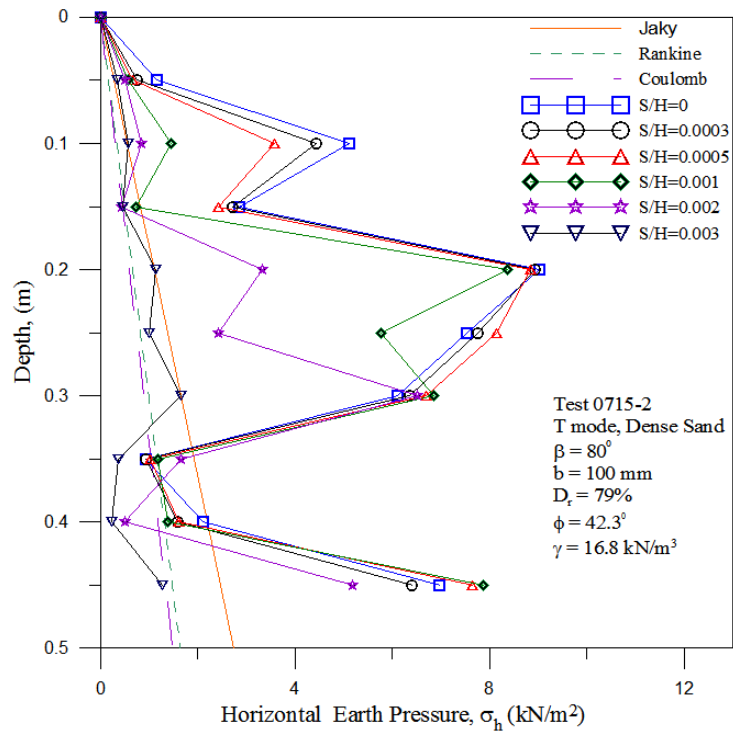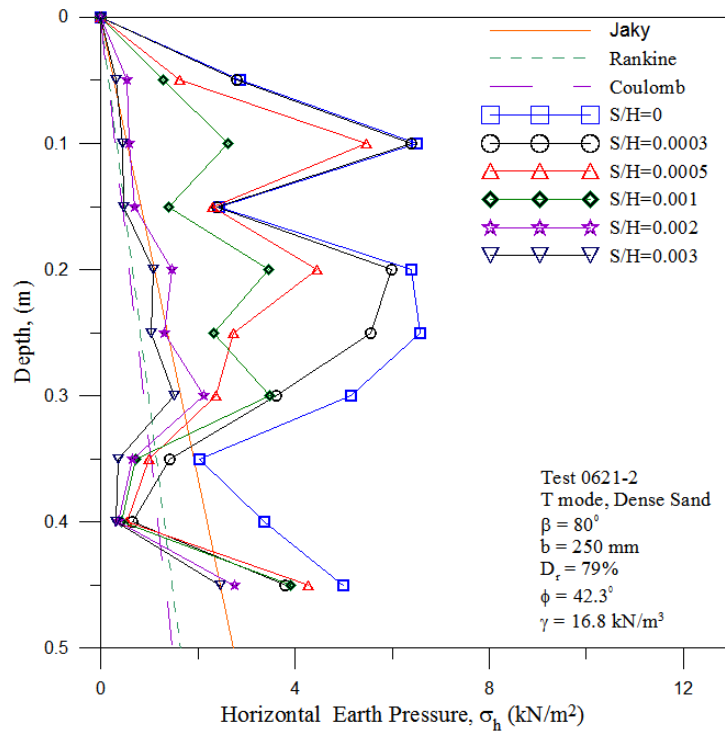
Fig. 6.50. Distribution of horizontal earth pressure for
b = 100 mm and β = 80° (Test 0715-2)
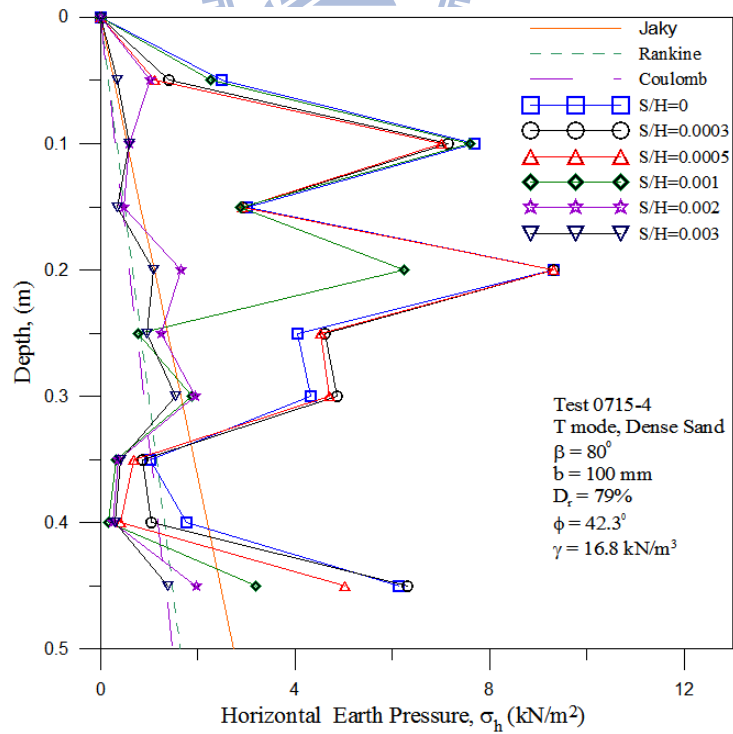
Fig. 6.51. Distribution of horizontal earth pressure for
b = 100 mm and β = 80°(Test 0715-4)
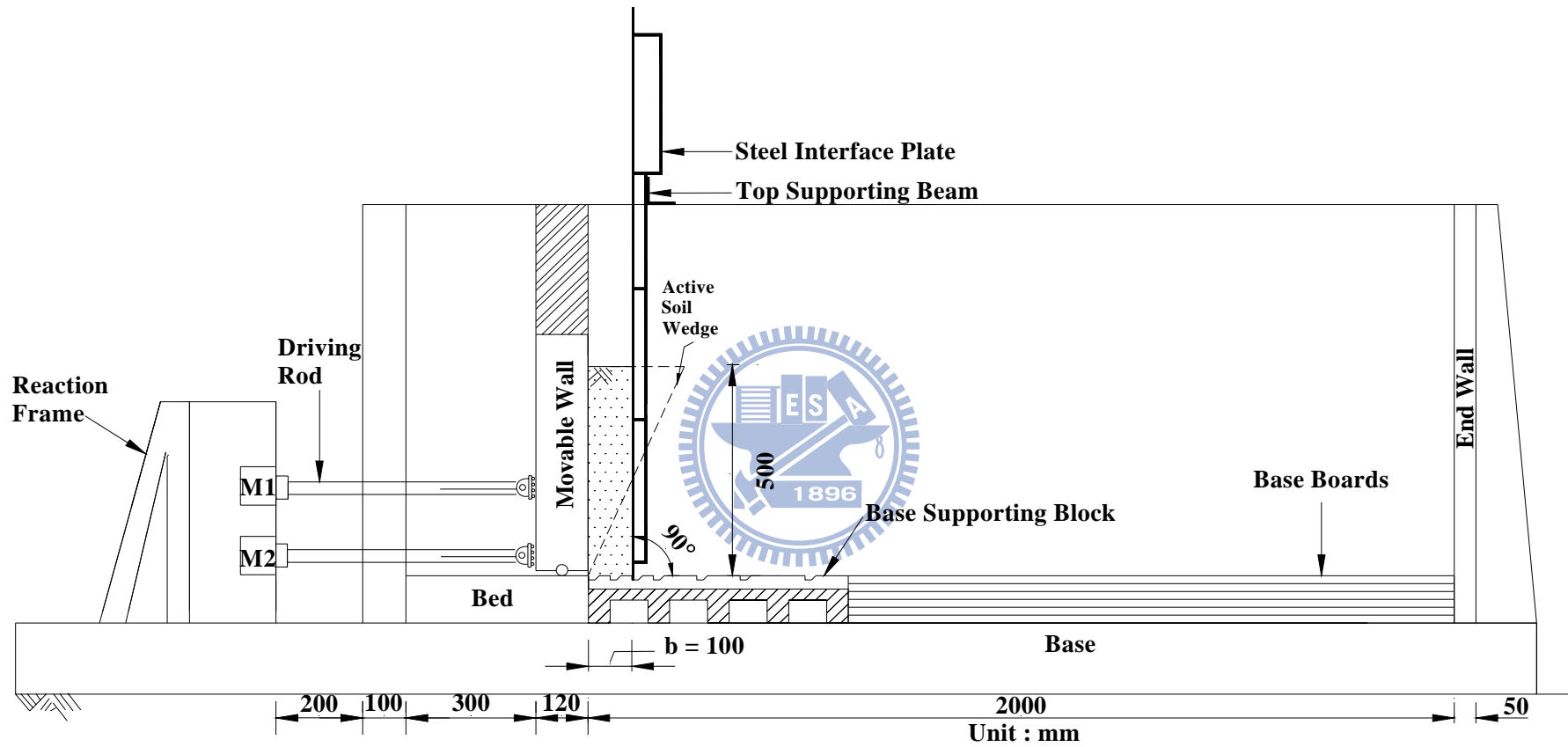
(a)

Fig. 6.52. Model wall test with interface inclination β = 90° and b = 100 mm

181

(b)

Fig. 6.52. Model wall test with interface inclination β = 90° and b = 100 mm
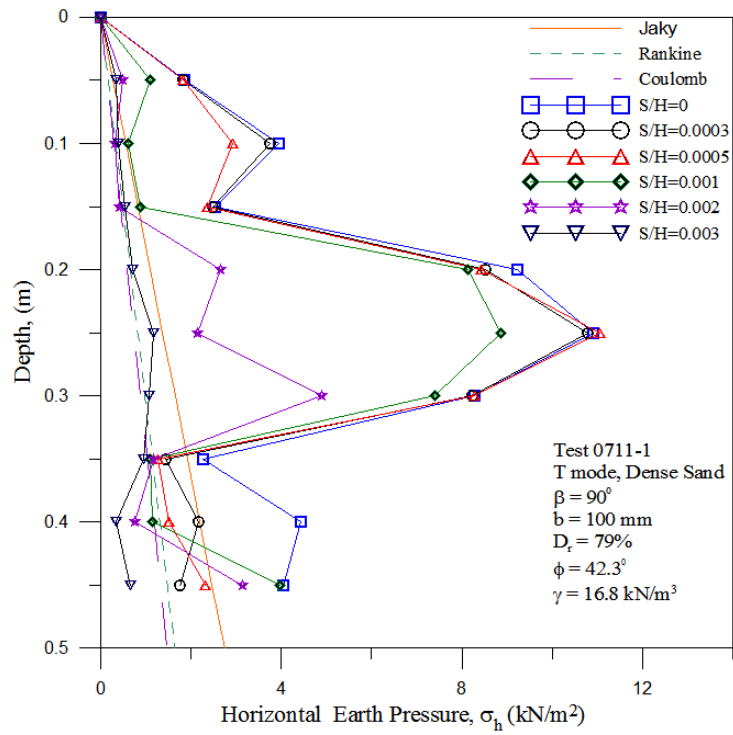
Fig. 6.53. Distribution of horizontal earth pressure for
b = 100 mm and β = 90° (Test 0711-1)
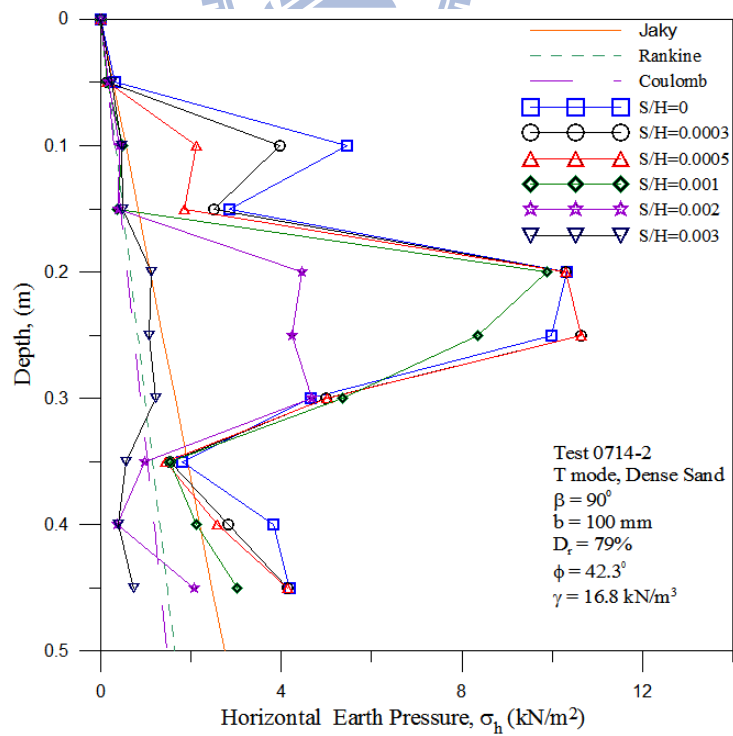
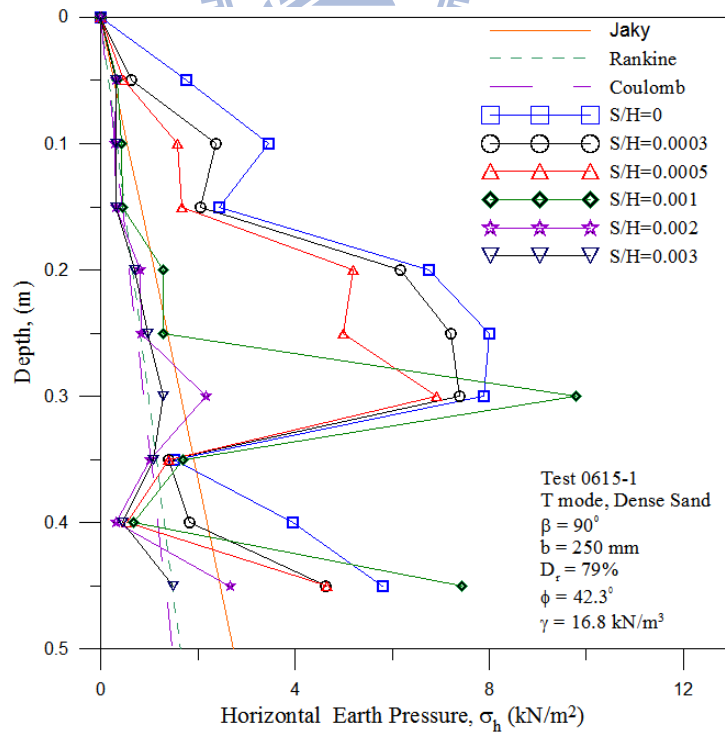Fig. 6.54. Distribution of horizontal earth pressure for
b = 100 mm and β = 90°(Test 0714-2)

183
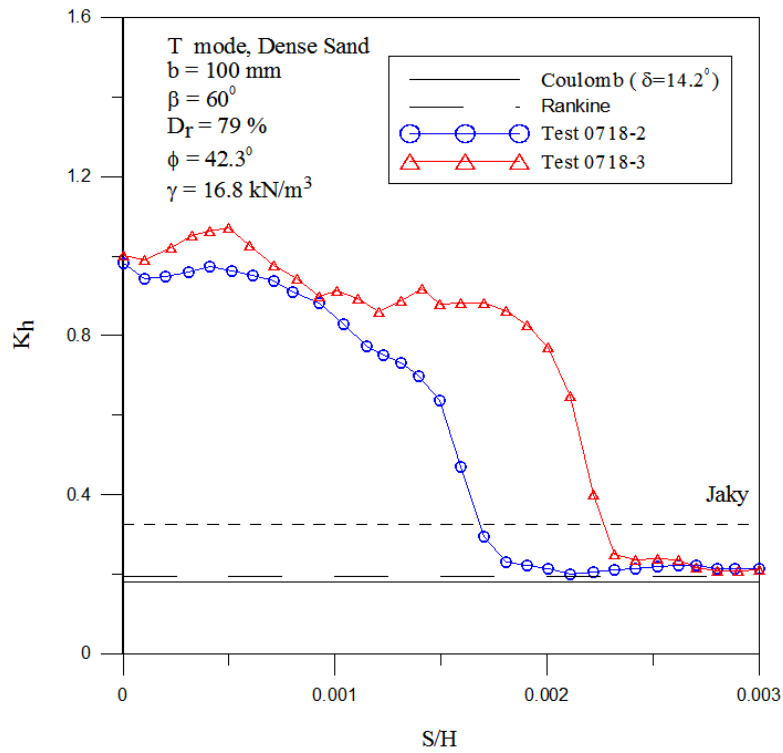
Fig. 6.55. Earth pressure coefficient K_h versus wall movement for
b = 100 mm and   β = 60°
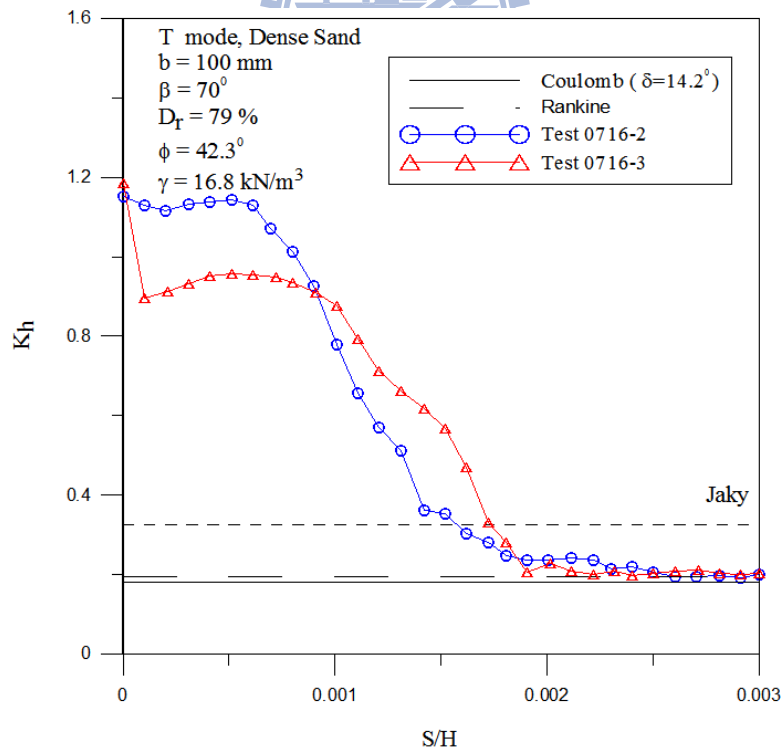
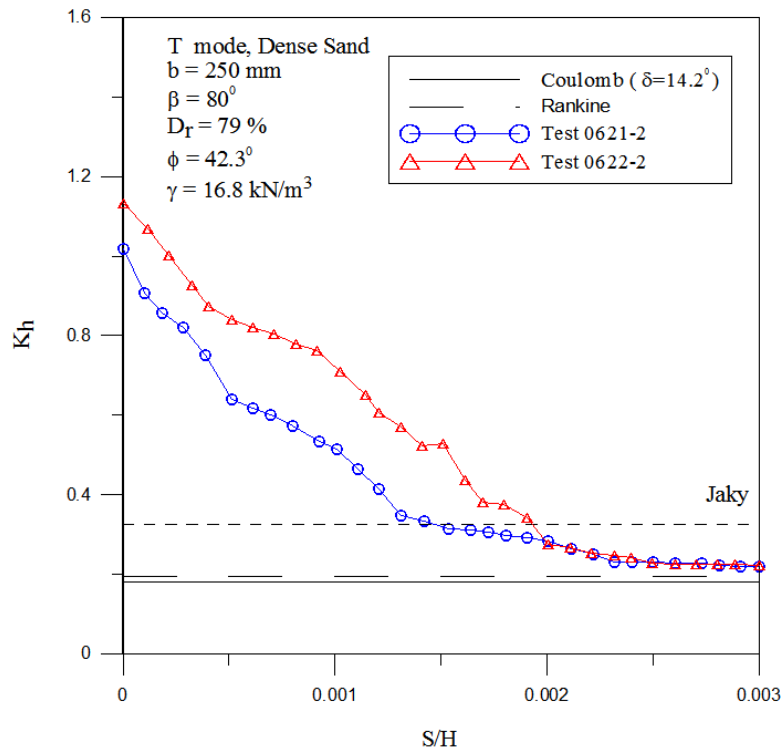Fig. 6.56. Earth pressure coefficient K_h versus wall movement for
b = 100 mm and   β = 70°
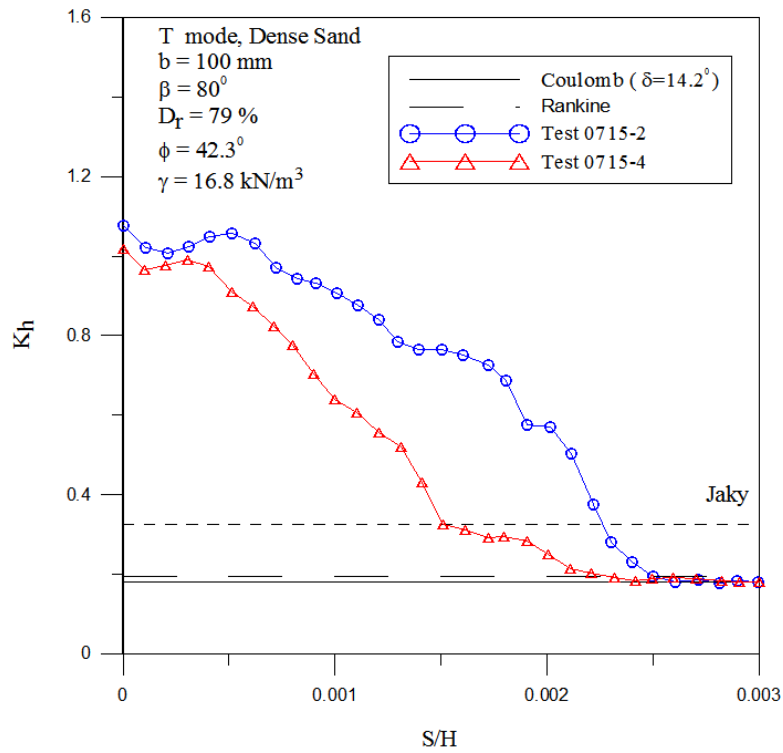
Fig. 6.57. Earth pressure coefficient K_h versus wall movement for
b = 100 mm and β = 80°
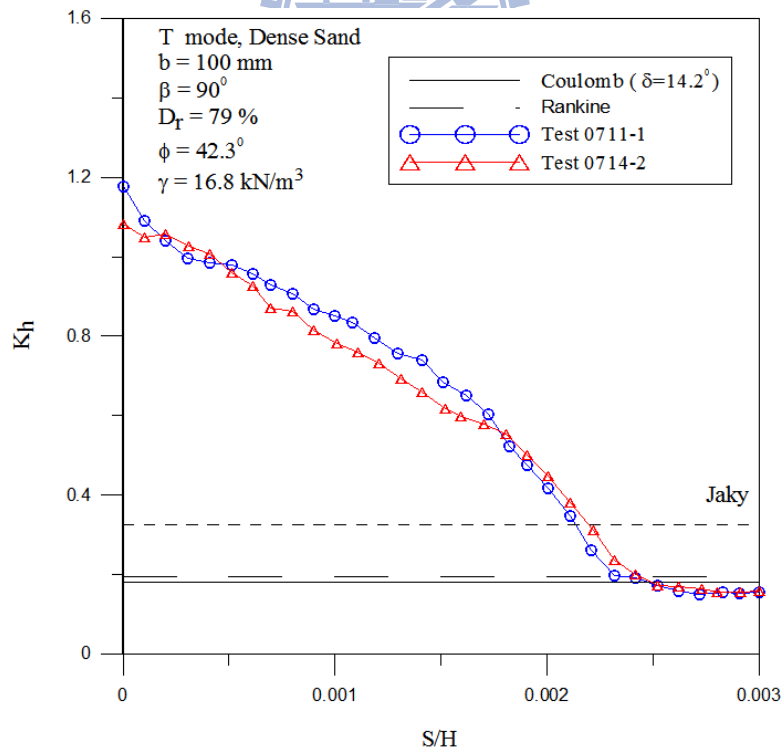
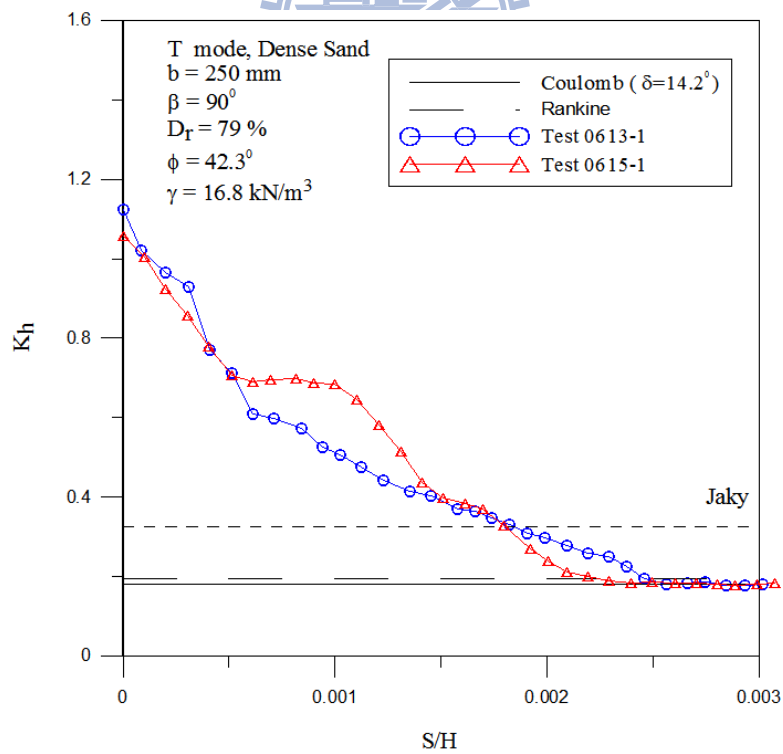Fig. 6.58. Earth pressure coefficient K_h versus wall movement for
b = 100 mm and β = 90°
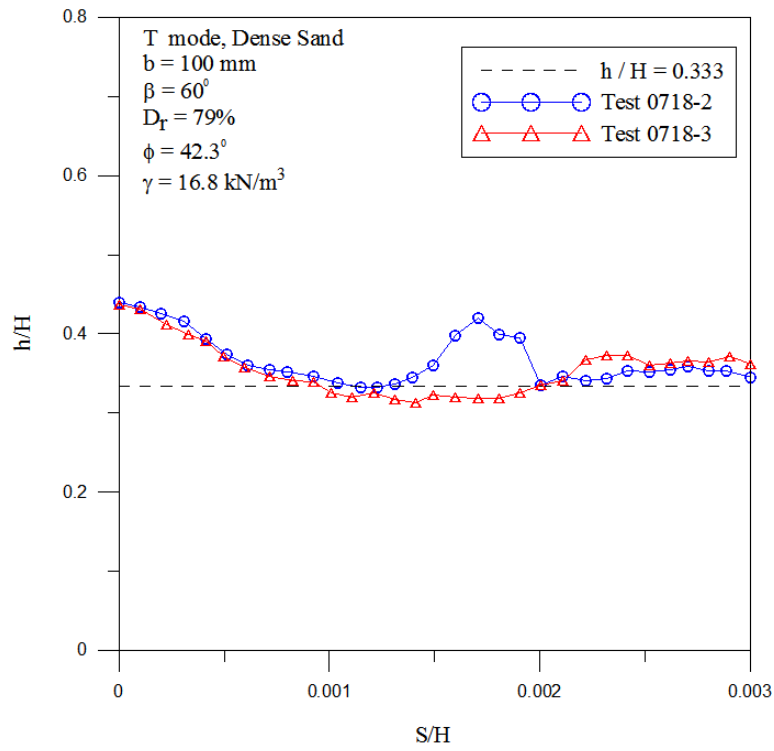
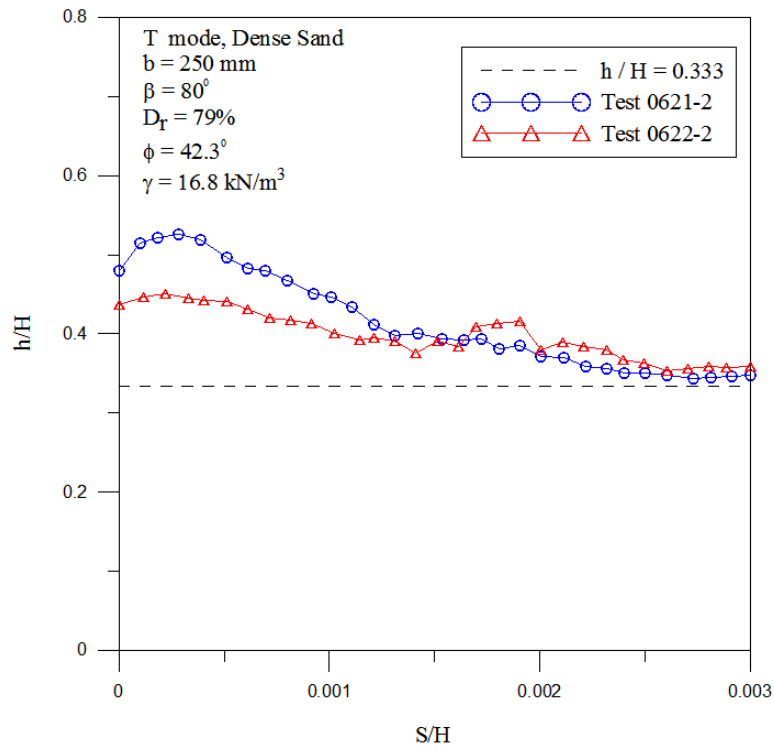Fig. 6.59. Location of total thrust application for b = 100 mm and β = 60°
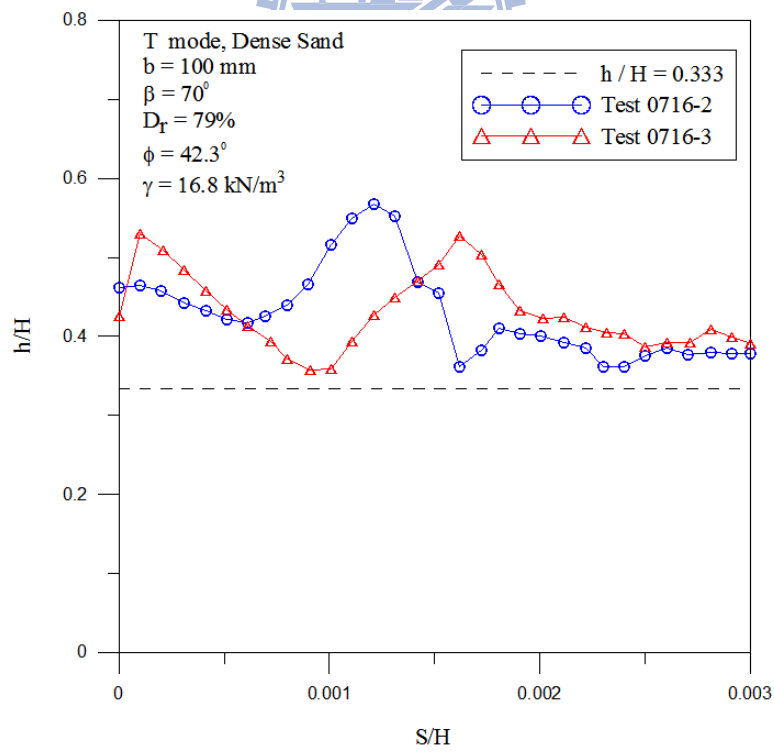
Fig. 6.60. Location of total thrust application for b = 100 mm and β = 70°

186
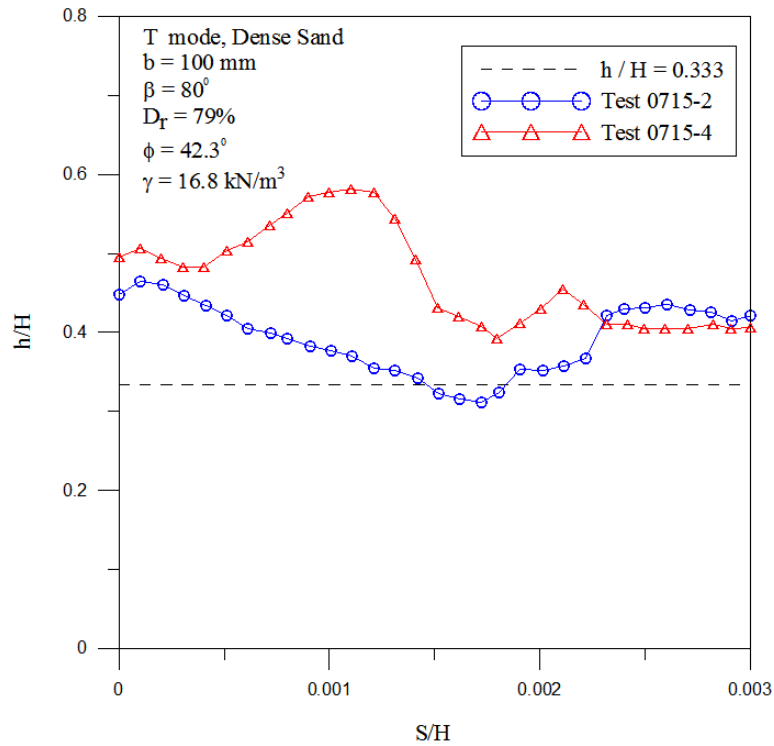
Fig. 6.61. Location of total thrust application for b = 100 mm and   β = 80°
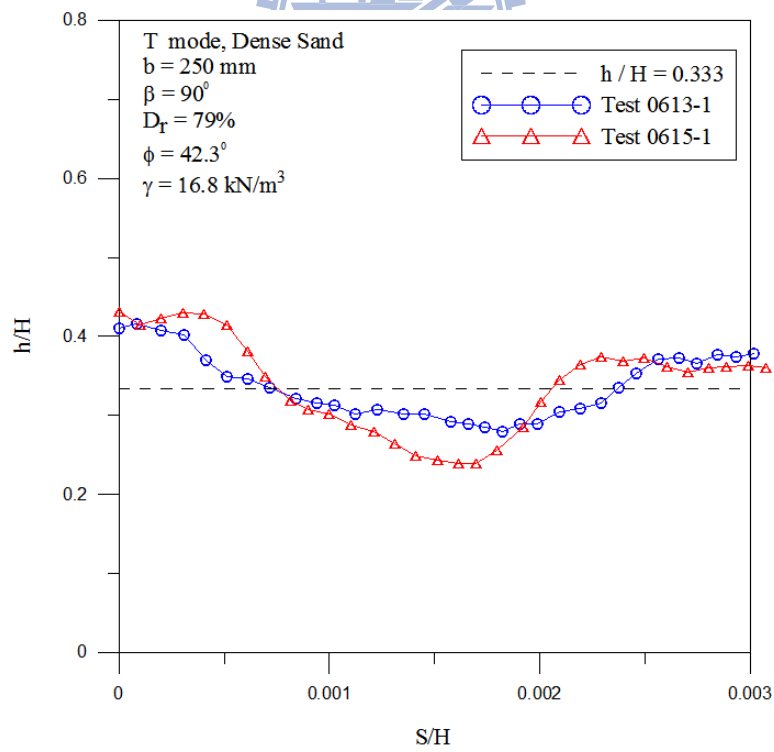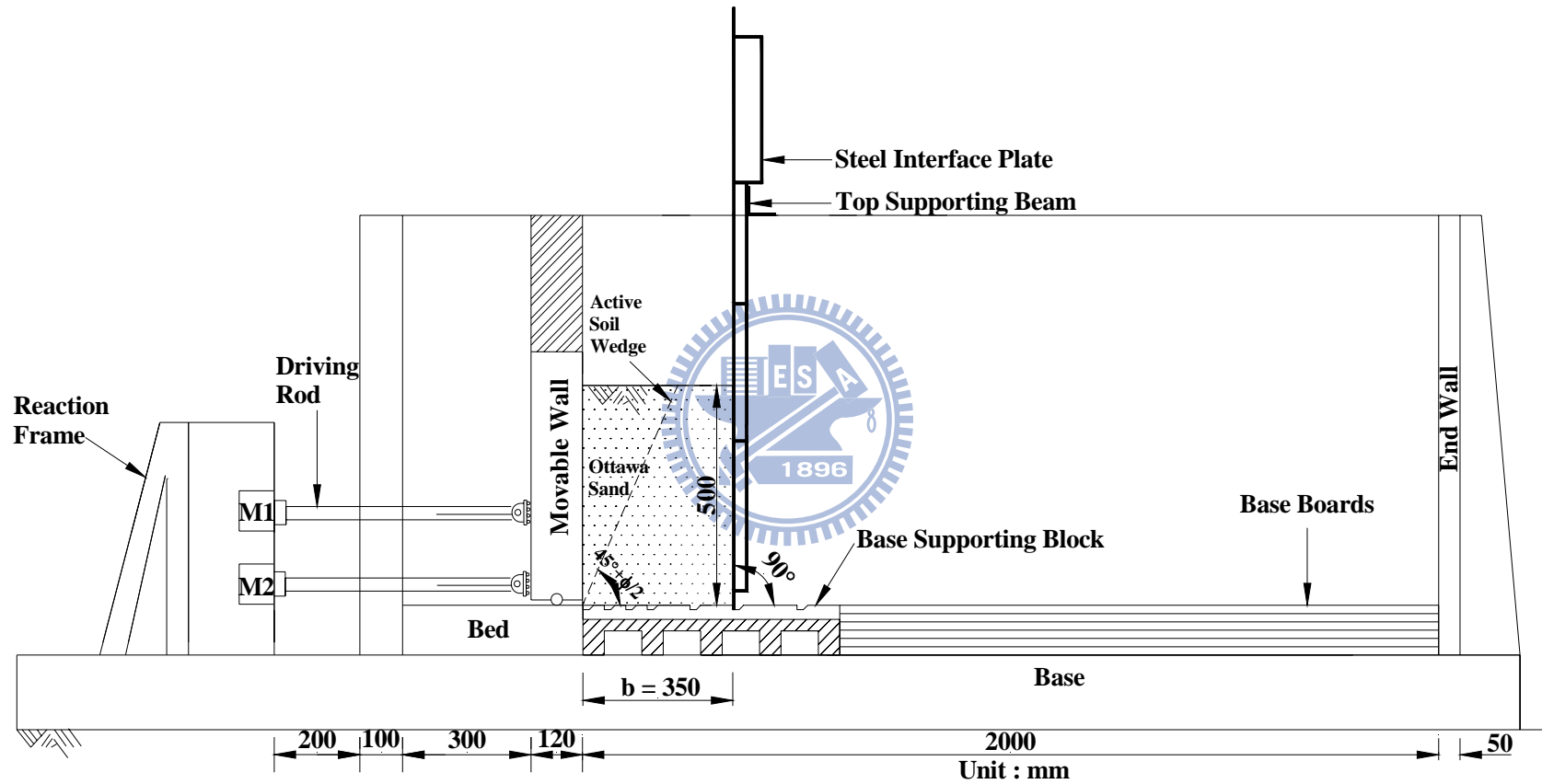

Fig. 6.62. Location of total thrust application for b = 100 mm and   β = 90°
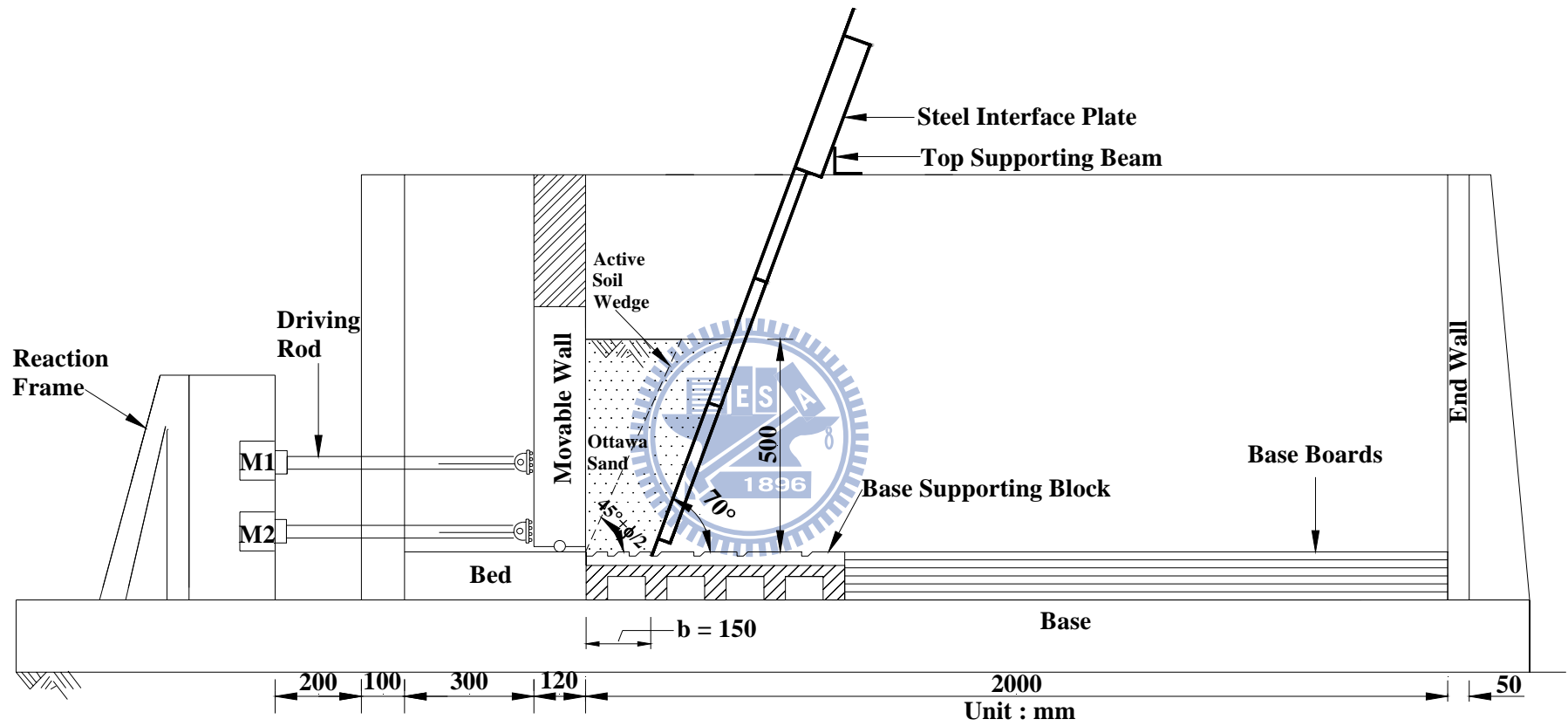
(a)

Fig. 6.63. Model wall test with interface inclination β = 70° and b = 150 mm
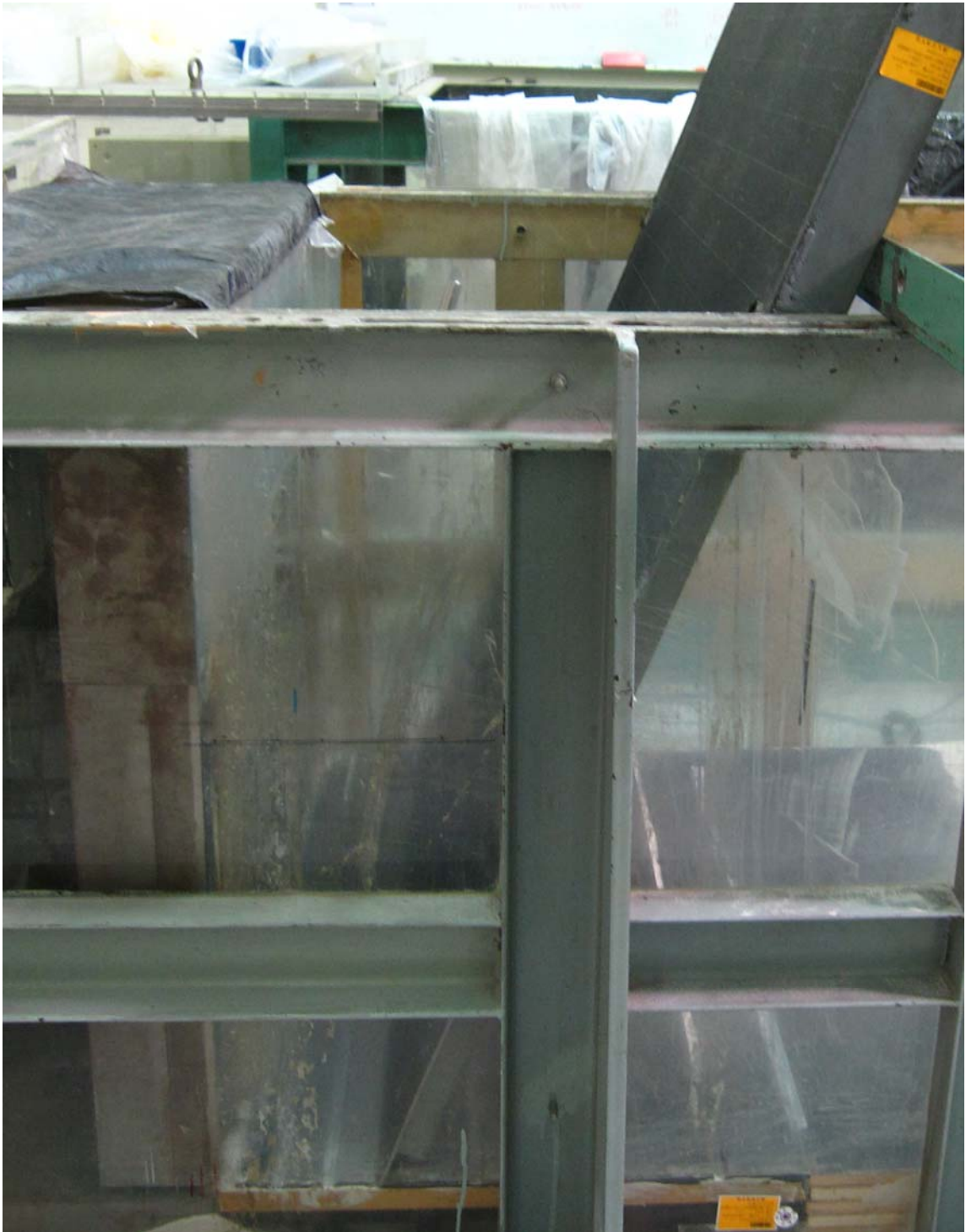
(b)

Fig. 6.63. Model wall test with interface inclination β = 70° and b = 150 mm

Fig. 6.64. Distribution of horizontal earth pressure for
b = 150 mm and β = 70° (Test 0708-1)
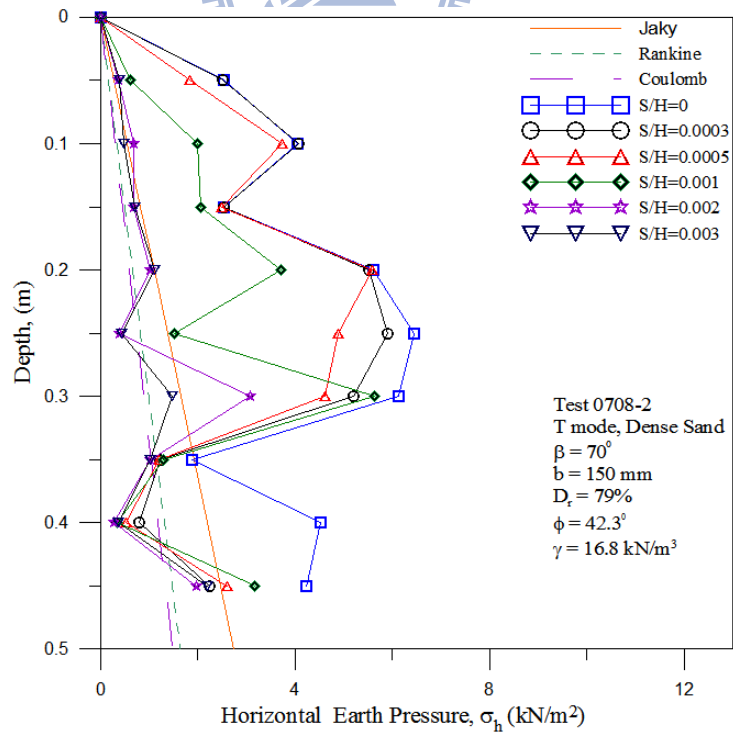
Fig. 6.65. Distribution of horizontal earth pressure for
b = 150 mm and β = 70° (Test 0708-2)

190
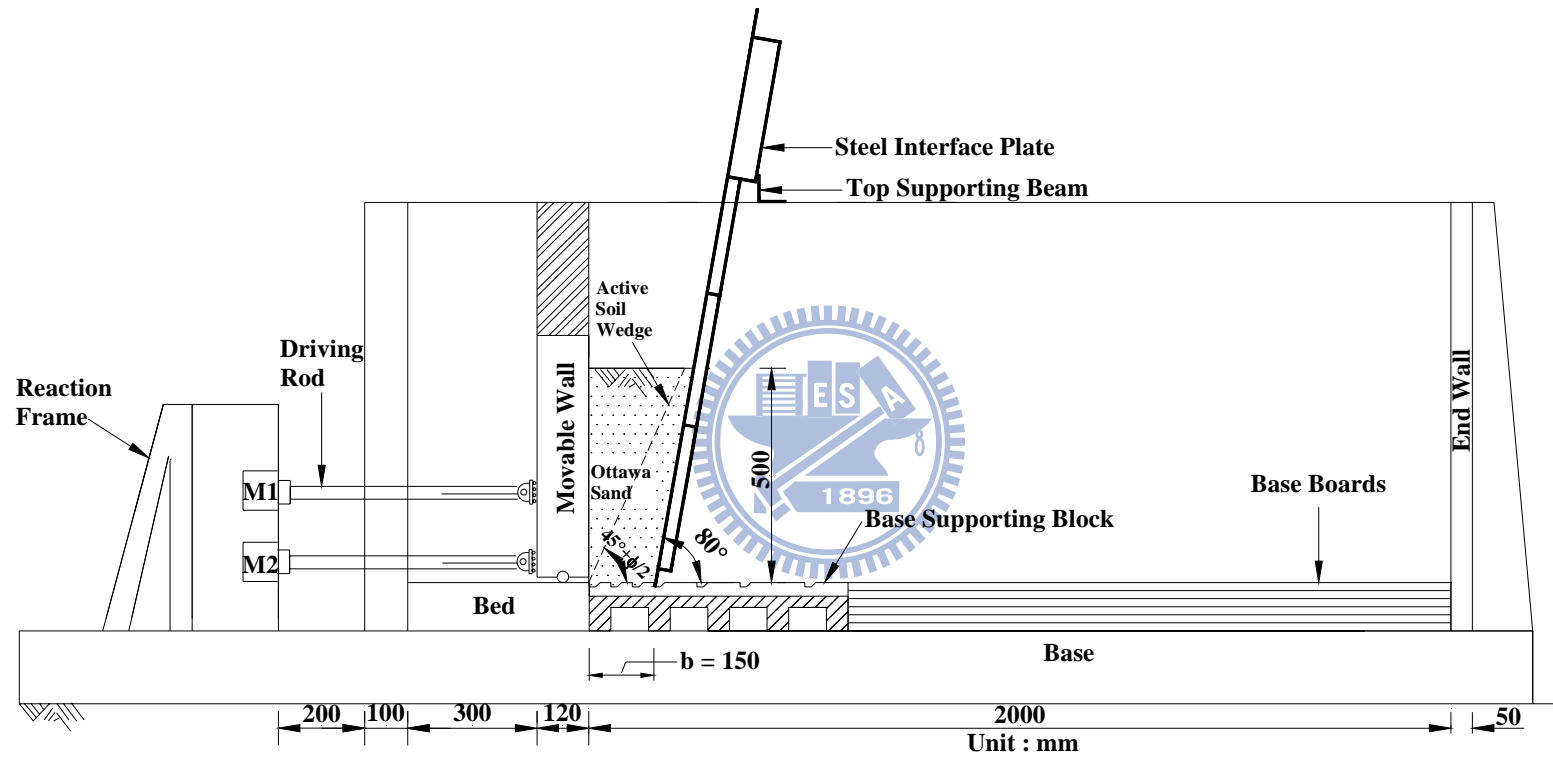
(a)

Fig. 6.66. Model wall test with interface inclination β = 80° and b = 150 mm

191

(b)

Fig. 6.66. Model wall test with interface inclination β = 80° and b = 150 mm
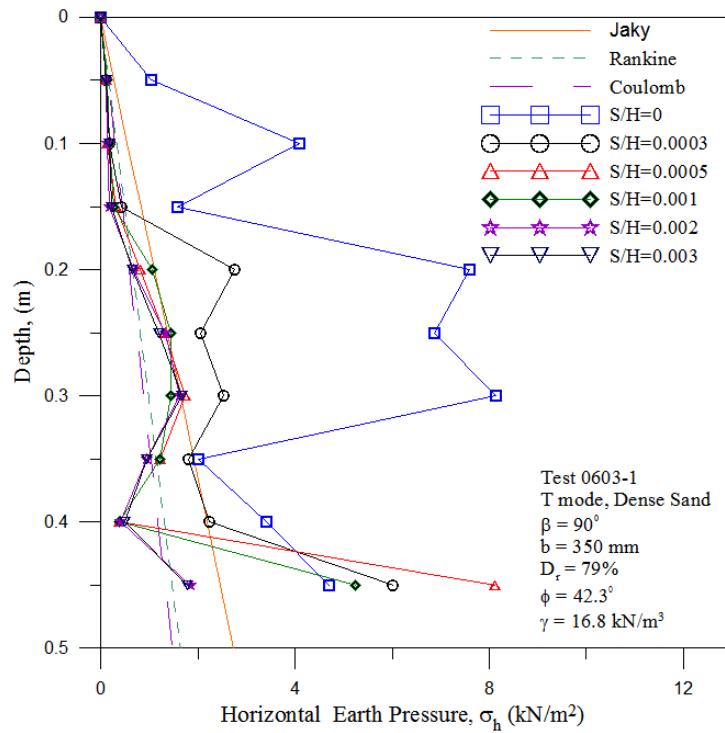
Fig. 6.67. Distribution of horizontal earth pressure for
b = 150 mm and β = 80° (Test 0702-1)
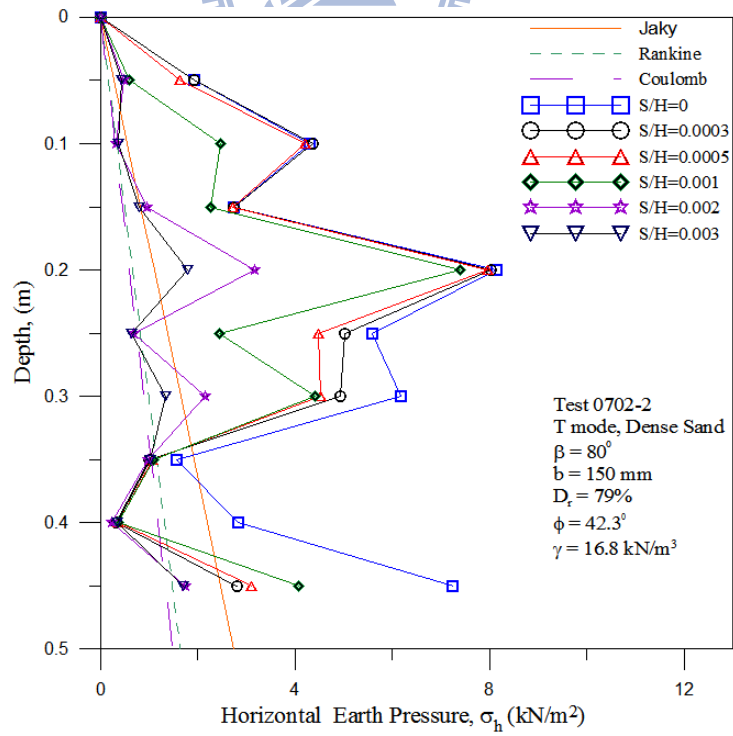
Fig. 6.68. Distribution of horizontal earth pressure for
b = 150 mm and β = 80° (Test 0702-2)
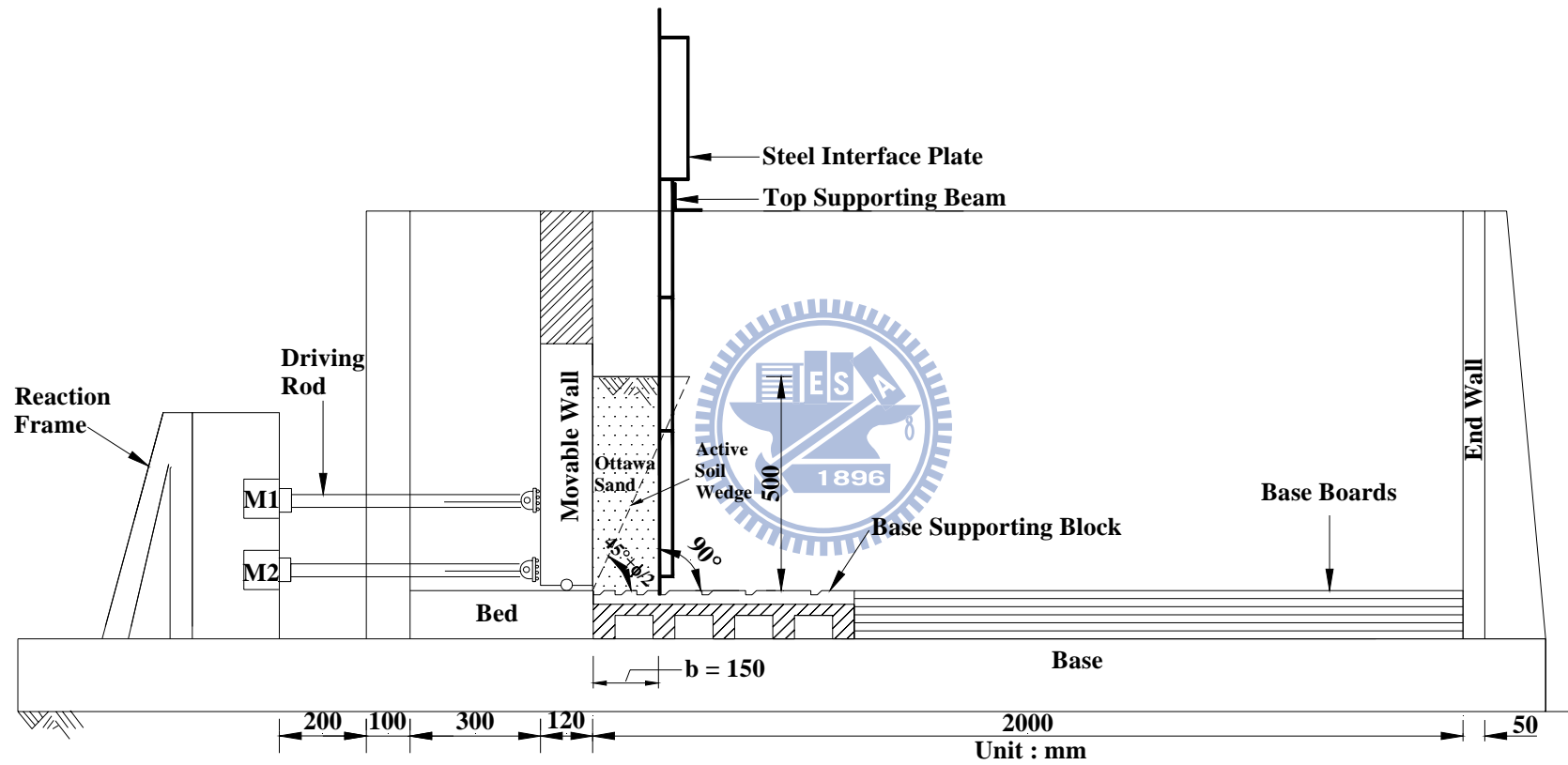
193

(a)

Fig. 6.69. Model wall test with interface inclination β = 90° and b = 150 mm

194

(b)

Fig. 6.69. Model wall test with interface inclination β = 90° and b = 150 mm

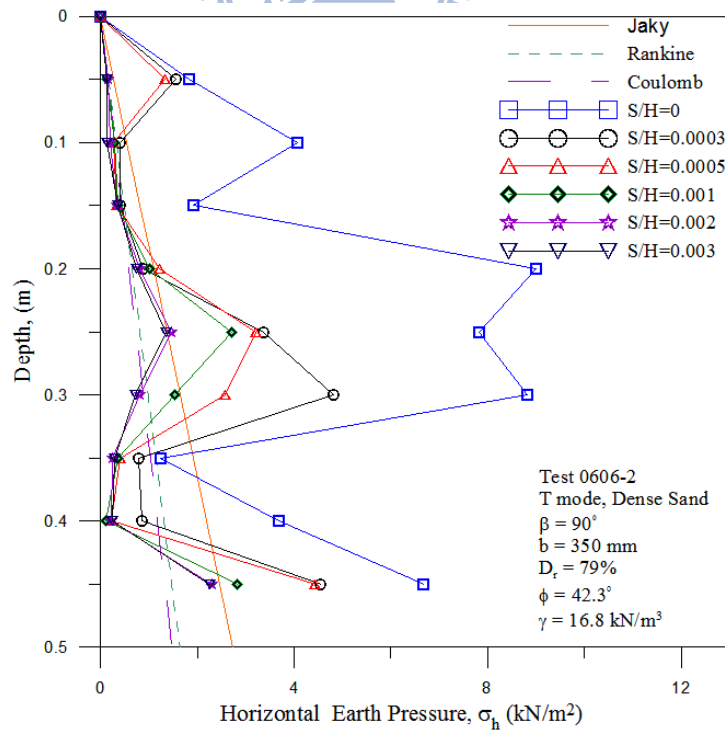Fig. 6.70. Distribution of horizontal earth pressure for
b = 150 mm and β = 90° (Test 0627-2)

Fig. 6.71. Distribution of horizontal earth pressure for
b = 150 mm and β = 90° (Test 0628-2)
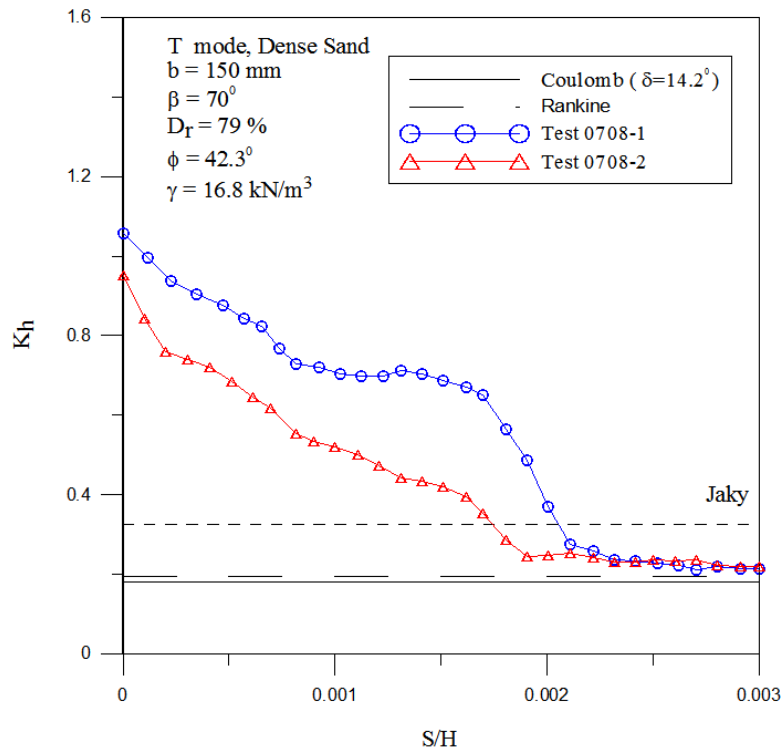
Fig. 6.72. Earth pressure coefficient K_h versus wall movement for
b = 150 mm and β = 70°

Fig. 6.73. Earth pressure coefficient K_h versus wall movement for
b = 150 mm and β = 80°

Fig. 6.74. Earth pressure coefficient K_h versus wall movement for
b = 150 mm and β = 90°
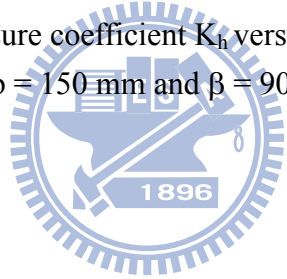
Fig. 6.75. Location of total thrust application for b = 150 mm and β = 70°

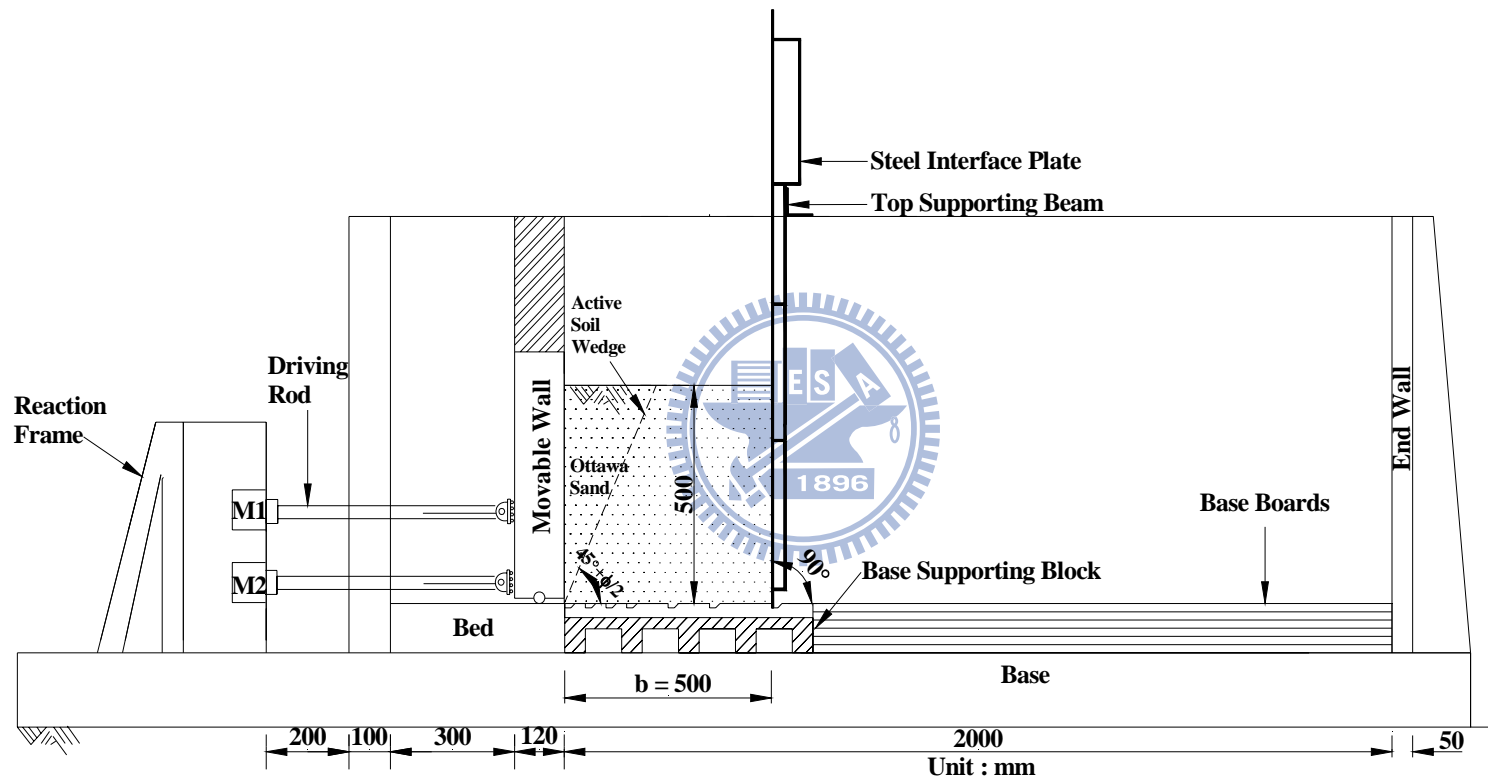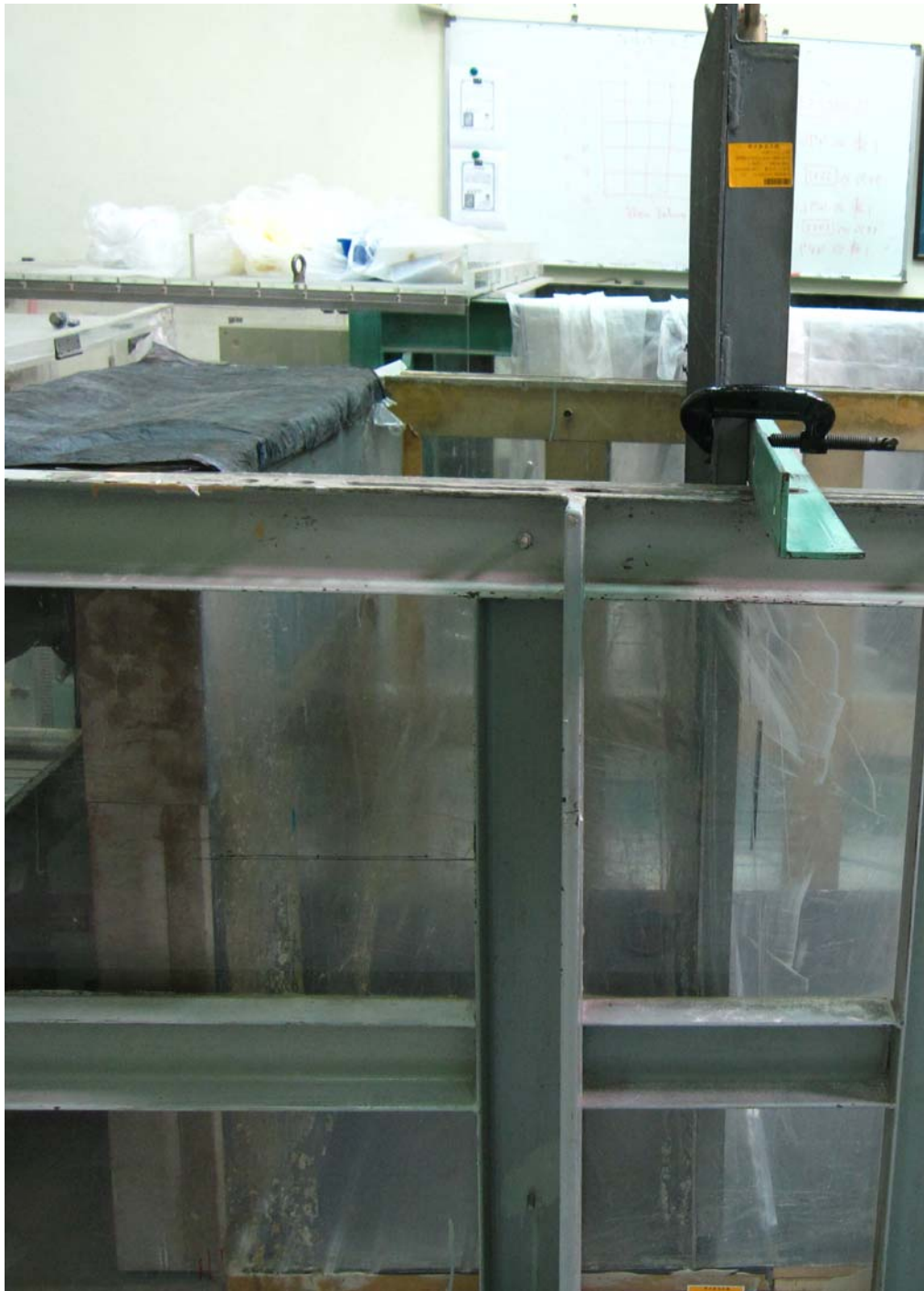Fig. 6.76. Location of total thrust application for b = 150 mm and β = 80°

199

Fig. 6.77. Location of total thrust application for b = 150 mm and β = 90°
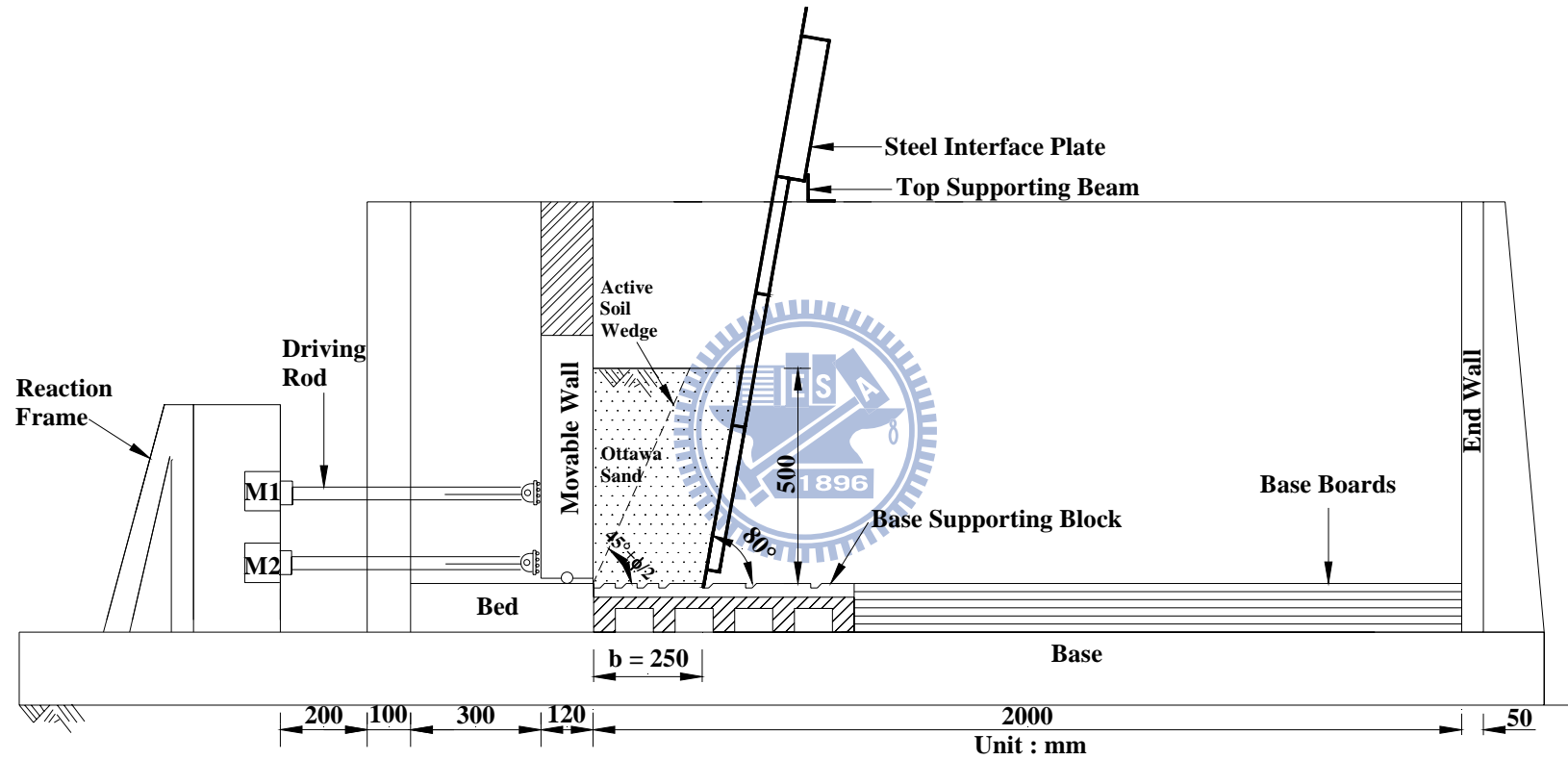
(a)

Fig. 6.78. Model wall test with interface inclination β = 80° and b = 250 mm

(b)

Fig. 6.78. Model wall test with interface inclination β = 80° and b = 250 mm

Fig. 6.79. Distribution of horizontal earth pressure for
b = 250 mm and β = 80° (Test 0621-2)
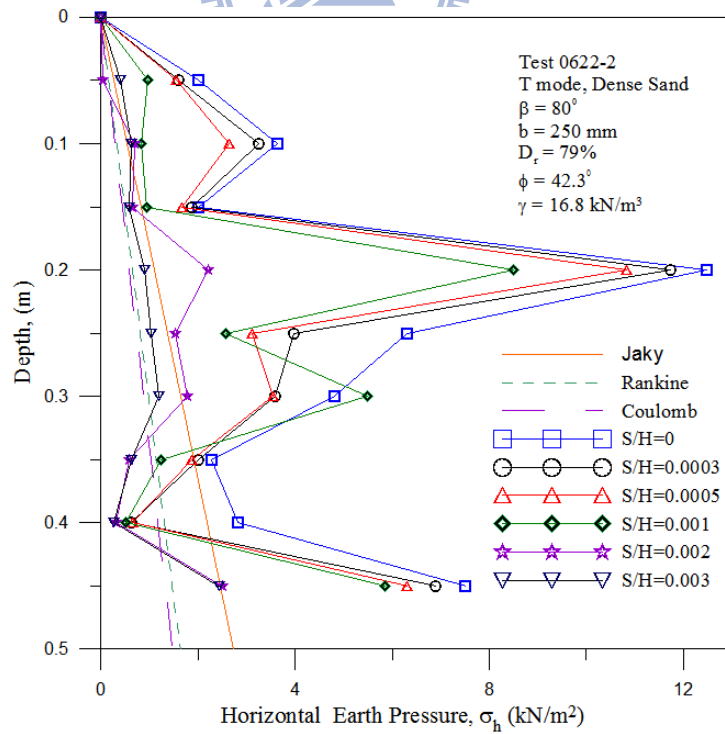
Fig. 6.80. Distribution of horizontal earth pressure for
b = 250 mm and β = 80° (Test 0622-2)
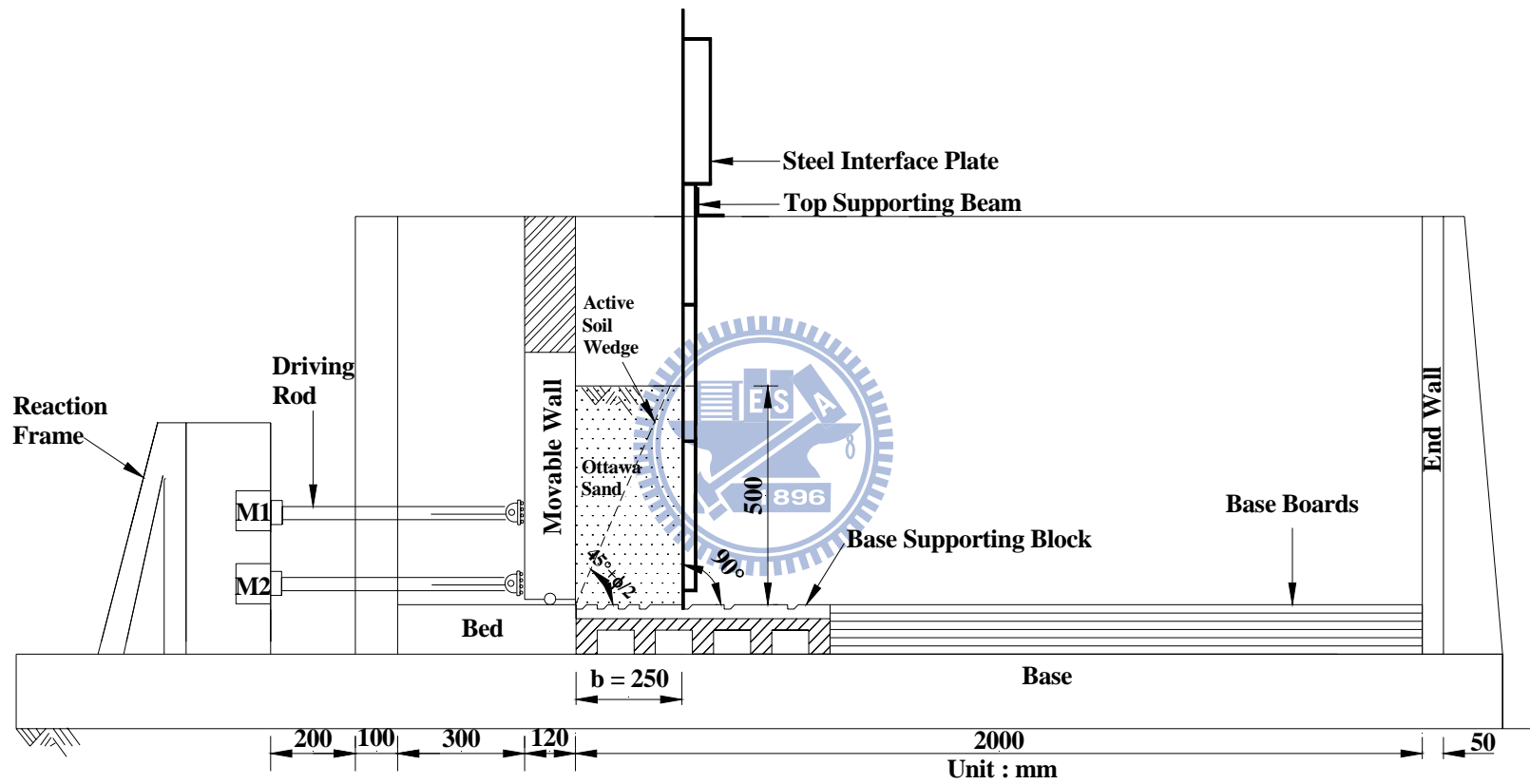
(a)

Fig. 6.81. Model wall test with interface inclination β = 90° and b = 250 mm

(b)

Fig. 6.81. Model wall test with interface inclination β = 90° and b = 250 mm
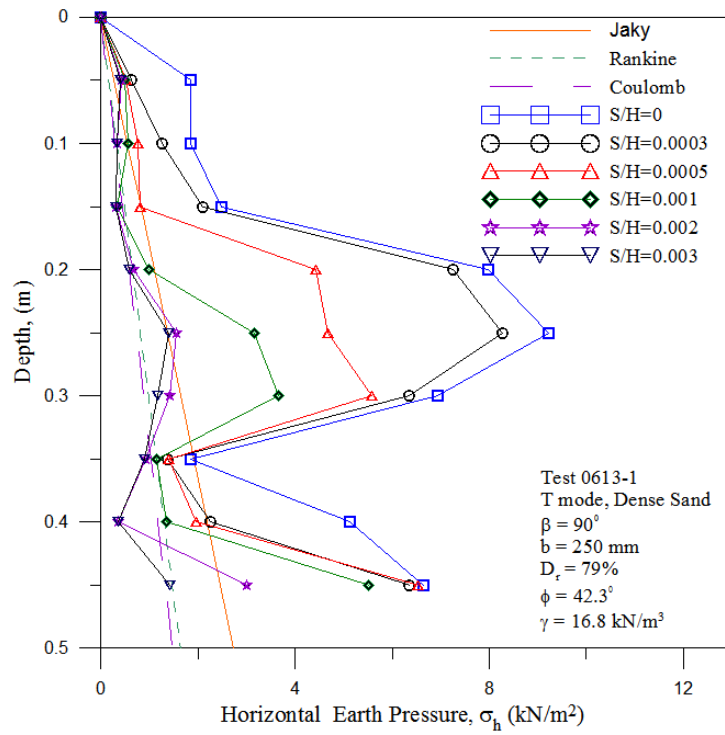
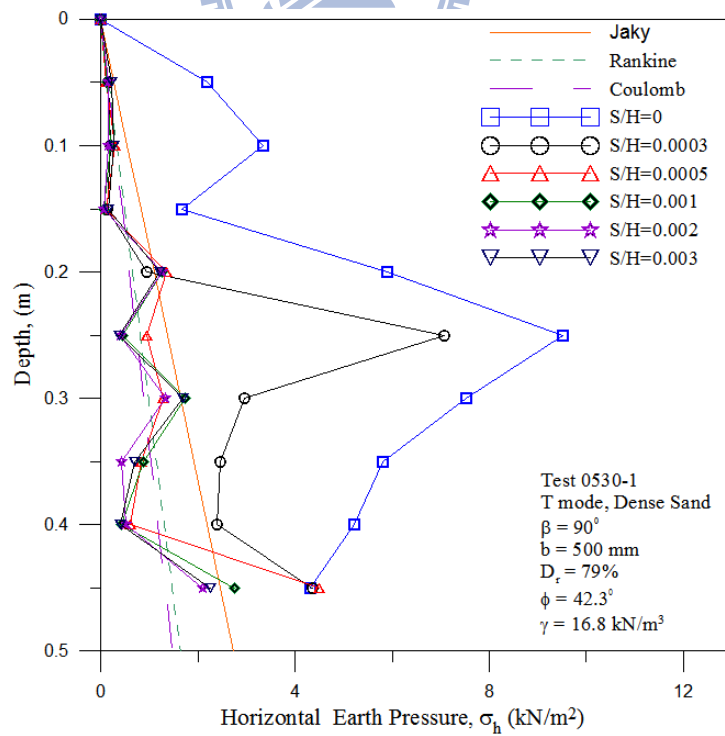Fig. 6.82. Distribution of horizontal earth pressure for
b = 250 mm and β = 90° (Test 0613-1)

Fig. 6.83. Distribution of horizontal earth pressure for
b = 250 mm and β = 90° (Test 0615-1)

Fig. 6.84. Earth pressure coefficient K_h versus wall movement for
b = 250 mm and β = 80°

Fig. 6.85. Earth pressure coefficient K_h versus wall movement for
b = 250 mm and β = 90°

207

Fig. 6.86. Location of total thrust application for b = 250 mm and β = 80°

Fig. 6.87. Location of total thrust application for b = 250 mm and β = 90°

208

Labels in figure:
- Steel Interface Plate
- Top Supporting Beam
- Reaction Frame
- Driving Rod
- Active Soil Wedge
- Movable Wall
- Ottawa Sand
- End Wall
- Base Boards
- Base Supporting Block
- Bed
- Base
- M1
- M2
- 500
- $45° + \phi/2$
- 90°
- b = 350
- 200
- 100
- 300
- 120
- 2000
- 50
- Unit : mm

(a)

Fig. 6.88. Model wall test with interface inclination β = 90° and b = 350 mm

(b)

Fig. 6.88. Model wall test with interface inclination β = 90° and b = 350 mm

Fig. 6.89. Distribution of horizontal earth pressure for
b = 350 mm and β = 90° (Test 0603-1)

Fig. 6.90. Distribution of horizontal earth pressure for
b = 350 mm and β = 90° (Test 0603-2)
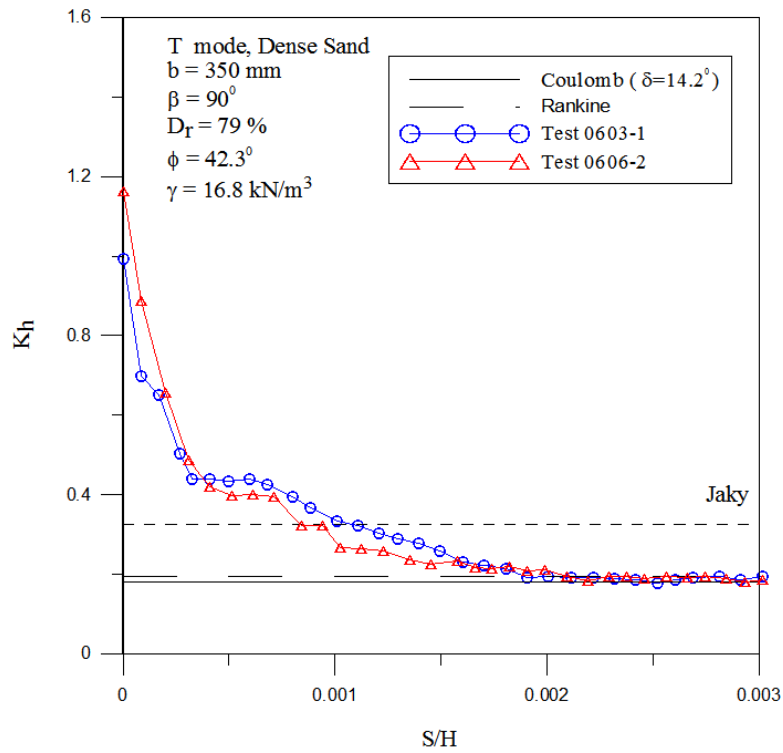
Fig. 6.91. Earth pressure coefficient K_h versus wall movement for
b = 350 mm and β = 90°
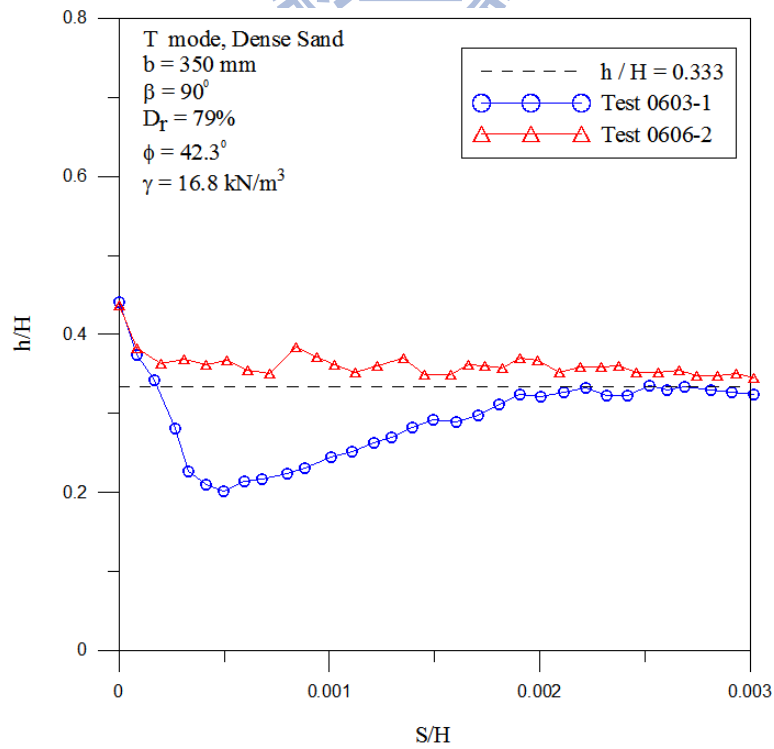
Fig. 6.92. Location of total thrust application for b = 350 mm and β = 90°

(a)

Fig. 6.93. Model wall test with interface inclination β = 90° and b = 500 mm

(b)

Fig. 6.93. Model wall test with interface inclination β = 90° and b = 500 mm
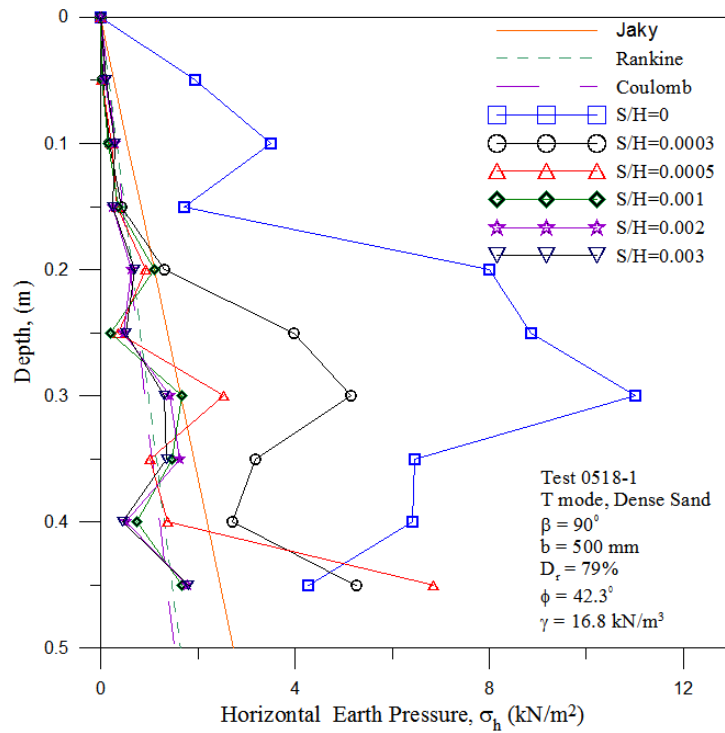
Fig. 6.94. Distribution of horizontal earth pressure for
b = 500 mm and β = 90° (Test 0518-1)

Fig. 6.95. Distribution of horizontal earth pressure for
b = 500 mm and β = 90° (Test 0530-1)
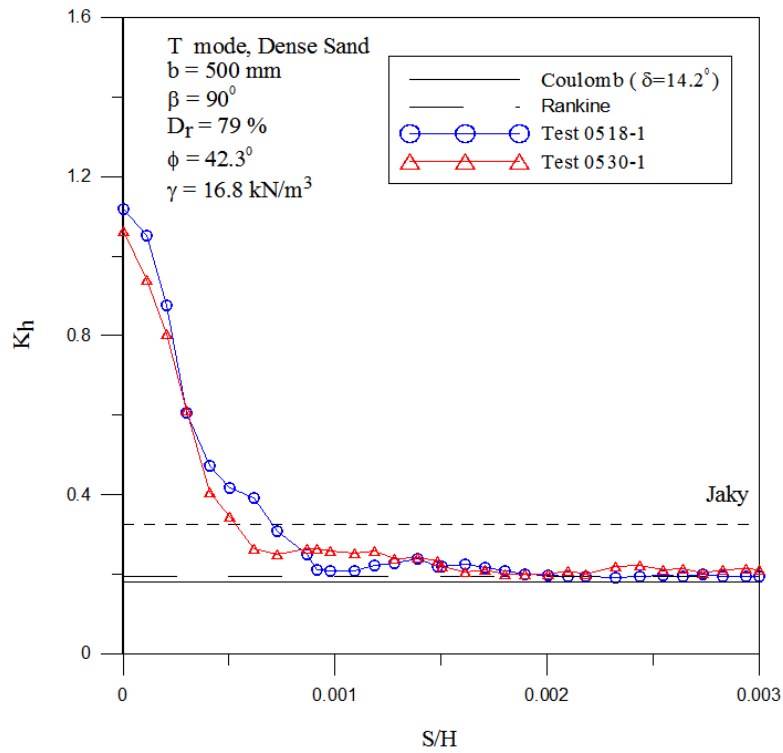
Fig. 6.96. Earth pressure coefficient K_h versus wall movement for
b = 500 mm and β = 90°
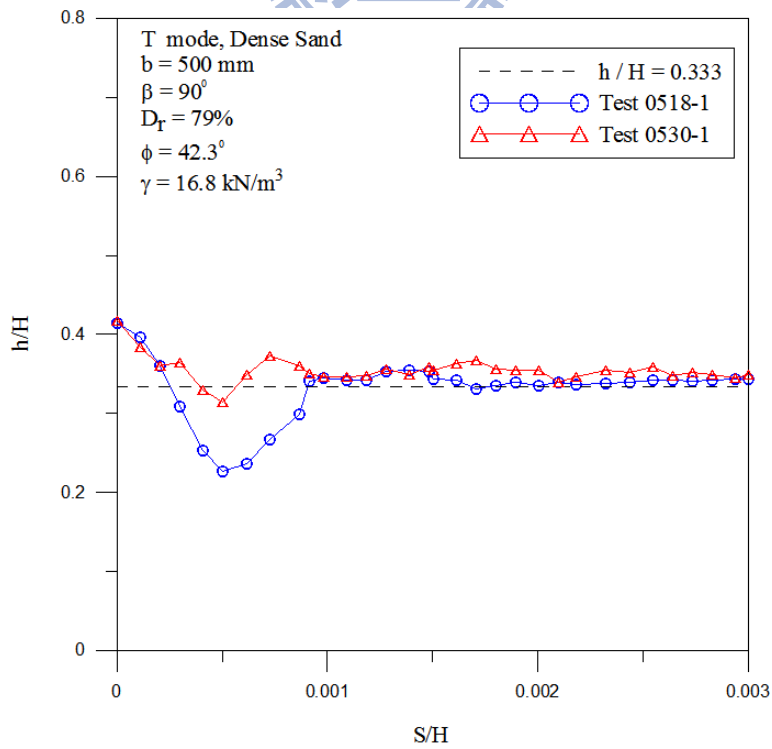
Fig. 6.97. Location of total thrust application for b = 500 mm and β = 90°

216
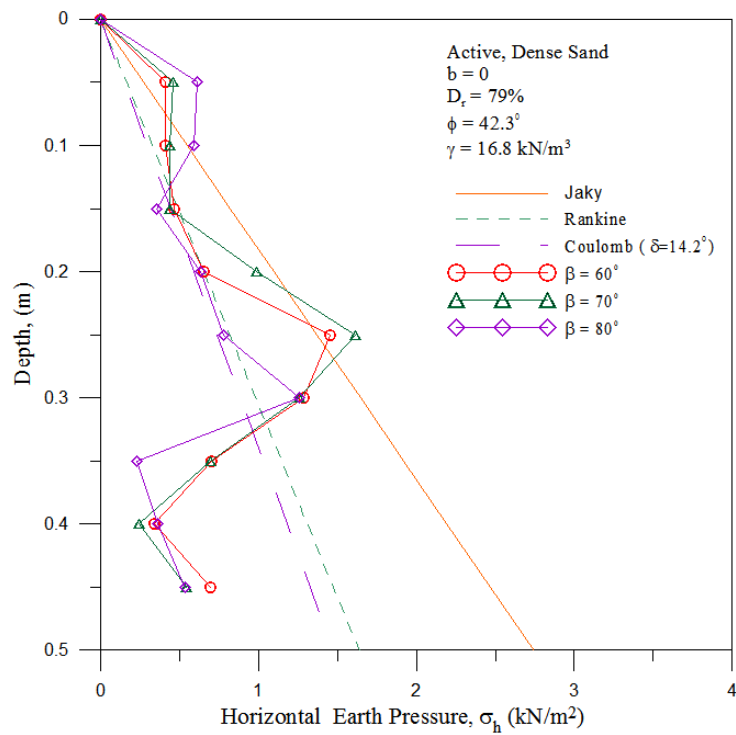
Fig. 6.98. Distribution of active earth pressure at different interface inclination angle β
for b = 0
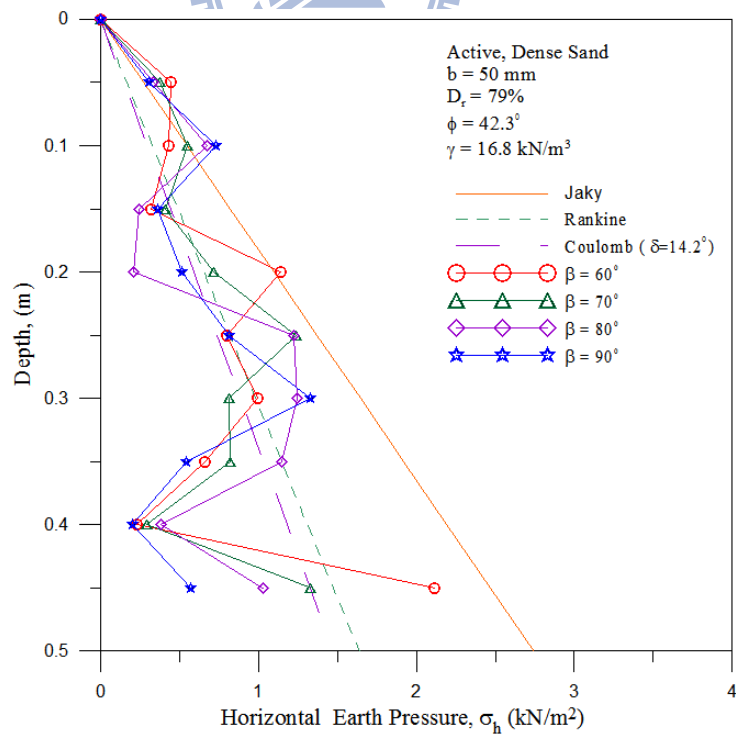
Fig. 6.99. Distribution of active earth pressure at different interface inclination angle β
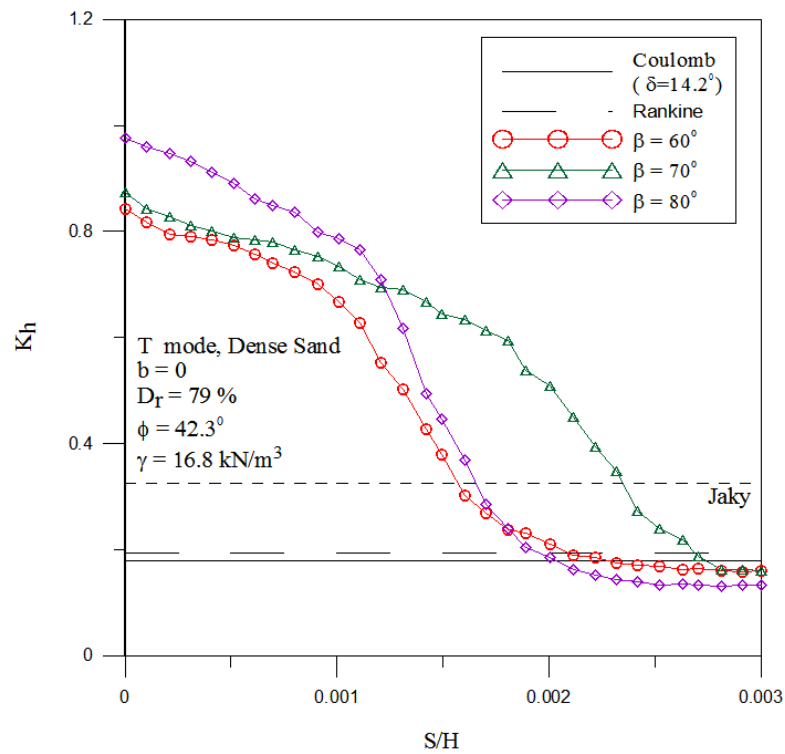for b = 50 mm
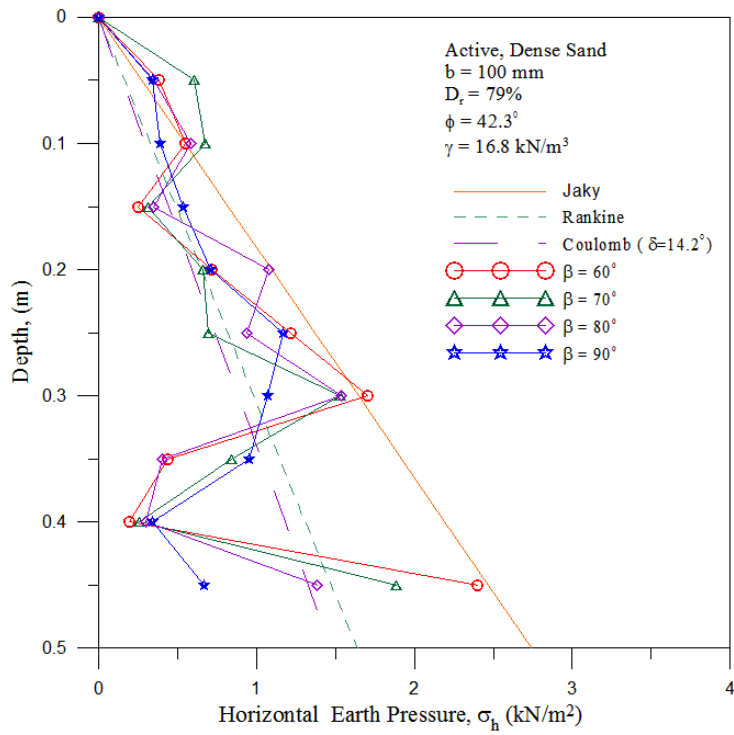
Fig. 6.100. Distribution of active earth pressure at different interface inclination angle
β for b = 100 mm
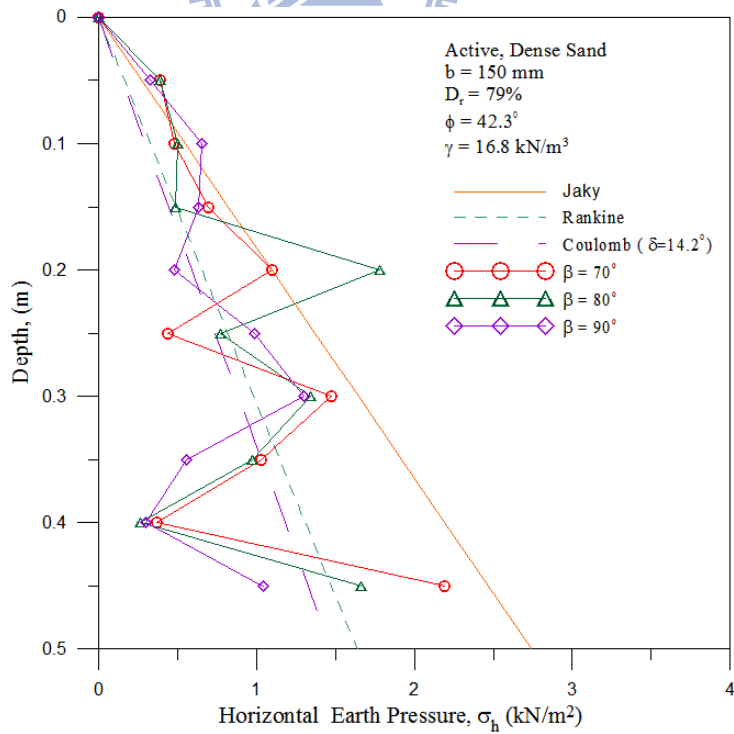
Fig. 6.101. Distribution of active earth pressure at different interface inclination angle
β for b = 150 mm

218
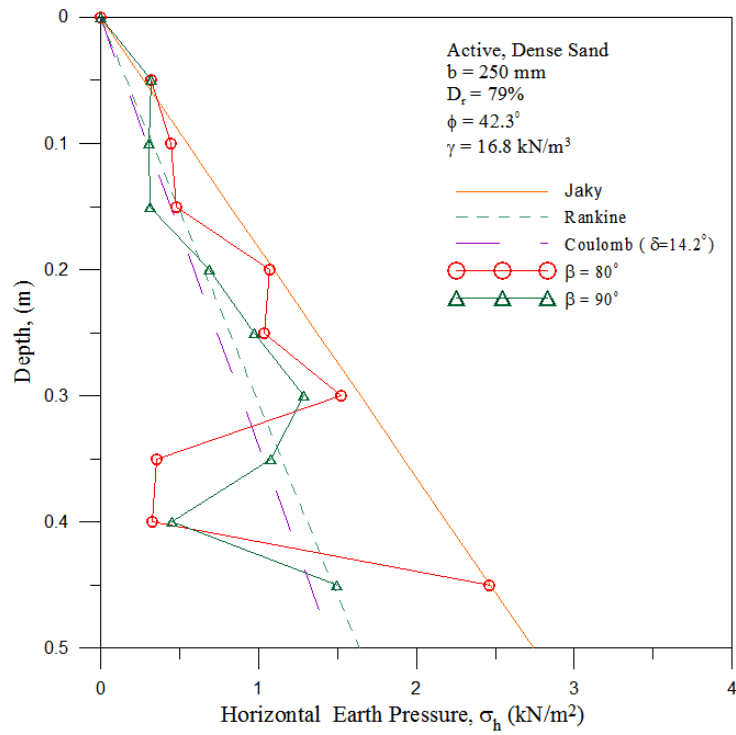
Fig. 6.102. Distribution of active earth pressure at different interface inclination angle
β for b = 250 mm
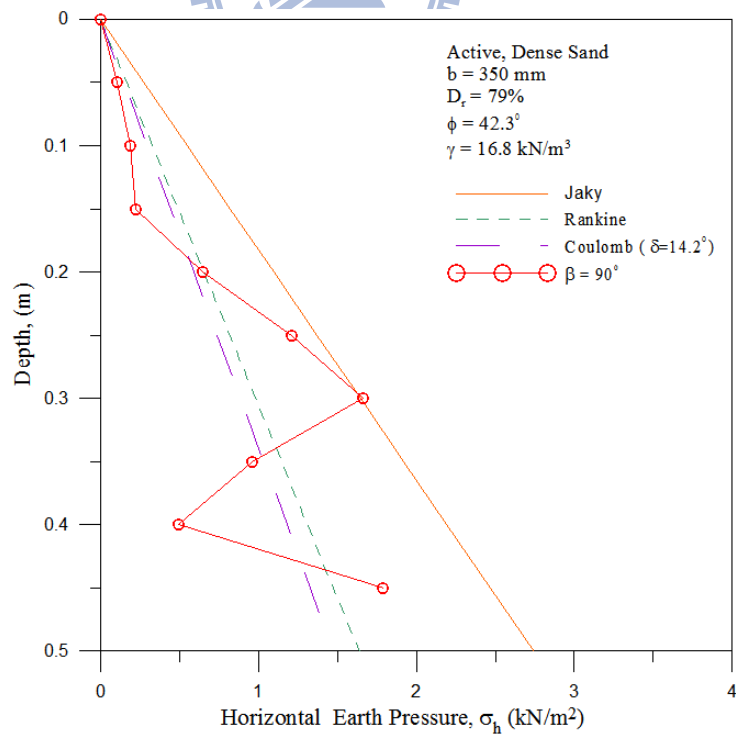
Fig. 6.103. Distribution of active earth pressure at different interface inclination angle
β for b = 350 mm
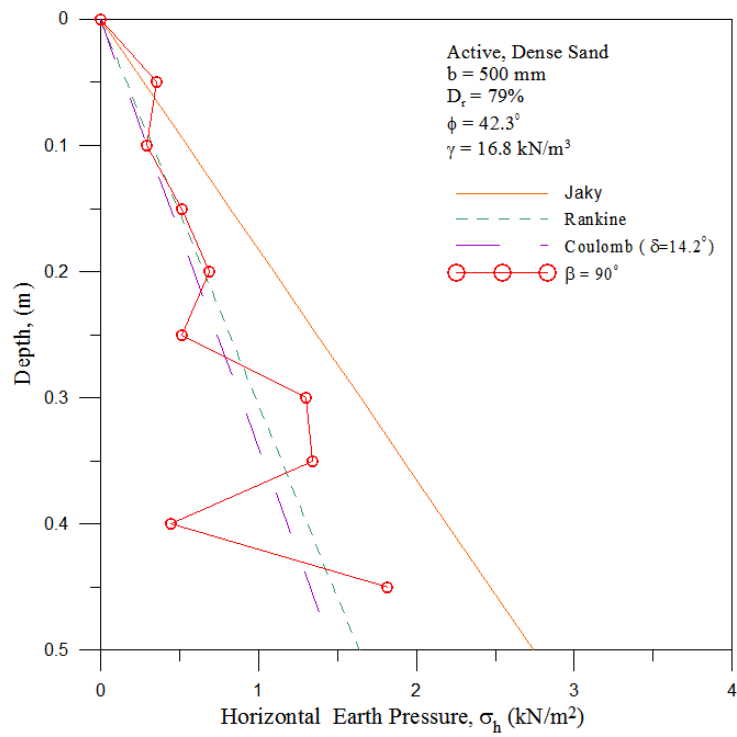
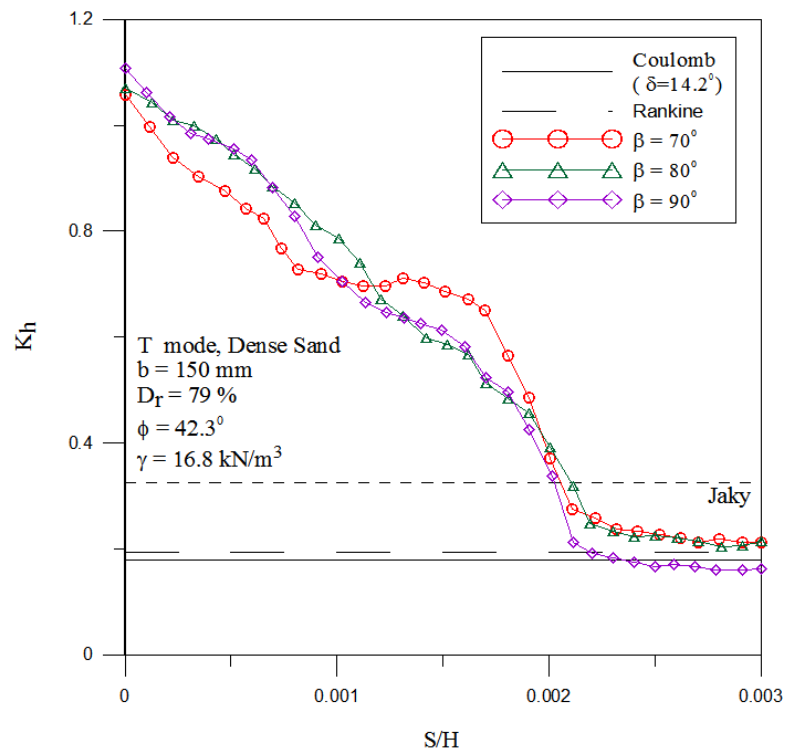Fig. 6.104. Distribution of active earth pressure at different interface inclination angle
β for b = 500 mm
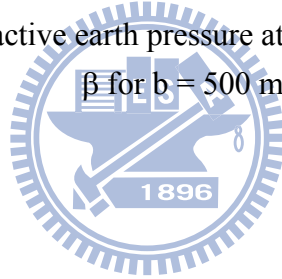
Fig. 6.105. Variation of earth pressure coefficient K_h with wall movement
for b = 0
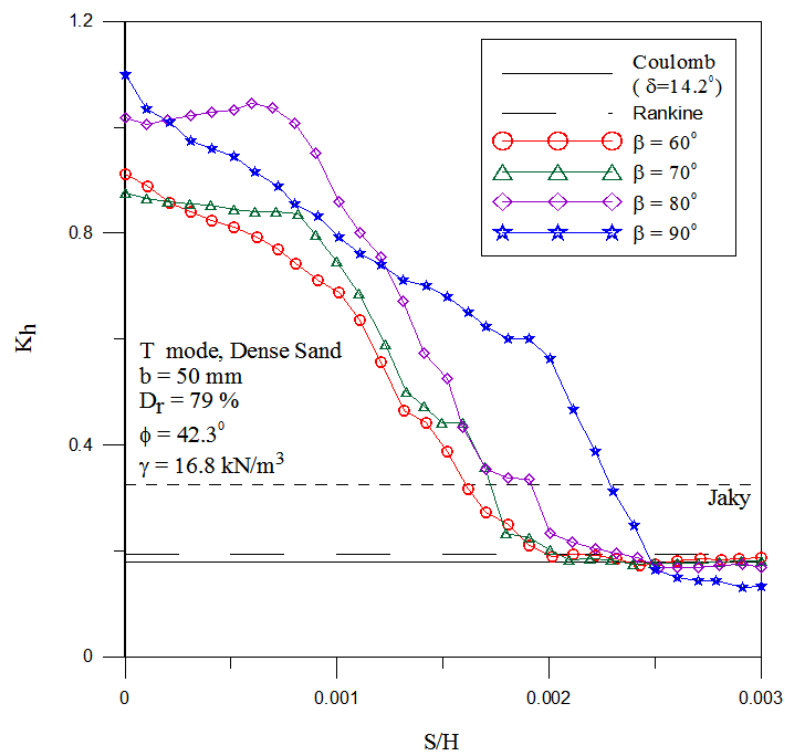
Fig. 6.106. Variation of earth pressure coefficient K_h with wall movement
for b = 50 mm

221
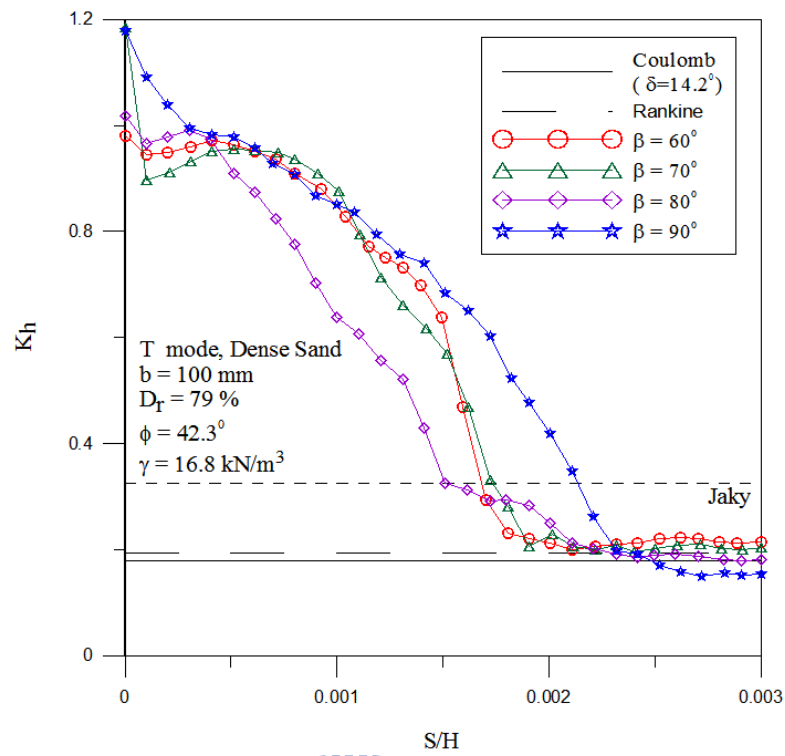
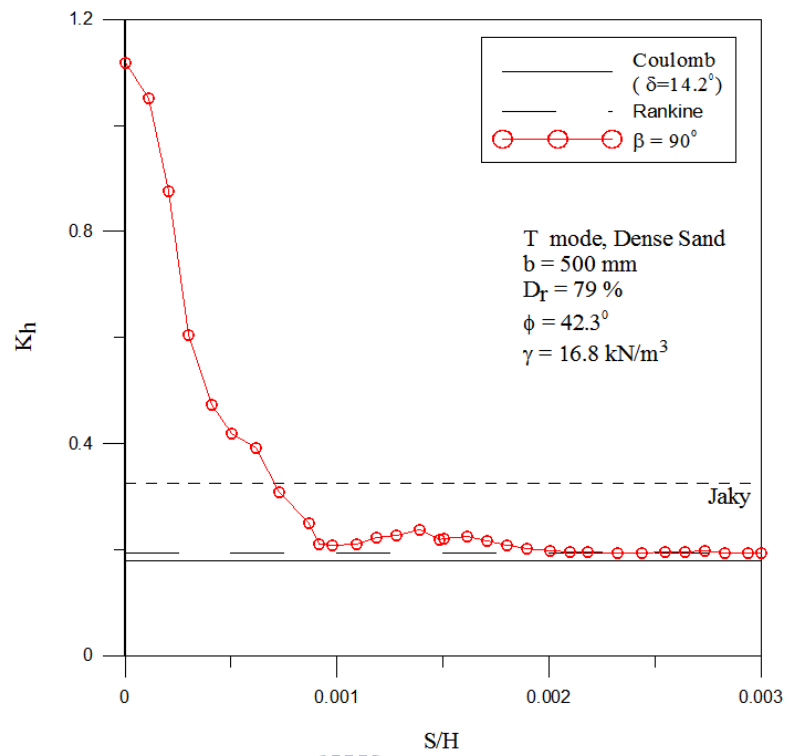Fig. 6.107. Variation of earth pressure coefficient K_h with wall movement for b = 100 mm

Fig. 6.108. Variation of earth pressure coefficient K_h with wall movement for b = 150 mm
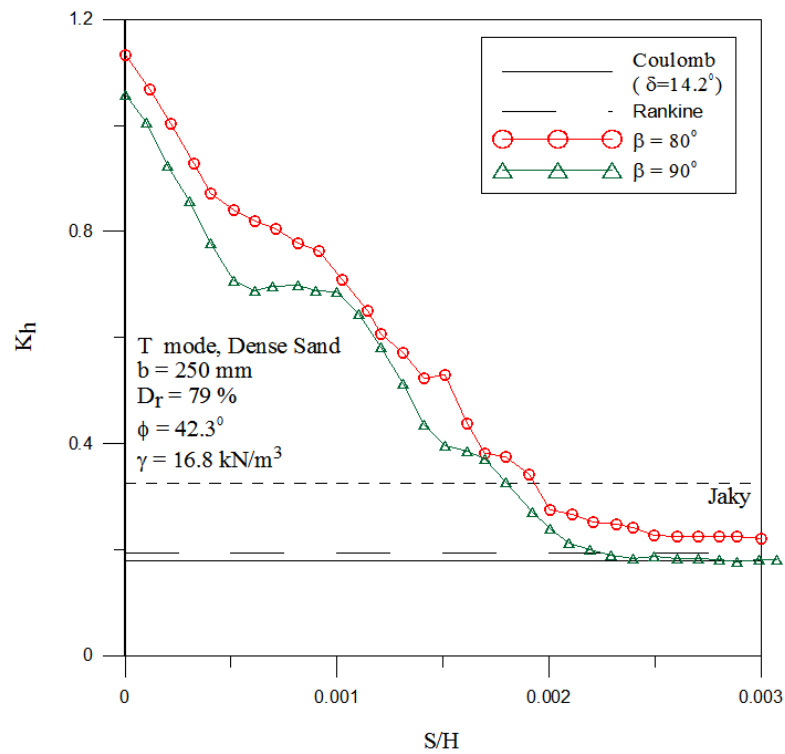
Fig. 6.109. Variation of earth pressure coefficient K_h with wall movement for b = 250 mm
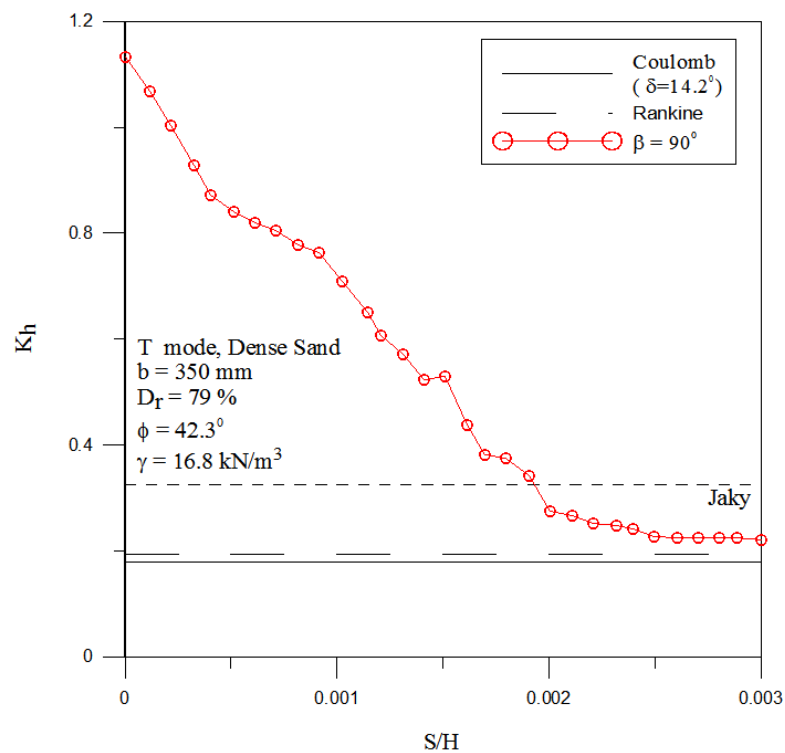
Fig. 6.110. Variation of earth pressure coefficient K_h with wall movement for b = 350 mm

223

Fig. 6.111. Variation of earth pressure coefficient K_h with wall movement
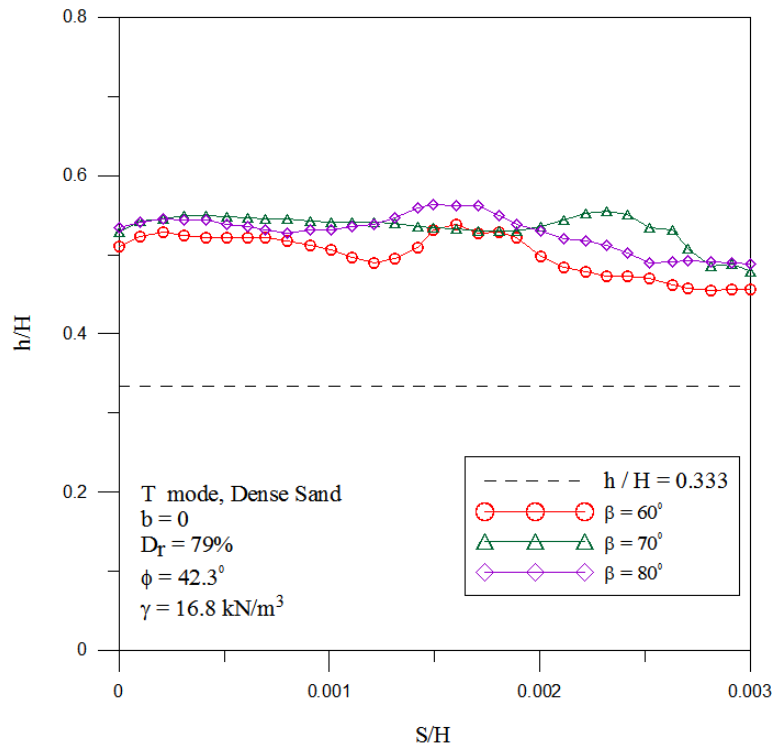for b = 500 mm
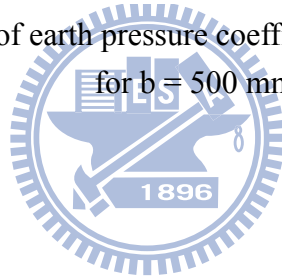
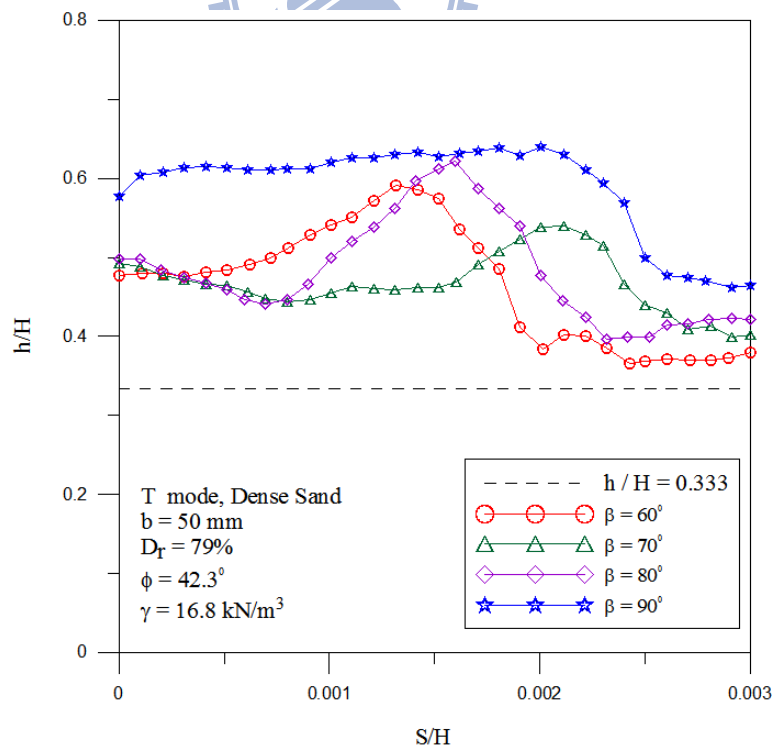Fig. 6.112. Variation of total thrust location with wall movement for
b = 0

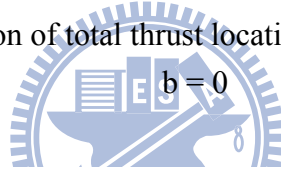

Fig. 6.113. Variation of total thrust location with wall movement for

b = 50 mm

225
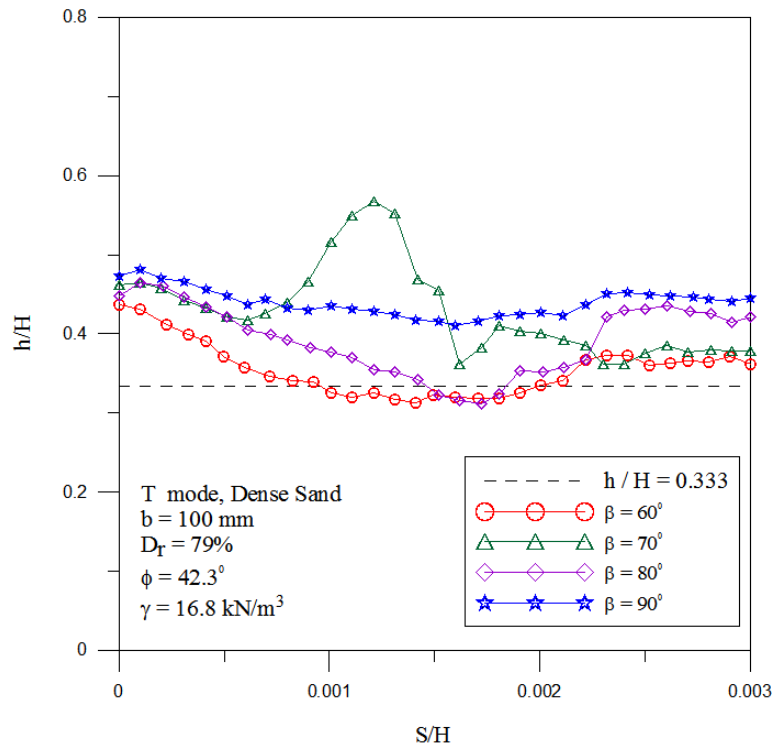
Fig. 6.114. Variation of total thrust location with wall movement for
b = 100 mm
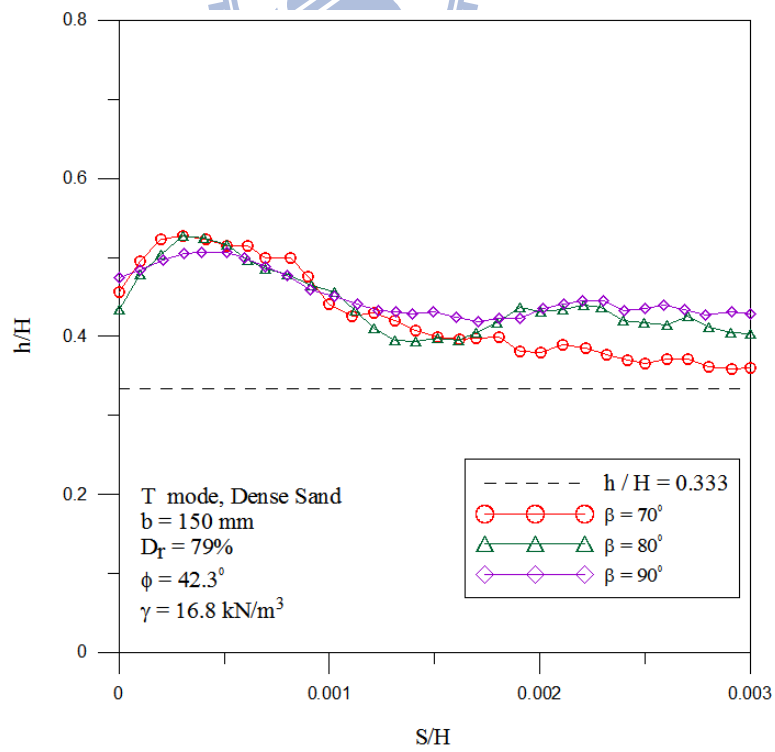

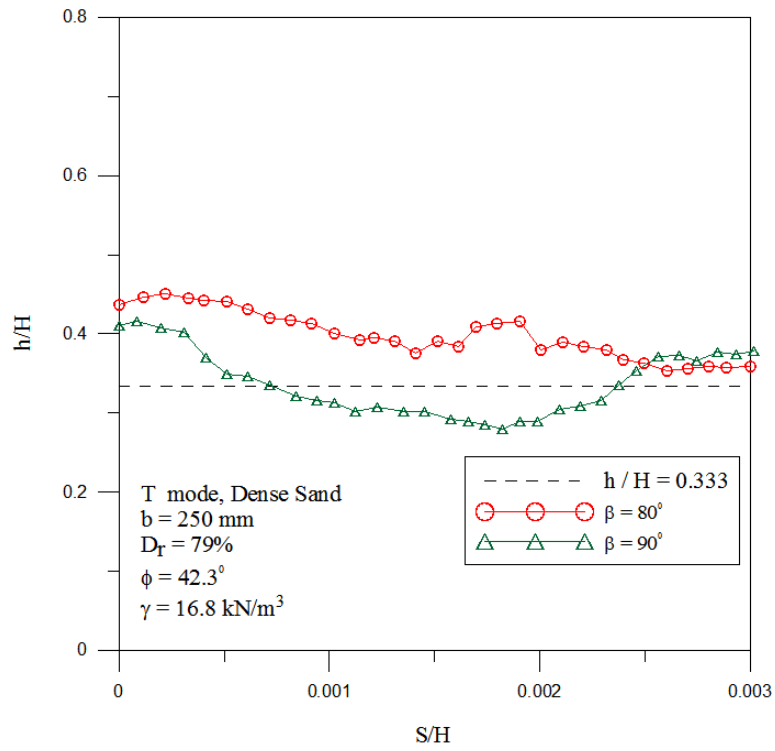Fig. 6.115. Variation of total thrust location with wall movement for
b = 150 mm

Fig. 6.116. Variation of total thrust location with wall movement for
b = 250 mm
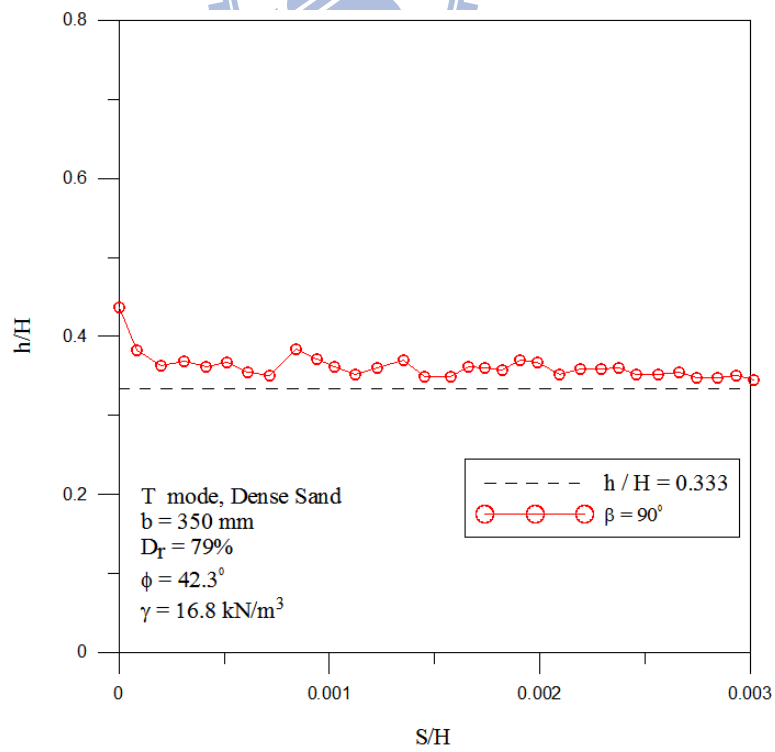

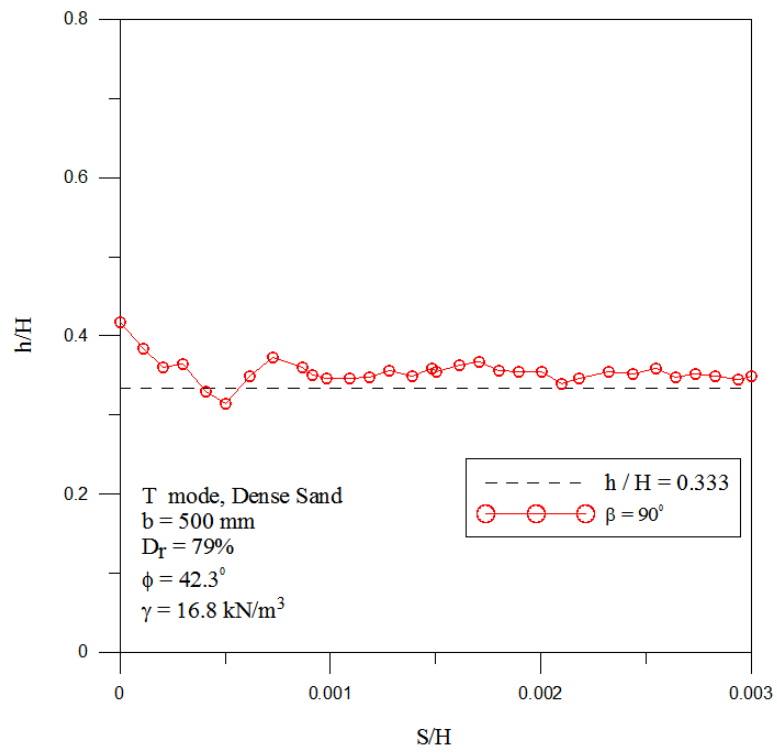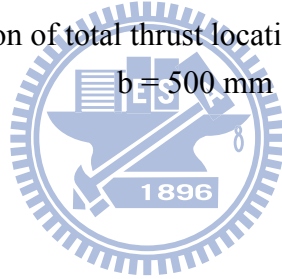Fig. 6.117. Variation of total thrust location with wall movement for
b = 350 mm

Fig. 6.118. Variation of total thrust location with wall movement for
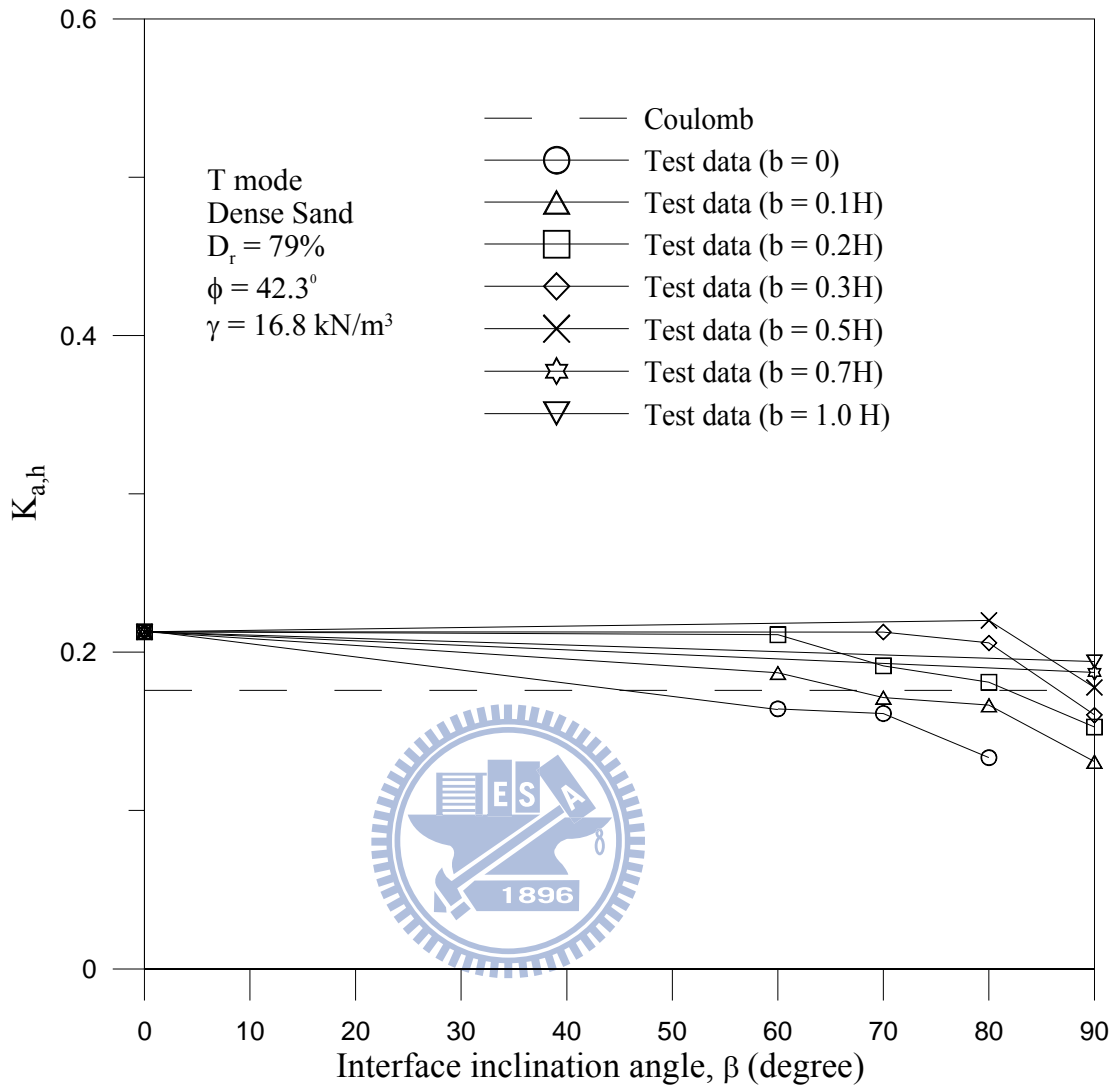b = 500 mm

Fig. 6.119. Variation of $K_{a,h}$ versus β angle
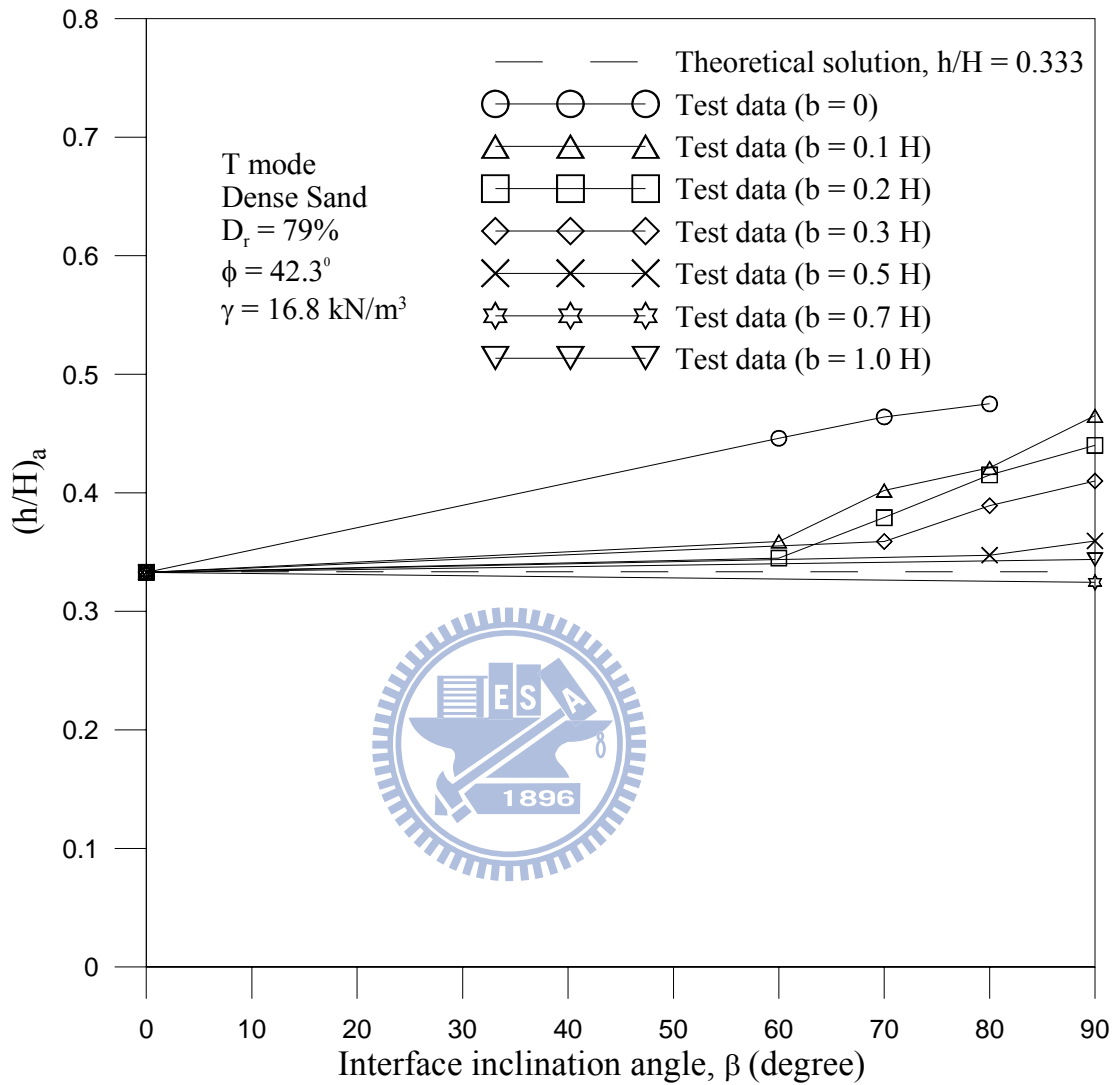
Fig. 6.120. Variation of $(h/H)_a$ versus β angle
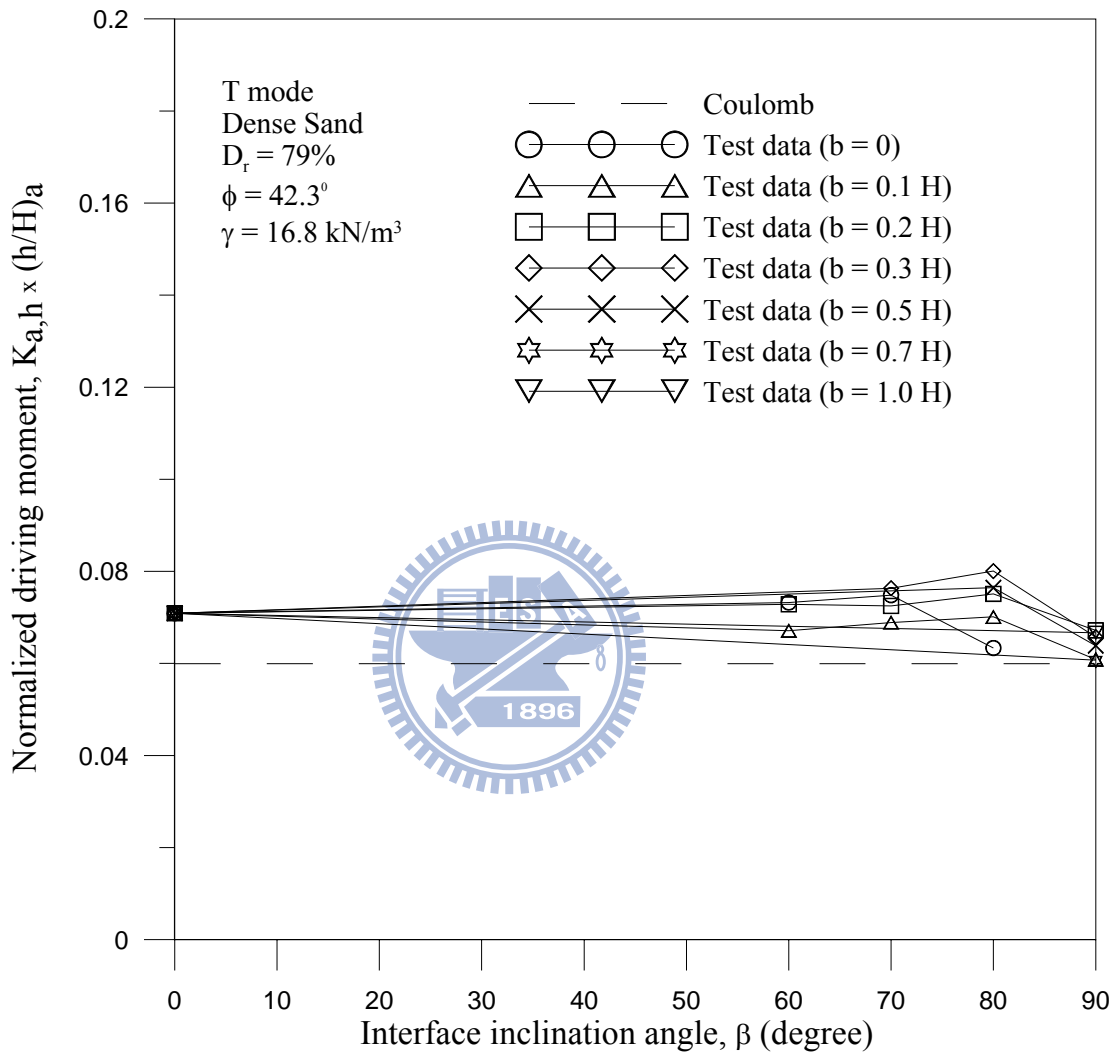
Fig. 6.121. Normalized overturning monent versus β angle
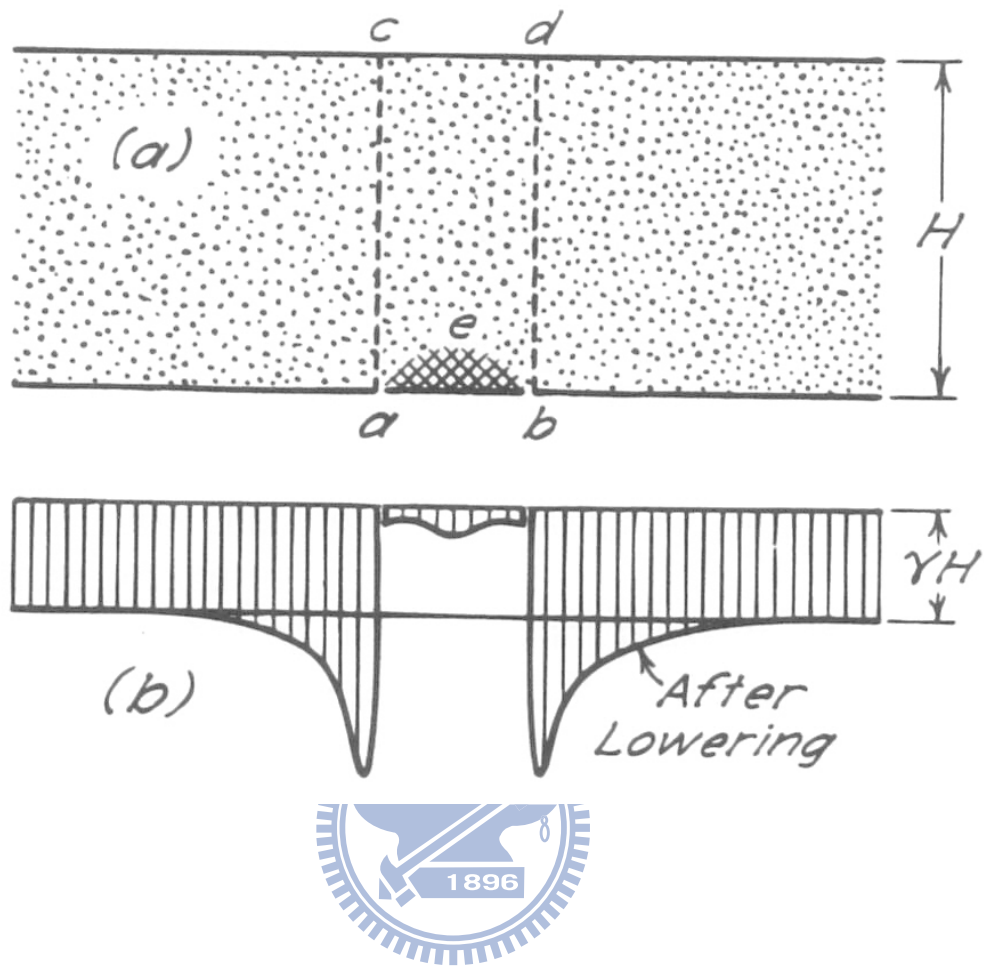
Fig. 6.122. (a) Apparatus for investigating arching in layer of sand above yielding

trap door in horizontal platform; (b) pressure on platform and trap door

before and after slight lowering of door

Wall Movement

Steel Interface Plate

σ_v'

σ'

σ'

σ_v'

σ'

σ'

Movable Wall

Backfill

Arching of Soil Particle

Generated Space

Fig. 6.123. Soil arching at two levels in cohesionless backfill

Appendix A:

Calibration of Soil Pressure Transducers

To investigate the lateral earth pressure acting on the model retaining wall, nine strain-gage type soil pressure transducers 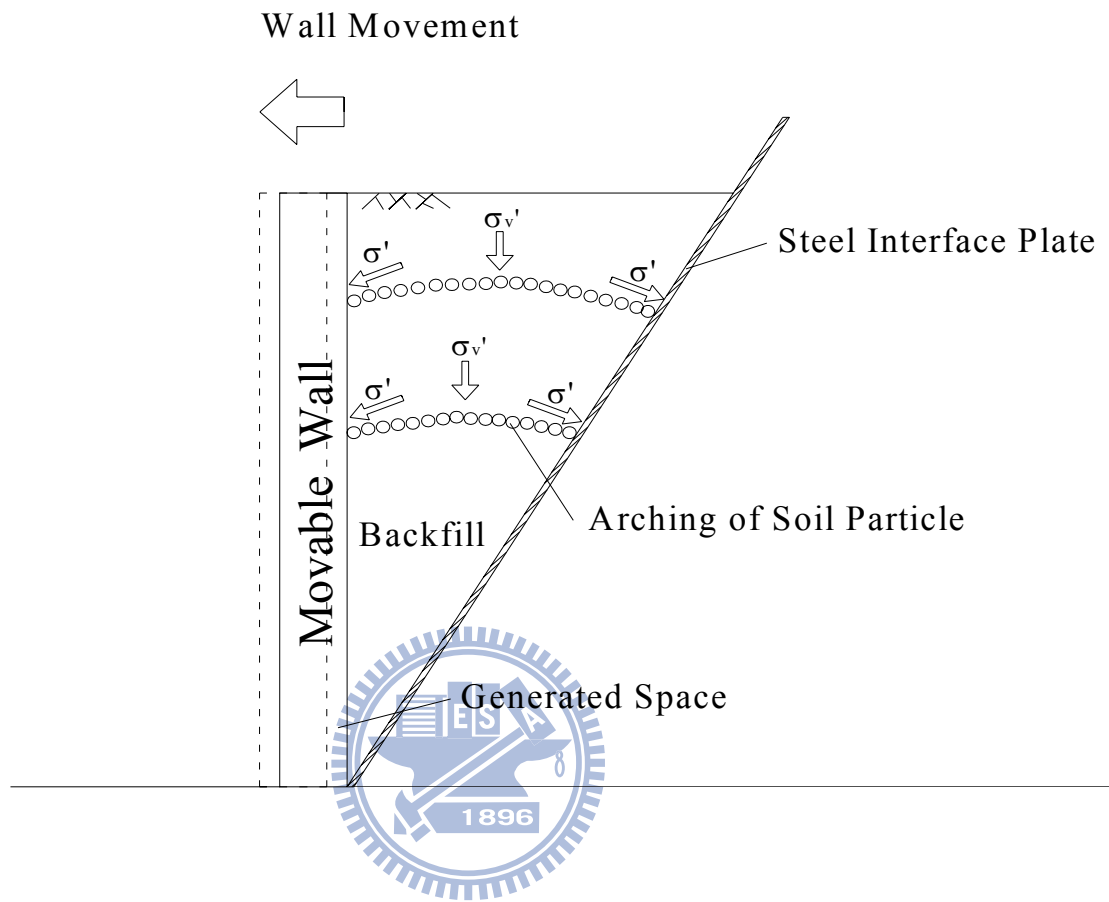(SPT) were used. The transducers PGM-02KG manufactured by KYOWA are installed on the surface of model retaining wall to measure the lateral earth pressure against the retaining wall. The pressure acts between soil particles and the transducer is quite different from the pressure that acts between liquid and transducer. It is necessary to calibrate the soil pressure transducer in an environment similar to that of the actual testing condition. A special system was designed for the calibration of the strain-gage type soil-pressure transducers. The system consists of the calibration device, the controlled air-pressure system, signal conditioner, and the sensor data acquisition system, as indicated in Fig. A1 and Fig. A2.

The calibration device is a shallow cylindrical chamber with an inner diameter of 400 mm and a height of 30 mm. The chamber is made of a solid steel plate, which is the same material as the model retaining wall. The soil-pressure transducer was inserted through the bottom of the chamber. It is important that the surface of the sensor was installed flush with the upper face of the chamber. To simulate the interface between the sand particle and soil pressure transducer, 10 mm-thick sand layer was poured into the calibration device over the transducer. Then a 0.2 mm-thick rubber membrane was placed over the sandy layer, as shown in Fig. A.1.

A uniformly distributed air-pressure was applied on the membrane, over the soil particles, and transmitted to the transducer. The output voltage of the transducer was found to increase linearly with the increase of applied pressure, as shown in Fig. A.3 to Fig. A.7.

A rubber O-ring was arranged to prevent air leakage between the chamber and the cap. It should be noted that the air pressure applied for the calibration of transducer should be consistent with the operating pressure range for model wall experiments. To reduce the effect of sidewall friction, the thickness of sand layer in the chamber should be limited, so that the side-friction between the sand the sidewall of the chamber could be minimized. Fig. A.3 to Fig. A.7 shows the test results of the soil pressure transducers calibrated without the compressible layer. Table A.1 is a summary of the calibration factors of each soil pressure transducer.
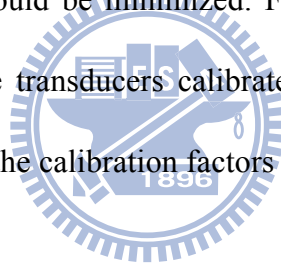
Table A1. Soil Pressure Transducer Calibration Factors

| Transducer No. | Dynamic Strain Amplifier | | | Capacity(kN/m^2) | Calibration Factor[(kN/m^2)/volt] |
	No.	Range Selector (*100 $\mu\xi$)	Calibration Setter($\mu\xi$)		
EZ0660029	1	5	1984	19.62	2.6688
YT4030032	2	5	2220	19.62	2.4831
EG6210005	3	5	2005	19.62	2.3121
FL8550012	4	5	1749	19.62	3.7238
EG6210026	5	5	1906	19.62	2.4413
FG9600006	6	5	1815	19.62	3.7774
FL8550010	7	5	1880	19.62	3.7389
YT4030029	8	5	2465	19.62	2.6630
FL8550011	9	5	2047	19.62	3.8036
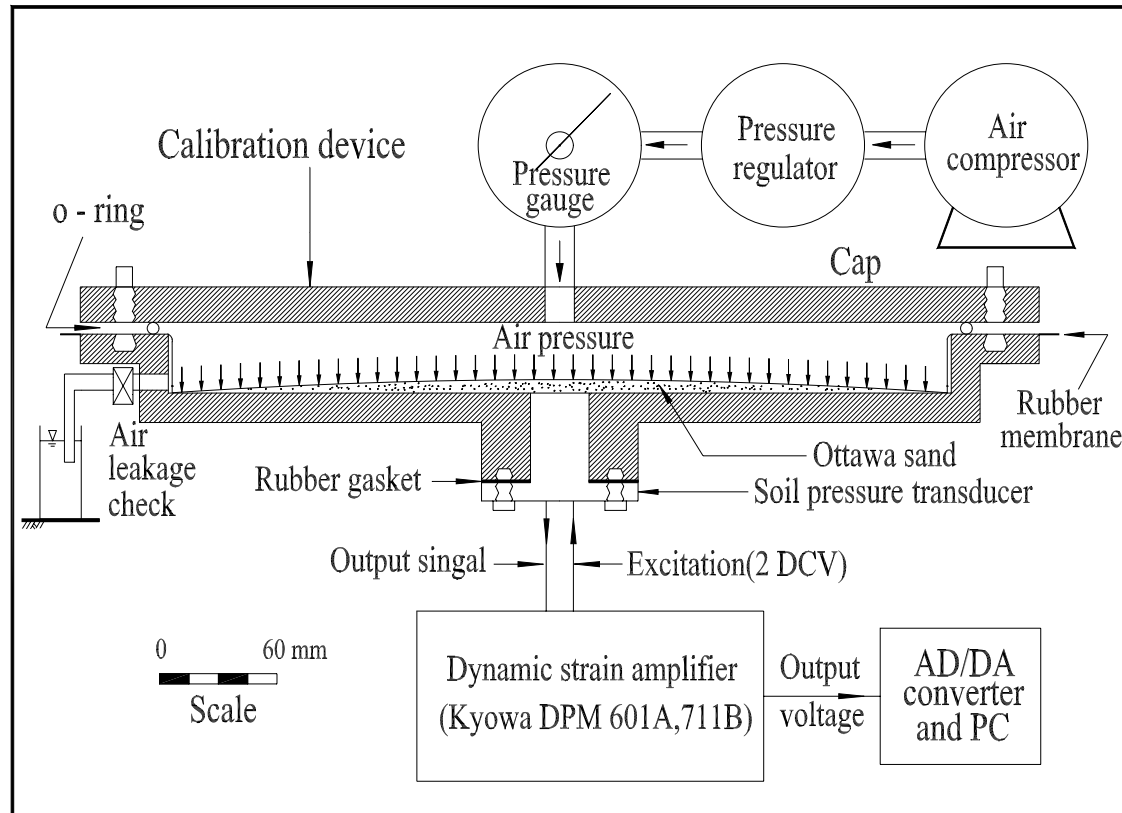
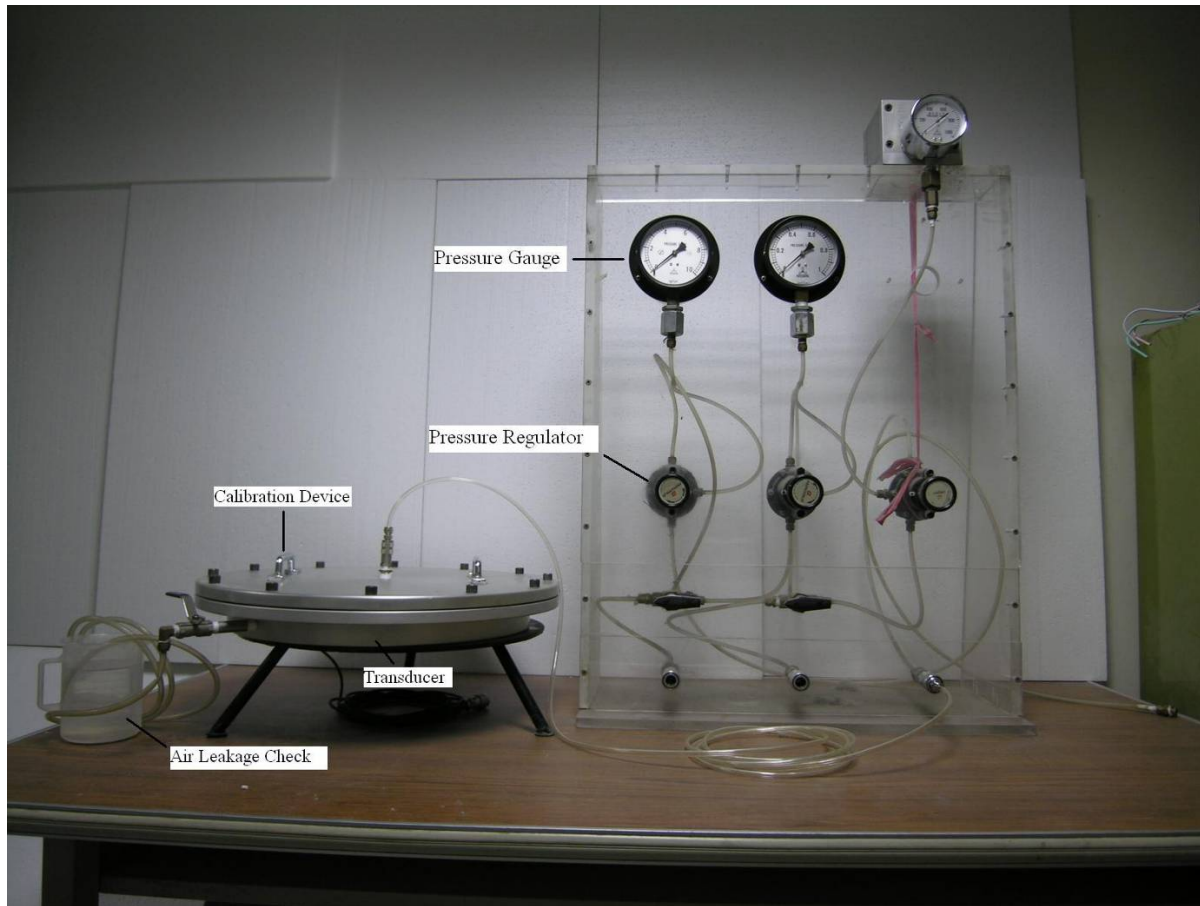Fig. A.1 Schematic diagram of the soil pressure transducer calibration system

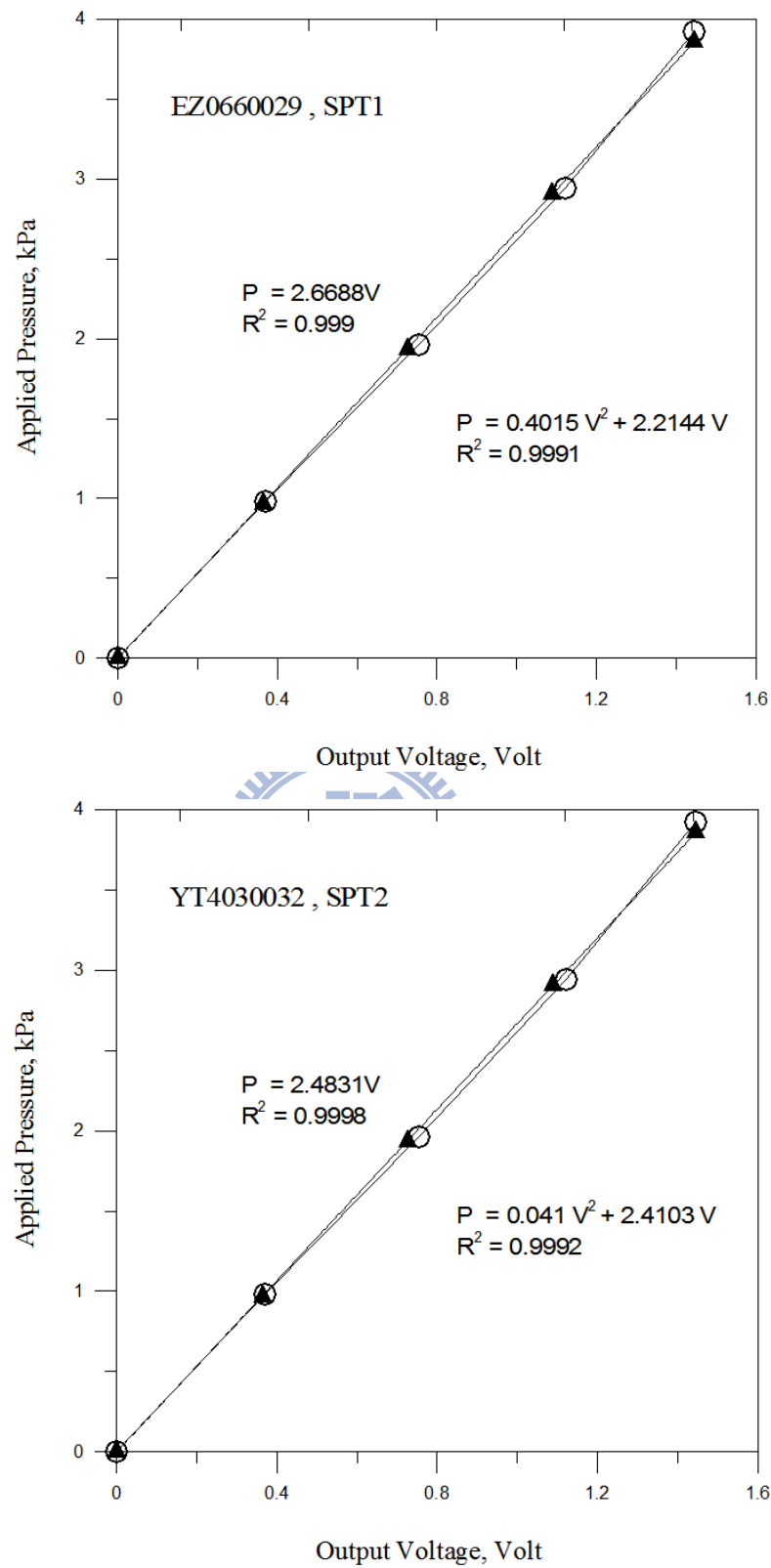Fig. A2. Soil pressure transducer calibration system

Fig. A3. Applied pressure versus voltage output for soil pressure
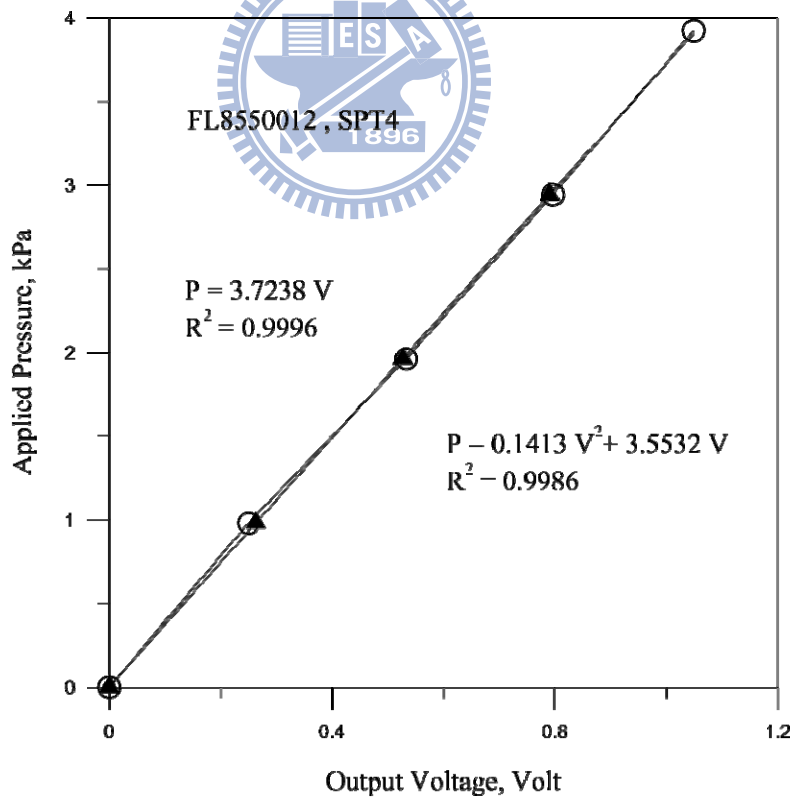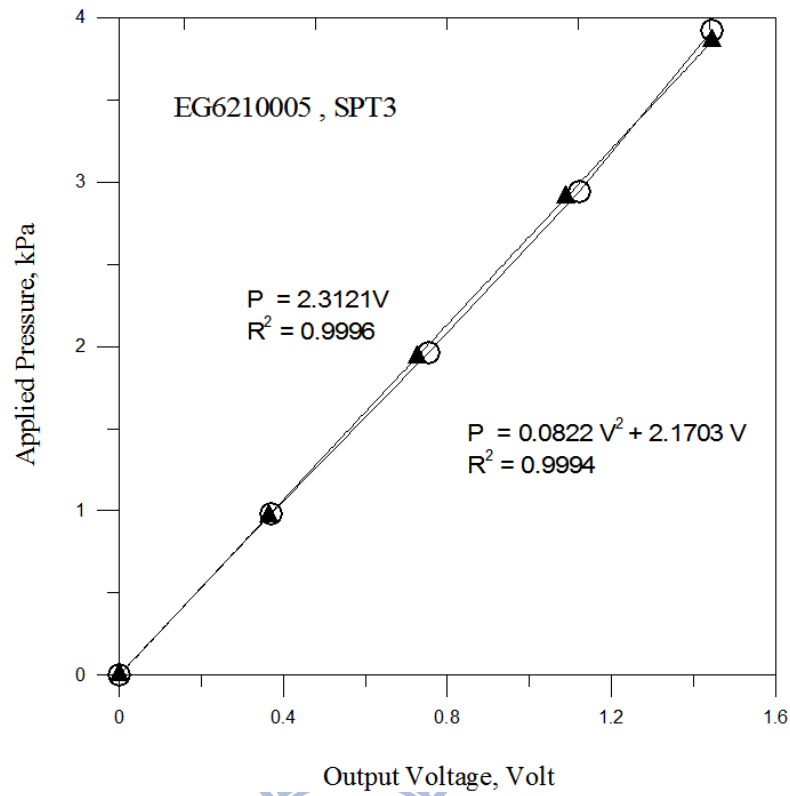
transducer SPT 1 and SPT 2

Fig. A4. Applied pressure versus voltage output for soil pressure
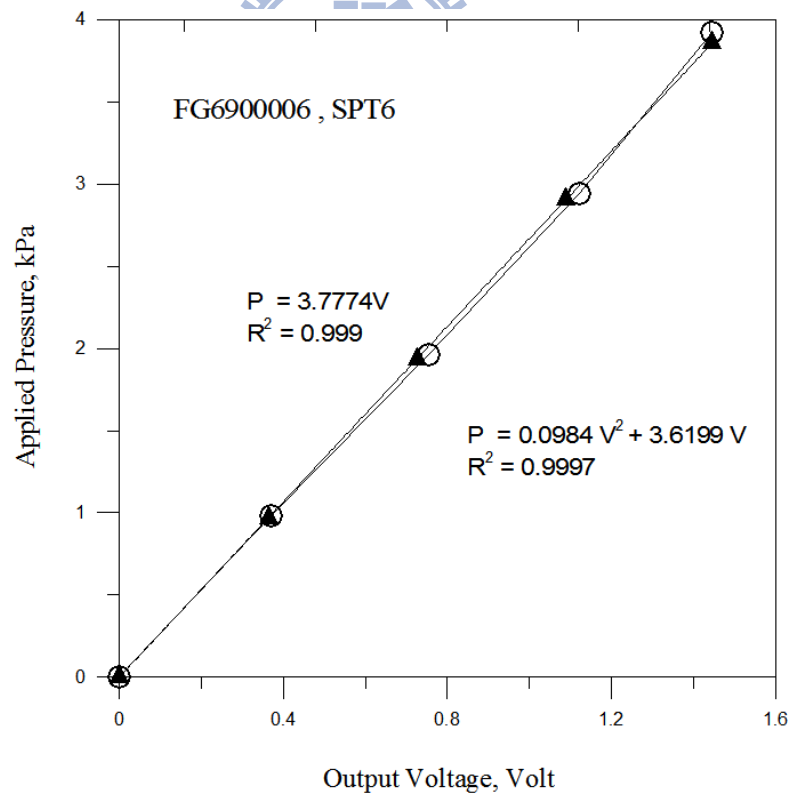
transducer SPT 3 and SPT 4

240

Fig. A5. Applied pressure versus voltage output for soil pressure

transducer SPT 5 and SPT 6

241

The graphs contain the following labels and equations:

Top graph (FL8550010, SPT7):

Y-axis: Applied Pressure, kPa
X-axis: Output Voltage, Volt

$P = 3.7389V$
$R^2 = 0.999$

$P = 0.0984 V^2 + 3.6199 V$
$R^2 = 0.9997$

Bottom graph (YT4030029, SPT8):

Y-axis: Applied Pressure, kPa
X-axis: Output Voltage, Volt

$P = 2.663V$
$R^2 = 0.9993$

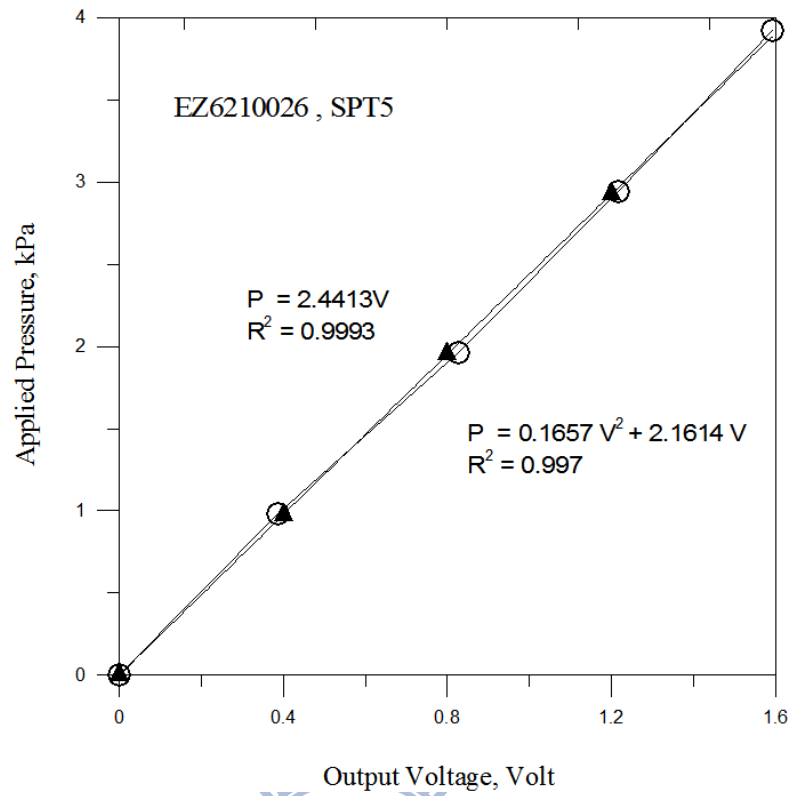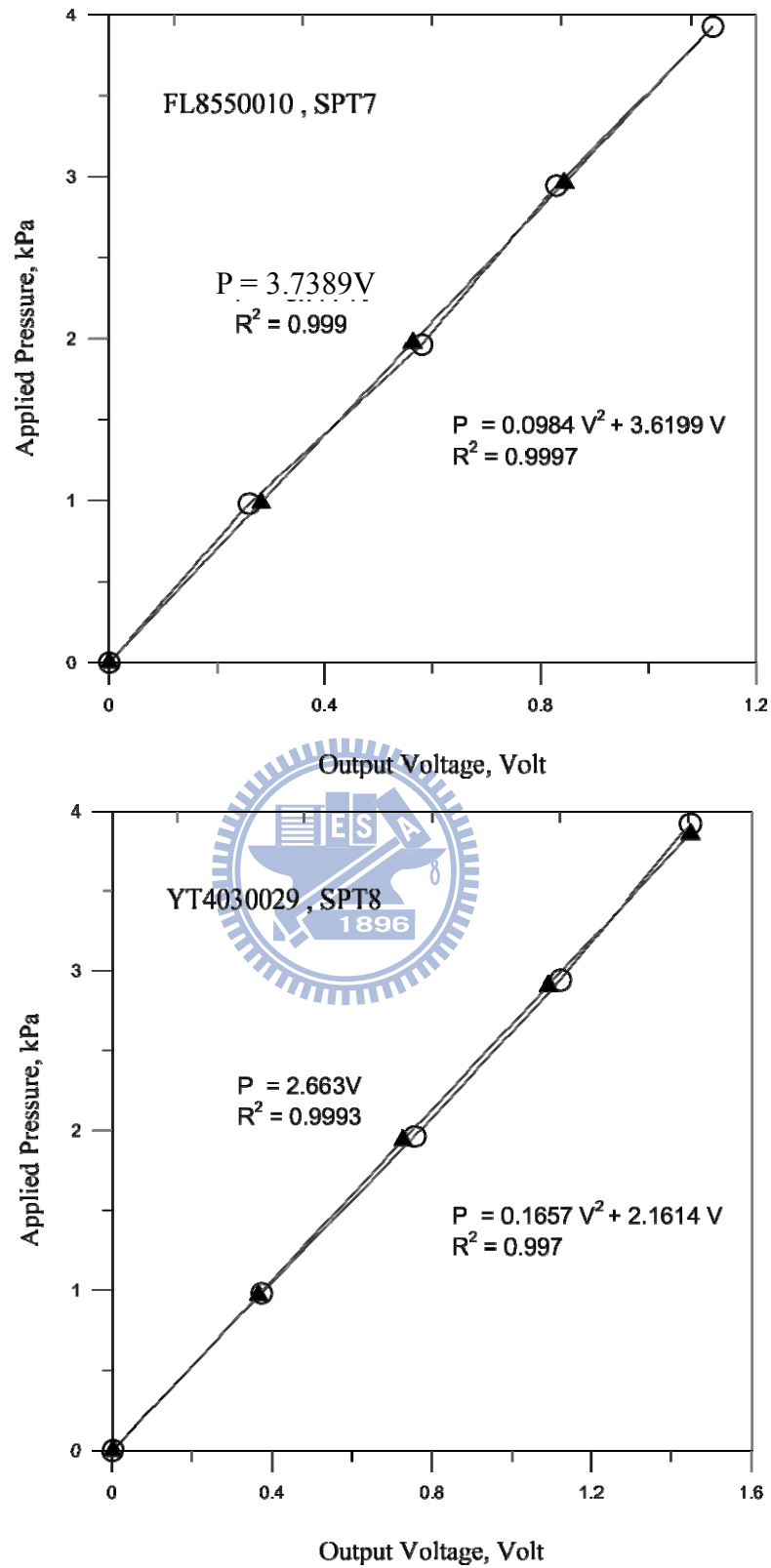$P = 0.1657 V^2 + 2.1614 V$
$R^2 = 0.997$

Fig. A6. Applied pressure versus voltage output for soil pressure
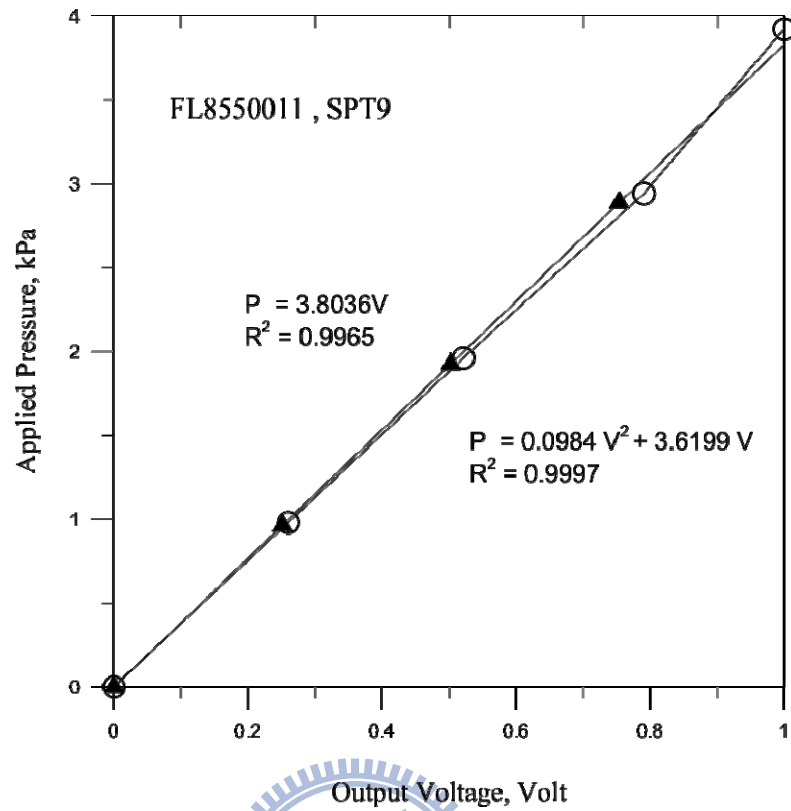
transducer SPT 7 and SPT 8

242

Fig. A7. Applied pressure versus voltage output for soil pressure
transducer SPT 9